

**Journal of
Mechanics of
Materials and Structures**

Volume 5, No. 3

March 2010

JOURNAL OF MECHANICS OF MATERIALS AND STRUCTURES

<http://www.jomms.org>

Founded by Charles R. Steele and Marie-Louise Steele

EDITORS

CHARLES R. STEELE Stanford University, U.S.A.
DAVIDE BIGONI University of Trento, Italy
IWONA JASIUK University of Illinois at Urbana-Champaign, U.S.A.
YASUhide SHINDO Tohoku University, Japan

EDITORIAL BOARD

H. D. BUI École Polytechnique, France
J. P. CARTER University of Sydney, Australia
R. M. CHRISTENSEN Stanford University, U.S.A.
G. M. L. GLADWELL University of Waterloo, Canada
D. H. HODGES Georgia Institute of Technology, U.S.A.
J. HUTCHINSON Harvard University, U.S.A.
C. HWU National Cheng Kung University, R.O. China
B. L. KARIHALOO University of Wales, U.K.
Y. Y. KIM Seoul National University, Republic of Korea
Z. MROZ Academy of Science, Poland
D. PAMPLONA Universidade Católica do Rio de Janeiro, Brazil
M. B. RUBIN Technion, Haifa, Israel
A. N. SHUPIKOV Ukrainian Academy of Sciences, Ukraine
T. TARNAI University Budapest, Hungary
F. Y. M. WAN University of California, Irvine, U.S.A.
P. WRIGGERS Universität Hannover, Germany
W. YANG Tsinghua University, P.R. China
F. ZIEGLER Technische Universität Wien, Austria

PRODUCTION

PAULO NEY DE SOUZA Production Manager
SHEILA NEWBERY Senior Production Editor
SILVIO LEVY Scientific Editor


Cover design: Alex Scorpan

See inside back cover or <http://www.jomms.org> for submission guidelines.

JoMMS (ISSN 1559-3959) is published in 10 issues a year. The subscription price for 2010 is US \$500/year for the electronic version, and \$660/year (+\$60 shipping outside the US) for print and electronic. Subscriptions, requests for back issues, and changes of address should be sent to Mathematical Sciences Publishers, Department of Mathematics, University of California, Berkeley, CA 94720-3840.

JoMMS peer-review and production is managed by EditFLOW™ from Mathematical Sciences Publishers.

PUBLISHED BY

 **mathematical sciences publishers**
<http://www.mathscipub.org>

A NON-PROFIT CORPORATION

Typeset in L^AT_EX

©Copyright 2010. Journal of Mechanics of Materials and Structures. All rights reserved.

CHAOTIC VIBRATIONS IN A DAMAGE OSCILLATOR WITH CRACK CLOSURE EFFECT

NOËL CHALLAMEL AND GILLES PIJAUDIER-CABOT

This paper deals with the dynamics of a single-degree-of-freedom unilateral damage oscillator. Using appropriate internal variables, the hysteretic dynamic system can be written as a nonsmooth autonomous system. The free dynamics of such a nonlinear system are simply reduced to periodic motion, eventually attractive trajectories, and divergent motion. The direct Lyapunov method is used to investigate the stability of the free damage system. A critical energy is highlighted that the oscillator can support while remaining stable. The natural frequency of the periodic motion depends on the stationary value of the damage internal variable. The inelastic forced oscillator, however, can exhibit very complex phenomena. When the damage parameter remains stationary, the dynamics are similar to those of an elastic oscillator with nonsymmetric stiffness. The dynamics appear to be controlled by the initial perturbations. Chaotic motions may appear in such a system, specifically for severely damaged oscillators. It is numerically shown that chaos is observed in the vicinity of the divergence zone (the collapse). This closeness of both behaviors — chaos and divergence — is probably related to the perturbation of the homoclinic orbit associated with the critical energy.

1. Introduction

Design procedures are becoming more and more oriented towards failure modes and structural ductility control. Modern building codes aim at incorporating basic characteristics that result from the nonlinear analysis of structures. In the case of seismic analysis, knowledge of the basic dynamics of inelastic systems (plastic or damageable systems) is among the main objectives. This is however quite an open issue because these models are nonsmooth dissipative systems and very few results have been established in this particular case [Wiercigroch 2000; Awrejcewicz and Lamarque 2003]. Although concrete structures are inelastic multiple-degree of freedom (DOF) systems, their dynamics are so complex that there is still room for use of a simple approach, based on single-DOF inelastic oscillators, in order to investigate and to illustrate their basic characteristics. The inelastic response of concrete structures is due to several causes: material nonlinearities, geometrical effects, interface, friction and contact problems, and others. Within the framework of a single-DOF inelastic oscillator, the influence of each source of nonlinearity on its dynamic response may be considered separately, its effect being investigated analytically or numerically. Here we consider material nonlinearities only with two consequences: a nonlinear softening response and a damage deactivation effect related to crack closure.

Up to now, most studies have been devoted to plastic oscillators. The pioneer analytical work of Caughey [1960] uses an equivalent asymptotic method to approximate the response of a plastic-kinematic

Keywords: damage oscillator, nonlinear dynamics, seismic design, concrete structures, chaos, unilateral effect, crack closure, breathing crack, bimodular material.

hardening oscillator loaded by a harmonic signal. Periodic motion has been found using numerical simulations of such a plastic oscillator, as in [Savi and Pacheco 1997]; see also [Challamel and Gilles 2007; Challamel et al. 2007; 2008] for the case of perfect plasticity. Limit cycles have been highlighted for the free undamped kinematic-hardening system [Pratap et al. 1994]. The same oscillator forced by a periodic load shows very rich phenomena in dynamics, and sometimes chaotic motion [Pratap and Holmes 1995]. The inelastic response of such a single-DOF oscillator results from a material nonlinear, plastic, response. Coupling with geometrical nonlinearities also leads to chaotic motion [Poddar et al. 1988]. Without being exhaustive, let us mention also that chaos may appear in a Bouc–Wen hysteretic oscillator [Lacarbonara and Vestroni 2003; Awrejcewicz et al. 2008]. It has to be pointed out that these material sources of nonlinearities are mainly investigated from a theoretical point of view, and very few papers have been devoted to the experimental evidence of chaos in these nonsmooth oscillators. [Wiercigroch and Sin 1988] can be cited for extensive experimental investigations on nonsmooth oscillators with piecewise linear restoring forces. [Ing et al. 2008] is also an experimental contribution on an impact oscillator with a one-sided elastic constraint. To the authors' knowledge, no paper has been published on the experimental study of nonlinear dynamics of forced damage oscillators.

Material damage is a degradation of the elastic stiffness in the oscillator due to microcracking which may become important [Aschheim and Black 1999; Williamson and Hjelmstad 2001]. The free dynamics of a damage oscillator exhibit a stationary periodic motion in a given perturbation domain [Challamel and Pijaudier-Cabot 2004]. The dynamics of a forced damage oscillator (without the crack closure effect) has been studied by DeSimone et al. [2001].

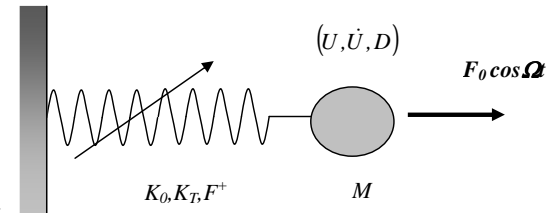
During the loading history, and more specifically for alternated loads, micro and macrocracks may open and close. Crack closure and contact conditions on the crack faces induce a characteristic response called the *unilateral* material response, which depends on the sign of the applied stresses: cracking and damage affect the material response in tension whereas the compression response remains elastic (see [Ortiz 1985; Mazars et al. 1990] or more recently [Challamel et al. 2005] for a discussion of this phenomenon in the framework of damage mechanics). In the case of crack closure, which induces typically some additional discontinuity in the response of the nonlinear single-DOF oscillator, chaotic responses have been found by investigating the solutions of the equations of motion in each subspace and gluing them together [Wiercigroch 2000]. Foong et al. [2003; 2007] compared experiments on a fatigue-testing rig involving crack closure effects to a numerical model of a bending cracked beam which exhibited chaos. Carpinteri and Pugno [2005a; 2005b] investigated the specific role of the breathing crack (the crack closure effect) on the response of a cracked cantilever beam (from an experimental and numerical point of view). They observed the period doubling bifurcation.

The objective of the present study is to investigate the dynamics of a nonlinear damage oscillator with nonsymmetric stiffness due to crack closure. The discontinuity induced by crack closure is taken into account in the model, unlike in the results of [DeSimone et al. 2001; Challamel and Pijaudier-Cabot 2004]. Compared to fracture mechanics, an advantage of continuous damage is that it folds microcracking, crack initiation (localization of damage), and crack propagation into a single framework [Mazars and Pijaudier-Cabot 1996]. As we will see further, the dissipative response of the oscillator can be introduced quite easily into a stability analysis, in addition to the nonsmooth character of the oscillator due to crack closure. We wish to investigate the influence of the degradation of the elastic properties of an oscillator due to (micro) cracking and damage deactivation due to crack closure at the same time within this rather general

framework which has become popular in structural analyses of failure (see for example the review by Bažant and Jirásek [2002]). Section 2 presents the basic equations. The free vibrations and the forced vibrations of the oscillator are discussed in the subsequent sections.

2. The general system

Consider the simple system shown on the right. A mass M is attached to a damage spring. The inelastic system is loaded by an external harmonic force. This oscillator is characterized by the displacement U , the velocity \dot{U} , and an additional internal variable characterizing the inelastic damage process. This damage variable, classically denoted by D , encodes the effect of microcracking in the spring of the oscillator in tension. It varies between 0 (the initial virgin state) and 1 (at failure). The damage law is schematized in Figure 1. Concrete, like many other geomaterials, has a nonsymmetric response in traction and compression. In tension, linear softening is assumed. This law depends on three parameters: the initial stiffness K_0 , the tangent stiffness K_T in the postpeak regime, which rules the damage evolution, and the maximum force F^+ . In the case of a softening process such as is considered in this paper, the tangent stiffness is negative ($K_T \leq 0$). It is assumed that concrete remains elastic in compression. Load levels where some nonlinear response is observed in compression are very high compared to tension and will not be considered for simplicity. The material response is unilateral, with a discontinuous stiffness upon the change of sign of the stress.



The material parameters of the model may be easily expressed in terms of characteristic displacements: U_Y is the maximum displacement of the initial elastic domain, and U_f is the displacement at failure, defined as

$$U_Y = \frac{F^+}{K_0}, \quad \frac{U_f}{U_Y} = 1 - \frac{K_0}{K_T}. \tag{1}$$

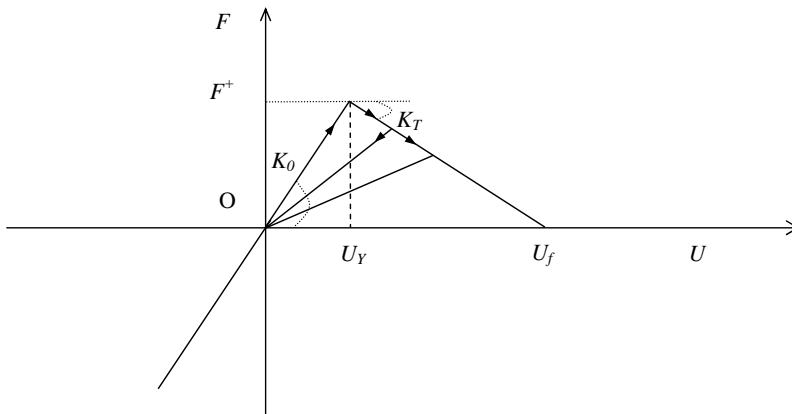


Figure 1. Damage incremental law for the inelastic spring.

In the meantime, the softening damage process can be characterized by one of the two dimensionless parameters u_f or κ^2 :

$$u_f = \frac{U_f}{U_Y}, \quad \kappa^2 = -\frac{K_T}{K_0} \Rightarrow u_f = 1 + \frac{1}{\kappa^2}. \tag{2}$$

The damage variable D can directly be expressed in terms of a memory variable V , defined as

$$V(t) = \max_t U(t), \tag{3}$$

and the relation between D and V is given by

$$D = \left\langle 1 + \frac{K_T}{K_0} \left\langle -1 - \frac{K_0 - K_T}{K_T} \frac{U_Y}{V} \right\rangle \right\rangle, \quad \text{where } \langle x \rangle = \begin{cases} x & \text{if } x \geq 0, \\ 0 & \text{if } x < 0. \end{cases} \tag{4}$$

It is easy to verify that the rate of damage is necessarily positive:

$$\dot{D} \geq 0, \tag{5}$$

and the classical thermodynamic inequality prescribing the positiveness of the damage dissipation rate of such scalar damage model is recovered.

Three dynamical states can be distinguished. These three states correspond to a reversible state (or elastic state) in the tension domain \hat{E}^+ , a reversible state in the compression domain \hat{E}^- , and an irreversible state \hat{D} (necessarily in the tension domain) associated with the evolution of damage:

$$\begin{cases} \hat{E}^+ \text{ state:} & M\ddot{U} + K_0(1 - D(V))U = F_0 \cos \Omega t, & \dot{D} = 0; \\ \hat{E}^- \text{ state:} & M\ddot{U} + K_0U = F_0 \cos \Omega t, & \dot{D} = 0; \\ \hat{D} \text{ state:} & M\ddot{U} + \langle K_T(U - U_f) \rangle = F_0 \cos \Omega t, & \dot{V} = \dot{U}. \end{cases} \tag{6}$$

Each state is defined from a partition of the phase space:

$$\begin{cases} \hat{E}^+ : (U > 0 \text{ or } (U = 0 \text{ and } \dot{U} \geq 0)) \text{ and } ((\dot{U} \leq 0) \text{ or } (\dot{U} \geq 0 \text{ and } U < V) \text{ or } (V < U_Y)); \\ \hat{E}^- : (U < 0 \text{ or } (U = 0 \text{ and } \dot{U} \leq 0)); \\ \hat{D} : (\dot{U} > 0) \text{ and } (U = V) \text{ and } (V \geq U_Y). \end{cases} \tag{7}$$

One can recognize in this set Kuhn–Tucker like conditions defining the growth of damage. In the \hat{E}^+ state (loading or unloading within the elastic domain), damage does not grow because the displacement is less than the history variable, or, if it is equal, unloading is being performed. In the \hat{E}^- state, crack closure occurs and the original stiffness of the oscillator is recovered. In the \hat{D} state, damage grows and the displacement U is equal to the history variable V at all times; the elastic domain grows at the same time. Note that the dissipative nature induces an additional regime compared to the usual nonsmooth oscillator.

Equations (6) and (7) describe a piecewise linear oscillator (see for instance [Shaw and Holmes 1983] for some fundamental properties of piecewise linear oscillators). The dimensionless phase variables are introduced as

$$(u, \dot{u}, v) = \left(\frac{U}{U_Y}, \frac{\dot{U}}{U_Y}, \frac{V}{U_Y} \right), \quad v = \max_t u(t). \tag{8}$$

New temporal derivatives are written directly with respect to the dimensionless time parameter

$$\tau = \frac{t}{t^*} \quad \text{with } t^* = \sqrt{\frac{M}{K_0}}, \quad (9)$$

where t^* is a time constant of the dynamical system. With dimensionless variables, the system of equations of the oscillator becomes

$$\left\{ \begin{array}{l} \hat{E}^+ : \quad \ddot{u} + (1 - D(v))u = f_0 \cos \omega \tau, \quad \dot{D} = 0, \\ \hat{E}^- : \quad \ddot{u} + u = f_0 \cos \omega \tau, \quad \dot{D} = 0, \\ \hat{D} : \quad \ddot{u} + \left\langle \frac{u - u_f}{1 - u_f} \right\rangle = f_0 \cos \omega \tau, \quad \dot{v} = \dot{u}, \end{array} \right\} \quad \text{with } f_0 = \frac{F_0}{F^+}, \quad \omega = \Omega t^*. \quad (10)$$

The damage function depends on the new dimensionless memory variable v :

$$D = \left\langle 1 + \frac{1}{1 - u_f} \left\langle -1 + \frac{u_f}{v} \right\rangle \right\rangle, \quad (11)$$

and the three states are now governed by

$$\left\{ \begin{array}{l} \hat{E}^+ : \quad (u > 0 \text{ or } (u = 0 \text{ and } \dot{u} \geq 0)) \text{ and } ((\dot{u} \leq 0) \text{ or } (\dot{u} \geq 0 \text{ and } u < v) \text{ or } (v < 1)); \\ \hat{E}^- : \quad (u < 0 \text{ or } (u = 0 \text{ and } \dot{u} \leq 0)); \\ \hat{D} : \quad (\dot{u} > 0) \text{ and } (u = v) \text{ and } (v \geq 1). \end{array} \right. \quad (12)$$

For $f_0 = 0$ (free vibrations), the system is autonomous with a three-dimensional phase space associated with the variables (u, \dot{u}, v) . The periodically forced oscillator ($f_0 \neq 0$) can be studied using an extended four-dimensional phase space with coordinates (u, \dot{u}, v, τ) .

Local solutions of (10) are known explicitly for each state. The solution of the \hat{E}^+ state, based on the initial conditions

$$(u(\tau_i), \dot{u}(\tau_i), v(\tau_i)) = (u_i, \dot{u}_i, v_i), \quad (13)$$

is written as

$$\left\{ \begin{array}{l} u(\tau) = A \cos \omega_i(\tau - \tau_i) + B \sin \omega_i(\tau - \tau_i) + \frac{f_0}{\omega_i^2 - \omega^2} \cos \omega \tau, \\ \dot{u}(\tau) = -\omega_i A \sin \omega_i(\tau - \tau_i) + \omega_i B \cos \omega_i(\tau - \tau_i) - \frac{f_0 \cdot \omega}{\omega_i^2 - \omega^2} \sin \omega \tau, \\ v(\tau) = v_i, \end{array} \right. \quad (14)$$

where

$$\begin{aligned} \omega_i &= \sqrt{1 - D(v_i)}, \\ A &= u_i - \frac{f_0}{\omega_i^2 - \omega^2} \cos \omega \tau_i, \\ B &= \frac{\dot{u}_i}{\omega_i} + \frac{f_0 \omega}{\omega_i(\omega_i^2 - \omega^2)} \sin \omega \tau_i. \end{aligned}$$

The solution of the \hat{E}^- state, based on the initial conditions (13), is

$$\begin{cases} u(\tau) = A \cos(\tau - \tau_i) + B \sin(\tau - \tau_i) + \frac{f_0}{1 - \omega^2} \cos \omega \tau, \\ \dot{u}(\tau) = -A \sin(\tau - \tau_i) + B \cos(\tau - \tau_i) - \frac{f_0 \cdot \omega}{1 - \omega^2} \sin \omega \tau, \\ v(\tau) = v_0, \end{cases} \tag{15}$$

where

$$A = u_i - \frac{f_0}{1 - \omega^2} \cos \omega \tau_i \quad B = \dot{u}_i + \frac{f_0 \omega}{1 - \omega^2} \sin \omega \tau_i.$$

The solution of the \hat{D} state, based on the initial conditions (13), is

$$\begin{cases} u(\tau) = A e^{-\kappa(\tau - \tau_i)} + B e^{\kappa(\tau - \tau_i)} - \frac{f_0}{\kappa^2 + \omega^2} \cos \omega \tau + 1 + \frac{1}{\kappa^2}, \\ \dot{u}(\tau) = -A \kappa e^{-\kappa(\tau - \tau_i)} + B \kappa e^{\kappa(\tau - \tau_i)} + \frac{f_0 \omega}{\kappa^2 + \omega^2} \sin \omega \tau, \\ v(\tau) = u(\tau), \end{cases} \tag{16}$$

where

$$A = \frac{f_0}{2\kappa(\kappa^2 + \omega^2)} (\kappa \cos \omega \tau_i + \omega \sin \omega \tau_i) - \frac{1}{2} \left(1 + \frac{1}{\kappa^2} \right) - \frac{1}{2\kappa} \dot{u}_i + \frac{1}{2} u_i,$$

$$B = \frac{f_0}{2\kappa(\kappa^2 + \omega^2)} (\kappa \cos \omega \tau_i - \omega \sin \omega \tau_i) - \frac{1}{2} \left(1 + \frac{1}{\kappa^2} \right) + \frac{1}{2\kappa} \dot{u}_i + \frac{1}{2} u_i.$$

The limit case of the oscillator completely broken ($D = 1$) yields the differential equation $\ddot{u} = f_0 \cos \omega \tau$ and the solution:

$$u(\tau) = A \tau + B - \frac{f_0}{\omega^2} \cos \omega \tau, \quad \dot{u}(\tau) = A + \frac{f_0}{\omega} \sin \omega \tau, \tag{17}$$

where

$$A = \dot{u}_i - \frac{f_0}{\omega} \sin \omega \tau_i, \quad B = u_i + \frac{f_0}{\omega^2} \cos \omega \tau_i - \left(\dot{u}_i - \frac{f_0}{\omega} \sin \omega \tau_i \right) \tau_i.$$

The times of flight in each region (each state) cannot be found in closed form in the general case and piecing together these known solutions is not directly possible directly. Before that, the time which characterizes the transition between each state is computed from a Newton–Raphson procedure. Note that this solution is considerably more accurate than the usual numerical solutions of ordinary differential equations, the only approximations being made at the boundary of each state.

3. Free vibrations: $f_0 = 0$

3.1. Existence of a stability domain. The following generic perturbation is considered:

$$\tau_0 = 0 : (u_0, \dot{u}_0, v_0) = (0, \dot{u}_0, 0), \quad \text{with } \dot{u}_0 \leq 0. \tag{18}$$

If $\dot{u}_0 \geq -1$, elastic behavior prevails and the trajectory is a circle in the phase space restricted to $D = 0$. On the opposite case, if $\dot{u}_0 < -1$, the motion is also composed of a damage inelastic phase. The time τ_1

necessary to initiate this damage phase is computed from

$$u(\tau_1) = 1, \quad \dot{u}(\tau_1) = \sqrt{\dot{u}_0^2 - 1}. \tag{19}$$

During this damage phase, the solution $u(\tau)$ is expressed by (16). Three types of dynamic responses can be distinguished from the sign of the constant B . A critical speed is then introduced:

$$\dot{u}_c = \sqrt{u_f}. \tag{20}$$

The size of the perturbation governs the stability of the origin point:

$$\begin{cases} |\dot{u}_0| > \dot{u}_c & \Rightarrow \lim_{\tau \rightarrow \infty} u(\tau) = \infty, \\ |\dot{u}_0| = \dot{u}_c & \Rightarrow \lim_{\tau \rightarrow \infty} u(\tau) = 0, \\ |\dot{u}_0| < \dot{u}_c & \Rightarrow \text{stationary periodic regime.} \end{cases} \tag{21}$$

In the last case, another elastic phase is initiated and the motion is periodic. Free dynamics of such an inelastic system can be reduced to the periodic regime (waiting for a certain time), and the attractive or divergent trajectories (see also [Challamel and Pijaudier-Cabot 2004]). For the broken oscillator, the autonomous system at failure is characterized by

$$\ddot{u} = 0 \quad \Rightarrow \quad \begin{cases} u(\tau) = \dot{u}_i(\tau - \tau_i) + u_f, \\ \dot{u}(\tau) = \dot{u}_i. \end{cases} \tag{22}$$

The phase portrait is a horizontal line parallel to the u -axis.

The same kind of classification would be observed for the free vibrations of the plastic softening oscillator [Challamel and Pijaudier-Cabot 2006]. These three cases are distinguished by the value of the initial speed \dot{u}_0 with respect to the critical speed \dot{u}_c . The different types of dynamics are plotted on Figure 2. For the simulations, parameters are chosen as $u_f = 3$ with the following initial conditions:

$$\begin{aligned} u_0 = v_0 = 0, \quad \dot{u}_0 &= -0.5; \\ u_0 = v_0 = 0, \quad \dot{u}_0 &= -1; \\ u_0 = v_0 = 0, \quad \dot{u}_0 &= -1.5; \\ u_0 = v_0 = 0, \quad \dot{u}_0 &= -\sqrt{3} = -\dot{u}_c; \\ u_0 = v_0 = 0, \quad \dot{u}_0 &= -2. \end{aligned} \tag{23}$$

For sufficiently large perturbations, the motion diverges. For sufficiently small perturbations, the motion is described by a circular (in the compression domain) or an elliptic (in the tension domain) periodic trajectory after a damage phase. The intermediate trajectory, represented on Figure 2, is an attractive trajectory. It asymptotically converges towards a fixed point. This attractive trajectory (homoclinic orbit) is structurally unstable. It is in fact the limit of the domain of perturbations generating bounded evolutions and also the limit of the domain associated with stability of the origin (in the sense of Lyapunov). This domain is defined by:

$$u_0^2 + \dot{u}_0^2 \leq u_f, \quad u_0 \leq v_0 \leq 1. \tag{24}$$

For seismic design applications, (24) can be interpreted as a critical energy (induced by seismic solicitation for instance) that the oscillator can support in order to remain stable. For a higher seismic energy

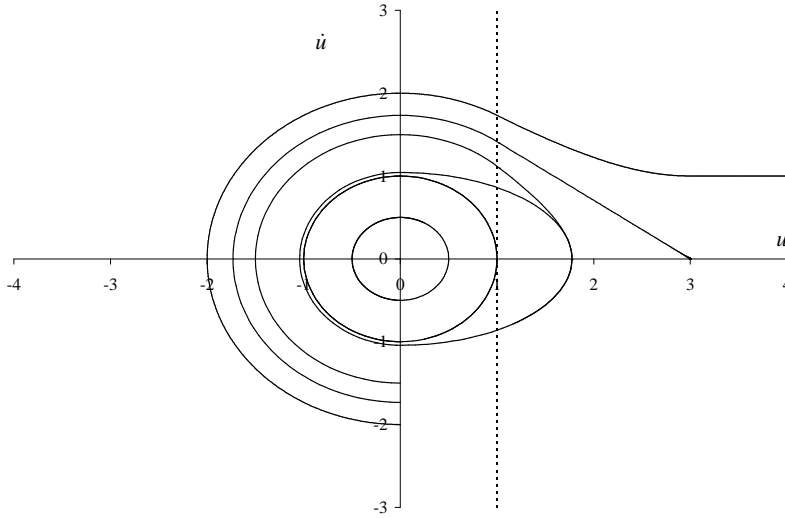


Figure 2. Dynamics of the free damage system.

level, a divergent evolution is present, leading to structural collapse. This critical energy is nothing but the energy dissipated by completely damaging the spring and is equal to the area under the monotonic force extension diagram (see [Challamel and Pijaudier-Cabot 2006] for the plastic softening oscillator). Moreover, when the motion is periodic, the damage reaches a stationary value denoted by \bar{D} . The global pulsation of this periodic motion can be obtained in closed-form solution from

$$\bar{\omega} = \frac{2\sqrt{1-\bar{D}}}{1+\sqrt{1-\bar{D}}}. \quad (25)$$

A similar relationship can be found in [Ryue and White 2007] where the damage parameter is replaced by the relative crack depth.

3.2. The direct Lyapunov method. The critical energy related to the stability domain can also be determined by means of a stability analysis based on the direct Lyapunov method. We follow the reasoning of [Kounadis 1996] for a smooth softening elastic system. We stress that the direct Lyapunov method was initially developed by Lyapunov for smooth systems; see for instance [la Salle and Lefschetz 1961]. The extension of such methodology to nonsmooth systems is a recent topic since the pioneer work of Filippov [1960; 1988]; for examples see [Shevitz and Paden 1994; Wu and Sepehri 2001; Bourgeot and Brogliato 2005; Leine 2006]. An application of this method to plastic systems can be found in [Challamel and Gilles 2007]. For the nonsmooth damage system, the Lyapunov function can be chosen as

$$V(u, \dot{u}, D) = \frac{1}{2}u^2 - \frac{1}{2}D\langle u \rangle^2 + \frac{1}{2}\dot{u}^2. \quad (26)$$

In this energy function, the damage variable is coupled to the positive part of the displacement (this is similar to the unilateral continuum damage model of [Challamel et al. 2005] at the material scale). $V(u, \dot{u}, D)$ is not a positive definite function over the complete space. The function V is vanishing for the trivial state $(u, \dot{u}, D) = (0, 0, 0)$, but also at failure when the oscillator is fully damaged: $(u, \dot{u}, D) = (u \geq 0, 0, 1)$.

However, if it is assumed that the oscillator is not fully damaged ($D < 1$), it can be rigorously proven that $V(u, \dot{u}, D)$ is effectively a definite positive function.

The direct Lyapunov method is based on the calculation of the time derivative of V . The time derivative of V involves the growth of damage, that is, the dissipative nature of the response of the oscillator in addition to the nonsmooth character captured with the positive part of the displacement introduced in the function. The time derivative of the Lyapunov function does not exist in the classical sense at the intersection of the elastic and the damage states (it only exists almost everywhere). It can be convenient to present the dynamic system with the nonsmooth functions:

$$\begin{cases} \ddot{u} + u - D(v)\langle u \rangle = 0, \\ \dot{v} = 2h(u - v)\dot{u}, \end{cases} \quad h(x) = \begin{cases} 1 & \text{if } x > 0, \\ \frac{1}{2} & \text{if } x = 0, \\ 0 & \text{if } x < 0, \end{cases} \quad (27)$$

where h is a step function. The nonsmooth character of such a system is no longer ambiguous with this unified presentation. In particular, the damage rate is discontinuous at the elastic-damage interface. Additionally, the displacement rates can be discontinuous at the origin if the damage is nonzero.

The application of the direct Lyapunov method is much simplified when one considers the internal variable v instead of D . It is possible to show that

$$\frac{dV(u, \dot{u}, v)}{d\tau} \in \dot{\hat{V}}, \quad \text{where } \dot{\hat{V}} = \left(\frac{\partial V}{\partial u}, \frac{\partial V}{\partial \dot{u}}, \frac{\partial V}{\partial v} \right) \begin{pmatrix} \dot{u} \\ -u + D(v)\langle u \rangle \\ 2K[h(u - v)]\dot{u} \end{pmatrix}. \quad (28)$$

K is called Filippov's set. It can be calculated for the Heaviside function:

$$K[h(x)] = H(x), \quad \text{with } H(x) = \begin{cases} 1 & \text{if } x > 0, \\ [0, 1] & \text{if } x = 0, \\ 0 & \text{if } x < 0. \end{cases} \quad (29)$$

$\dot{\hat{V}}$ can then be simplified as:

$$\dot{\hat{V}} = \frac{\partial V}{\partial D} \frac{\partial D}{\partial v} 2\dot{u}H(u - v) = -\frac{1}{2}\langle u \rangle^2 \frac{\partial D}{\partial v} 2\dot{u}H(u - v). \quad (30)$$

The final result is obtained:

$$\begin{cases} \hat{E}^+, \hat{E}^- : & \dot{\hat{V}} = 0, \\ \hat{D} : & \dot{\hat{V}} = -\frac{u^2}{2} \dot{D} \leq 0. \end{cases} \quad (31)$$

V is a positive and definite function. Each element of $\dot{\hat{V}}$ is negative or zero — as the damage is necessarily an increasing function of the time, see (5). Then, the origin $(0, 0, 0)$ is stable in the sense of Lyapunov for sufficiently small perturbations (in fact all perturbations leading to $D < 1$). The boundary of this stability domain is exactly the stability domain exhibited by Equation (24). It is worth mentioning that the particular case of the fully damaged oscillator leads to:

$$D = 1 \quad \Rightarrow \quad V(u, \dot{u}) = \frac{1}{2}u^2 + \frac{1}{2}\dot{u}^2 \quad \Rightarrow \quad \dot{V} = u\dot{u} \geq 0 \quad \text{since } \ddot{u} = 0. \quad (32)$$

In this case, one cannot apply rigorously the instability theorem of the direct Lyapunov method, but (32) gives us some information about the instability of the fully damaged oscillator.

4. Forced vibrations: general case

Numerical simulations show that two types of responses may be observed, namely the shakedown response (damage shakedown means that $\dot{D} = 0$ after a critical time), and the collapse characterized by a divergent evolution (in such a case, failure is reached and $D = 1$). The theoretical analysis consists in treating the bounded dynamics (in the case of damage shakedown) as an equivalent elastic oscillator after a critical time (as in [Poddar et al. 1988], for instance). The extended four-dimensional phase space with coordinates (u, \dot{u}, v, τ) can be reduced to a three-dimensional phase space with coordinates (u, \dot{u}, τ) . The new oscillator is an elastic oscillator with different stiffnesses in tension and compression. The results of [Shaw and Holmes 1983; Thompson et al. 1983; Mahfouz and Badrakhhan 1990] can be used for the dynamics of the oscillator studied in the three-dimensional phase space.

We shall employ the Poincaré section method to investigate the response of the forced inelastic oscillator. In the case of elastic evolutions, damage remains constant ($D = \bar{D}$) and the motion can be studied using the three-dimensional phase space with coordinates (u, \dot{u}, τ) . The vector field defined by (6) is easily seen to be $2\pi/\omega$ periodic in τ . The Poincaré section is useful to investigate properties of the dynamical system: the phase space is sliced by the map

$$\frac{(u, \dot{u}, \tau)}{\tau} \equiv \tau_0 \left[\frac{2\pi}{\omega} \right]. \tag{33}$$

Numerical simulations have been conducted with the following realistic parameters:

$$u_f = 3, \quad f_0 = 0.05, \quad \omega = 0.2, \quad u_0 = 0, \quad \dot{u}_0 = 0. \tag{34}$$

The value of v_0 (equivalently, the value of the initial damage D_0) was varied in order to investigate the damage effect. Periodic, quasiperiodic, chaotic, and divergent behaviors are observed, distributed as Figure 3.

For the virgin material ($v_0 \leq 1$ or $D_0 = 0$), with the parameters chosen, the motion is periodic (Figure 4, left) and the Poincaré map of the harmonic motion (Figure 4, right) is a single point $(0, 0)$. With the chosen initial conditions ($u_0 = 0; \dot{u}_0 = 0$), the damage parameter remained stable ($\bar{D} = D_0 = 0$). Quasiperiodic motion (Figure 5) has also been found for a system with moderate damage ($v_0 > 1$ or $D_0 \neq 0$). The quasiperiodic nature of the motion is checked in the Poincaré map on Figure 5, right. The damage value has not varied during the simulation ($v_0 = 1.25, \bar{D} = D_0 = 0.30$): the constant stiffness ratio in tension and compression is equal to $1 - \bar{D}$. The parameter f_0 is not so significant if only elastic

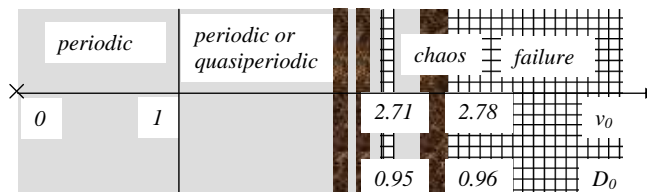


Figure 3. Bifurcation diagram for $f_0 = 0.05; \omega = 0.2; u_f = 3; u_0 = 0; \dot{u}_0 = 0$.

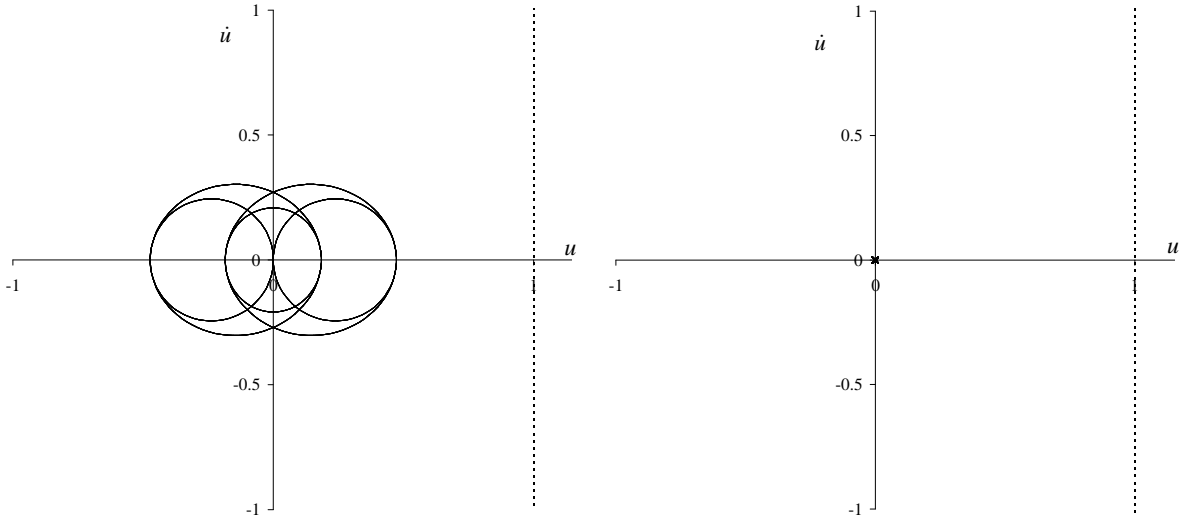


Figure 4. Periodic motion: phase portrait (left) and Poincaré map (right) for $f_0 = 0.25$, $\omega = 0.2$, $u_f = 3$, $v_0 = 0$ ($D_0 = 0$).

states prevail during the evolution ($\dot{D} = 0$). In such a case, all phase portraits are geometrically similar, transformed from a reference case (with adapted initial conditions). For size reasons, $f_0 = 0.25$ has been adopted for simulations of Figures 4 and 5 but the case $f_0 = 0.05$ can be directly deduced from these graphics (as in the bifurcation diagram of Figure 3). With the initial conditions chosen, failure can be reached for $v_0 \in [2.62, 2.66]$ or $v_0 > 2.78$ (except for the marginal value of $v_0 = 2.82$). It strongly depends on initial conditions. In the simulation plotted in Figure 6 ($v_0 = 2.65$ or $D_0 = 0.934$), damage shakedown does not occur and failure is reached after several cycles ($\bar{D} = 1$). For $v_0 = 2.71$ ($D_0 = \bar{D} = 0.946$),

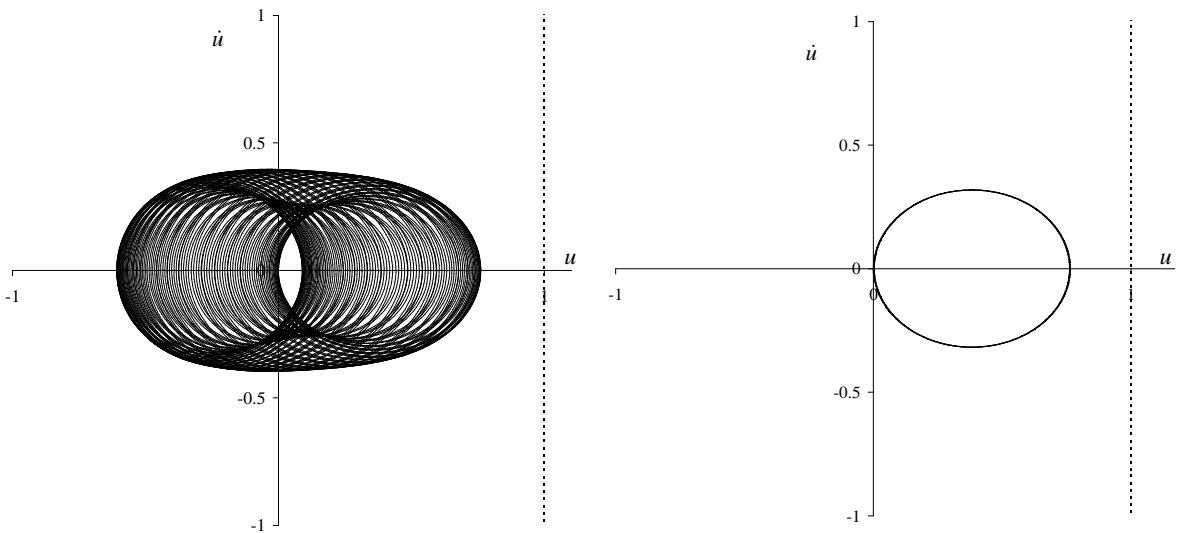


Figure 5. Quasiperiodic motion: phase portrait (left) and Poincaré map (right) for $f_0 = 0.25$, $\omega = 0.2$, $u_f = 3$, $v_0 = 1.25$ ($D_0 = 0.3$).

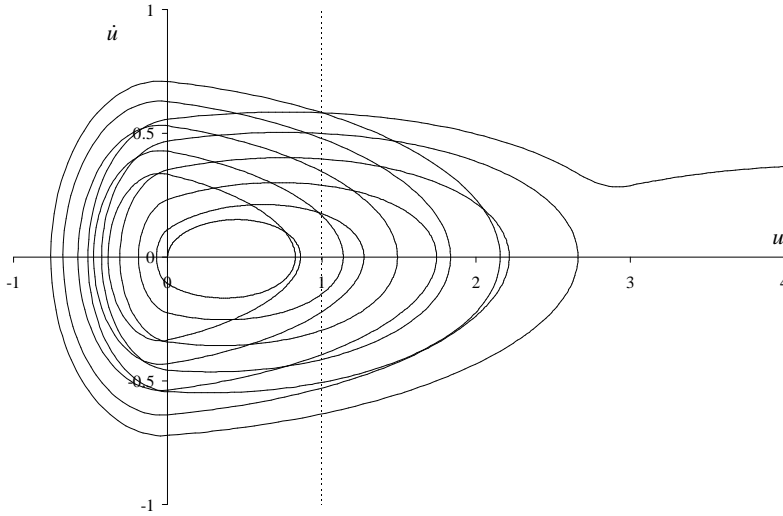


Figure 6. Divergent motion: phase portrait for $f_0 = 0.05$, $\omega = 0.2$, $u_f = 3$, $v_0 = 2.65$ ($D_0 = 0.934$).

chaos is observed (see further in [Figure 9](#), right). Chaotic vibrations are also observed for higher damage values ($v_0 \in [2.71, 2.78]$ or $D_0 \in [0.946, 0.960]$) or smaller damage values ($v_0 \in [2.26, 2.32]$ or $D_0 \in [0.836, 0.853]$; $v_0 \in [2.48, 2.49]$ or $D_0 \in [0.895, 0.898]$; $v_0 \in [2.55, 2.58]$ or $D_0 \in [0.912, 0.919]$). These intermittent characteristic damage parameters are close to 1, that is close to the failure value. Figures [7](#) and [8](#) show phase portraits and Poincaré maps of the motion numerically observed before the transition to chaotic motion. In fact, the crisis is sudden. A subharmonic motion of order 3 is recognized on [Figure 7](#), right, and a subharmonic of order 43 for [Figure 8](#), right. The phase portrait of [Figure 9](#), left, is difficult to analyze, whereas chaotic motion is clearly exhibited in [Figure 9](#), right, and [Figure 10](#). A symmetry is

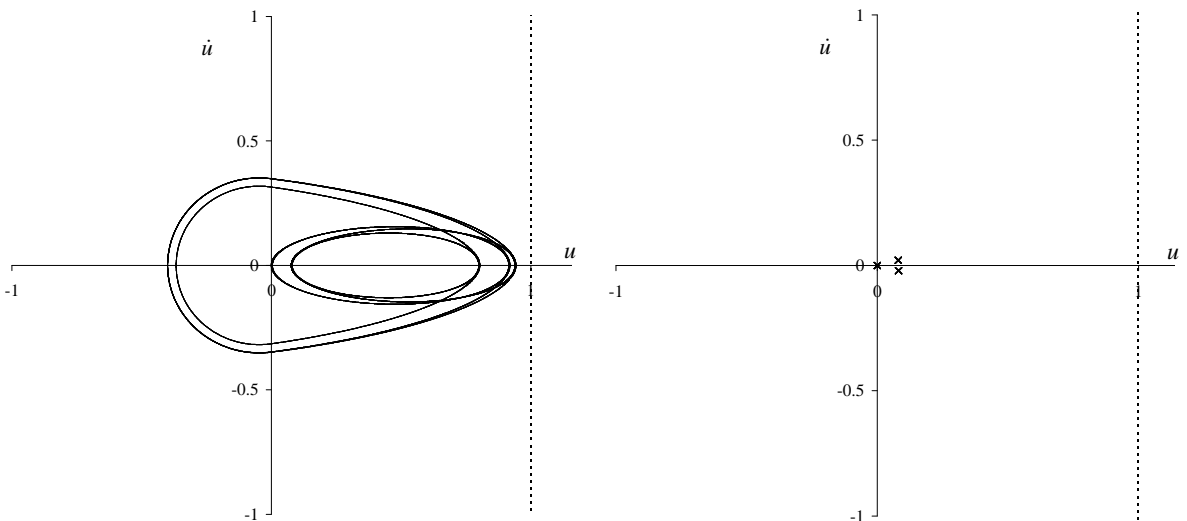


Figure 7. Periodic motion: phase portrait (left) and Poincaré map (right) for $f_0 = 0.05$, $\omega = 0.2$, $u_f = 3$, $v_0 = 2.68$ ($D_0 = 0.940$).

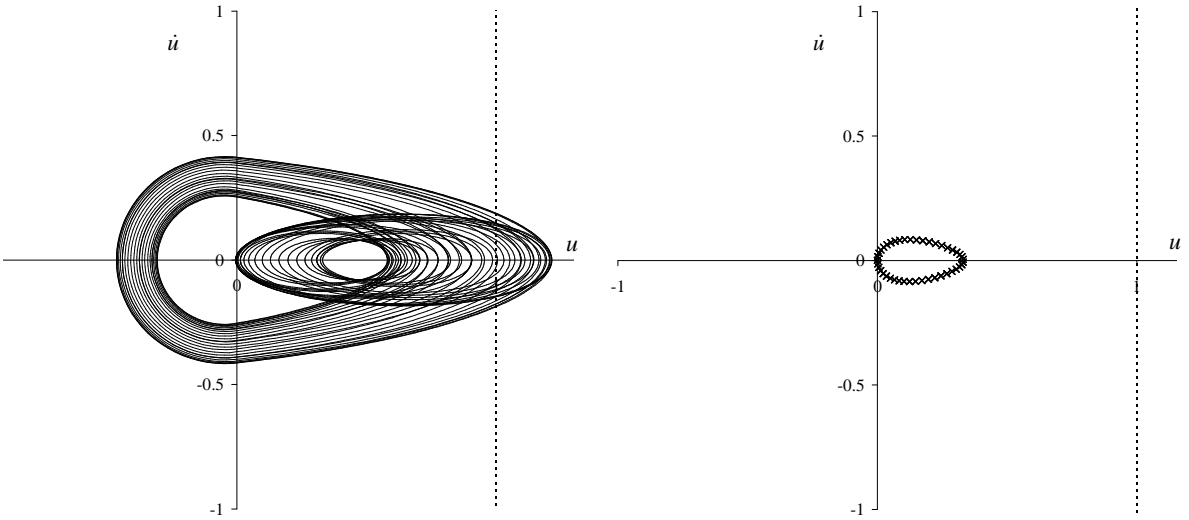


Figure 8. Periodic motion: phase portrait (left) and Poincaré map (right) for $f_0 = 0.05$, $\omega = 0.2$, $u_f = 3$, $v_0 = 2.70$ ($D_0 = 0.944$).

observed in the phase space. Twenty-four thousand cycles have been considered for the Poincaré section applied to chaotic motion. Hence, it is numerically shown that chaos is observed in the vicinity of the divergence zone (see Figure 9, right, and Figure 10, for instance). This closeness of both behaviors, chaos and divergence, is probably related to the perturbation of the homoclinic orbit, associated with the critical energy. The Appendix details this argument, and the possible application of the Melnikov method to an analogous elastic oscillator.

For the simulations considered, chaos is found for large values of the damage: chaos can be considered as a route to collapse. Nevertheless, chaos has been difficult to observe from the initial state ($D_0 = 0$), meaning that this phenomenon is generally a transient phenomenon. Mahfouz and Badrakhan [1990] show that chaos can appear for large stiffness ratios. The asymptotic case is here the limit where the

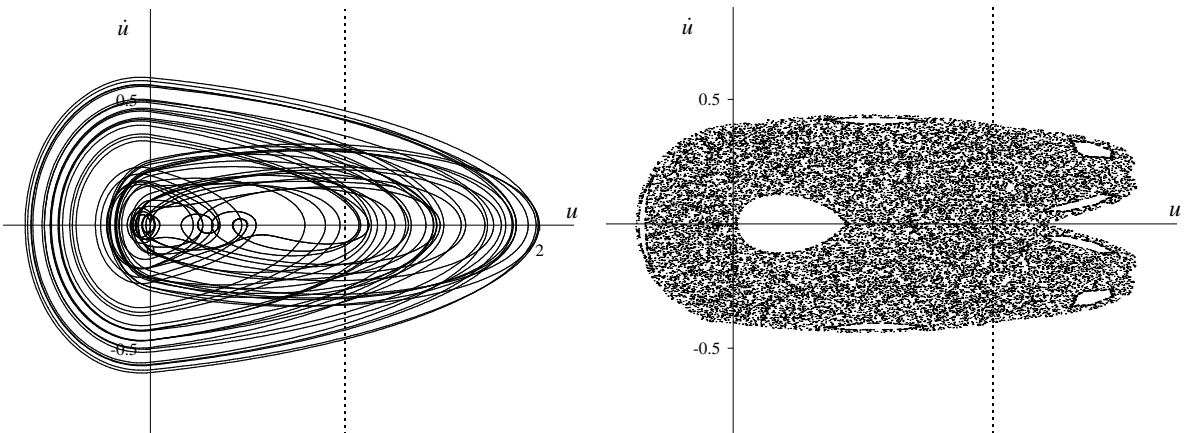


Figure 9. Chaotic motion: phase portrait (left) and Poincaré map (right) for $f_0 = 0.05$, $\omega = 0.2$, $u_f = 3$, $v_0 = 2.71$ ($D_0 = 0.946$).

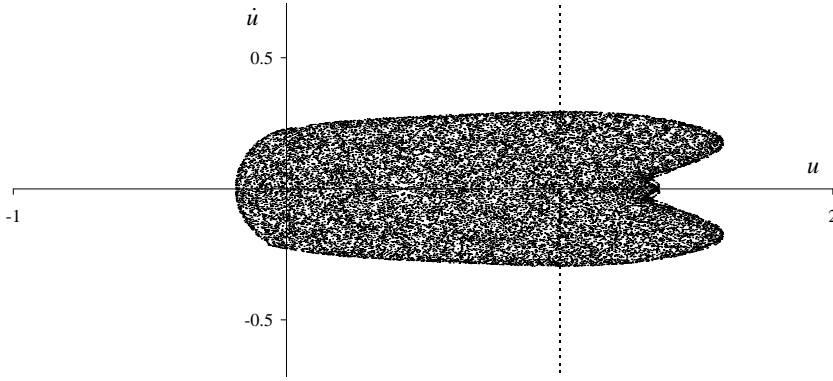


Figure 10. Chaotic motion: Poincaré map for $f_0 = 0.05$; $\omega = 0.2$; $u_f = 3$; $v_0 = 2.75$ ($D_0 = 0.955$).

stiffness ratio vanishes (the case treated by [Thompson et al. 1983] for instance). Understanding damage shakedown is also important for investigating the safety margins of concrete structures. Figure 11 shows a case of successful damage shakedown. The oscillator started in its initial state ($D_0 = 0$) and the stationary damage value associated with the final periodic motion is equal to $\bar{D} = 0.423$. In view of this result and of those in Figures 6–10, we see that damage shakedown is strongly dependent on initial conditions. For instance, a divergent evolution can be achieved for a sufficiently perturbed damage oscillator. This is different from the results observed for an elastic, perfectly plastic oscillator, where elastoplastic shakedown does not depend on initial conditions [Challamel 2005; Challamel et al. 2005].

This study was restricted to an undamped system, but existing results from [Shaw and Holmes 1983; Thompson et al. 1983; Mahfouz and Badrakhan 1990] suggest that the main phenomena exhibited in this

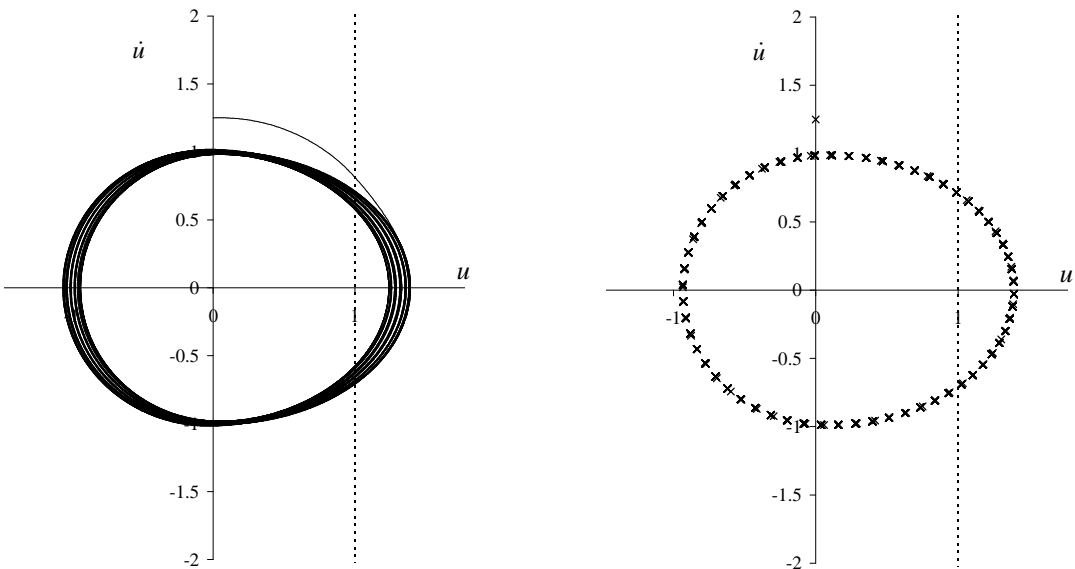


Figure 11. Stationary periodic motion (damage shakedown): phase portrait (left) and Poincaré map (right) for $f_0 = 0.05$, $\omega = 0.2$, $u_f = 3$, $u_0 = 0$, $\dot{u}_0 = 1.25$, $v_0 = 0$ ($D_0 = 0$).

paper may be also observed for a weakly damped system, where a damping term is added to (10):

$$\begin{cases} \hat{E}^+ : & \ddot{u} + 2\zeta\dot{u} + (1 - D(v))u = f_0 \cos \omega\tau, & \dot{D} = 0, \\ \hat{E}^- : & \ddot{u} + 2\zeta\dot{u} + u = f_0 \cos \omega\tau, & \dot{D} = 0, \\ \hat{D} : & \ddot{u} + 2\zeta\dot{u} + \left\langle \frac{u - u_f}{1 - u_f} \right\rangle = f_0 \cos \omega\tau, & \dot{v} = \dot{u}, \end{cases} \quad (35)$$

Here ζ is a dimensionless damping ratio. Equations (11) and (12) are still valid. The bifurcation diagrams of Figure 12, showing the dependence on the choice of the initial parameter v_0 or D_0 , confirm the appearance of chaotic phenomena for a severely damaged oscillator. Bifurcation diagrams similar to

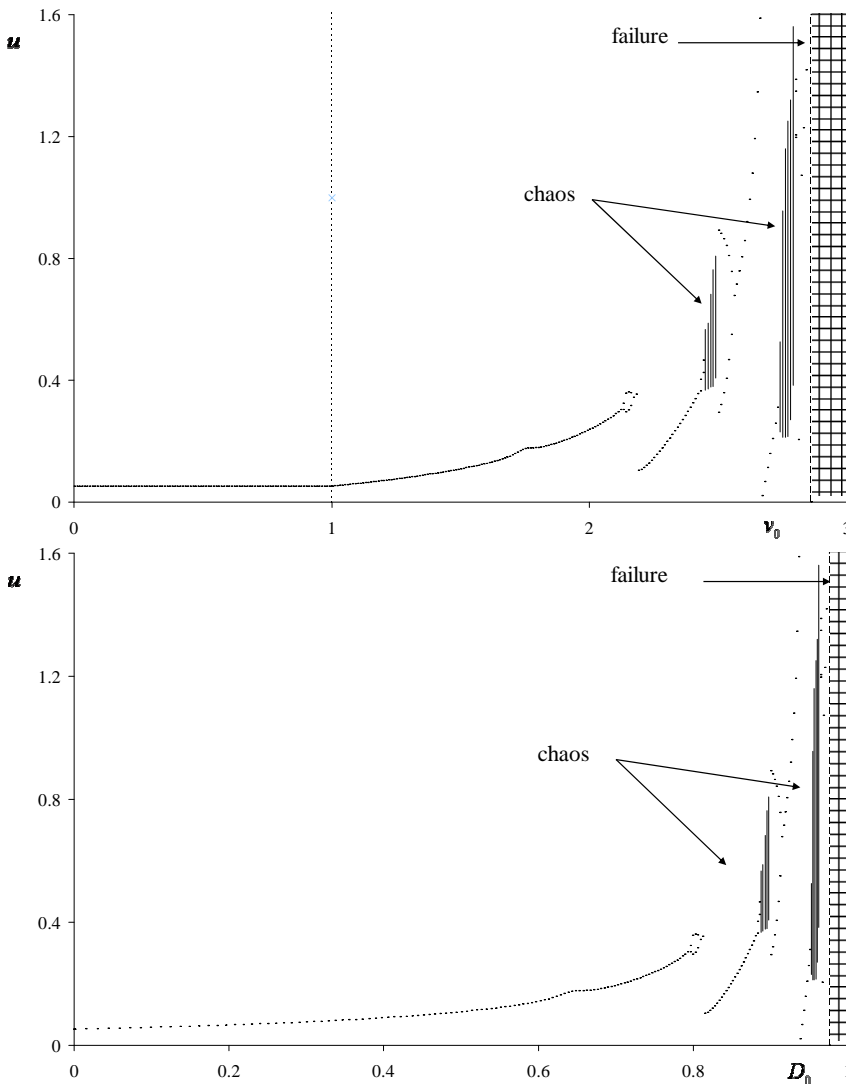


Figure 12. Bifurcation diagram in (v_0, u) space (top) and in (D_0, u) space: damped system, for $f_0 = 0.05$, $\omega = 0.2$, $u_f = 3$, $u_0 = 0$, $\dot{u}_0 = 0$, $\zeta = 0.01$.

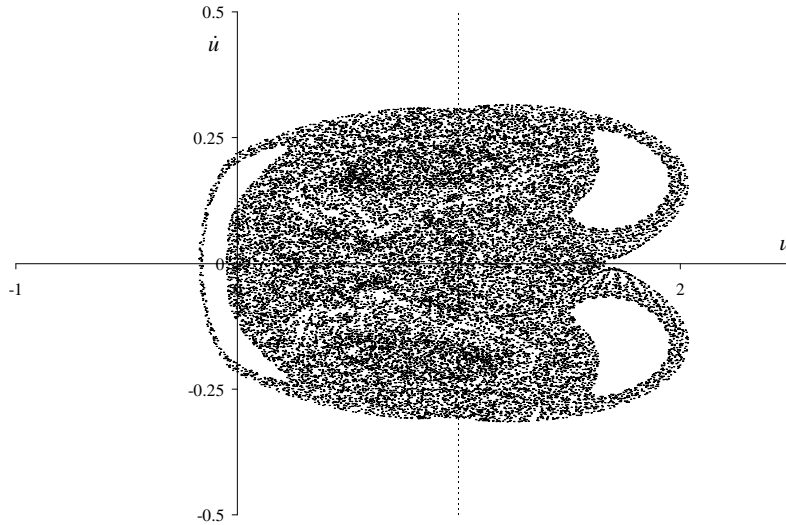


Figure 13. Chaotic motion, Poincaré map, undamped system. $f_0 = 0.05$; $\omega = 0.2$; $u_f = 3$; $u_0 = 0$; $\dot{u}_0 = 0$; $v_0 = 2.77$ ($D_0 = 0.958$); $\zeta = 0$.

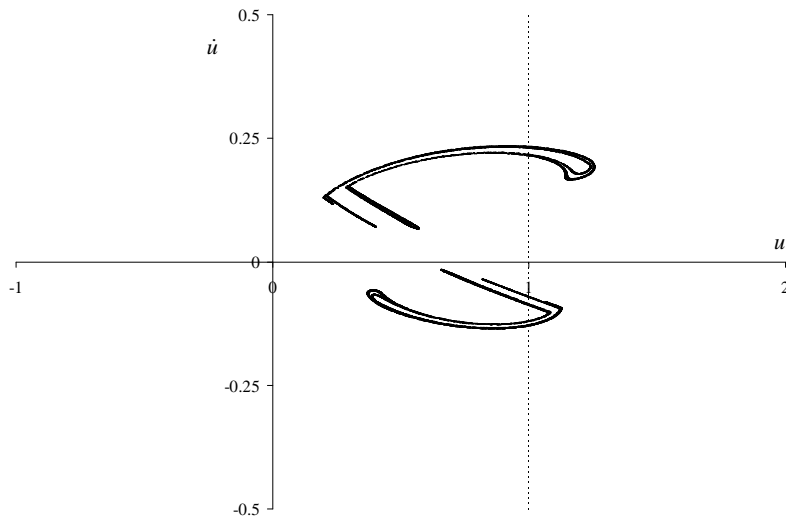


Figure 14. Chaotic motion: Poincaré map, damped system, for $f_0 = 0.05$, $\omega = 0.2$, $u_f = 3$, $u_0 = 0$, $\dot{u}_0 = 0$, $v_0 = 2.77$ ($D_0 = 0.958$), $\zeta = 0.01$.

those in [Figure 12](#) were obtained in [\[Foong et al. 2003\]](#) from a fatigue-testing rig (without the divergence phenomenon). The structure of the chaotic attractor is affected by the damping ratio; compare [Figures 13](#) and [14](#). The attractor can deform in shape, depending on the strength of damping, and can even become a chaotic sea with islands of quasiperiodic trajectories for the undamped system, as also observed in [\[Cao et al. 2008\]](#). It is worth mentioning that the chaotic attractor associated with the damaged system is very analogous to the Hénon's attractor; see, for example, [\[Thompson 1982\]](#).

5. Conclusions

This paper deals with the stability of a single-DOF damage softening oscillator with crack closure effect. This system can be understood as an archetypal damage oscillator for concrete structures. Using appropriate internal variables (a damage variable or an equivalent memory variable), the free dynamics of such a nonlinear system can be written as a nonsmooth autonomous system with three regimes describing elasticity, elastic stiffness recovery, and energy dissipation due to damage growth, respectively. It is shown that the free vibrations of such an oscillator are reduced to stationary periodic regimes, attractive trajectories, or divergent motion.

The stability of this free oscillator is investigated with the direct Lyapunov method extended to nonsmooth systems. Following physical arguments, the Lyapunov function of the problem is chosen as the nonsmooth energy of the system. A critical energy that the oscillator can support in order to remain stable is obtained (induced by seismic loads for instance). For energy levels higher than this critical value, a divergent evolution is observed, leading to structural collapse. This result may have some implications in seismic design applications.

The behavior of the forced harmonic damage oscillator is much more complex. It is worth mentioning that the present damage model is different from a nonlinear elastic one essentially because the damage behavior is irreversible in nature. As a consequence, the inelastic (damage) problem has additional regimes (that the nonlinear elastic problem does not have), loading-unloading conditions, an energy threshold associated with the elastic domain, numerical analysis to compute the transition from the elastic state to the damage state and vice versa, and so on. The dynamics of a forced elastodamage oscillator with the crack closure effect have been numerically investigated. Periodic, quasiperiodic, chaotic, and divergent motions are observed. Chaotic motions are observed for severely damaged oscillators, in the vicinity of the divergence area. This oscillator is typically a simple physical model associated with the coexistence of chaos and divergence.

Damage shakedown, a fundamental feature related to the structural integrity, means that the damage value is stationary after a critical time. Damage shakedown is typically controlled by initial conditions and structural parameters (for example, stiffness ratios). For instance, a divergent evolution can be achieved for a sufficiently perturbed damage oscillator. In the case of damage shakedown, the stationary response is the same as that of an elastic oscillator with different stiffnesses in tension and in compression. Chaotic motions are observed for severely damaged oscillators (for sufficiently small stiffness in tension). Furthermore, it is numerically shown that chaos is observed in the vicinity of the divergence zone. This closeness of both behaviors, chaos and divergence, is probably related to the perturbation of the homoclinic orbit, associated with the critical energy. Therefore, chaos may be understood as a route to collapse. A more theoretical analysis would be probably needed to understand the specific route to chaos, for example, using the Melnikov method (even if the application of the Melnikov method to nonsmooth systems is a mathematically difficult problem [Kukučka 2007]).

Classically, chaotic systems are extremely sensitive to initial conditions and numerical simulations require specific attention when devising computational schemes [Symonds and Yu 1985; Tongue 1987]. The structure of the chaotic attractor is notably affected by the damping ratio. The attractor can deform in shape, depending on the strength of damping, and can even become a chaotic sea with islands of quasiperiodic trajectories for the undamped system, as also observed in [Cao et al. 2008]. It is worth

mentioning that the chaotic attractor associated with the damaged system is very analogous to the Hénon’s attractor [Thompson 1982]. One of the characteristics of the inelastic system considered here is that the dynamic collapse of concrete structures may involve chaotic phenomena. It is expected that large-scale models of concrete structures may also reveal the complex phenomena highlighted in this paper from an archetypal damage oscillator.

Appendix: A possible application of the Melnikov method to the analogous elastic oscillator

We study in this Appendix a piecewise elastic system with softening restoring force, somewhat reminiscent of the single-DOF system associated with a simple arch model (which includes snap-through buckling). This later system was considered in [Cao et al. 2008] as an archetypal oscillator exhibiting chaotic phenomena.

The constitutive elastic law of our dimensionless piecewise elastic system is

$$\ddot{u} + 2\zeta\dot{u} + f(u) = f_0 \cos \omega\tau, \text{ where } f(u) = \begin{cases} u & \text{if } u \leq 1, \\ \frac{u-u_f}{1-u_f} & \text{if } u \geq 1, \end{cases}$$

with $u_f \geq 1$. This oscillator is similar to the damage oscillator (inelastic system) studied in the paper, but differs from it in that the restoring force depends only on the position. This piecewise elastic system has limited tension strength.

Cao et al. [2008] also investigated a symmetrical piecewise elastic constitutive law and used Melnikov’s method to detect the homoclinic tangling under the perturbation of damping and driving. The Melnikov method can be used to show the possible occurrence of chaos, for certain range of parameters of the system. We mention the application of the Melnikov method to nonsmooth dynamics [Awrejcewicz and Lamarque 2003; Awrejcewicz and Holické 2007; Kukučka 2007]. As shown by Kukučka [2007], the mathematical background of the Melnikov method applied to nonsmooth systems is very recent and complex.

The Hamiltonian function associated with the free undamped piecewise elastic system is given by

$$H(u, \dot{u}) = \frac{1}{2}\dot{u}^2 + \begin{cases} \frac{1}{2}u^2 & \text{if } u \leq 1, \\ \frac{1}{2} \frac{(u - u_f)^2}{1 - u_f} + \frac{1}{2}u_f & \text{if } u \geq 1. \end{cases}$$

This system is very close to the system studied by Cao et al. [2008] who investigated a piecewise linear model, based on the following constitutive elastic law written with respect to the unstable equilibrium solution:

$$f(u) = \begin{cases} -\omega_1^2 u & \text{if } |u| \leq u_0, \\ \omega_2^2 (u - \text{sgn}(u)u_f) & \text{if } |u| \geq u_0, \end{cases} \quad u_f = \omega_2,$$

which is a symmetrical piecewise elastic model with a softening restoring force (the equilibrium solution at the origin is unstable). There is a correspondence between both systems for the set of parameters:

$$\omega_1^2 = \frac{1}{u_f - 1} = \frac{1}{u_0}, \quad \omega_2 = 1.$$

The reasoning concerning the application of the Melnikov method is identical to the case treated by Cao et al. [2008], as the symmetrical part of the constitutive law does not change the result of the perturbed orbit around the homoclinic orbit.

The equation of the homoclinic orbit is given by

$$\begin{aligned} u^2 + \dot{u}^2 &= u_f \quad \text{if } u \leq 1, \\ \frac{u}{u_f} + \frac{\sqrt{u_f - 1}}{u_f} |\dot{u}| - 1 &= 0 \quad \text{if } u \geq 1. \end{aligned}$$

The Melnikov function is defined by the formula for the undamped system:

$$M(\tau_0) = \int_{-\infty}^{\infty} \dot{u}(\tau) f_0 \cos \omega(\tau + \tau_0) d\tau.$$

If the function $M(\tau_0)$ has simple zeros, then for a sufficiently small parameter f_0 , the motion governed by the forced dynamic system can be chaotic. The reader is referred to [Cao et al. 2008] for the technical calculation of the Melnikov integral. It is shown that chaos may occur for a certain range of parameters for the equivalent elastic oscillator. This result cannot be strictly used in the case of the damage oscillator, for two reasons. First, the dimension of the phase space is augmented in the presence of damage (additional state variable). Secondly, the homoclinic nature of the orbit is lost for the damaged system. Therefore, the proximity of the chaotic response of the damage oscillator with the divergence area is actually a numerical finding, without a rigorous theoretical proof, based on the Melnikov method.

References

- [Aschheim and Black 1999] M. Aschheim and E. Black, “Effects of prior earthquake damage on response of simple stiffness-degrading structures”, *Earthquake Spectra* **15**:1 (1999), 1–24.
- [Awrejcewicz and Holicke 2007] J. Awrejcewicz and M. M. Holicke, *Smooth and nonsmooth high dimensional chaos and the Melnikov-type methods*, World Scientific, New Jersey, 2007.
- [Awrejcewicz and Lamarque 2003] J. Awrejcewicz and C. H. Lamarque, *Bifurcations and chaos in nonsmooth mechanical systems*, World Scientific, Singapore, 2003.
- [Awrejcewicz et al. 2008] J. Awrejcewicz, L. Dzyubak, and C.-H. Lamarque, “Modelling of hysteresis using Masing–Bouc–Wen’s framework and search of conditions for the chaotic responses”, *Commun. Nonlinear Sci. Numer. Simul.* **13**:5 (2008), 939–958.
- [Bažant and Jirásek 2002] Z. P. Bažant and M. Jirásek, “Nonlocal integral formulations of plasticity and damage: survey of progress”, *J. Eng. Mech. (ASCE)* **128**:11 (2002), 1119–1149.
- [Bourgeot and Brogliato 2005] J.-M. Bourgeot and B. Brogliato, “Tracking control of complementarity Lagrangian systems”, *Int. J. Bifurc. Chaos* **15**:6 (2005), 1839–1866.
- [Cao et al. 2008] Q. Cao, M. Wiercigroch, E. E. Pavlovskaja, J. M. T. Thompson, and C. Grebogi, “Piecewise linear approach to an archetypal oscillator for smooth and discontinuous dynamics”, *Phil. Trans. R. Soc. A* **366**:1865 (2008), 635–652.
- [Carpinteri and Pugno 2005a] A. Carpinteri and N. Pugno, “Towards chaos in vibrating damaged structures, 1: Theory and period doubling cascade”, *J. Appl. Mech. (ASME)* **72**:4 (2005), 511–518.
- [Carpinteri and Pugno 2005b] A. Carpinteri and N. Pugno, “Towards chaos in vibrating damaged structures, 2: Parametrical investigation”, *J. Appl. Mech. (ASME)* **72**:4 (2005), 519–526.
- [Caughey 1960] T. K. Caughey, “Sinusoidal excitation of a system with bilinear hysteresis”, *J. Appl. Mech. (ASME)* **27**:4 (1960), 649–652.

- [Challamel 2005] N. Challamel, “Dynamic analysis of elastoplastic shakedown of structures”, *Int. J. Struct. Stab. Dyn.* **5**:2 (2005), 259–278.
- [Challamel and Gilles 2007] N. Challamel and G. Gilles, “Stability and dynamics of a harmonically excited elastic-perfectly plastic oscillator”, *J. Sound Vib.* **301**:3–5 (2007), 608–634.
- [Challamel and Pijaudier-Cabot 2004] N. Challamel and G. Pijaudier-Cabot, “Stabilité et dynamique d’un oscillateur endommageable”, *Eur. J. Environ. Civ. Eng.* **8**:4 (2004), 483–505.
- [Challamel and Pijaudier-Cabot 2006] N. Challamel and G. Pijaudier-Cabot, “Stability and dynamics of a plastic softening oscillator”, *Int. J. Solids Struct.* **43**:18–19 (2006), 5867–5885.
- [Challamel et al. 2005] N. Challamel, C. Lanos, and C. Casandjian, “Strain-based anisotropic damage modelling and unilateral effects”, *Int. J. Mech. Sci.* **47**:3 (2005), 459–473.
- [Challamel et al. 2007] N. Challamel, C. Lanos, A. Hammouda, and B. Redjel, “Stability analysis of dynamic ratcheting in elastoplastic systems”, *Phys. Rev. E* **75**:2 (2007), 026204.
- [Challamel et al. 2008] N. Challamel, C. Lanos, and T. Rouxel, “An application of Curie’s principle to elastoplastic dynamics”, *Mech. Res. Commun.* **35**:6 (2008), 376–382.
- [DeSimone et al. 2001] A. DeSimone, J.-J. Marigo, and L. Teresi, “A damage mechanics approach to stress softening and its application to rubber”, *Eur. J. Mech. A Solids* **20**:6 (2001), 873–892.
- [Filippov 1960] A. F. Filippov, “Дифференциальные уравнения с разрывной правой частью”, *Mat. Sb. (N. S.)* **51**(93):1 (1960), 99–128. Translated as “Differential equations with discontinuous right-hand side” in *Amer. Math. Soc. Transl. Ser. 2* **42**:2 (1964), 199–231.
- [Filippov 1988] A. F. Filippov, *Differential equations with discontinuous righthand sides*, edited by F. M. Arscott, Mathematics and its Applications (Soviet Series) **18**, Kluwer, Dordrecht, 1988.
- [Foong et al. 2003] C.-H. Foong, E. Pavlovskaja, M. Wiercigroch, and W. F. Deans, “Chaos caused by fatigue crack growth”, *Chaos Solitons Fract.* **16**:5 (2003), 651–659.
- [Foong et al. 2007] C.-H. Foong, M. Wiercigroch, E. Pavlovskaja, and W. F. Deans, “Nonlinear vibration caused by fatigue”, *J. Sound Vib.* **303**:1–2 (2007), 58–77.
- [Ing et al. 2008] J. Ing, E. Pavlovskaja, M. Wiercigroch, and S. Banerjee, “Experimental study of impact oscillator with one-sided elastic constraint”, *Phil. Trans. R. Soc. A* **366**:1866 (2008), 679–705.
- [Kounadis 1996] A. N. Kounadis, “Non-linear dynamic buckling of a simple model via the Liapunov direct method”, *J. Sound Vib.* **193**:5 (1996), 1091–1097.
- [Kukučka 2007] P. Kukučka, “Melnikov method for discontinuous planar systems”, *Nonlinear Anal. Theory Methods Appl.* **66**:12 (2007), 2698–2719.
- [Lacarbonara and Vestroni 2003] W. Lacarbonara and F. Vestroni, “Nonclassical responses of oscillators with hysteresis”, *Nonlinear Dyn.* **32**:3 (2003), 235–258.
- [Leine 2006] R. I. Leine, “Bifurcations of equilibria in non-smooth continuous systems”, *Physica D* **233**:1 (2006), 121–137.
- [Mahfouz and Badrakhhan 1990] I. A. Mahfouz and F. Badrakhhan, “Chaotic behaviour of some piecewise-linear systems, I: Systems with set-up spring or with unsymmetric elasticity”, *J. Sound Vib.* **143**:2 (1990), 255–288.
- [Mazars and Pijaudier-Cabot 1996] J. Mazars and G. Pijaudier-Cabot, “From damage to fracture mechanics and conversely: a combined approach”, *Int. J. Solids Struct.* **33**:20–22 (1996), 3327–3342.
- [Mazars et al. 1990] J. Mazars, Y. Berthaud, and S. Ramtani, “The unilateral behaviour of damaged concrete”, *Eng. Fract. Mech.* **35**:4–5 (1990), 629–635.
- [Ortiz 1985] M. Ortiz, “A constitutive theory for the inelastic behaviour of concrete”, *Mech. Mater.* **4**:1 (1985), 67–93.
- [Poddar et al. 1988] B. Poddar, F. C. Moon, and S. Mukherjee, “Chaotic motion of an elastic-plastic beam”, *J. Appl. Mech. (ASME)* **55**:1 (1988), 185–189.
- [Pratap and Holmes 1995] R. Pratap and P. J. Holmes, “Chaos in a mapping describing elastoplastic oscillations”, *Nonlinear Dyn.* **8**:1 (1995), 111–139.
- [Pratap et al. 1994] R. Pratap, S. Mukherjee, and F. C. Moon, “Dynamic behavior of a bilinear hysteretic elasto-plastic oscillator, I: Free oscillations”, *J. Sound Vib.* **172**:3 (1994), 321–337.

- [Ryue and White 2007] J. Ryue and P. R. White, “The detection of cracks in beams using chaotic excitations”, *J. Sound Vib.* **307**:3–5 (2007), 627–638.
- [la Salle and Lefschetz 1961] J. la Salle and S. Lefschetz, *Stability by Liapunov’s direct method with applications*, Academic Press, New York, 1961.
- [Savi and Pacheco 1997] M. A. Savi and P. M. C. L. Pacheco, “Non-linear dynamics of an elasto-plastic oscillator with kinematic and isotropic hardening”, *J. Sound Vib.* **207**:2 (1997), 207–226.
- [Shaw and Holmes 1983] S. W. Shaw and P. J. Holmes, “A periodically forced piecewise linear oscillator”, *J. Sound Vib.* **90**:1 (1983), 129–155.
- [Shevitz and Paden 1994] D. Shevitz and B. Paden, “Lyapunov stability theory of nonsmooth systems”, *IEEE Trans. Autom. Control* **39**:9 (1994), 1910–1914.
- [Symonds and Yu 1985] P. S. Symonds and T. X. Yu, “Counterintuitive behavior in a problem of elastic-plastic beam dynamics”, *J. Appl. Mech. (ASME)* **52**:3 (1985), 517–522.
- [Thompson 1982] J. M. T. Thompson, *Instabilities and catastrophes in science and engineering*, Wiley, Chichester, 1982.
- [Thompson et al. 1983] J. M. T. Thompson, A. R. Bokaian, and R. Ghaffari, “Subharmonic resonances and chaotic motions of a bilinear oscillator”, *IMA J. Appl. Math.* **31**:3 (1983), 207–234.
- [Tongue 1987] B. H. Tongue, “Characteristics of numerical simulations of chaotic systems”, *J. Appl. Mech. (ASME)* **54**:3 (1987), 695–699.
- [Wiercigroch 2000] M. Wiercigroch, “Modelling of dynamical systems with motion dependent discontinuities”, *Chaos Solitons Fract.* **11**:15 (2000), 2429–2442.
- [Wiercigroch and Sin 1988] M. Wiercigroch and V. W. T. Sin, “Experimental study of a symmetrical piecewise base-excited oscillator”, *J. Appl. Mech. (ASME)* **65**:3 (1988), 657–663.
- [Williamson and Hjelmstad 2001] E. B. Williamson and K. D. Hjelmstad, “Nonlinear dynamics of a harmonically-excited inelastic inverted pendulum”, *J. Eng. Mech. (ASCE)* **127**:1 (2001), 52–57.
- [Wu and Sepehri 2001] Q. Wu and N. Sepehri, “On Lyapunov’s stability analysis of non-smooth systems with applications to control engineering”, *Int. J. Non-Linear Mech.* **36**:7 (2001), 1153–1161.

Received 10 Nov 2008. Revised 13 Oct 2009. Accepted 19 Oct 2009.

NOËL CHALLAMEL: noel.challamel@insa-rennes.fr

Laboratoire de Génie Civil et de Génie Mécanique, INSA de Rennes, Université Européenne de Bretagne, 20, Avenue des Buttes de Coësmes, 35043 Rennes, France

GILLES PIJAUDIER-CABOT: gilles.pijaudier-cabot@univ-pau.fr

Laboratoire des Fluides Complexes (UMR 5150), ISA BTP, Allée du Parc Montaury, 64600 Anglet, France

ELASTIC BUCKLING CAPACITY OF BONDED AND UNBONDED SANDWICH PIPES UNDER EXTERNAL HYDROSTATIC PRESSURE

KAVEH ARJOMANDI AND FARID TAHERI

Sandwich pipes can be a potentially optimal system for use in deep-water applications. In recent years, there has been considerable interest in understanding the stability characteristics of these pipes under the governing loading conditions, with the aim of generating optimal design. External hydrostatic pressure is a critical loading condition that a submerged pipeline experiences during its installation and operational period.

This article presents an analytical approach for estimating the buckling capacity of sandwich pipes with various structural configurations and core materials, subject to external hydrostatic pressure. The influence of adhesion between the core layer and inner or outer pipes is also a focus of this study. Beside the exact solution, two simplified equations are developed for estimating the buckling capacity of two configurations commonly used in practice. Details of both the exact and simplified analytical formulations are presented and the required parameters are defined. The efficiency and integrity of the proposed simplified solutions are compared with a solution developed by other researchers. A comprehensive series of finite element eigenvalue buckling analyses was also conducted to evaluate the accuracy and applicability of the proposed solutions.

A list of symbols can be found on page 407.

Introduction

As shallow offshore oil reserves are depleted, the demand for deep water oil reserves is increasing. Extracting oil from deep waters will not be possible, unless new pipeline systems can be developed to accommodate the new loading and environmental conditions. High external hydrostatic pressure, pipeline buoyancy during installation, and low water temperatures restrict the application of single metallic pipelines to a limited depth. Sandwich pipes can be a potentially optimal design alternative in addressing the requirements of deep waters. Sandwich pipe (SP) systems employ the structural and thermal insulation benefits provided by two stiffer pipes sandwiching a lighter-weight and less stiff core material. Moreover, the secondary containment provided by the outer pipe improves the reliability of the system in the case of product leak.

A typical pipe in pipe (PIP) system consists of an inner pipe, a relatively thick lightweight core layer, and an outer pipe. Each layer in this system can be designed for a specific purpose. The inner pipe, also referred to as the product pipe, usually is designed to endure the internal pressure and to facilitate the transport of the product safely. The core layer's function can be different depending on the application. For example, it can be designed to act as a thermal insulator, or to improve the structural performance of the pipeline, depending on the core's material properties and the interaction mechanism between the

Keywords: sandwich pipes, pipe-in-pipe, stability, buckling, hydrostatic pressure.

core layer and the surrounding pipes. A wide range of core materials such as plastics, gels, ceramics, and composites can be used to achieve the system's thermal and structural requirements. The outer pipe, also called the sleeve pipe, separates the inner and core layers from the surrounding environment. The sleeve pipe may individually carry the externally applied loads, as in a PIP system, or may act as the main part of a sandwich system, as in an SP system. The outer pipe also provides secondary containment for the product being transported, in case of leakage of the product through the inner pipe.

To design an optimal SP system, understanding of its structural behavior is a prerequisite. A great number of works have been written in recent years to clarify the structural characteristics of such a system under different loading conditions. Some of those works have considered the stability of a sandwich cylindrical shell, which can be a general geometry for a sandwich pipe. For example Kyriakides and his coworkers studied buckle propagation phenomena [Kyriakides 2002; Kyriakides and Netto 2002; 2004; Kyriakides and Vogler 2002] from both numerical and experimental perspectives. Kardomateas and Simitse [2002; 2005] studied analytically the buckling of long sandwich cylindrical shells under external pressure. Ohga et al. [2005] studied, both numerically and analytically, the reduced stiffness buckling of sandwich cylindrical shells under uniform external pressure. Sato and Patel [2007] and Sato et al. [2008] studied the buckling behavior of a PIP system under hydrostatic pressure and developed a simplified solution for estimating a PIP system's buckling capacity. Castello and Estefen [2006; 2008] and Estefen et al. [2005] studied the feasibility of a sandwich pipe system for deep water applications with both numerical and experimental approaches. In another study, Castello and Estefen [2007] investigated the ultimate strength of sandwich pipes under combined external pressure and bending for several degrees of adhesion between the core layer and outer pipe. They also investigated the effect of cyclic loads applied during a reeling installation on the collapse pressure. Very recently, Castello et al. [2009] also conducted an investigation, comparing PIP and SP systems designed for a hypothetical oil field with several core materials. In this study they used polypropylene and polyurethane foams with various densities as the core materials and investigated the influences of both their mechanical and thermal properties. They concluded that the combination of steel and foams could produce effective SP systems with good buoyancy and thermal insulation properties.

1. Motivation and aims

Our preliminary investigation indicated that most of the available simplified solutions developed for predicting buckling capacity of PIP systems subject to hydrostatic pressure produce results with very large margins of error under certain conditions. This fact prompted an analytical investigation, with the aim of developing exact and simplified solutions for establishing the buckling capacity of PIPs subject to externally applied hydrostatic pressure. Moreover, a comprehensive finite element investigation is also conducted to establish the performance of PIPs with a wide range of material and physical properties, and to verify the integrity of the proposed solutions. Four different interlayer bonding configurations are considered. The parameters used to define the characteristic equation of the system are outlined. An important aim of this investigation is also extracting simplified solutions from the exact solution for use in practical design. As a result, the simplified and exact solutions are compared and the accuracy of their results discussed. Finally, the error margins resulting from the use of the proposed simplified equations and those resulting from the proposals of other researchers are established.

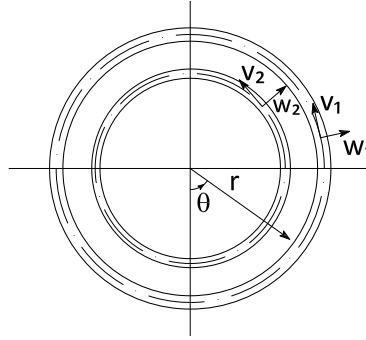


Figure 1. The coordinate system and the idealized geometry.

2. The analytical model

A long, circular cylindrical shell with three layers (steel, core, and steel) is considered. Due to the symmetry in structural configuration and loading, this problem can be idealized as a two-dimensional plane strain problem. The use of polar coordinates also aids in the formulation the problem. [Figure 1](#) shows the geometry and polar coordinate system of the model.

Equilibrium equations of the system. The potential energy of the system can be used to derive the equilibrium equations. It can be represented as follows [[Kyriakides and Corona 2007](#)]:

$$\Pi = U_{P,1} + U_{P,2} + U_c + W_p, \quad (1)$$

where the potential energies of the inner and outer pipes are given by

$$U_{P,i} = \int_0^{2\pi} \frac{1}{2} [N_{\theta\theta,i} \varepsilon_{\theta\theta,i}^o + M_{\theta\theta,i} k_{\theta\theta,i}] r_i \cdot d\theta, \quad (2)$$

where $i = 1$ for the outer pipes and $i = 2$ for the inner one, $N_{\theta\theta}$ is the internal axial force, $\varepsilon_{\theta\theta}^o$ is the circumferential strain of the centroid fiber, $M_{\theta\theta}$ is the internal moment, and $k_{\theta\theta}$ is the curvature change in the centroid surface.

In (1), the effect of the core layer can be considered as the work done by the entire layer's stresses applied to the inner and outer pipes. These works can be represented by

$$U_c = U_{c,1} + U_{c,2}, \quad \text{where} \quad U_{c,i} = \int_0^{2\pi} (\sigma_r|_{a_i} \cdot w|_{a_i} + \tau_{r\theta}|_{a_i} \cdot v|_{a_i}) a_i \cdot d\theta, \quad (3)$$

where $a_1 = r_1 - t_1/2$ and $a_2 = r_2 + t_2/2$.

The work done by the external hydrostatic pressure is given by

$$W_P = P \int_0^{2\pi} (wr_1 + \frac{1}{2}(v^2 + w^2 - vw' + v'w)) \cdot d\theta, \quad (4)$$

where the $'$ indicates the differentiation with respect to θ .

Sander's shell equations are used to describe the strain-displacement relationships. Sander's kinematic equations are nonlinear and are based on small strain and moderate rotation assumptions, which are appropriate for establishing the linear buckling equations. The kinematic equations in polar coordinate

can be written as

$$\varepsilon_{\theta\theta} = \varepsilon_{\theta\theta}^o + z k_{\theta\theta}, \quad \varepsilon_{\theta\theta}^o = \frac{w+v'}{r} + \frac{1}{2}\beta^2, \quad k_{\theta\theta} = \frac{\beta'}{r}. \quad (5)$$

In these equations β represents the rotation of a circumferential element located at the midplane of the pipes. β for an intermediate class of deformation (small midsurface strains and small but finite rotations) can be defined as in [Farshad 1994] by as

$$\beta = \frac{v-w'}{r}. \quad (6)$$

Using the plane strain material constitutive relation, we get for the force and moment intensities in (2)

$$N_{\theta\theta} = C\varepsilon_{\theta\theta}^o, \quad M_{\theta\theta} = Dk_{\theta\theta}, \quad (7)$$

where $C = Et/(1 - \nu_p^2)$ and $D = \frac{1}{12}Et^3/(1 - \nu_p^2)$.

By substituting the kinematic and constitutive equations and using variational calculus, we can write the equilibrium equations of the system as

$$\alpha_{1,1}(w_1 + v_1') - \alpha_{2,1}(v_1 - w_1''') + p(w_1'' + w_1) + a_1\sigma_r|_{a_1} = 0, \quad (8a)$$

$$\alpha_{1,1}(w_1 + v_1')' + \alpha_{2,1}(v_1 - w_1'') + a_1\tau_{r\theta}|_{a_1} = 0, \quad (8b)$$

$$\alpha_{1,2}(w_1 + v_1') - \alpha_{2,2}(v_1 - w_1''') - a_2\sigma_r|_{a_2} = 0, \quad (8c)$$

$$\alpha_{1,2}(w_1 + v_1')' + \alpha_{2,2}(v_1 - w_1'') - a_2\tau_{r\theta}|_{a_2} = 0, \quad (8d)$$

where

$$\alpha_{1,i} = \frac{C_i}{r_i}, \quad \alpha_{2,i} = \frac{D_i}{r_i^3} \quad (i = 1, 2). \quad (8e)$$

These Euler differential equations are written in terms of the four independent variables u_1 , v_1 , u_2 , and v_2 , which represent the deformation of the inner and outer pipes, and four dependent variables $\sigma_r|_{a_1}$, $\tau_{r\theta}|_{a_1}$, $\sigma_r|_{a_2}$, and $\tau_{r\theta}|_{a_2}$. The dependent variables can be described as functions of the independent variables, using the core properties. An elasticity approach is used here to characterize the core behavior.

The displacement function that could satisfy the equilibrium equations can be assumed to be circumferentially periodic. Considering this assumption, the following stress function would satisfy the equilibrium equations [Sato and Patel 2007]:

$$\phi(r, \theta) = f_n(r) \cos n\theta, \quad (9)$$

where n is the buckling mode number. To yield a possible stress distribution, the stress function must be such that the following compatibility equation is satisfied [Timoshenko and Goodier 1970]:

$$\left(\frac{\partial^2}{\partial r^2} + \frac{1}{r} \frac{\partial}{\partial r} + \frac{1}{r^2} \frac{\partial^2}{\partial \theta^2} \right) \left(\frac{\partial^2 \phi}{\partial r^2} + \frac{1}{r} \frac{\partial \phi}{\partial r} + \frac{1}{r^2} \frac{\partial^2 \phi}{\partial \theta^2} \right) = 0. \quad (10)$$

In order for ϕ to be an admissible solution of this equation, the general form of f_n must be as follows [Timoshenko and Goodier 1970]:

$$f_n(r) = A_n r^{-n} + B_n r^{2-n} + C_n r^{2+n} + D_n r^n \quad (n \geq 2), \quad (11)$$

in which the constants A_n , B_n , C_n , and D_n are calculated from the distribution of forces and displacements at the boundaries. The stress and displacement components in polar coordinates are

$$\sigma_r = \frac{1}{r} \frac{\partial \phi(r, \theta)}{\partial r} + \frac{1}{r^2} \frac{\partial^2 \phi(r, \theta)}{\partial \theta^2}, \quad \tau_{r\theta} = -\frac{\partial}{\partial r} \left(\frac{1}{r} \frac{\partial \phi(r, \theta)}{\partial \theta} \right), \quad \tilde{w} = \int \varepsilon_r \cdot dr, \quad \tilde{v} = \int (r\varepsilon_\theta - w) \cdot d\theta. \quad (12)$$

Using these relations, stresses at the boundary of the core can be described as a function of the deformation of the boundary. The following general core boundary conditions are considered:

$$\tilde{w}|_{a_1} = \tilde{W}_1 \cos n\theta, \quad \tilde{v}|_{a_1} = \tilde{V}_1 \sin n\theta, \quad \tau_{r\theta}|_{a_1} = 0, \quad (13)$$

$$\tilde{w}|_{a_2} = \tilde{W}_2 \cos n\theta, \quad \tilde{v}|_{a_2} = \tilde{V}_2 \sin n\theta, \quad \tau_{r\theta}|_{a_2} = 0. \quad (14)$$

Four sets of boundary conditions are chosen depending on the problem:

- I. Core is fully bonded to both inner and outer pipes: boundary conditions (13)_{1,2} and (14)_{1,2}.
- II. Core is unbonded to the outer pipe in the tangential direction, but is fully bonded to the inner pipe: boundary conditions (13)_{1,3} and (14)_{1,2}.
- III. Core is unbonded to the inner pipe in the tangential direction, but is fully bonded to the outer pipe: boundary conditions (13)_{1,2} and (14)_{1,3}.
- IV. Core can slide freely against both inner and outer pipes: boundary conditions (13)_{1,3} and (14)_{1,3}.

Characteristic equation of the system. We denote the stiffness matrices of the pipes and core by $K_p = [p_{ij}]_{0 \leq i, j \leq 4}$ and $K_c = [c_{ij}]_{0 \leq i, j \leq 4}$. The nonzero coefficients of K_p are

$$p_{11} = \alpha_1 \left[1 + \frac{1}{12} \left(\frac{t_1}{r_1} \right)^2 n^4 \right] + q(n^2 - 1), \quad p_{22} = \alpha_1 n^2 \left[-1 + \frac{1}{12} \left(\frac{t_1}{r_1} \right)^2 \right], \quad p_{12} = -p_{21} = \alpha_1 n \left[1 + \frac{1}{12} \left(\frac{t_1}{r_1} \right)^2 n^2 \right],$$

$$p_{33} = \alpha_2 \left[1 + \frac{1}{12} \left(\frac{t_2}{r_2} \right)^2 n^4 \right], \quad p_{44} = \alpha_2 n^2 \left[-1 + \frac{1}{12} \left(\frac{t_2}{r_2} \right)^2 \right], \quad p_{34} = -p_{43} = \alpha_2 n \left[1 + \frac{1}{12} \left(\frac{t_2}{r_2} \right)^2 n^2 \right],$$

where

$$a_1 = r_1 - \frac{t_1}{2}, \quad a_2 = r_2 + \frac{t_2}{2}, \quad \alpha_1 = \frac{E_p t_1}{r_1 (1 - \nu_p^2)}, \quad \alpha_2 = \frac{E_p t_2}{r_2 (1 - \nu_p^2)}.$$

The coefficients of K_c are more complex and are given in the [Appendix](#).

The characteristic equation of the system can be written as

$$[K_p + K_c]\{\delta\} = 0, \quad (15)$$

where δ represents the deformation of the structure in the form of a vector representing the radial and circumferential deformations of the inner and outer pipes. To obtain a nontrivial solution, the determinant of the coefficient matrix must be set to zero. By solving this eigenvalue equation, the buckling pressure of the sandwich pipe is determined.

The characteristic equation of a sandwich pipe is more complex than that of a single pipe. Because of this complexity, the mode number that yields the lowest buckling pressure is not necessarily 2. In the system under investigation, the first buckling mode ($n = 1$) corresponds to a rigid body motion; therefore the characteristic equation must be solved for higher buckling modes.

3. Simplified solutions

A simplified solution was developed independently by [Brush and Almroth \[1975\]](#) and [Sato and Patel \[2007\]](#) for calculating the buckling pressure of a sandwich pipe under externally applied hydrostatic pressure; hereafter it is abbreviated as SS. The SS equation is

$$P_{cr} = P_{crs} + \frac{1}{n^2 - 1}k, \quad (16)$$

where

$$k = E_c \frac{2n(\nu_c - 1) - 2\nu_c + 1}{4\nu_c^2 + \nu_c - 3}, \quad P_{crs} = \left(\frac{t_1}{r_1}\right)^3 \frac{E_p(n^2 - 1)}{(1 - \nu_p^2)((t_1/r_1)^2 + 12)}.$$

This equation was developed by solving the buckling pressure of a ring supported internally by an elastic foundation. This would indicate that the continuity of the shear stresses between the core and outer pipe is ignored. Furthermore, the above equation was developed based on the assumption that the core can be replaced by a set of springs. The solution has been improved in this study by considering a proper stress function representing the core layer's response. In the mathematical model developed in this study, the continuity of the interlayer deformations and stresses was considered, and the characteristic equation of the system, which included the response of both core and pipes, was solved simultaneously.

In this section a set of simplified equations will be developed with the assumptions that $r_2 \rightarrow 0$ and $h_2 \rightarrow 0$, indicating that the inner portion of the system (surrounded by the outer pipe) is filled entirely by the core material. It is indeed recognized that this assumption may not be entirely correct, violating the exact proportional equivalency of the inner steel pipe in terms of the core material; however, as will be seen later, this simplifying assumption facilitates the solution of an otherwise complex equation. Moreover, as will also be shown, the produced solution is capable of generating relatively accurate results.

The assumption above enables one to establish the buckling pressure of a sandwich pipe by satisfying the equation

$$\lim_{R \rightarrow 0} \lim_{h_2 \rightarrow 0} [K_p + K_c]\{\delta\} = 0. \quad (17)$$

The accuracy of the proposed simplified solution is discussed in the following sections.

A: Core free to slide against outer pipe. Using the simplifying assumptions above, the characteristic equation of the system was solved using Mathematica, leading to the following equation, which can be used to establish the critical buckling capacity (pressure) of a sandwich pipe whose core layer is unbonded from the outer pipe:

$$P_{cr} = P_{crs} + \frac{E_c}{[2n(1 - \nu_c) + 2\nu_c - 1](1 + \nu_c)}. \quad (18)$$

This satisfies (17), using boundary conditions [II](#) or [IV](#).

B: Core bonded to outer pipe. Using the same method, the following buckling pressure has been calculated by solving (17) with case [I](#) boundary conditions:

$$P_{cr} = \frac{\xi_1}{\xi_2}, \quad (19)$$

where

$$\begin{aligned} \xi_1 &= 192E_c^2 a_1 r_1^3 (v_p^2 - 1)^2 + E_p^2 t_1^4 n^2 \Lambda (n^2 - 1) (\Lambda + 7)^2 + 2E_c E_p r_1 t_1 (v_p^2 - 1) (\Lambda + 7) \\ &\quad \times \{t_1^2 n^2 [n(\Lambda - 1) - \Lambda - 1] - 6t_1 r_1 [(n + 1)^2 + (n - 1)^2 \Lambda] - 12r_1^2 [n(\Lambda - 1) - \Lambda - 1]\}, \\ \xi_2 &= r_1 (v_p^2 - 1) (\Lambda + 7) \{-12E_c r_1^2 a_1 (v_p^2 - 1) [n(\Lambda - 1) - \Lambda - 1] + E_p t_1 n^2 \Lambda (t_1^2 + 12r_1^2) (\Lambda + 7)\}. \end{aligned}$$

Here

$$\Lambda = 4\nu_c - 3. \quad (20)$$

For brevity, the simplified solutions just developed will be referred to as the ATS.

4. Results and discussion

The histogram in [Figure 2](#) illustrates the number of standard and heavy wall line pipes available in the API standard [[API 2000](#)]. This histogram has been generated for API pipes with radii greater than 0.1 m, which is the most widely used range for offshore pipeline applications. As shown in this graph, the thickness to radius ratio in API pipe charts varies between 0.02 and 0.18.

Exact solution results. The ratio of the buckling pressure of an integral sandwich pipe to the buckling pressure of the outer pipe of a SP system can be written as a function of nondimensional parameters:

$$\frac{P_{cr}}{P_{crs}} = f\left(\frac{E_c}{E_p}, \frac{t_1}{r_1}, \nu_p, \nu_c, n\right), \quad (21)$$

where P_{crs} is the buckling pressure of the outer pipe; see the beginning of [Section 3](#). This ratio is used hereafter to present the results obtained from the proposed and SS solutions.

[Figure 3](#) shows the variation of the buckling pressure of a sandwich pipe with respect to the change in pipe geometry (r_2/r_1) and pipe material properties (E_c/E_p) in the aforementioned practical range. As stated, the buckling pressures of the sandwich pipes in these figures have been normalized with respect to that of the outer pipe. These graphs have been developed for a sandwich pipe with inner and outer pipe thickness to radius ratios of 0.05. In this study, Poisson's ratios of the core and pipes are taken as 0.5 and 0.3, respectively. As can be seen, the continuity of the shear stresses between the pipes and the core layer would significantly affect the buckling resistance of the pipe under external pressure. As

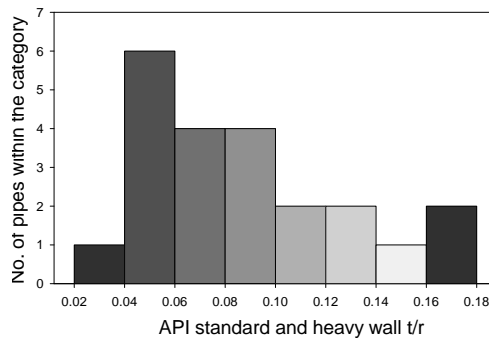


Figure 2. Histogram of t/r for API heavy and standard wall pipes with diameter greater than 0.1 m.

expected, the fully bonded configuration provides the greatest buckling capacity in comparison with the other configurations. The configuration in which the core layer and surrounding pipes are free to slide against each other exhibits the lowest buckling pressure. The difference between the buckling pressures of these two extreme configurations can be more than 100 times for certain values of r_2/r_1 and E_c/E_p .

Figure 3, top left, shows that for the fully bonded case, the buckling pressure of sandwich pipes with wide ranges of r_2/r_1 and E_c/E_p values is not significantly affected by the variation in the r_2/r_1 parameter. This fact was used as the basis for driving the simplified equations based on the assumption that the equivalent structure would be a pipe (the outer pipe) filled with the core material. The same conclusion can be made by considering Figure 3, top right, for the lower range of r_2/r_1 . As also seen, the buckling pressure in the other configurations is significantly dependent on the inner pipe diameter.

The other interesting results are associated with the pipe configuration in which the core and inner pipe can slide on one another. As can be seen in Figure 3, bottom left, there is no consistent trend for the buckling pressure within the studied range of parameters. By comparing the bottom left panes of Figures 3 and 5, which illustrate the buckling mode numbers for the same configuration, it can be concluded that the uneven behavior of the graph in the former is due to the oscillation in the buckling mode response of the pipe. Note that the actual buckling mode response of such sandwich pipes would not be exactly the same as what has been captured in our investigation. Indeed, the discrepancy between

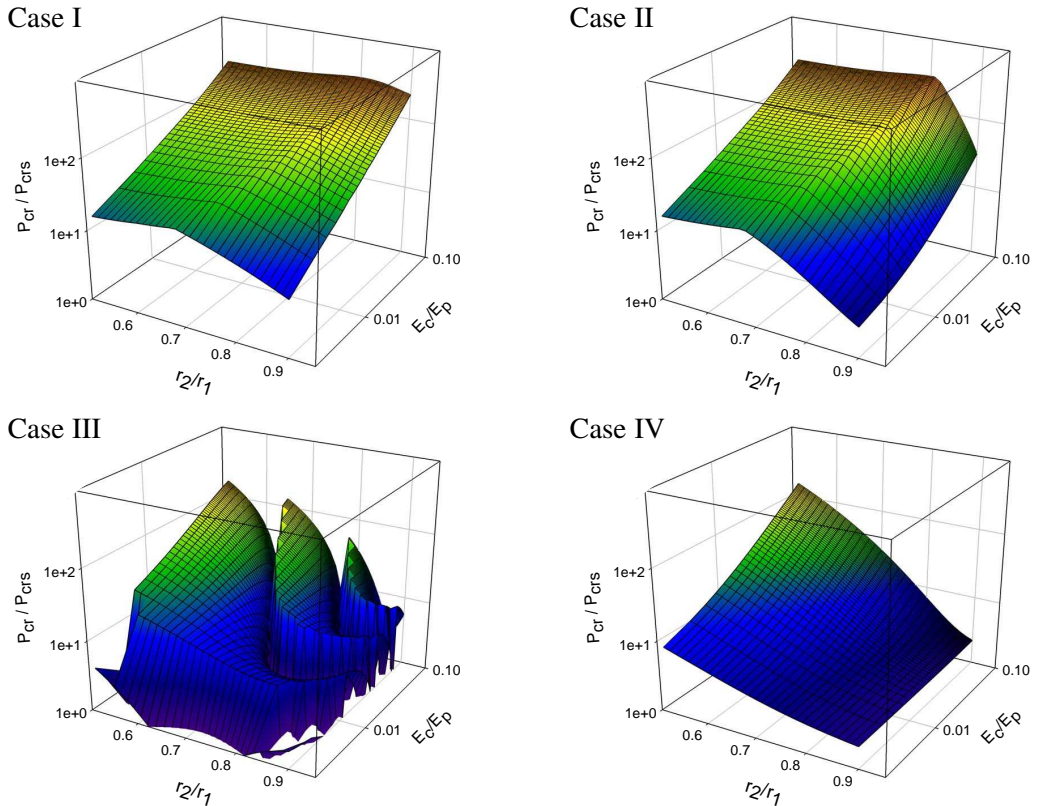


Figure 3. Ratio of buckling capacity of sandwich pipe versus outer pipe as a function of geometric and material properties for the cases discussed on page 395.

what has been considered as the general buckling mode shape in this study and what would happen in reality becomes more significant in sandwich pipes in which the core can freely slide on the inner pipe. This phenomenon is believed to be the cause the oscillation in the calculated buckling pressures corresponding to the different buckling mode shapes. For the sake of consistency, the logarithmic scale has been used in these figures, which magnifies the unevenness.

Figure 4 shows the variation of buckling pressure of the sandwich system as a function of the inner pipe's geometry (t_1/r_1) and the pipeline material properties (E_c/E_p) within the practical range. In these figures, the ratios r_2/r_1 and t_2/r_2 have been taken as 0.8 and 0.05, respectively. These graphs show that the buckling pressure of the system is significantly influenced by t_1/r_1 . The bottom right graph in Figure 4 shows that if the core layer is free to slide on both the inner and outer pipes, then the increase in the core modulus of elasticity would not improve the structural performance of the pipe when subject to external pressure. For other configurations, however, the increase in the core's modulus of elasticity would increase the buckling pressure of the system.

According to the results exhibited in Figures 3 and 4, in order to design an optimal sandwich pipe under external hydrostatic pressure, close attention should be paid to the bonding properties between the layers, as well as the geometrical and material related parameters like E_c/E_p , r_2/r_1 , and t_1/r_1 .

Figure 5 shows the mode number associated with the minimum buckling pressure of the SPs with various geometries and material properties. As illustrated in the figures, for the system under investigation,

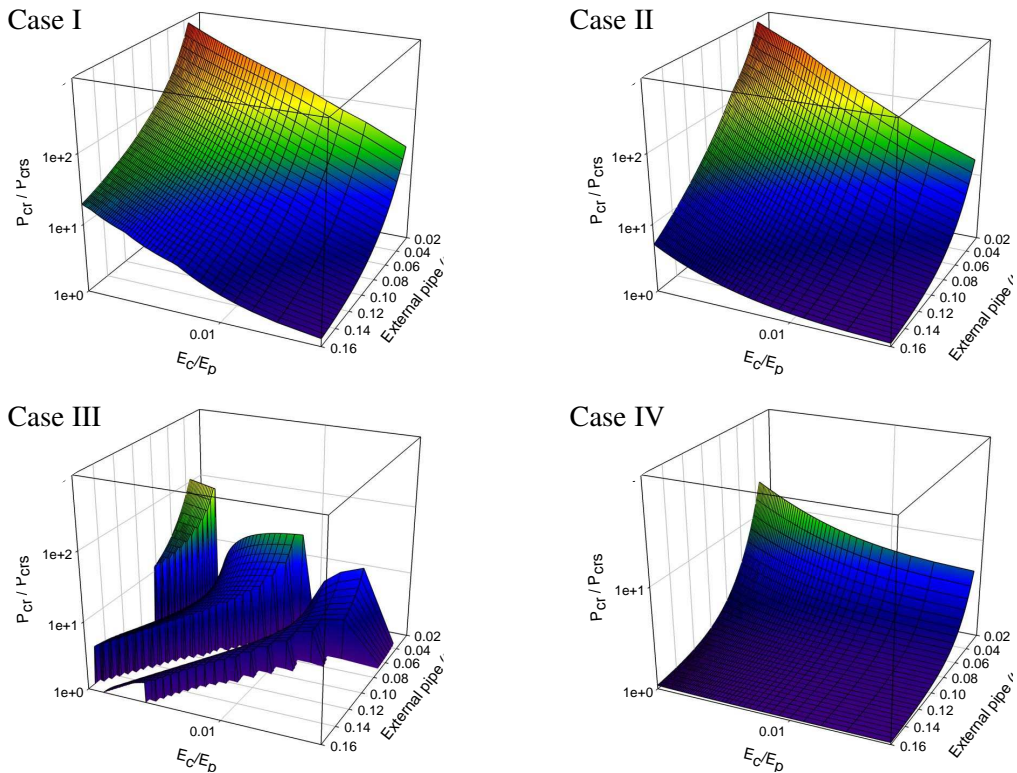


Figure 4. Ratio of buckling capacity of sandwich pipe to outer pipe as a function of geometric and material properties.

the buckling mode associated with the minimum buckling pressure of a sandwich pipe is not necessarily mode number 2. In fact, in most of the configurations studied, the buckling mode corresponding to the lowest capacity shifts upward as the core's stiffness is increased. The bottom right graph in [Figure 5](#) shows that for the fully unbonded case, the corresponding buckling mode number is mode number 2 for all the studied parameters ranges. This conclusion would help to simplify the calculations significantly.

Accuracy of the simplified equations. In this section, both simplified solutions (that is, both Sato and Patel's and our proposed solutions) are compared with the exact solution. The comparison is done for a sandwich system with core and pipe Poisson's ratios of 0.5 and 0.3, respectively. The percentage error is calculated by

$$\% \text{ error} = \left| \frac{P_{\text{cr}}(\text{Exact}) - P_{\text{cr}}(\text{Simplified})}{P_{\text{cr}}(\text{Exact})} \right| \times 100. \quad (22)$$

[Figure 6](#) shows the buckling pressure error in the SS solution, (16), relative to the exact values calculated by solving (15). This graph has been generated for case I boundary conditions (fully bonded case). As seen in the left half of the figure, this simplified equation would produce error up to 180% for the illustrated range of parameters. The right half reports the margin of error for a sandwich pipe with $t_1/r_1 = 0.05$ and inner to outer pipe radius ratio of 0.8. We see that the error produced by (15) for the sample pipe is at least 120% and can be as large as 200%. In conclusion, the error produced by this equation increases as the core stiffness decreases and the outer pipe thickness to radius ratio increases.

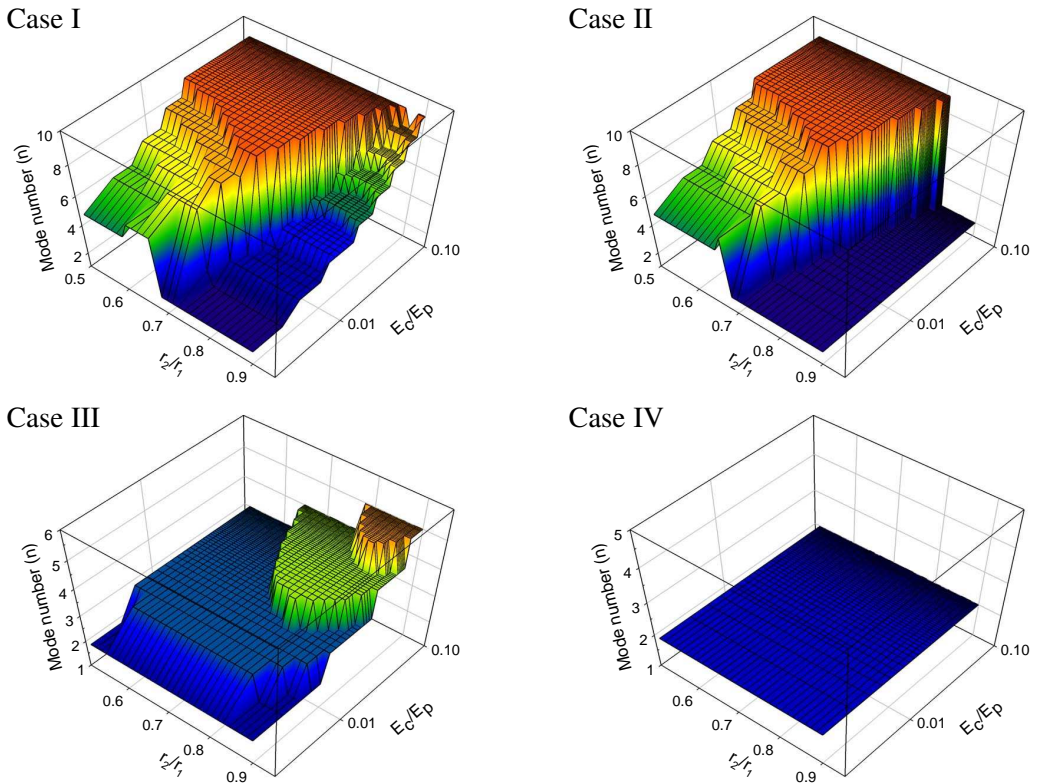


Figure 5. Sandwich pipe buckling mode numbers for the cases discussed on page 395.

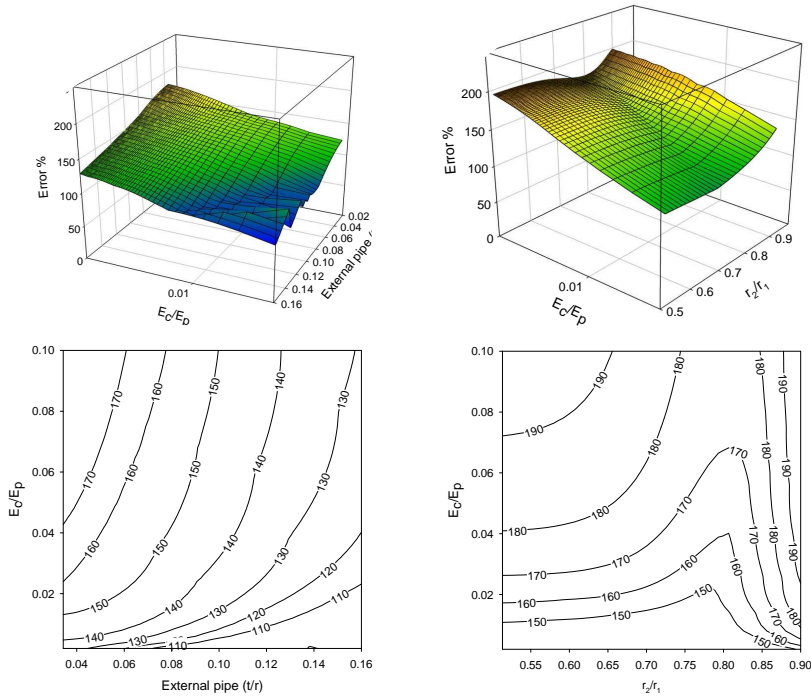


Figure 6. Percent error produced by the SS in the fully bonded case, as a function of E_c/E_p and the outer pipe's t/r ratio (left) and as a function of E_c/E_p and r_2/r_1 (right).

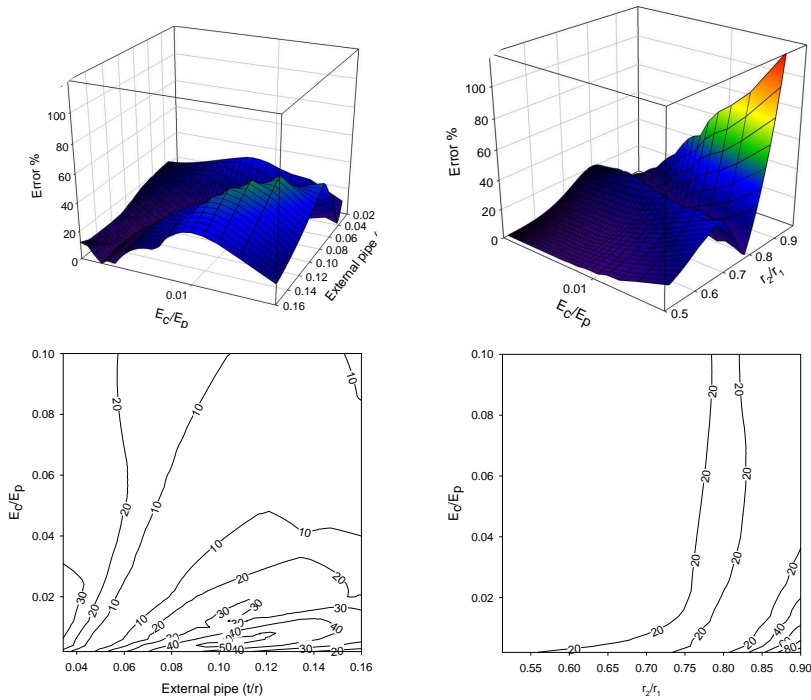


Figure 7. Percent error produced by the ATS in the fully bonded case, as a function of E_c/E_p and the outer pipe's t/r ratio (left) and as a function of E_c/E_p and r_2/r_1 (right).

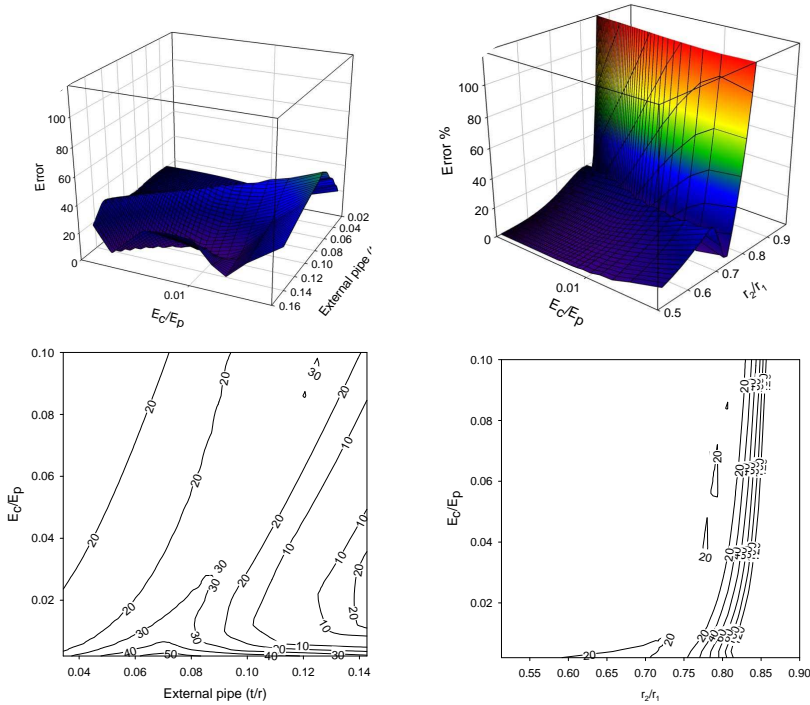


Figure 8. Percent error produced by the ATS for the case of the outer pipe sliding over the core, as a function of E_c/E_p and the outer pipe's t/r ratio (left) and as a function of E_c/E_p and r_2/r_1 (right).

Figure 7 shows the percent error resulting from the ATS (19) (that is, the simplified solution developed in this study), for the case of a fully bonded SP. The figure suggests that the ATS yields more accurate results than the SS from (16). The SS produced a maximum error of 120%, where for the same pipe the ATS produces a maximum error of 50% in predicting the buckling pressure (in the worst possible case).

Figure 8 shows the percentage error produced by our simplified solution in predicting the buckling pressure of the pipe with core layer unbonded to the outer pipe. The exact results are obtained by solving (15), using type II boundary condition. As can be seen, the ATS produces very large errors for values of r_2/r_1 above 0.75. However, if the inner to outer pipes radius ratio is below 0.75, the error is less than 20%. In practice, most PIP systems use $r_2/r_1 < 0.75$. Therefore, the ATS (19), would be admissible for use in practice. Figure 8, top right, shows the percent error for a sandwich pipe with a thickness to radius ratio of 0.05 and an inner to outer pipe radius ratio of 0.8.

Numerical results

In this section a series of finite element (FE) eigenvalue analyses are performed for a parametric study to assess the accuracy of the proposed simplified solution. ABAQUS Version 6.8 was used to construct and analyze the FE models. Due to the assumption of uniform structural properties and loading conditions along the length of the pipeline, a sandwich ring was modeled as the equivalent structure, to study the buckling characteristic of the SP under hydrostatic pressure. The 20-node, reduced integration

brick element (C3D20R) was used to construct the finite element model of the pipes. In this paper, SP systems with incompressible core layers were investigated to establish the margin of error produced by the solutions outlined earlier. Therefore, the core layer was modeled with 20-node, reduced integration hybrid brick elements (C3D20RH), suited for modeling soft materials. Appropriate boundary conditions were applied to restrain the rigid body motions of the model; however, they were kept to a minimum so that the higher order buckling modes could be captured.

The “tie” multipoint constraint option of ABAQUS was used to model the fully bonded contacts between the core and inner and outer pipes. However, in those configurations in which the core layer was disbonded from the pipes, the contact mechanism was modeled using the linear two point constraint equations of ABAQUS. With this approach, the radial displacement of the core on the contact surfaces is set to follow the radial displacement of the contacting surfaces of the pipes, but no constraint is imposed on the tangential displacements. This approach is prone to error, because the elements may intersect. To minimize this possibility, a fine mesh must be used. A mesh convergence study was conducted to investigate the effect of the mesh density on the calculated buckling pressure. Figure 9 shows the buckling mode shapes of the four studied PIP configurations.

To test the integrity of the simplified solution, four sets of parametric studies were performed on the four analytically studied configurations. In each set, 1296 FE models were analyzed and the results were compared with those obtained using the simplified solution. Figure 10 shows the percent error produced by the simplified equations with respect to the FE results for the SS from (16), AST from (19), and AST from (18) cases.

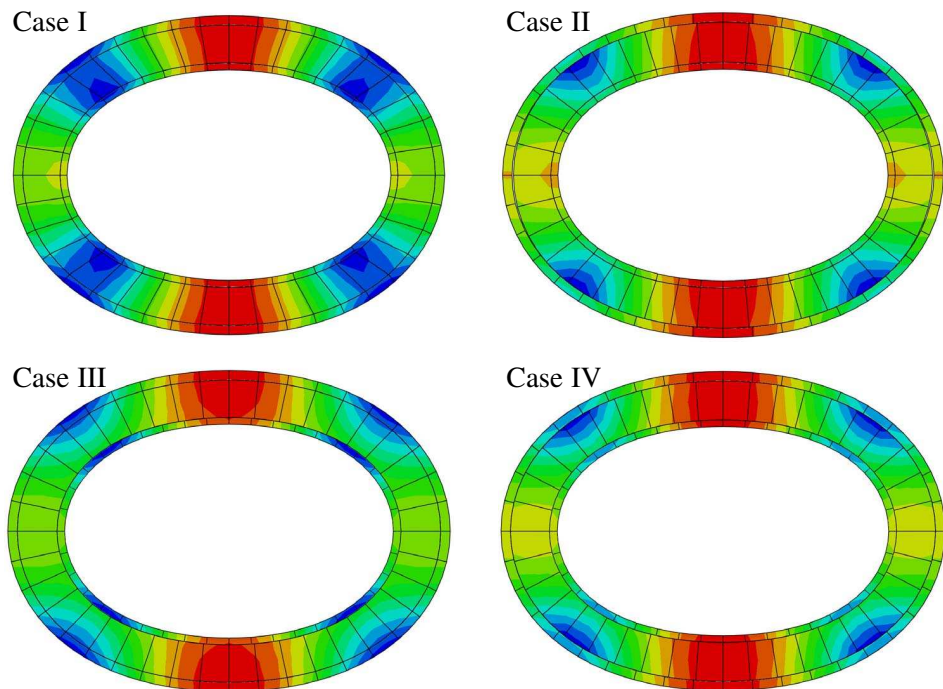


Figure 9. Buckling mode shapes for the cases discussed on page 395.

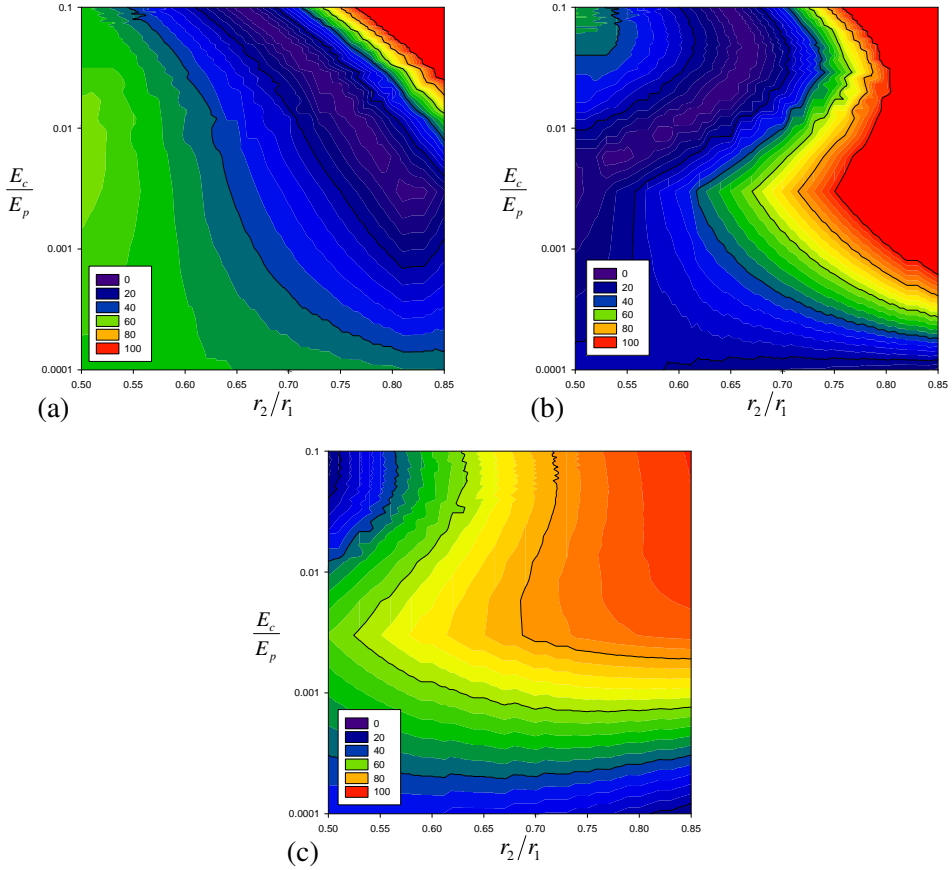


Figure 10. Percentage error produced by the simplified equations with respect to the FE results for (a) SS from (16), (b) AST from (19), and (c) AST from (18).

As shown in Figure 10a, the SS solution results in an error of less than 50% for larger values of r_2/r_1 . The comparison of the results obtained by the ATS simplified from (19) and FE are illustrated in Figure 10b. As can be seen, the solution yields a maximum error of slightly less than 50% for smaller values of r_2/r_1 . These graphs show that either solution can predict the buckling pressure of a sandwich pipe, for a limited range of the parameters, with reasonable accuracy.

Figure 10c shows the error margins when using (18) for a SP system in which the core layer is disbonded from the outer pipe. As illustrated in this figure, for E_c/E_p greater than 10^{-3} , this equation yields an error of greater than 60%. However, for smaller values of E_c/E_p , which would pertain to most of the commonly used plastic materials, (18) would yield acceptable accuracy.

Figure 11 shows the admissible parameter ranges for which one could use the simplified equations, keeping the margin of error below 50%. Also within a small range of parameters (that is, $r_2/r_1 > 0.75$ and $E_c/E_p > 0.01$), both solutions — given by Equations (16) and (19) — would yield error margins greater than 50%. Therefore, in order to obtain reliable results in the noted ranges (that is, the parameter ranges that fall within the cyan region in Figure 11), it is recommended that a FE buckling analysis be conducted.

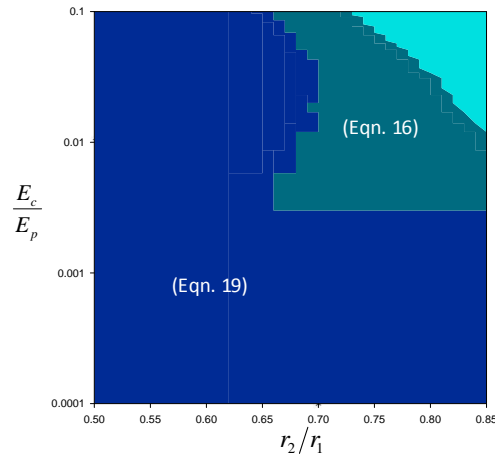


Figure 11. Range of parameters for which each of the simplified equations can predict the buckling pressure with less than 50% error.

Conclusions

We used an analytical approach to develop exact and simplified (approximate) solutions for the elastic buckling pressure of sandwich pipes under external hydrostatic pressure. The parameters required to describe the characteristic equation of the system were discussed in detail. The integrity of the approximate solution given in [Brush and Almroth 1975; Sato and Patel 2007] was compared with that of this study. The practical and admissible ranges for physical and material parameters were established. The results were compared with those obtained through an extensive series of FE parametric case studies and the accuracy of the equations was assessed. Here is a summary of our conclusions:

- The contact mechanism between the core layer and the inner and outer pipes significantly affects the buckling capacity of the system.
- While for a single pipe the first buckling mode shape always corresponds to the second eigenmode (the first eigenmode would correspond to the rigid-body mode), the same does not always hold in the case of a sandwich pipe. Therefore, to find the buckling capacity of a sandwich pipe, one should explore the higher eigenmodes.
- The results obtained from the exact solution were used to validate the assumptions made in developing the simplified solution and to establish the range of applicability of the simplified solution.
- Comparison of the results obtained from the simplified solutions for the fully bonded system with those obtained from either the FE or exact analytical solutions indicated that the approximate solutions could produce reasonable accuracy for predicting the buckling capacity of the system, but for a limited range of the investigated parameters. It was shown that for stiffer core materials and greater ratios of inner to outer pipe radii, the simplified solution of [Sato and Patel 2007] would yield more accurate results. However, for the other ranges, which would fall within a more practical domain for SPs with plastic core materials, the simplified solution presented in this study would predict the buckling capacity with a higher accuracy.

- The choice from among the simplified solutions is facilitated by the graphs produced in this study. These graphs can be used to gain a sense as to what error margin one could expect when using the proposed simplified equation within a practical range.
- The comparison of the results produced by the FE analyses and those obtained from the simplified solutions for the case where the core layer could slide on the external pipe demonstrated that the simplified equation (the ATS) would produce large error margins within certain ranges; however, the solution would generate acceptable accuracy for SP systems with conventionally used core materials.

Appendix: Coefficients of the core material stiffness matrix K_c

We set $K_c = \frac{1}{\psi} LA$, where L is given by

$$L = \begin{bmatrix} 1 & 0 & 0 & 0 \\ -nt_1/2r_1 & 1 - t_1/2r_1 & 0 & 0 \\ 0 & 0 & 1 & 0 \\ 0 & 0 & nt_2/2r_2 & 1 + t_2/2r_2 \end{bmatrix}$$

and ψ and the coefficients A_{ij} of A (for $0 \leq i, j \leq 4$) are given in terms of $R = \frac{a_2}{a_1}$ and $\Lambda = 4\nu_c - 3$ by case-dependent formulas:

Case I: core is fully bonded to inner and outer pipes (nonvanishing entries only).

$$\psi = (7 + \Lambda) \{ \Lambda^2(1 + R^{4n}) - R^{2n-2}[(n^2 - 1)(R^2 - 1)^2 + (1 + R^4)\Lambda^2] \}$$

$$A_{11} = 2E_c \{ \Lambda[n(\Lambda - 1) - \Lambda - 1] - R^{4n}\Lambda[n(\Lambda - 1) + \Lambda + 1] \\ + 2R^{2n-2}[2(\Lambda - 1) + n^2(R^2 - 1)(R^2 + \Lambda - 2) + R^2(3 - \Lambda) + R^4(\Lambda^2 - 1)] \}$$

$$A_{33} = 2E_c \{ \Lambda[n(\Lambda - 1) + \Lambda + 1] - R^{4n}\Lambda[n(\Lambda - 1) - \Lambda - 1] \\ + 2R^{2n-2}[1 - \Lambda^2 + n^2(R^2 - 1)(1 + R^2(\Lambda - 2)) + R^2(\Lambda - 3) - 2R^4(\Lambda - 1)] \}$$

$$A_{22} = 2E_c \{ \Lambda[n(\Lambda - 1) - \Lambda - 1] - R^{4n}\Lambda[\Lambda + 1 + n(\Lambda - 1)] + 2R^{2n-2}[n^2\Lambda - (n^2 - 1)R^2(1 + \Lambda) + R^4(n^2 - 1 + \Lambda^2)] \}$$

$$A_{44} = 2E_c \{ \Lambda[n(\Lambda - 1) + \Lambda + 1] + R^{4n}\Lambda[\Lambda + 1 - n(\Lambda - 1)] - 2R^{2n-2}[(1 + \Lambda)(R^2 - 1 + \Lambda) + n^2(R^2 - 1)(R^2\Lambda - 1)] \}$$

$$A_{12} = A_{21} = -2E_c \{ \Lambda[1 + n + (n - 1)\Lambda] + R^{4n-2}\Lambda(n(1 + \Lambda) + \Lambda - 1) - 2nR^{2n-2}[(n^2 - 1)(R^2 - 1)^2 + R^4\Lambda^2 + \Lambda] \}$$

$$A_{34} = A_{43} = 2E_c \{ R^{4n}\Lambda[1 + n + (n - 1)\Lambda] + \Lambda(n(1 + \Lambda) + \Lambda - 1) - 2nR^{2n-2}[(n^2 - 1)(R^2 - 1)^2 + R^4\Lambda + \Lambda^2] \}$$

$$A_{13} = A_{31} = -2E_c(\Lambda - 1) \{ R^{3n-1}[(n^2 - 1)(R^2 - 1) - (1 + n + (n - 1)R^2)\Lambda] \\ + R^{n-1}[(1 + n)R^2 + n - 1)\Lambda + (n^2 - 1)(R^2 - 1)] \}$$

$$A_{14} = A_{41} = -2E_c(\Lambda - 1) \{ R^{3n-1}[(n^2 - 1)(R^2 - 1) - (1 + n - (n - 1)R^2)\Lambda] \\ + R^{n-1}[(1 + n)R^2 - n + 1)\Lambda - (n^2 - 1)(R^2 - 1)] \}$$

$$A_{23} = A_{32} = -2E_c(\Lambda - 1) \{ -R^{3n-1}[(n^2 - 1)(R^2 - 1) + (1 + n + R^2 - nR^2)\Lambda] \\ + R^{n-1}[(n^2 - 1)(R^2 - 1) + (1 + R^2 + n(R^2 - 1))\Lambda] \}$$

Case II: Core can slide against outer pipe but is bonded to inner pipe (nonvanishing entries only).

$$\psi = (7 + \Lambda) \{ \Lambda[n(\Lambda - 1) - 1 - \Lambda] - R^{4n}\Lambda[1 + \Lambda + n(\Lambda - 1)] + 2R^{2n-2}[n^2\Lambda - (n^2 - 1)R^2(1 + \Lambda) + R^4(n^2 - 1 + \Lambda^2)] \}$$

$$\begin{aligned}
A_{11} &= 8E_c(n^2-1)\{-\Lambda - R^{4n}\Lambda + R^{2n-2}[2R^2+n^2(R^2-1)^2+R^4(\Lambda^2-1)]\} \\
A_{13} &= A_{31} = 4E_c(n^2-1)(\Lambda-1)\{R^{3n-1}[n(R^2-1)+R^2(1-\Lambda)]+R^{n-1}[R^2(1-\Lambda)+n(1-R^2)]\} \\
A_{14} &= A_{41} = 4E_c(n^2-1)(\Lambda-1)\{R^{n-1}[n(R^2-1)-R^2(1+\Lambda)]+R^{3n-1}[R^2(1+\Lambda)-n(1-R^2)]\} \\
A_{33} &= 2E_c\{-2R^{2n-2}[2R^4(2-2\Lambda+n^2(\Lambda-2))-2n^2\Lambda-(n^2-1)R^2(\Lambda-3)(1+\Lambda)] \\
&\quad +[n^2(\Lambda-1)^2-(1+\Lambda)^2]+R^{4n}[n^2(\Lambda-1)^2-(1+\Lambda)^2]\} \\
A_{34} &= A_{34} = 2E_c\{-R^{4n}[\Lambda+1+n(\Lambda-1)][1-\Lambda+n(1+\Lambda)] \\
&\quad +[n(\Lambda-1)-\Lambda-1][\Lambda-1+n(1+\Lambda)]+4nR^{2n-2}[n^2\Lambda-(n^2-1)R^2(1+\Lambda)+R^4(n^2\Lambda-1)]\} \\
A_{44} &= 2E_c\{[n^2(\Lambda-1)^2-(1+\Lambda)^2]+R^{4n}[n^2(\Lambda-1)^2-(1+\Lambda)^2]+2R^{2n-2}[2n^2\Lambda(1+R^4)-(n^2-1)R^2(1+\Lambda)^2]\}
\end{aligned}$$

Case III: Core can slide against inner pipe but is bonded to outer pipe (nonvanishing entries only).

$$\begin{aligned}
\psi &= (7+\Lambda)\{\Lambda[1+\Lambda+n(\Lambda-1)]-R^{4n}\Lambda[n(\Lambda-1)-1-\Lambda]-2R^{2n-2}[(1+\Lambda)(R^2-1+\Lambda)+n^2(R^2-1)(R^2\Lambda-1)]\} \\
A_{11} &= 2E_c\{[n^2(\Lambda-1)^2-(1+\Lambda)^2]+R^{4n}[n^2(\Lambda-1)^2-(1+\Lambda)^2] \\
&\quad +2R^{2n-2}[4(\Lambda-1)-R^2(\Lambda-3)(1+\Lambda)+n^2(4-2\Lambda+2R^4\Lambda+R^2(\Lambda-3)(1+\Lambda))]\} \\
A_{21} &= A_{12} = -2E_c\{a_1^{4n}R^2[1+n(\Lambda-1)+\Lambda][1+n+(n-1)\Lambda]-R^2(a_1R)^{4n}[n(\Lambda-1)-\Lambda-1] \\
&\quad [n-1+\Lambda+n\Lambda]-4a_1^{2n}n(a_1R)^{2n}[\Lambda-1+R^2(1+\Lambda)+n^2(R^2-1)(R^2\Lambda-1)]\} \\
A_{31} &= A_{13} = -4a_1^nE_c(n^2-1)(\Lambda-1)\{R^{3n-1}(\Lambda-1+n(1-R^2))+R^{n-1}[\Lambda-1+n(R^2-1)]\} \\
A_{22} &= 2E_c\{[n^2(\Lambda-1)^2-(1+\Lambda)^2]+R^{4n}[n^2(\Lambda-1)^2-(1+\Lambda)^2]+2R^{2n-2}[2n^2\Lambda+2n^2R^4\Lambda-(n^2-1)R^2(1+\Lambda)^2]\} \\
A_{32} &= A_{23} = -4E_c(n^2-1)(\Lambda-1)\{R^{n-1}[n(R^2-1)-1-\Lambda]+R^{3n-1}[1+\Lambda+n(R^2-1)]\} \\
A_{33} &= 8E_c(n^2-1)\{\Lambda(-2-R^{4n})+R^{2n-2}[n^2(R^2-1)^2+\Lambda^2-1+2R^2]\}
\end{aligned}$$

Case IV: Core can slide against both inner and outer pipes (nonvanishing entries only).

$$\begin{aligned}
\psi &= (7+\Lambda)\{[n^2(\Lambda-1)^2-(1+\Lambda)^2]+R^{4n}[n^2(\Lambda-1)^2-(1+\Lambda)^2]+2R^{2n-2}[2n^2\Lambda(1+R^4)-(n^2-1)R^2(1+\Lambda)^2]\} \\
A_{11} &= -8E_c(n^2-1)\{-R^{4n}[n(\Lambda-1)-1-\Lambda]+[1+\Lambda+n(\Lambda-1)]-2R^{2n-2}[R^2(1+\Lambda)+n^2(R^2-1)(R^2\Lambda-1)]\} \\
A_{31} &= A_{13} = -8E_cn(n^2-1)(\Lambda-1)\{R^{n-1}[(n-1)R^2-1-n]+R^{3n-1}[1+R^2+n(R^2-1)]\} \\
A_{33} &= -8E_c(n^2-1)\{-1-\Lambda+n(\Lambda-1)]-R^{4n}[1+\Lambda+n(\Lambda-1)]+2R^{2n-2}[n^2R^4+n^2\Lambda-(n^2-1)R^2(1+\Lambda)]\}
\end{aligned}$$

List of symbols

AST	Simplified solution developed in this study	r_1, r_2	Outer and inner pipe nominal radius
E_c, E_p	Elastic moduli of core and pipe material	SS	Simplified solution from [Brush and Almroth 1975; Sato and Patel 2007]
h	Constituent's thickness		
K_c, K_p	Stiffness matrices of core and pipe layers	σ_r	Radial stress
n	Buckling mode number	t_1, t_2	Outer and inner pipe wall thickness
ν_c, ν_p	Poisson ratios of core and pipe material	$\tau_{r\theta}$	Tangential stress
P	External pressure	v	Tangential deformation
P_{cr}	Sandwich pipe buckling pressure	w	Radial deformation
P_{crs}	External pipe buckling pressure	ϕ	Stress function

References

- [API 2000] *API spec 5L: specification for line pipe*, 42nd ed., American Petroleum Institute, Washington, DC, 2000.
- [Brush and Almroth 1975] D. O. Brush and B. Almroth, *Buckling of bars, plates and shells*, McGraw-Hill, New York, 1975.
- [Castello and Estefen 2006] X. Castello and S. F. Estefen, “Adhesion effect on the ultimate strength of sandwich pipes”, in *Proceedings of the 25th International Conference on Offshore Mechanics and Arctic Engineering* (Hamburg, 2006), ASME, New York, 2006. Paper OMAE2006-92481.
- [Castello and Estefen 2007] X. Castello and S. F. Estefen, “Limit strength and reeling effects of sandwich pipes with bonded layers”, *Int. J. Mech. Sci.* **49**:5 (2007), 577–588.
- [Castello and Estefen 2008] X. Castello and S. F. Estefen, “Sandwich pipes for ultra deepwater applications”, in *Offshore Technology Conference, OTC 08: Waves of change* (Houston, 2008), Curran Associates, Redhook, NY, 2008. Paper 19704-MS.
- [Castello et al. 2009] X. Castello, S. F. Estefen, H. R. Leon, L. C. Chad, and J. Souza, “Design aspects and benefits of sandwich pipes for ultra deepwaters”, in *Proceedings of the 28th International Conference on Ocean, Offshore and Arctic Engineering* (Honolulu, HI, 2009), ASME, New York, 2009. Paper OMAE2009-79528.
- [Estefen et al. 2005] S. F. Estefen, T. A. Netto, and I. P. Pasqualino, “Strength analyses of sandwich pipes for ultra deepwaters”, *J. Appl. Mech. (ASME)* **72**:4 (2005), 599–608.
- [Farshad 1994] M. Farshad, *Stability of structures*, Elsevier, Amsterdam, 1994.
- [Kardomateas and Simitse 2002] G. A. Kardomateas and G. J. Simitse, “Buckling of long, sandwich cylindrical shells under pressure”, pp. 327–328 in *Proceedings of the 6th International Conference on Computational Structures Technology* (Prague, 2002), edited by B. H. V. Topping and Z. Bittnar, Civil-Comp Press, Stirlingshire, 2002. Paper 140.
- [Kardomateas and Simitse 2005] G. A. Kardomateas and G. J. Simitse, “Buckling of long sandwich cylindrical shells under external pressure”, *J. Appl. Mech. (ASME)* **72**:4 (2005), 493–499.
- [Kyriakides 2002] S. Kyriakides, “Buckle propagation in pipe-in-pipe systems, I: Experiments”, *Int. J. Solids Struct.* **39**:2 (2002), 351–366.
- [Kyriakides and Corona 2007] S. Kyriakides and E. Corona, *Mechanics of offshore pipelines*, Elsevier, Amsterdam, 2007.
- [Kyriakides and Netto 2002] S. Kyriakides and T. A. Netto, “Dynamic propagation and arrest of buckles in pipe-in-pipe systems”, pp. 199–205 in *Proceedings of the 21st International Conference on Offshore Mechanics and Arctic Engineering* (Oslo, 2002), vol. 4, edited by T. Jones et al., ASME, New York, 2002. Paper OMAE2002-28600.
- [Kyriakides and Netto 2004] S. Kyriakides and T. A. Netto, “On the dynamic propagation and arrest of buckles in pipe-in-pipe systems”, *Int. J. Solids Struct.* **41**:20 (2004), 5463–5482.
- [Kyriakides and Vogler 2002] S. Kyriakides and T. J. Vogler, “Buckle propagation in pipe-in-pipe systems, II: Analysis”, *Int. J. Solids Struct.* **39**:2 (2002), 367–392.
- [Ohga et al. 2005] M. Ohga, A. Sanjeeva Wijenayaka, and J. G. A. Croll, “Reduced stiffness buckling of sandwich cylindrical shells under uniform external pressure”, *Thin-Walled Struct.* **43**:8 (2005), 1188–1201.
- [Sato and Patel 2007] M. Sato and M. H. Patel, “Exact and simplified estimations for elastic buckling pressures of structural pipe-in-pipe cross sections under external hydrostatic pressure”, *J. Mar. Sci. Technol.* **12**:4 (2007), 251–262.
- [Sato et al. 2008] M. Sato, M. H. Patel, and F. Trarieux, “Static displacement and elastic buckling characteristics of structural pipe-in-pipe cross-sections”, *Struct. Eng. Mech.* **30**:3 (2008), 263–278.
- [Timoshenko and Goodier 1970] S. Timoshenko and J. N. Goodier, *Theory of elasticity*, 3rd ed., McGraw-Hill, New York, 1970.

Received 9 Jun 2009. Revised 21 Oct 2009. Accepted 30 Oct 2009.

Department of Civil and Resource Engineering, Dalhousie University

KAVEH ARJOMANDI: kaveh.arjomandi@dal.ca

Dalhousie University, Department of Civil and Resource Engineering, 1360 Barrington Street, Halifax, NS B3J 1Z1, Canada

FARID TAHERI: farid.taheri@dal.ca

Dalhousie University, Department of Civil and Resource Engineering, 1360 Barrington Street, Halifax, NS B3J 1Z1, Canada

ELASTIC ANALYSIS OF CLOSED-FORM SOLUTIONS FOR ADHESIVE STRESSES IN BONDED SINGLE-STRAP BUTT JOINTS

GANG LI

In this paper, the adhesive stresses in unbalanced bonded single-strap butt joints are theoretically studied. Mathematical difficulties in the analysis of high order differential equations were solved and closed-form solutions for both the adhesive peel and shear stresses have been successfully developed. In the proposed solutions the adherends and doublers can be different in material and thickness. Peak stresses are located at the bonded overlap edges, especially at the inner edges. In addition, two-dimensional geometrically nonlinear finite element analyses were carried out to study the adhesive stresses in two different bonded butt joints. One was a special butt joint case with the adherends and doubler of identical material and thickness, and the other was a general butt joint case with different adherends and doubler. Good agreement in the adhesive stresses between the closed-form solutions and finite element results has been achieved. The single-strap butt joint actually consists of two single-lap joints; thus, the adhesive stress solutions can be further applied to unbalanced single-lap joints.

1. Introduction

The elastic analysis of bonded joints can be traced back to the 1930s, and was first practiced on balanced single-lap joints by [Volkersen \[1938\]](#). Since then, extensive theoretical studies have been carried out on this joint configuration [[Goland and Reissner 1944](#); [Hart-Smith 1973](#); [Chen and Cheng 1983](#); [Adams and Wake 1984](#); [Oplinger 1994](#); [Tsai and Morton 1994](#); [Li and Lee-Sullivan 2006a](#); [2006b](#)]. To date, closed-form solutions of balanced single-lap joints for predicting bending moments and shear forces at the overlap edges, as well as the adhesive shear and peel stresses in the adhesive layer, have been well established. A balanced symmetric, adhesive single-lap joint is defined as a single-lap joint made by adhesively bonding two identical adherends. When the two adherends have different geometries and/or mechanical properties, the joints are referred to as unbalanced (see [Figure 1\(a\)](#)). The complexity of this joint configuration is much greater than that of the balanced case. In addition, due to the complicated and tedious derivation and lengthy stress expressions, the corresponding complete closed-form adhesive stress solutions have not been provided in the open literature [[Hart-Smith 1973](#); [Williams 1975](#); [Bigwood and Crocombe 1989](#); [Cheng et al. 1991](#)]. With the progress achieved in adhesively bonded single- and double-lap joints (see [Figure 1\(b\)](#)), single-strap butt joint configuration became the subsequent topic of study (see [Figure 1\(c\)](#)). The extent of study on single-strap butt joints was less than that on the single-lap joints and the theoretical progress was slow. This situation could be attributed to the inherent theoretical difficulties in the required mathematics and identification of its potential roles in engineering structural applications, as claimed by [Hart-Smith \[1985\]](#).

Keywords: adhesive stress, closed-form solution, single-strap butt joint, finite element analysis.

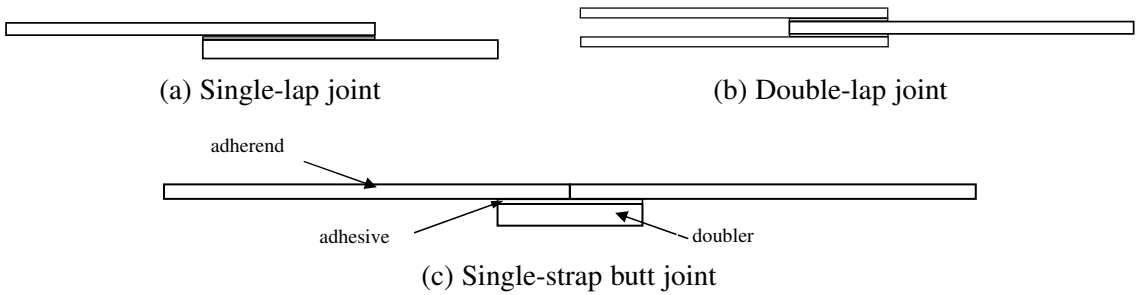


Figure 1. Several adhesively bonded joint configurations.

A single-strap joint consists of two single-lap joints. For joints with identical doubler and adherends, a special joint case, closed-form adhesive stress solutions can be easily obtained using the same approach as in the balanced single-lap joint configuration. For the butt joints with different doubler and adherends, a coupling relationship exists between the adhesive peel and shear stresses, and the corresponding complete closed-form solutions in explicit expressions in the adhesive stresses have not been reported in the open literature. [Delale et al. \[1981\]](#) reported on a bonded panel-to-substrate joint structure, which could be approximately treated as an unbalanced butt joint configuration with one piece of the adherend bonded with a sort of doubler. They gave general expressions of the closed-form solutions for the adhesive peel and shear stresses, and presented the boundary conditions used to determine the integral constants. Complex terms with nonzero imaginary terms were present in the adhesive stress expressions, the integral constants, and the final expressions of the adhesive stresses, and were not further investigated.

Currently, there is a strong and growing trend towards optimizing the strength, weight, and durability of aircraft structures. The substantial developments in high performance composite structures and special automated fiber placement machines encourage expectations for the extensive application of composite joints to both the secondary and primary structures in aircraft. The fuselage structures for the new generation of aircraft are being built by assembling several precured one-piece composite fuselage barrels. A bonded single-strap butt joint configuration could be one of the possible configurations for the assembly of the fuselage structure. In addition, this joint configuration has a better aerodynamic efficiency than most other joint configurations. As reported by [Kweon et al. \[2006\]](#), the static strength of bonded double-lap joints using film adhesives FM73 could be much higher than that of bolted joints. With the development in joint bonding techniques, the peak peel stress can be effectively reduced, as reported by [da Silva and Adams \[2007a; 2007b\]](#). To maximize the joint efficiency, an adequate understanding of the variation in adhesive stresses under various influences is essential. This paper presents theoretical explorations of the adhesive stresses in an adhesively bonded general single-strap joint configuration with different adherends and doubler. Without losing generality of the solutions and avoiding unnecessary complexity in the theoretical derivation, the joints will be restricted to being made from isotropic materials. The aim of the work is to obtain closed-form solutions for the adhesive stresses in isotropic butt joints so that the solutions can later be extended to composite joints including unbalanced single-lap joints. The obtained theoretical solutions can be used to quantitatively study the effect of each component on the variation in adhesive stresses, guide practical joint design, and make possible sound bases for practical applications

in the aerospace industry. For the provided complete closed-form solutions, the integration constants are quite long, which should be acceptable for such a complicated analysis of high order differential equations. Furthermore, they can be a solid basis for further effective development of simplified stress solutions for more practical applications in the near future. For the sake of brevity, only the main contents of the adhesive stress derivations are present in this paper. An extended version including a parametric study using the developed closed-form solutions can be found elsewhere [Li 2008].

2. Theoretical formulations

Joint deflection. Secondary bending occurs in butt joints when they are loaded in tension. Within the elastic deformation range, it is appropriate to treat both adherends and doubler as beams using cylindrical bent plate theory, as initially proposed by Goland and Reissner [1944], and then applied by others in works including [Hart-Smith 1973; Cheng et al. 1991; Oplinger 1994; Li and Lee-Sullivan 2006a; Li 2008]. The deformation of a single-strap butt joint in tension is shown in Figure 2. The geometrical nonlinearity induced by the out-of-plane deflection w should be involved in identifying the joint bending

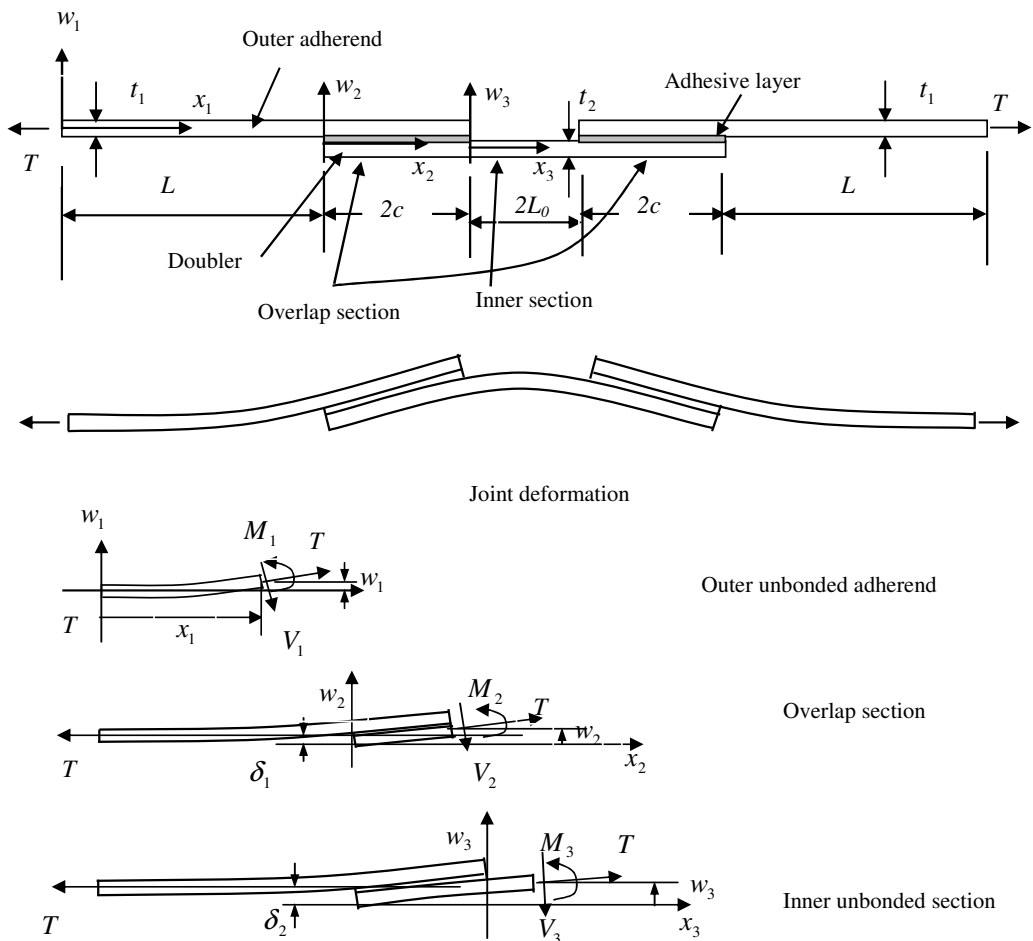


Figure 2. Deformation of the adhesively bonded single-strap butt joint in tension (not to scale).

moment. An accurate joint deflection and shear force can then be determined using cylindrical bent plate or beam theory. The variables in this joint configuration include both dimension and material parameters. The length of the outer unbonded adherend is L , the bonded overlap length is $2c$ on each side, the length of the inner unbonded doubler is $2L_0$, the total length of the doubler is $4c + 2L_0$, and the total joint length is $2L + 4c + 2L_0$. The adherend thickness is t_1 and the doubler thickness is t_2 . The plane strain condition is applicable for the joint configuration, and thus, the per-unit-width forces of tensile force, T , the shear force, V_i , and the bending moment, M_i , are the three forces assumed in the joint. By convention, when $i = 1$ the forces are in the outer unbonded adherends, when $i = 2$ the forces are in the bonded overlap section, and when $i = 3$ the forces are in the inner unbonded doubler section. The tensile force T is applicable to any section of the joint.

Brief descriptions of the joint deflection derivation are given in the following. Detailed expressions of the deflection within each section can be found in [Li 2008].

Bending moments and shear forces. The per-unit-width bending moment and shear force at specific positions can be obtained using the relations

$$M_i = D_i \frac{d^2 w_i}{dx_i^2} \quad (i = 1, 2, 3), \quad V_i = \frac{dM_i}{dx_i} = D_i \frac{d^3 w_i}{dx_i^3} \quad (i = 1, 2, 3), \quad (1a)$$

where

$$\begin{aligned} D_1 &= \frac{E'_{\text{adherend}} t_{\text{adherend}}^3}{12} = \frac{E_1 t_1^3}{12(1 - \nu_1^2)} \quad (\text{plane strain}), \\ D_2 &= E'_{\text{adhesive}} \left(\frac{\eta^3}{12} + \eta \left(\delta_1 - \frac{t_{\text{adherend}} + \eta}{2} \right)^2 \right) + E'_{\text{adherend}} \left(\frac{t_{\text{adherend}}^3}{12} + t_{\text{adherend}} \delta_1^2 \right) \\ &\quad + E'_{\text{doubler}} \left(\frac{t_{\text{doubler}}^3}{12} + t_{\text{doubler}} (\delta_2 - \delta_1)^2 \right) \\ &\approx E'_{\text{adherend}} \left(\frac{t_{\text{adherend}}^3}{12} + t_{\text{adherend}} \delta_1^2 \right) + E'_{\text{doubler}} \left(\frac{t_{\text{doubler}}^3}{12} + t_{\text{doubler}} (\delta_2 - \delta_1)^2 \right) \\ &= E'_1 \left(\frac{t_1^3}{12} + t_1 \delta_1^2 \right) + E'_2 \left(\frac{t_2^3}{12} + t_2 (\delta_2 - \delta_1)^2 \right), \\ D_3 &= \frac{E'_{\text{doubler}} t_{\text{doubler}}^3}{12} = \frac{E_2 t_2^3}{12(1 - \nu_2^2)}. \end{aligned} \quad (1b)$$

The parameter D_i ($i = 1, 2, 3$) is the per-unit-width bending stiffness in the plane strain condition of the outer unbonded adherends, overlap, and inner unbonded doubler sections, respectively. In the bonded overlap section, the impact of the adhesive stiffness to the stiffness D_2 can be neglected, because it is small enough compared to those of the adherends and doubler. The origins of the coordinate frames are located at the centroid in the left end cross-sectional area of each section. δ_1 and δ_2 are the transverse (vertical) distances between the neutral planes, as shown in Figure 3 and given by

$$\delta_1 = \frac{t_1 + t_2 + 2\eta}{2(1 + E'_1 t_1 / (E'_2 t_2))}, \quad \delta_2 = \frac{t_1 + t_2 + 2\eta}{2}. \quad (1c)$$

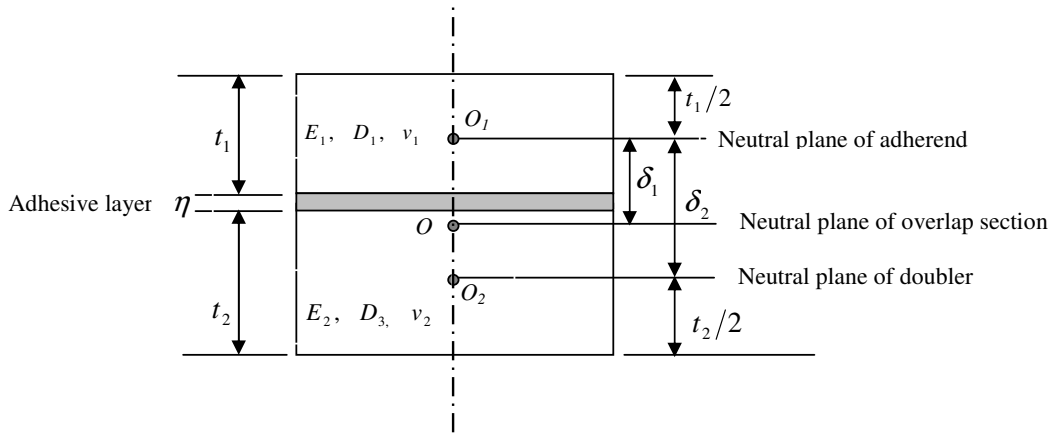


Figure 3. Neutral planes of the cross-sectional area of the bonded overlap section.

Overlap section. The sign convention for the positive tensile force, shear force, and bending moment is defined in Figure 4. The subscripts u and d apply to the upper adherend and doubler in the overlap section, respectively.

The bending moments and shear forces at the two outer overlap edges are

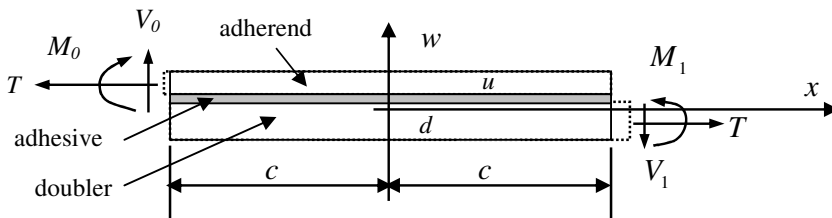
$$M_0 = D_u \frac{d^2 w_1(x_1)}{dx_1^2} \Big|_{x_1=L}, \quad V_0 = D_u \frac{d^3 w_1(x_1)}{dx_1^3} \Big|_{x_1=L} \quad (2a)$$

The bending moment and shear forces at the two inner overlap edges are

$$M_1 = D_d \frac{d^2 w_3(x_3)}{dx_3^2} \Big|_{x_3=0}, \quad V_1 = D_d \frac{d^3 w_3(x_3)}{dx_3^3} \Big|_{x_3=0} \quad (2b)$$



(a) Sign convention (positive force definition)



(b) Coordinate frame in the left overlap section at the overlap centroid and edge forces

Figure 4. Illustrations of force sign convention and the loading condition at the joint overlap edge.

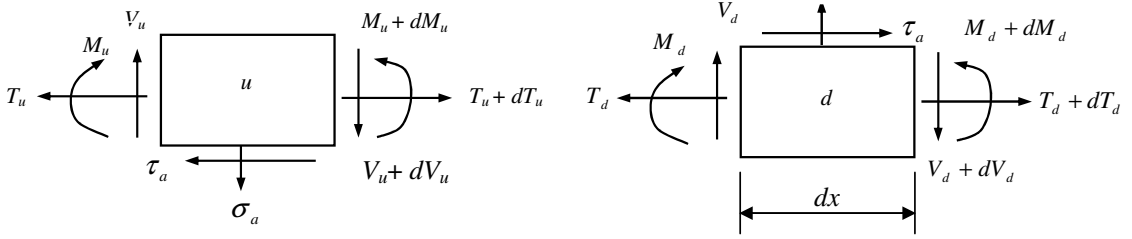


Figure 5. Illustration of loading state in infinitesimal elements for upper adherend (u) and lower doubler (d) in the overlap section.

Please note that the relations, $D_u = D_1$ (the adherend) and $D_d = D_3$ (the doubler) exist throughout the entire paper. To clearly display the variation in moments at the outer and inner overlap edges and directly study the quantitative relationship between the two edge moment magnitudes affected by each joint component and tensile load, these being the edge moments normalized by the moment parameter $(t_1 + \eta)T/2$, the edge moment factors are introduced and defined as

$$k_1 = \frac{2}{(t_1 + \eta)T} M_0 \approx \frac{2M_0}{Tt_1} \quad (\text{outer edges}), \quad k_2 = \frac{2}{(t_1 + \eta)T} M_1 \approx \frac{2M_1}{Tt_1} \quad (\text{inner edges}). \quad (2c)$$

Adhesive shear and peel stresses. Adhesive stresses can be determined from the equilibrium in the overlap section, as shown in Figure 5, where σ_a is the peel stress, τ_a the shear stress, and η the adhesive thickness. The adherend thickness is t_1 and the doubler thickness is t_2 . The force and the moment equilibrium equations for the upper and lower infinitesimal elements in the bonded overlap section can be described by

$$\begin{aligned} \frac{dM_u}{dx} - V_u - \tau_a \left(\frac{t_1 + \eta}{2} \right) &= 0, & \frac{dT_u}{dx} - \tau_a &= 0, & \frac{dV_u}{dx} + \sigma_a &= 0, & \frac{d^2w_u}{dx^2} &= \frac{M_u}{D_u}, \\ \frac{dM_d}{dx} - V_d - \tau_a \left(\frac{t_2 + \eta}{2} \right) &= 0, & \frac{dT_d}{dx} + \tau_a &= 0, & \frac{dV_d}{dx} - \sigma_a &= 0, & \frac{d^2w_d}{dx^2} &= \frac{M_d}{D_d}. \end{aligned} \quad (3a)$$

The axial strains of the adherend-adhesive and adhesive-doubler interfaces are

$$\varepsilon_{ux} = \frac{du_u}{dx} = \frac{T_u}{E'_u t_1} + \frac{t_1}{2} \frac{M_u}{D_u}, \quad \varepsilon_{dx} = \frac{du_d}{dx} = \frac{T_d}{E'_d t_2} - \frac{t_2}{2} \frac{M_d}{D_d}, \quad (3b)$$

where $E' = E/(1 - \nu^2)$ under the plane strain condition.

Generally, the adherends and doubler may behave in a linear elastic manner, but under relatively severe loading and temperature the adhesive may exhibit viscoelastic and/or nonlinear properties. The nonlinearities in the material properties make exact analytical treatment of the structural and material problems very complicated. Therefore, the theoretical analysis was carried out using simplified assumptions. The adherends, doubler, and adhesive were treated as linear elastic materials. For the elastic adhesive layer, the relationships between the adhesive peel and shear stresses and the displacements of the upper adherend and lower doubler can be defined by

$$\frac{\sigma_a}{E_a} = \frac{w_u - w_d}{\eta}, \quad \frac{\tau_a}{G_a} = \frac{u_u - u_d}{\eta}, \quad (3c)$$

where E_a and G_a are elastic and shear moduli of the adhesive material.

Differentiating Equation (3c) and utilizing these equilibrium relations, the coupling relations existing between the peel and shear stresses can be identified as

$$\frac{d^3\tau_a}{dx^3} + a_1 \frac{d\tau_a}{dx} + a_2\sigma_a = 0, \quad \frac{d^4\sigma_a}{dx^4} + b_1\sigma_a + b_2 \frac{d\tau_a}{dx} = 0, \quad (4a)$$

where

$$\begin{aligned} a_1 &= -\frac{G_a}{\eta} \left(\frac{1}{E'_u t_1} + \frac{1}{E'_d t_2} + \frac{t_1(t_1 + \eta)}{4D_u} + \frac{t_2(t_2 + \eta)}{4D_d} \right), & a_2 &= \frac{G_a}{\eta} \left(\frac{t_1}{2D_u} - \frac{t_2}{2D_d} \right), \\ b_1 &= \frac{E_a}{\eta} \left(\frac{1}{D_u} + \frac{1}{D_d} \right), & b_2 &= \frac{E_a}{\eta} \left(\frac{t_2 + \eta}{2D_d} - \frac{t_1 + \eta}{2D_u} \right). \end{aligned} \quad (4b)$$

The coupling relations vanish provided the coupling parameters $a_2 = b_2 = 0$, when the same material with identical thickness is used for the adherends and doubler.

3. Solutions for the adhesive stresses

Definition of the butt joints in general and special cases. The general case refers to joints with different adherends and doubler in their materials and/or thicknesses. The special case refers to joints in which the coupling between the adhesive peel and shear stresses vanishes, for instance, in joints with the same material and thickness in the adherends and doubler. For this situation, the adhesive peel and shear stresses can be decoupled as in balanced single-lap joints; thus, it is easy to obtain the closed-form solutions [Oplinger 1994; Li and Lee-Sullivan 2006a; Li 2008].

Efforts to explore the closed-form solutions are carried out for the general butt joint case in the following.

Determination of the adhesive stresses in the general case.

Adhesive shear stress. By eliminating the peel stress in the coupling Equation (4a), the equation of the adhesive shear stress can be written as

$$\frac{d^7\tau_a}{dx^7} + a_1 \frac{d^5\tau_a}{dx^5} + b_1 \frac{d^3\tau_a}{dx^3} + (a_1 b_1 - a_2 b_2) \frac{d\tau_a}{dx} = 0. \quad (5a)$$

The characteristic equation of this equation is

$$\lambda^7 + a_1 \lambda^5 + b_1 \lambda^3 + (a_1 b_1 - a_2 b_2) \lambda = 0 \quad (5b)$$

(see [AEP 1979; Derrick and Grossman 1987; Kreyszig 1993]). One root is $\lambda_0 = 0$, and then the equation above becomes $\lambda^6 + a_1 \lambda^4 + b_1 \lambda^2 + (a_1 b_1 - a_2 b_2) = 0$. Assuming $\phi = \lambda^2$, the equation can be written as $\phi^3 + a_1 \phi^2 + b_1 \phi + (a_1 b_1 - a_2 b_2) = 0$. Substituting $\phi = \gamma - a_1/3$ into the above equation [AEP 1979], the above equation becomes

$$\gamma^3 + p\gamma + q = 0, \quad (5c)$$

where

$$p = b_1 - \frac{a_1^2}{3}, \quad q = \frac{2a_1^3}{27} + \frac{2a_1 b_1}{3} - a_2 b_2. \quad (5d)$$

We use the classical formula to solve (5c). Setting

$$r' = \sqrt[3]{-\frac{q}{2} + \sqrt{\left(\frac{q}{2}\right)^2 + \left(\frac{p}{3}\right)^3}} \quad \text{and} \quad r'' = \sqrt[3]{-\frac{q}{2} - \sqrt{\left(\frac{q}{2}\right)^2 + \left(\frac{p}{3}\right)^3}},$$

the three roots of (5c) are

$$\gamma_1 = r' + r'', \quad \gamma_2 = \omega r' + \omega^2 r'', \quad \gamma_3 = \omega^2 r' + \omega r'', \quad (5e)$$

where $\omega = (-1 + i\sqrt{3})/2$, $\omega^2 = (-1 - i\sqrt{3})/2$, and $i^2 = -1$. The root γ_1 is real; γ_2 and γ_3 , and γ_2^2 and γ_3^2 , are complex conjugates and can be further expressed as

$$\gamma_2 = -\frac{\gamma_1}{2} + i\frac{\sqrt{3}}{2}(r' - r''), \quad \gamma_3 = -\frac{\gamma_1}{2} - i\frac{\sqrt{3}}{2}(r' - r''). \quad (5f)$$

Using these expressions, the three roots of parameter ϕ can be expressed as

$$\phi_k = \gamma_k - \frac{a_1}{3} \quad (k = 1, 2, 3). \quad (6a)$$

Thus, the second and third roots of λ for (5b) can be determined as

$$\lambda_{1,2} = \pm \sqrt{\gamma_1 - \frac{a_1}{3}} \quad \left(\text{provided } \gamma_1 - \frac{a_1}{3} \geq 0\right). \quad (6b)$$

The second and third roots of ϕ can be expressed as follows [AEP 1979; Derrick and Grossman 1987; Kreyszig 1993]:

$$\phi_2 = |\phi| \exp(i\beta) = |\phi|(\cos \beta + i \sin \beta), \quad \phi_3 = |\phi| \exp(-i\beta) = |\phi|(\cos \beta - i \sin \beta), \quad (6c)$$

where the argument β is the directed angle from the positive x -axis to the complex vector on the complex plane, given by $\beta = \min\{\beta_1, \beta_2\}$, where the angles are defined within the range from 0 to 2π . The sum of the two angles β_1 and β_2 is 2π .

The modulus, $|\phi|$, of ϕ_2 and ϕ_3 is

$$|\phi| = \sqrt{\left(-\frac{\gamma_1}{2} - \frac{a_1}{3}\right)^2 + \frac{3}{4}(r' - r'')^2}, \quad (6d)$$

The angles are measured in radians and are positive in the counterclockwise sense. For instance, if the angle β_1 is within the range $[0, \pi/2]$, then the angles can be calculated as

$$\beta_1 = \arg \phi_2 = \arctan \frac{(\sqrt{3}/2)(r' - r'')}{-\frac{\gamma_1}{2} - \frac{a_1}{3}} \quad (6e)$$

and $\beta_2 = 2\pi - \beta_1$.

Based on the actual positions of ϕ_2 and ϕ_3 on the complex plane, the angle values can be determined. The real part of ϕ_2 and ϕ_3 is $|\phi| \cos \beta = -\gamma_1/2 - a_1/3$, and the imaginary parts of the ϕ_2 and ϕ_3 are

$$\pm |\phi| \sin \beta = \pm \frac{\sqrt{3}}{2}(r' - r'').$$

Based on (6c), the remaining four roots of λ can then be determined as

$$|\phi|^{\frac{1}{2}}\left(\cos \frac{\beta}{2} + i \sin \frac{\beta}{2}\right), -|\phi|^{\frac{1}{2}}\left(\cos \frac{\beta}{2} + i \sin \frac{\beta}{2}\right), |\phi|^{\frac{1}{2}}\left(\cos \frac{\beta}{2} - i \sin \frac{\beta}{2}\right), -|\phi|^{\frac{1}{2}}\left(\cos \frac{\beta}{2} - i \sin \frac{\beta}{2}\right). \quad (6f)$$

Expression of the adhesive shear stress. Provided $\phi_1 = \gamma_1 - a_1/3 \geq 0$, the general solution of the adhesive shear stress can be expressed as

$$\begin{aligned} \tau_a = & C_0 + C_1 \cosh\left(x\sqrt{\gamma_1 - \frac{a_1}{3}}\right) + C_2 \sinh\left(x\sqrt{\gamma_1 - \frac{a_1}{3}}\right) \\ & + C_3 \cosh\left(x|\phi|^{\frac{1}{2}} \cos \frac{\beta}{2}\right) \cos\left(x|\phi|^{\frac{1}{2}} \sin \frac{\beta}{2}\right) + C_4 \sinh\left(x|\phi|^{\frac{1}{2}} \cos \frac{\beta}{2}\right) \cos\left(x|\phi|^{\frac{1}{2}} \sin \frac{\beta}{2}\right) \\ & + C_5 \cosh\left(x|\phi|^{\frac{1}{2}} \cos \frac{\beta}{2}\right) \sin\left(x|\phi|^{\frac{1}{2}} \sin \frac{\beta}{2}\right) + C_6 \sinh\left(x|\phi|^{\frac{1}{2}} \cos \frac{\beta}{2}\right) \sin\left(x|\phi|^{\frac{1}{2}} \sin \frac{\beta}{2}\right). \quad (7a) \end{aligned}$$

In this expression, all seven terms are real (no imaginary part). This shear stress can be directly used for practical joint analysis under the influence of joint components and external loading conditions. This shear stress expression is more practical than the one given in [Delale et al. 1981], where imaginary and real terms were used together.

The seven constants C_j (where j ranges from 0 to 6) can be determined using the following seven boundary conditions:

$$\begin{aligned} \int_{-c}^c \tau_a dx &= -T, \\ \frac{d\tau_a}{dx} \Big|_{x=-c} &= \frac{G_a}{\eta} \frac{d}{dx}(u_u - u_d) \Big|_{x=-c} = \frac{G_a}{\eta} \left(\frac{T}{E'_u t_1} + \frac{t_1}{2} \frac{M_u}{D_u} \right) \Big|_{x=-c} = \frac{G_a}{\eta} \left(\frac{T}{E'_u t_1} + \frac{t_1}{2} \frac{M_0}{D_u} \right), \\ \frac{d\tau_a}{dx} \Big|_{x=c} &= \frac{G_a}{\eta} \frac{d}{dx}(u_u - u_d) \Big|_{x=c} = \frac{G_a}{\eta} \left(-\frac{T}{E'_d t_2} + \frac{t_2}{2} \frac{M_d}{D_d} \right) \Big|_{x=c} = \frac{G_a}{\eta} \left(-\frac{T}{E'_d t_2} + \frac{t_2}{2} \frac{M_1}{D_d} \right), \\ \frac{d^2\tau_a}{dx^2} + a_1\tau_a \Big|_{x=-c} &= \frac{G_a}{\eta} \frac{t_1 V_u}{2D_u} \Big|_{x=-c} = \frac{G_a}{\eta} \frac{t_1}{2} \frac{V_0}{D_u}, \\ \frac{d^2\tau_a}{dx^2} + a_1\tau_a \Big|_{x=c} &= \frac{G_a}{\eta} \frac{t_2 V_d}{2D_d} \Big|_{x=c} = \frac{G_a}{\eta} \frac{t_2}{2} \frac{V_1}{D_d}, \\ \frac{d^5\tau_a}{dx^5} + a_1 \frac{d^3\tau_a}{dx^3} \Big|_{x=-c} &= -a_2 \frac{E_a}{\eta} \frac{M_u}{D_u} \Big|_{x=-c} = -a_2 \frac{E_a}{\eta} \frac{M_0}{D_u}, \\ \frac{d^5\tau_a}{dx^5} + a_1 \frac{d^3\tau_a}{dx^3} \Big|_{x=c} &= a_2 \frac{E_a}{\eta} \frac{M_d}{D_d} \Big|_{x=c} = a_2 \frac{E_a}{\eta} \frac{M_1}{D_d}, \end{aligned} \quad (7b)$$

The expressions of the seven constants in the adhesive shear stress are given in the [Online Supplement](#). The above first boundary condition is obtained through the equilibrium relation of the joint adherend tensile load with the integral of the resulting shear stress in the adhesive layer. The rest of the six boundary conditions relate different derivatives of the adhesive shear stress at the outer and inner overlap ends with the applied loads at the same positions. Assuming continuity of axial strains in the adherends

and doubler at the interfaces with the adhesive layer and the adhesive stresses in the adhesive layer, the second and third boundary conditions at the two overlap ends are obtained by combining the first derivative of the adhesive shear stress in (3c) and the expressions of the axial strains at the adherend-adhesive and adhesive-doubler interfaces in (3b). The adhesive shear stress in (3c) is differentiated twice, using the equilibrium equations of moment and tensile force in (3a) to substitute for the fourth and fifth boundary conditions. To obtain the sixth and seventh boundary conditions for the uncoupled adhesive shear stress, two differentiations are applied to the first coupled adhesive stress equation in (4a) with the aid of the peel stress expression in (3c) and moment-curvature relation in (1a).

Adhesive peel stress. Exploration of the closed-form solution for the adhesive peel stress should be carried out based on its fundamental behavior expressed in (4a). This nonhomogeneous equation degrades to its corresponding homogeneous equation in the special butt joint case when the coupling parameter b_2 vanishes. The nonhomogeneous equation can be investigated using variation of constants or Lagrange's method [AEP 1979; Derrick and Grossman 1987]. The general solution is established by combining the general solution of the homogeneous equation and any one particular solution of the nonhomogeneous equation. If we define

$$X = x \sqrt[4]{\frac{b_1}{4}},$$

the general solution of the homogeneous equation is

$$\sigma_{aH} = C_{1H} \cosh X \cos X + C_{2H} \sinh X \cos X + C_{3H} \cosh X \sin X + C_{4H} \sinh X \sin X. \quad (8a)$$

One particular solution for the nonhomogeneous equation can be expressed in the form

$$\sigma_{ap} = G_{1p}(x) \cosh X \cos X + G_{2p}(x) \sinh X \cos X + G_{3p}(x) \cosh X \sin X + G_{4p}(x) \sinh X \sin X, \quad (8b)$$

where the functions $G_{1p}(x)$, $G_{2p}(x)$, $G_{3p}(x)$, and $G_{4p}(x)$ are determined using the following simultaneous equations [AEP 1979; Derrick and Grossman 1987]:

$$\begin{aligned} G'_{1p}(x) \cosh X \cos X + G'_{2p}(x) \sinh X \cos X + G'_{3p}(x) \cosh X \sin X + G'_{4p}(x) \sinh X \sin X &= 0, \\ G'_{1p}(x) \frac{d}{dx}(\cosh X \cos X) + G'_{2p}(x) \frac{d}{dx}(\sinh X \cos X) \\ &\quad + G'_{3p}(x) \frac{d}{dx}(\cosh X \sin X) + G'_{4p}(x) \frac{d}{dx}(\sinh X \sin X) = 0, \\ G'_{1p}(x) \frac{d^2}{dx^2}(\cosh X \cos X) + G'_{2p}(x) \frac{d^2}{dx^2}(\sinh X \cos X) \\ &\quad + G'_{3p}(x) \frac{d^2}{dx^2}(\cosh X \sin X) + G'_{4p}(x) \frac{d^2}{dx^2}(\sinh X \sin X) = 0, \\ G'_{1p}(x) \frac{d^3}{dx^3}(\cosh X \cos X) + G'_{2p}(x) \frac{d^3}{dx^3}(\sinh X \cos X) \\ &\quad + G'_{3p}(x) \frac{d^3}{dx^3}(\cosh X \sin X) + G'_{4p}(x) \frac{d^3}{dx^3}(\sinh X \sin X) = -b_2 \frac{d\tau_a}{dx}. \end{aligned} \quad (8c)$$

The expressions for $G_{ip}(x)$ ($i = 1, \dots, 4$) functions are given in the [Online Supplement](#). The general solution for the adhesive peel stress in the general butt joint case can be established as

$$\begin{aligned}\sigma_a &= \sigma_{aH} + \sigma_{ap} \\ &= C_{1H} \cosh X \cos X + C_{2H} \sinh X \cos X + C_{3H} \cosh X \sin X + C_{4H} \sinh X \sin X \\ &\quad + G_{1p}(x) \cosh X \cos X + G_{2p}(x) \sinh X \cos X + G_{3p}(x) \cosh X \sin X + G_{4p}(x) \sinh X \sin X.\end{aligned}\quad (8d)$$

The expressions for the constants C_{1H} , C_{2H} , C_{3H} , and C_{4H} are also given in the [Online Supplement](#), and are determined using the boundary conditions

$$\begin{aligned}\frac{d^2\sigma_a}{dx^2}\Big|_{x=-c} &= \frac{E_a}{\eta} \frac{M_u}{D_u}\Big|_{x=-c} = \frac{E_a}{\eta} \frac{M_0}{D_u}, & \frac{d^2\sigma_a}{dx^2}\Big|_{x=c} &= -\frac{E_a}{\eta} \frac{M_d}{D_d}\Big|_{x=c} = -\frac{E_a}{\eta} \frac{M_1}{D_d}, \\ \frac{d^3\sigma_a}{dx^3} + b_2\tau_a\Big|_{x=-c} &= \frac{E_a}{\eta} \frac{V_u}{D_u}\Big|_{x=-c} = \frac{E_a}{\eta} \frac{V_0}{D_u}, & \frac{d^3\sigma_a}{dx^3} + b_2\tau_a\Big|_{x=c} &= -\frac{E_a}{\eta} \frac{V_d}{D_d}\Big|_{x=c} = -\frac{E_a}{\eta} \frac{V_1}{D_d}.\end{aligned}\quad (8e)$$

These four boundary conditions relate the derivatives of the adhesive peel stress with the applied loads at the outer and inner overlap ends. Two differentiations are conducted on the peel stress expression in (3c) with the aid of the moment-curvature relation in (1a) to obtain the first two boundary conditions. One more differentiation is applied to the second derivative of the peel stress expression with the aid of the moment equilibrium relation in (3a) to obtain the third and fourth boundary conditions.

Joint special case: parameters of $a_2 = b_2 = 0$. It can be seen from (4b) that the coupling parameters a_2 and b_2 vanish when the butt joints are balanced, a special case. The adhesive shear and peel stresses are then decoupled. The other two parameters in (4b) are

$$a_1 = -\frac{G_a}{\eta} \left(\frac{2}{E't} + \frac{t(t+\eta)}{2D} \right), \quad b_1 = \frac{2E_a}{\eta D}.\quad (9a)$$

The shear and peel stress equations can be simplified as

$$\frac{d^3\tau_a}{dx^3} + a_1 \frac{d\tau_a}{dx} = 0, \quad \frac{d^4\sigma_a}{dx^4} + b_1\sigma_a = 0.\quad (9b)$$

Adhesive shear stress. The general solution for the adhesive shear stress is then

$$\tau_a = C_{0S} + C_{1S} \cosh \left(x \sqrt{\frac{G_a}{\eta} \left(\frac{2}{E't} + \frac{t(t+\eta)}{2D} \right)} \right) + C_{2S} \sinh \left(x \sqrt{\frac{G_a}{\eta} \left(\frac{2}{E't} + \frac{t(t+\eta)}{2D} \right)} \right).\quad (10)$$

The expressions of these three constants, C_{iS} ($i = 0, 1, 2$), are given in the [Online Supplement](#) and are determined using the three boundary conditions

$$\int_{-c}^c \tau_a dx = -T, \quad \frac{d\tau_a}{dx}\Big|_{x=-c} = \frac{G_a}{\eta} \left(\frac{T}{E'_u t_1} + \frac{t_1}{2} \frac{M_u}{D_u} \right)\Big|_{x=-c}, \quad \frac{d\tau_a}{dx}\Big|_{x=c} = \frac{G_a}{\eta} \left(-\frac{T}{E'_d t_2} + \frac{t_2}{2} \frac{M_d}{D_d} \right)\Big|_{x=c}.$$

Similarly to the general butt joint case, the first boundary condition is the equilibrium relation in the adherend between the applied tensile load with the integral of the resulting shear stress in the adhesive layer. The second and third boundary conditions relate the first derivative of shear stress to the loads at

the two overlap ends, and are obtained by combining the first derivative of the adhesive shear stress in (3c) with the expressions of the axial strains at the adherend-adhesive and adhesive-doubler interfaces in (3b).

Adhesive peel stress. The general solution for the adhesive peel stress is

$$\sigma_a = C_{3S} \cosh X \cos X + C_{4S} \sinh X \cos X + C_{5S} \cosh X \sin X + C_{6S} \sinh X \sin X. \quad (11)$$

The constants C_{iS} ($i = 3, 4, 5, 6$) are given in the [Online Supplement](#). They are determined using the boundary conditions

$$\begin{aligned} \left. \frac{d^2 \sigma_a}{dx^2} \right|_{x=-c} &= \frac{E_a}{\eta} \frac{M_u}{D_u} \Big|_{x=-c} = \frac{E_a}{\eta} \frac{M_0}{D}, & \left. \frac{d^2 \sigma_a}{dx^2} \right|_{x=c} &= -\frac{E_a}{\eta} \frac{M_d}{D_d} \Big|_{x=c} = -\frac{E_a}{\eta} \frac{M_1}{D}, \\ \left. \frac{d^3 \sigma_a}{dx^3} \right|_{x=-c} &= \frac{E_a}{\eta} \frac{V_u}{D_u} \Big|_{x=-c} = \frac{E_a}{\eta} \frac{V_0}{D}, & \left. \frac{d^3 \sigma_a}{dx^3} \right|_{x=c} &= -\frac{E_a}{\eta} \frac{V_d}{D_d} \Big|_{x=c} = -\frac{E_a}{\eta} \frac{V_1}{D}. \end{aligned}$$

As in the general butt joint case, the above four boundary conditions relate the derivatives of the adhesive peel stress with the applied loads at the outer and inner overlap ends of the balanced butt joint.

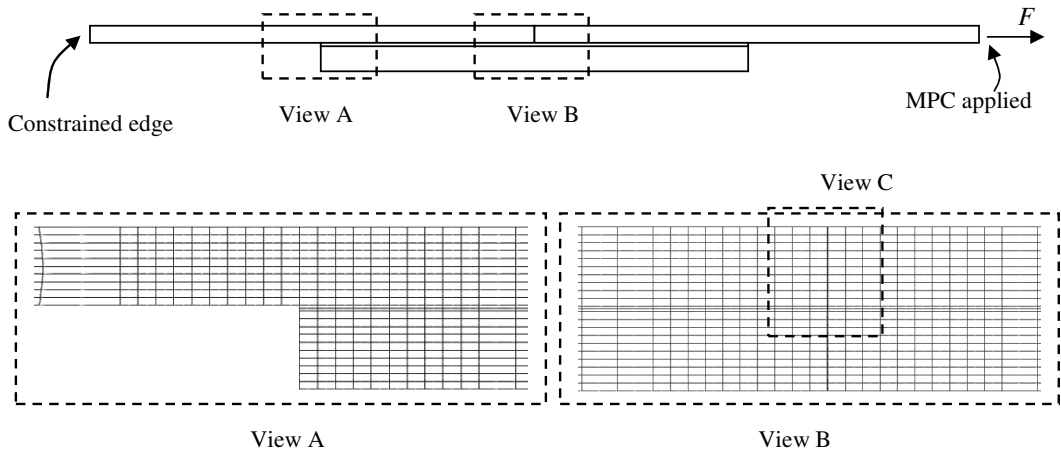
Consistence of the adhesive stresses from the general to the special joint cases. The derivations in the closed-form stress solutions were carried out based on their fundamental equations, thus, when the general case approaches the special butt joint case, both the adhesive peel and shear stresses will converge to their corresponding adhesive stresses in the special joint case, which has been validated in [Li 2008].

Validation of the closed-form solutions of the adhesive stresses using finite element methods. Due to the geometrical nonlinearity caused by the secondary bending deformation in butt joints, two-dimensional geometrically nonlinear finite element (FE) analyses were carried out under the plane strain condition, using MSC Patran and Marc version 2008r1. Linear elastic material properties were used for the FE analyses. Two different joint situations, as given in [Table 1](#) and [Figure 6](#), were considered. The FE results obtained for the adhesive stresses were compared with the corresponding closed-form solutions.

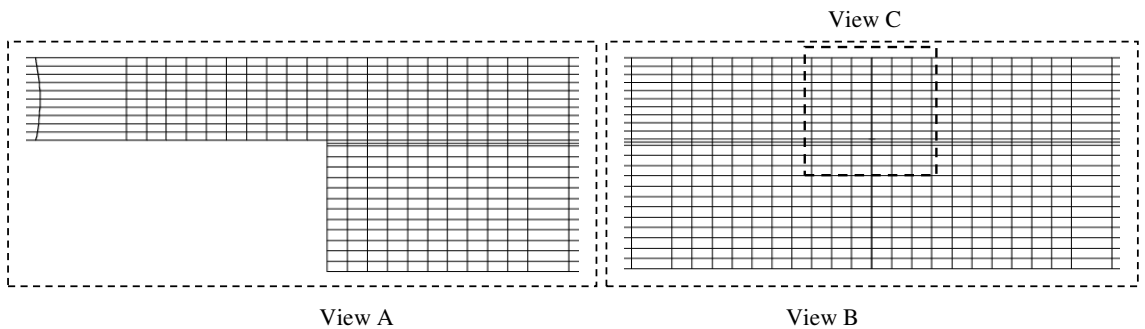
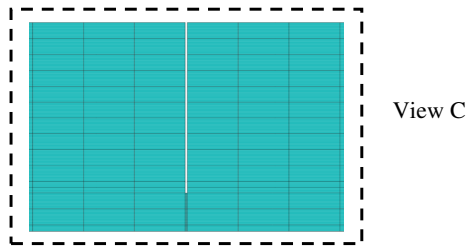
Assuming a small clearance in the joint, a gap of 0.02 mm was assumed to represent the inner section length without adherends and adhesive, as shown in [Figure 6](#). Two elements were used through the adhesive thickness. A fine mesh was applied to the overlap edge areas. Ten elements were used across

Item	Mechanical parameters	Length (mm)	Thickness (mm)
Adherends	$E = 70 \text{ GPa}$, $\nu = 0.3$	$L = 50$ (each outer adherend)	$t_1 = 2.1$
Doubler	$E = 70 \text{ GPa}$, $\nu = 0.3$	$4c + 2L_0 = 101.6$ (inner section length of $2L_0 = 0.02$)	$t_2 = 2.1$ and 3.2 for special and general (thicker doubler) cases
Adhesive	$E_a = 3 \text{ GPa}$, $\nu_a = 0.3$	$4c = 101.58$	$\eta = 0.15$

Table 1. Parameters for the unit width single-strap butt joint. The total gauge length of the joint is $2L + 4c + 2L_0 = 201.6 \text{ mm}$.



(a) Special case, 2.1 mm thick doubler and adherends



(b) General case, 3.2 mm thick doubler and 2.1 thick mm adherends

Figure 6. Schematic diagrams for the two simulated butt joints with a 0.02 mm inner gap section for both adherends and adhesive for the special (2.1 mm doubler) and general (3.2 mm doubler) joints.

the adherends and doubler thicknesses for the special case, and 12 elements were used for the 3.2 mm thick doubler. A total of 3,284 eight-node quadrilateral elements with 10,273 nodes were created for the special case. A total of 3,516 eight-node quadrilateral elements with 10,971 nodes were generated for the thicker doubler general case joint. The left edge was clamped without any displacement in both the horizontal and vertical directions, while the right adherend far end edge was uniformly loaded with a

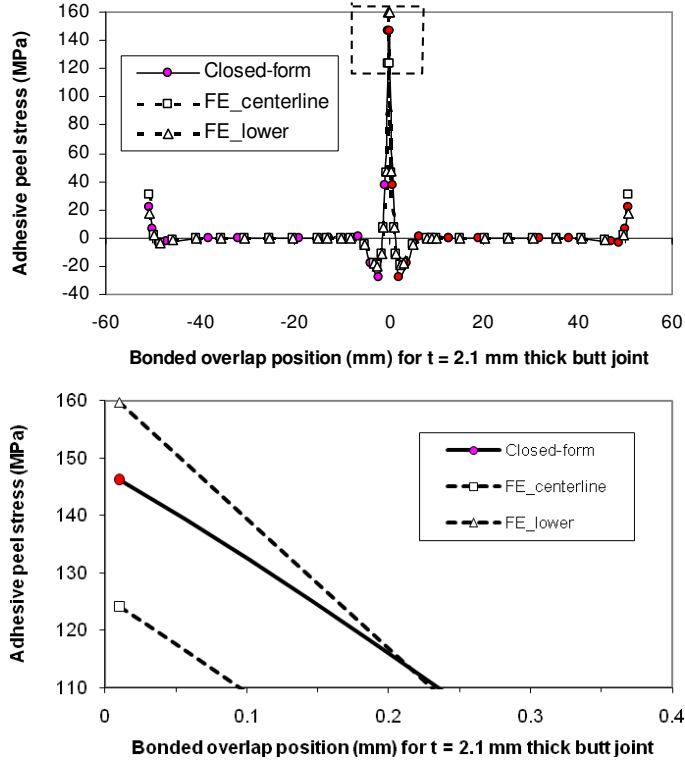


Figure 7. Comparison of the adhesive peel stresses obtained from closed-form solutions and FE results for a special butt joint with identical adherends and doubler (above) with dashed box marking the detail (below). FE_lower refers to the lower path along the midnodes of the lower adhesive layer elements.

tensile stress of 100 MPa. Multipoint-constrain conditions were applied to the right edge nodes having the same displacement during the tensile loading stage.

Comparison of the adhesive stresses between the closed-form solutions and FE results. Five nodes were used through the thickness of the adhesive layer. The peel and shear stresses at the nodes along the adherend-adhesive or adhesive-doubler interface are dominated by the mechanical parameters of both the adherend (or doubler) and adhesive, and cannot be treated as the adhesive stresses. Thus, the adhesive stresses at the upper element midnode, adhesive centerline, and lower elements midnode were extracted and analyzed. The stresses at the lower node were greater than the corresponding stresses at the centerline and upper node. The average stresses along the three paths were identical to the stresses along the centerline. For the closed-form stress solutions, the first step was to determine the bonded overlap edge forces such as the bending moments and shear forces as introduced in [Section 2](#) and elsewhere [[Li 2008](#)], then to follow the steps in [Section 3](#), as well as the [Online Supplement](#), to get the adhesive stresses. Variations in the adhesive peel and shear stresses obtained from the closed-form solutions and finite element results are presented in [Figures 7–10](#) for both butt joint cases. Based on these figures, the following observations can be made: the adhesive stresses are uniform in the thickness direction except at the overlap edge nodes; high stresses are present in the vicinity of the overlap edges, the highest

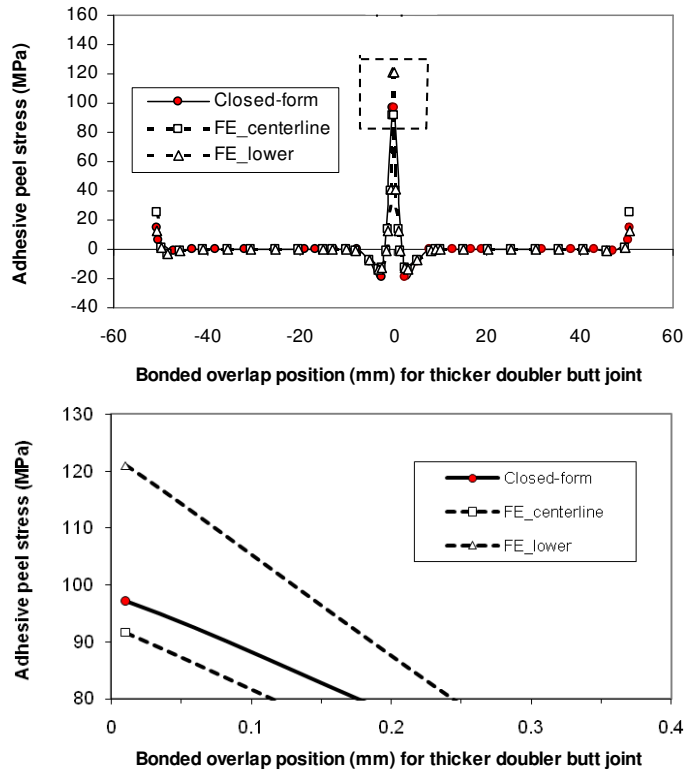


Figure 8. Comparison of the adhesive peel stresses obtained from closed-form solutions and FE results for a general butt joint with 2.1 mm thick adherends and a 3.2 mm thick doubler. FE_lower refers to the lower path along the midnodes of the lower adhesive layer elements.

being at the inner overlap edge position; the stress magnitudes are lower using the thicker doubler; the closed-form solutions are approximately the same as the FE results, except at the edge positions; and at the inner overlap edge position, the peel stresses obtained from the closed-form solutions are within the FE stresses at the centerline and lower path nodes, and the shear stresses obtained from the closed-form solutions are almost identical to the FE results at the lower path nodes and slightly larger than the centerline values. The peak stress values and stress singularity, which existed at the adherend-adhesive and adhesive-doubler interfaces in the vicinity of the overlap edges, are not within the scope of the paper, and thus were not covered in the current FE analyses.

The above comparisons clearly show that the closed-form stress solutions are reliable and accurate in predicting the stress variations. The closed-form stress solutions can also be used to analyze the mode I and mode II strain energy release rates for cohesive crack propagation behavior in a generic situation of butt joints using the approach suggested by Hu [1995] on the single-lap joints.

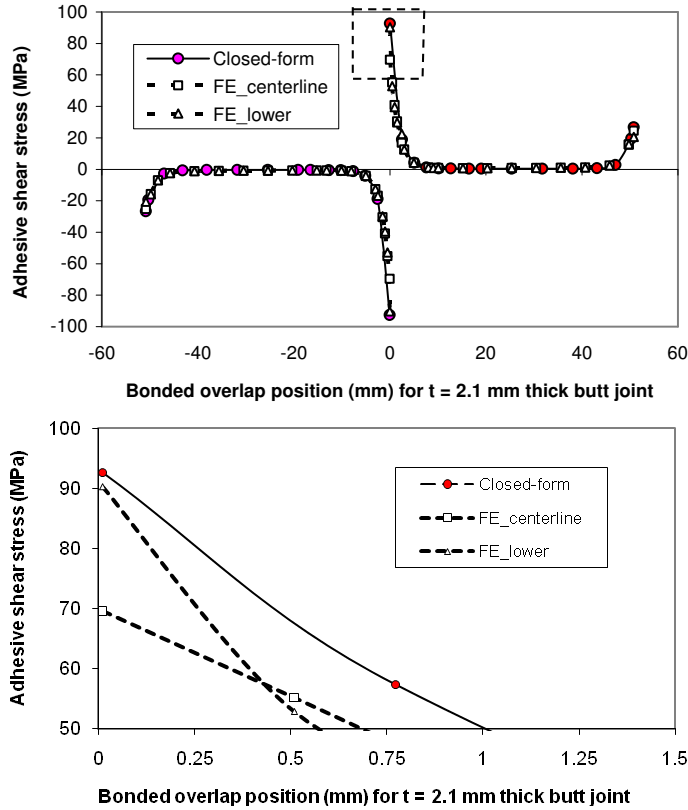


Figure 9. Comparison of the adhesive shear stresses obtained from closed-form solutions and FE results for a special butt joint with identical adherends and doubler.

4. Concluding remarks

In the study of unbalanced butt joint, the derived high order differential equation was the same as the one initially obtained by [Delale et al. \[1981\]](#) for the uncoupled adhesive shear stress. They provided general stress expressions containing complex terms with nonzero imaginary terms, and did not present the final complete adhesive stress solutions. Among the seven boundary conditions, two were slightly different. However, the impact on the final solutions could be neglected based on our previous study [\[Li and Lee-Sullivan 2006a\]](#). Due to the page limit, the study of the impact of small differences on the set of boundary conditions on the adhesive stress variation is not carried further. Difficulties and complexities in the derivation process using these high order differential equations have been solved. Closed-form solutions for the adhesive peel and shear stresses have been successfully developed in this paper for the general butt joint case. Good agreement was achieved in the adhesive stresses obtained from the closed-form solutions and finite element results for both the special and general butt joints. The obtained results validate that the used boundary conditions are accurate. Since the closed-form solutions have been obtained from their fundamental behavior equations, the consistence of the adhesive stresses between the general and special joint cases can be theoretically ensured. Moreover, the obtained stress solutions allows the quantitatively study of the effect of each joint component on the variation in the

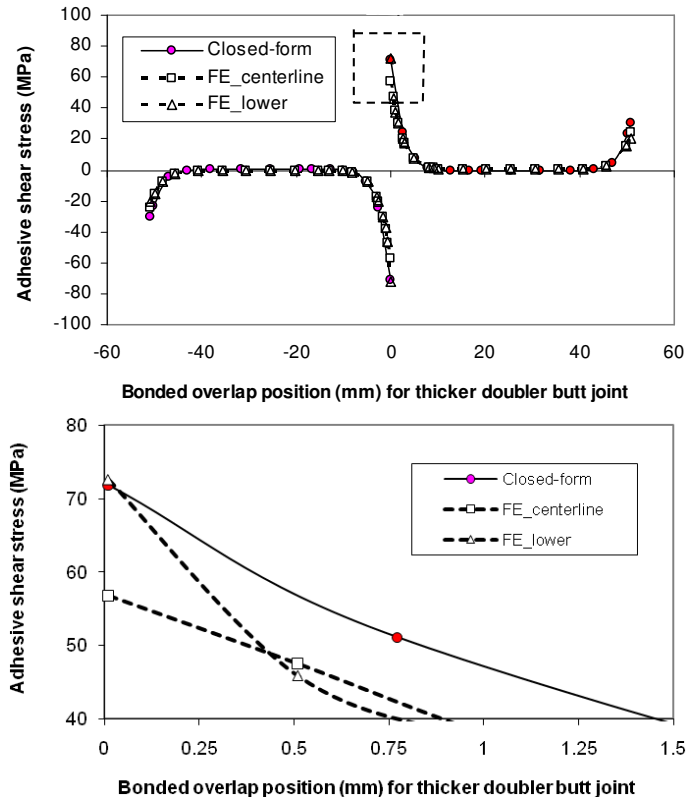


Figure 10. Adhesive shear stresses obtained from closed-form solutions and FE results for a general butt joint with 2.1 mm thick adherends and a 3.2 mm thick doubler.

adhesive stresses for more joint geometries and materials, as can be found elsewhere [Li 2008]. Thus, a practical evaluation of this joint configuration can be easily carried out using the Excel spreadsheet tool. Usually the length of the inner gap section (the inner unbonded doubler section) in a butt joint is very small and much shorter than the outer adherend length; the two single-lap joints of the butt joint should be then treated as in the unbalanced single-lap joint case. Thus, the adhesive stress solutions obtained from the butt joint configuration can be applied to the unbalanced single-lap joint case if the overlap edge loads are known. The next stage could be: the exploration of the simplified stress solutions for better practical applications, the development of the adhesive stresses in composite butt joints, and the identification of the proper hole positions for introducing extra fasteners to fabricate a strong hybrid attached joint.

Acknowledgements. This work was carried out under IAR Program 303 Aerospace Structures, IAR/NRC 2007 NIF Project 46NS-8CTCJ, *Mechanical behavior of bonded/bolted composite-to-composite joints*. The financial support received from IAR is acknowledged and greatly appreciated. Many thanks to those people who have, in one way or another, contributed to the work.

References

[Adams and Wake 1984] R. D. Adams and W. C. Wake, *Structural adhesive joints in engineering*, Elsevier, London, 1984.

- [AEP 1979] Editorial group, *Mathematics handbook*, Advanced Education Press (AEP), Beijing, 1979. In Chinese.
- [Bigwood and Crocombe 1989] D. A. Bigwood and A. D. Crocombe, “Elastic analysis and engineering design formulae for bonded joints”, *Int. J. Adhes. Adhes.* **9**:4 (1989), 229–242.
- [Chen and Cheng 1983] D. Chen and S. Cheng, “An analysis of adhesive-bonded single-lap joints”, *J. Appl. Mech. (ASME)* **50**:1 (1983), 109–115.
- [Cheng et al. 1991] S. Cheng, D. Chen, and Y. Shi, “Analysis of adhesive-bonded joints with nonidentical adherends”, *J. Eng. Mech. (ASCE)* **117**:3 (1991), 605–623.
- [Delale et al. 1981] F. Delale, F. Erdogan, and M. N. Aydinoglu, “Stresses in adhesively bonded joints: a closed-form solution”, *J. Compos. Mater.* **15**:3 (1981), 249–271.
- [Derrick and Grossman 1987] W. R. Derrick and S. I. Grossman, *A first course in differential equations with applications*, 3rd ed., West Publishing Company, St. Paul, MN, 1987.
- [Goland and Reissner 1944] M. Goland and E. Reissner, “The stresses in cemented joints”, *J. Appl. Mech. (ASME)* **11** (1944), A17–A27.
- [Hart-Smith 1973] L. J. Hart-Smith, “Adhesive-bonded single-lap joints”, Contractor Report 112236, NASA Langley Research Center, Hampton, VA, 1973, Available at <http://tinyurl.com/NASA-CR-112236>.
- [Hart-Smith 1985] L. J. Hart-Smith, “Designing to minimize peel stresses in adhesive-bonded joints”, pp. 238–266 in *Delamination and debonding of materials* (Pittsburgh, PA, 1983), edited by W. S. Johnson, ASTM Special Technical Publication **876**, American Society for Testing and Materials, Philadelphia, 1985.
- [Hu 1995] G. Hu, “Mixed mode fracture analysis of adhesive lap joints”, *Compos. Eng.* **5**:8 (1995), 1043–1050.
- [Kreyszig 1993] E. Kreyszig, *Advanced engineering mathematics*, 7th ed., Wiley, New York, 1993.
- [Kweon et al. 2006] J.-H. Kweon, J.-W. Jung, T.-H. Kim, J.-H. Choi, and D.-H. Kim, “Failure of carbon composite-to-aluminum joints with combined mechanical fastening and adhesive bonding”, *Compos. Struct.* **75**:1–4 (2006), 192–198.
- [Li 2008] G. Li, “Exploration of closed-form solutions for adhesive stresses in adhesively bonded single-strap butt joints”, Technical report LTR-SMPL-2008-0174, National Research Council Canada, Institute for Aerospace Research, Ottawa, ON, 2008.
- [Li and Lee-Sullivan 2006a] G. Li and P. Lee-Sullivan, “Re-visiting the beam models for adhesively bonded single-lap joints, I: Comparison of bending moment predictions”, *Can. Aeronaut. Space. J.* **52**:4 (2006), 149–171.
- [Li and Lee-Sullivan 2006b] G. Li and P. Lee-Sullivan, “Re-visiting the beam models for adhesively bonded single-lap joints, II: Comparison of adhesive stress predictions”, *Can. Aeronaut. Space. J.* **52**:4 (2006), 173–180.
- [Oplinger 1994] D. W. Oplinger, “Effects of adherend deflections in single lap joints”, *Int. J. Solids Struct.* **31**:18 (1994), 2565–2587.
- [da Silva and Adams 2007a] L. F. M. da Silva and R. D. Adams, “Adhesive joints at high and low temperatures using similar and dissimilar adherends and dual adhesives”, *Int. J. Adhes. Adhes.* **27**:3 (2007), 216–226.
- [da Silva and Adams 2007b] L. F. M. da Silva and R. D. Adams, “Techniques to reduce the peel stresses in adhesive joints with composites”, *Int. J. Adhes. Adhes.* **27**:3 (2007), 227–235.
- [Tsai and Morton 1994] M. Y. Tsai and J. Morton, “An evaluation of analytical and numerical solutions to the single-lap joint”, *Int. J. Solids Struct.* **31**:18 (1994), 2537–2563.
- [Volkersen 1938] O. Volkersen, “Die Nietkraftverteilung in zugbeanspruchten Nietverbindungen mit konstanten Laschenquerschnitten”, *Luftfahrtforsch.* **15** (1938), 41–47.
- [Williams 1975] J. H. Williams, Jr., “Stress in adhesive between dissimilar adherends”, *J. Adhesion* **7**:2 (1975), 97–107.

Received 15 Jun 2009. Revised 21 Sep 2009. Accepted 5 Dec 2009.

GANG LI: Gang.Li@nrc-cnrc.gc.ca

Structures and Materials Performance Laboratory, Institute for Aerospace Research, National Research Council Canada, 1200 Montreal Road, M-3, Ottawa, Ontario K1A 0R6, Canada

THEORETICAL AND EXPERIMENTAL STUDIES OF BEAM BIMORPH PIEZOELECTRIC POWER HARVESTERS

SHUDONG YU, SIYUAN HE AND WEN LI

This paper presents a theoretical model for simulating a piezoelectric beam bimorph power harvester consisting of a laminated piezoelectric beam, a proof mass, and an electrical load. The vertical offset of the proof mass center from the beam centroid couples the bending and longitudinal motions, which makes it necessary to consider both longitudinal and lateral vibrations simultaneously. Experiments were carried out on a beam bimorph prototype mounted on a shaker to measure the electrical output. Numerical results obtained using the proposed procedure for piezoelectric bimorph power harvesters are in good agreement with the experimental data.

1. Introduction

Power harvesting devices scavenge energy from ambient mechanical vibrations. When a cantilever bimorph piezoelectric beam is attached to a vibrating base, electrical energy is produced continuously. Devices of this kind are often used to replace or extend the life time of electrochemical batteries for wireless sensors, implanted medical devices, handheld electronic devices, and other portable electronic devices [Roundy et al. 2004; Yang 2006; Liao and Sodano 2008]. Compared with other energy scavenging methods such as electromagnetic [Glynne-Jones et al. 2004] and electrostatic methods [Mitcheson et al. 2004], piezoelectric vibration based energy harvesting systems have been attracting a lot of attention recently because of their simple structure, direct conversion of vibration energy into electrical energy with a high voltage level, lower number of additional electrical components, and not requiring an electric power source [Sodano et al. 2004; Anton and Sodano 2007]. The most popular structures for vibration based piezoelectric power harvesting systems are piezoelectric cantilever (unimorph or bimorph) beams, which are suitable for small amplitude ambient vibration. Most test results available in the literature were obtained for sinusoidal mechanical motion. Cantilever-type energy harvesting devices function most effectively when the excitation frequencies vary in the vicinity of the fundamental resonant frequency of the electromechanical system.

Models of distributed-parameter energy harvesting systems were presented in [Erturk and Inman 2008b], and approaches based on modal analysis were proposed to solve the dynamical response of the electromechanical system. An energy-based formulation of piezoelectric structures is given in [Dutoit et al. 2005]. Some simplified analytical models for a cantilever piezoelectric beam energy harvester are available in the literature. However, as pointed out in [Erturk and Inman 2008a], errors were unfortunately present in deriving the simplified analytical solutions in several published papers. The authors of the current paper also had the opportunity to examine the analytical results published in the literature, and observed that errors and mistakes of a nontypographical nature indeed existed in the earlier works

Keywords: power harvesting, finite element modeling, piezoelectric structures, bending, axial deformation, rotary inertia.

concerning the derivations of analytical solutions for bimorph piezoelectric structures. The timely paper [Erturk and Inman 2009] deals with the analytical solution for a bimorph piezoelectric beam energy harvester carrying a symmetrically placed proof mass.

In this paper, the finite element method is employed to obtain the governing equations of the electromechanical system consisting of a piezoelectric beam, a proof mass, and a resistive load. The three-node beam element [Yu and Cleghorn 2002], presented in this paper, is of a higher order type and is ideal for dynamic problems. The authors anticipate that energy harvesting devices of this type can be modeled accurately using the proposed method. Effects of mass, mass moment of inertia, and offsets of the mass center with respect to the mass-beam interface can be studied for a proof mass of general configuration.

2. Formulation of mechanical and electrical energies

A piezoelectric power harvester consisting of a piezoelectric bimorph beam and a proof mass is sketched in Figure 1. The piezoelectric beam is clamped onto a vibrating base. As the base vibrates, the mechanical energy is converted into electrical energy through the piezoelectric power harvester. In this section, the mechanical (kinetic, strain, and dissipative) energy, the electrical energy, and the electrical work done on a power-consuming resistor are studied and related to a set of electromechanical variables.

Axial strain. The axial strain everywhere in the piezoelectric beam is induced by the axial and lateral deformations in the x - z coordinate plane (see Figure 1). Within the context of classical beam theory, a plane of a beam normal to its neutral axis before deformation remains a plane and normal to the deformed neutral axis after deformation. The total axial displacement of a material point in the beam structure,

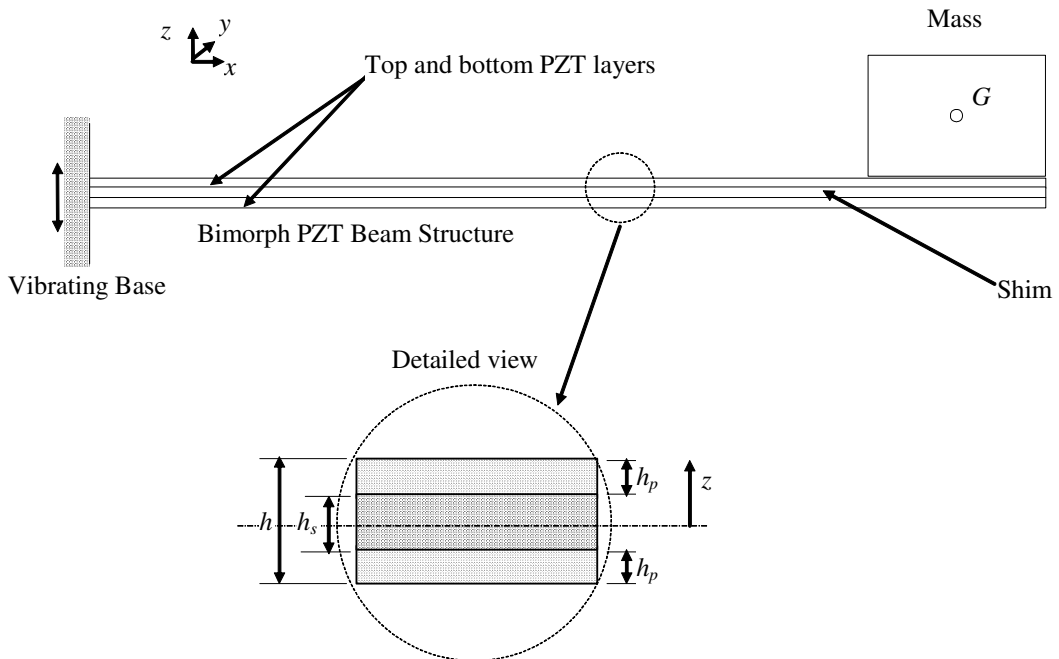


Figure 1. Illustration of a typical piezoelectric power generator.

bounded by $0 \leq x \leq l$, $-b/2 \leq y \leq b/2$, and $-h/2 \leq z \leq h/2$, may be written as

$$u(x, z, t) = u_0(x, t) - \theta(x, t)z, \quad (1)$$

where $u_0(x, t)$ is the axial displacement due to uniform axial stretching, $w(x, t)$ is the lateral displacement of the centroid due to in-plane bending, z is the vertical distance of the material from the centroid, and b is the beam width.

According to Euler–Bernoulli beam theory, the angle of rotation of a beam cross section, normal to the centroid axis, is everywhere related to the slope of the deformed centroid axis as follows:

$$\theta(x, t) = \frac{\partial w(x, t)}{\partial x}, \quad 0 \leq x \leq l. \quad (2)$$

For small deformations, the axial strain everywhere in the beam is

$$S_1(x, z, t) = \frac{\partial u_0(x, t)}{\partial x} - \frac{\partial^2 w(x, t)}{\partial x^2}z. \quad (3)$$

Constitutive equations. The constitutive equation for the nonactive shim material, bounded by $-h_s/2 \leq z \leq h_s/2$, may be written as

$$T_{1,s} = c_{11,s}S_1, \quad (4)$$

where $T_{1,s}$ is the axial stress in the shim material and $c_{11,s}$ is the modulus of elasticity of the shim material.

For the two piezoelectric layers, bounded by $h_s/2 \leq z \leq h/2$ and $-h/2 \leq z \leq -h_s/2$, the constitutive equations may be written as [Roundy et al. 2004]

$$T_{1,p} = c_{11,p}S_1 - e_{31,p}E_{3,p}, \quad D_{3,p} = e_{31,p}S_1 + \epsilon_{33,p}E_{3,p}, \quad (5)$$

where $T_{1,p}$ is the axial stress in the piezoelectric material, $c_{11,p}$ is the elastic constant of the piezoelectric material, $\epsilon_{33,p}$ is the permittivity in the thickness direction, $d_{31,p}$ is the piezoelectric constant, $E_{3,p}$ is the electric field in the thickness direction, and $D_{3,p}$ is the electric displacement in the thickness direction.

A bimorph piezoelectric beam in the {3-1} mode is made of two identical piezoelectric layers at the top and bottom and a shim in the middle, which makes the structure a symmetrically laminated beam. In a symmetrically laminated beam, the axial stretching does not induce bending, and vice versa. For a composite beam of very large length-to-thickness ratios, the dominating strains and stresses in each constitutive layer are the axial strains and stresses due to the bending and axial stretching when it is operated in the vicinity of the fundamental natural frequency of the in-plane bending. Other stress components, for example the transverse shear stress, are negligible.

For piezoelectric composite beams of moderate or large thickness, the electrical field in a piezoelectric layer may vary considerably in the thickness direction [Wang et al. 2007]. However, for a very thin piezoelectric laminate, the electrical field across each piezoelectric layer may be considered constant in the thickness direction. In this paper, the piezoelectric structure is thin and symmetric. The following simplified relationship between the electric field and the voltage differential (v) across a single piezoelectric

layer is employed:

$$E_{3,p} = \begin{cases} -v/h_p & \text{if } h_s \leq 2z \leq h, \\ 0 & \text{if } -h_s \leq 2z \leq h_s, \\ v/h_p & \text{if } -h \leq 2z \leq -h_s, \end{cases} \quad (6)$$

where h_p is the thickness of the top or bottom piezoelectric layer and v is the voltage across one piezoelectric layer.

Motion analysis. A rigid proof mass is commonly attached to the beam at the free end to enhance power generation. When the beam-mass system is clamped to a rigid moving base, the beam-mass system participates in two motions: the rigid body motion with the base and the elastic motion relative to the base. The rigid reference motion is responsible for providing an excitation in the form of a distributed inertial force field. The relative elastic motion is desired to yield necessary straining of materials for producing electrical charges.

A beam-mass system is capable of various types of elastic deformations when the excitation frequencies vary considerably. They include bending, axial stretching/compression, and torsion. However, when the system is excited in the vicinity of the fundamental natural frequency, the beam motion is predominantly bending in the x - z coordinate plane. The proof mass motion is of the type of general plane motion. Since the lateral motion is coupled to the lateral bending motion for nonsymmetric attachments of the proof mass, the longitudinal deformation and lateral bending are considered. Bending in the y - z coordinate plane and torsion about the z axis are negligible.

To determine the deformations of a flexible beam at time t , a set of moving coordinates fixed to the moving ground are employed. For translational base motion in the vertical direction, the base-fixed coordinate translates with velocity \dot{v}_b . A material point P , located a distance x from the reference point on the neutral axis before deformations, as shown in Figure 2, moves to P' after deformations. If the

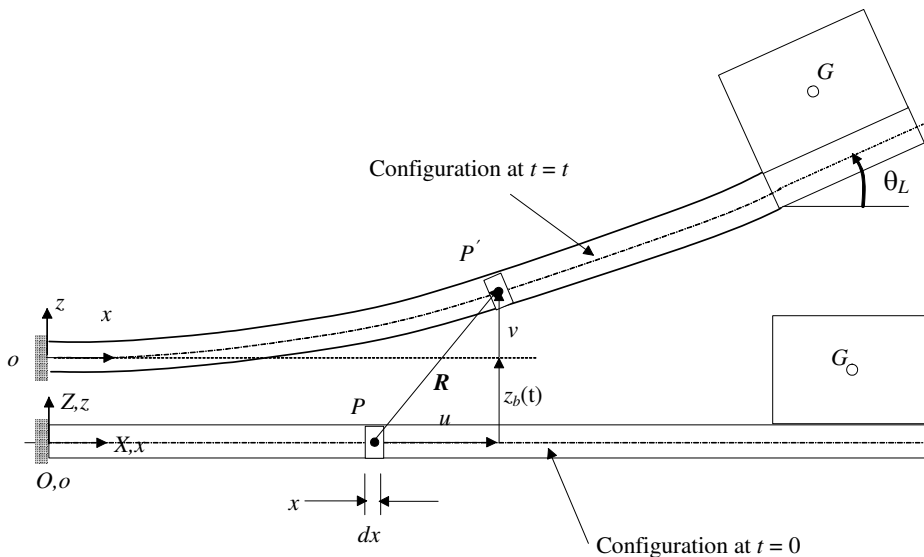


Figure 2. Sketch of deformed piezoelectric structure with respect to the reference configuration.

longitudinal and lateral displacements measured with respect to the body-fixed coordinate system x - z are $u(x, t)$ and $w(x, t)$, respectively, the absolute position of P' may be written in terms of the base-fixed coordinates as

$$\mathbf{R} = \{\mathbf{e}_x \ \mathbf{e}_y\} \begin{Bmatrix} x + u_0(x, t) \\ w_b(t) + w(x, t) \end{Bmatrix}, \quad (7)$$

where \mathbf{R}_o is the rigid-body position vector of reference point o , and \mathbf{e}_x and \mathbf{e}_y are the two unit vectors of the base-fixed coordinate system. For a nonrotating base motion, these two unit vectors are constant and identical to the unit vectors in the space-fixed coordinates.

The velocity of point P' may be written in the body-fixed coordinate system as

$$\dot{\mathbf{R}} = \{\mathbf{e}_x \ \mathbf{e}_z\} \begin{Bmatrix} \dot{u}_0 \\ \dot{w}_b + \dot{w} \end{Bmatrix}, \quad (8)$$

where \dot{w}_b is the velocity of the vibrating base and \dot{u}_0 and \dot{w} are the time rates of longitudinal and lateral deflections with respect to the moving coordinate system.

Kinetic energy. The kinetic energy of the dynamical system may be conveniently written as

$$T = T_{\text{beam}} + T_{\text{mass}}, \quad (9)$$

where T_{beam} is the kinetic energy of the beam and T_{mass} is the kinetic energy of the proof mass plus the portion of the beam bonded to the mass.

The kinetic energy of the beam may be written as

$$T_{\text{beam}} = \underbrace{\frac{1}{2} \int_0^l \bar{m} \dot{\mathbf{R}}^2 dx}_{\text{translational}} + \underbrace{\frac{1}{2} \int_0^l \bar{i}_y \dot{\theta}^2 dx}_{\text{rotational}}, \quad (10)$$

where \bar{m} is the mass of the beam per unit length, \bar{i}_y is the mass moment of inertia of the beam about the y -axis per unit length, and $\dot{\theta}$ is the rate of the angle of rotation of a plane normal to the centroid. For a symmetrically laminated beam of constant width b , we can compute \bar{m} and \bar{i}_y by

$$\bar{m} = \sum_{k=1}^n \rho_k h_k b, \quad \bar{i}_y = \frac{1}{3} \sum_{k=1}^n \rho_k b \{ (z_2^{(k)})^3 - (z_1^{(k)})^3 \}, \quad (11)$$

where $z_1^{(k)}$ and $z_2^{(k)}$ are the z -coordinates of the lower and upper faces of k -th layer, ρ_k is the density of the material in k -th layer, and h_k is the thickness of k -th layer. For large length-to-thickness ratios, the rotary inertia of the beam bimorph is very small, and will be ignored in this paper.

The kinetic energy of the proof mass attached to the free end of the piezoelectric beam structure may be written as

$$T_{\text{mass}} = \frac{1}{2} m [\dot{X}_G^2 + \dot{Z}_G^2] + \frac{1}{2} J_{G,y} \dot{\theta}_l^2, \quad (12)$$

where \dot{X}_G and \dot{Z}_G are the velocities of the proof mass center along the x and z directions respectively, $J_{G,y}$ is the mass moment of inertia of the proof mass about the y_G axis, m is the mass of the proof mass, and $\dot{\theta}_l$ is the angle of rotation of the beam at $x = l$.

At a given instant, the proof mass center is related to the beam deflection as

$$X_G = u_{0,l} + a_G \cos \theta_l - c_G \sin \theta_l, \quad Y_G = w_b + w_l + a_G \sin \theta_l + c_G \cos \theta_l, \quad (13)$$

where a_G and c_G are the axial and lateral distances, respectively, of proof mass center (G) with reference to the end point of the beam neutral axis at $x = l$, and $u_{0,l}$ and w_l are the axial and lateral deformations of the beam at $x = l$.

Finally, the kinetic energy of the proof mass may be written as

$$T_{\text{mass}} = \frac{1}{2} m (\dot{X}_G^2 + \dot{Y}_G^2) + \frac{1}{2} J_{G,y} \dot{\theta}_l^2. \quad (14)$$

Strain energy. The strain energy of the composite beam associated with the longitudinal and lateral deformations is

$$\begin{aligned} V &= \frac{1}{2} \int_{V_p} T_{1,p} S_1 dV_p + \frac{1}{2} \int_{V_s} T_{1,s} S_1 dV_s \\ &= \frac{1}{2} \int_{V_p} c_{11,p} (S_1)^2 dV_p + \frac{1}{2} \int_{V_p} e_{31} h_p^{-1} v S_1 dV_p + \frac{1}{2} \int_{V_s} c_{11,s} (S_1)^2 dV_s, \end{aligned} \quad (15)$$

where V_s is the volume of the shim material and V_p is the volume of the piezoelectric material.

Substituting (3) into (15), the strain energy for the symmetrically laminated composite beam may be expressed in terms of a line integral as

$$V = \frac{1}{2} \int_0^l R_u \left(\frac{\partial u_0}{\partial x} \right)^2 dx + \frac{1}{2} \int_0^l R_w \left(\frac{\partial^2 w}{\partial x^2} \right)^2 dx - \frac{1}{2} \int_0^l \gamma \frac{\partial^2 w}{\partial x^2} v dx, \quad (16)$$

where

$$\begin{aligned} R_u &= 2c_{11,p} 2A_p + c_{11,s} A_s, & R_w &= c_{11,p} I_p + c_{11,s} I_s, & \gamma &= 2e_{31} A_p \bar{z}_p h_p^{-1}, & A_p &= \frac{1}{2} b (h - h_s), \\ A_s &= b h_s, & I_p &= \frac{1}{12} b (h^3 - h_s^3), & I_s &= \frac{1}{12} b h_s^3, & \bar{z}_p &= \frac{1}{4} (h + h_s). \end{aligned}$$

Electrical energy. The electrical energy in the two layers of piezoelectric material may be written as

$$W_e = \frac{1}{2} \int_{V_p} E_3 D_3 dV = \frac{1}{2} \int_0^l \gamma v \frac{\partial^2 w}{\partial x^2} dx + 2 \left(\frac{1}{2} c_0 v^2 \right), \quad (17)$$

where $c_0 = \varepsilon_{33} b l h_p^{-1}$.

Energy dissipation. Energy loss in a vibrating piezoelectric structure can be handled mathematically if it is in a form of proportionality damping. The proportionality damping accounts for both the environmental damping due to the viscosity of the surrounding medium and the internal structural damping. Within the context of Lagrange equations, the Rayleigh dissipation function is an effective way of bringing damping into consideration. The energy loss function may be assumed as

$$U = \frac{1}{2} \int_0^l \alpha_u \bar{m} \dot{u}_0^2 dx + \frac{1}{2} \int_0^l \alpha_w \bar{m} \dot{w}^2 dx + \frac{1}{2} \int_0^l \beta_u R_u \left(\frac{\partial \dot{u}_0}{\partial x} \right)^2 dx + \frac{1}{2} \int_0^l \beta_w R_w \left(\frac{\partial^2 \dot{w}}{\partial x^2} \right)^2 dx, \quad (18)$$

where α_u , α_w , β_u , and β_w are proportionality constants. Their values are not determined individually. Instead, a combined damping ratio associated with a particular mode is measured and used in simulations for a specific setup.

Work done on resistor. The rate of electrical work done by the resistor per unit voltage is

$$\dot{Q}_R = \begin{cases} -i & \text{for piezoelectric layers in parallel,} \\ -2i & \text{for piezoelectric layers in series,} \end{cases} \quad (19)$$

where i is the current passing through the resistor.

The work done by the resistor per unit voltage is then

$$Q_R = \begin{cases} -q & \text{for piezoelectric layers in parallel,} \\ -2q & \text{for piezoelectric layers in series,} \end{cases} \quad (20)$$

where q is the charge flowing through the resistor.

3. Governing equations of the electromechanical system

In this section, a finite element procedure for obtaining a set of ordinary differential equations for the piezoelectric power harvesting system is presented.

Beam finite elements. The three-node beam element used in this paper has three axial nodal displacements, u_1^e , u_2^e , and u_3^e , three lateral displacements, w_1^e , w_2^e , and w_3^e , and three angles of rotation, θ_1^e , θ_2^e , and θ_3^e . To facilitate the formation of element matrices, a local axial coordinate originating at the first node of a beam element is used. For a straight beam, the local axial coordinate is related to the body-fixed coordinates by $\zeta = x - x_1^e$ and $0 \leq \zeta \leq l_e$, where x_1^e is the axial coordinate of the first node of element e and ζ is the local coordinate for element e . The longitudinal and lateral displacements of a material point within a beam finite element may be determined by the shape function and nodal variables from the equations

$$u_e = [N_1(\zeta)][D_1^e]\{q_u^e\}, \quad w_e = [N_2(\zeta)][D_2^e]\{q_w^e\}. \quad (21)$$

(see [Yu and Cleghorn 2002]). For convenience in assembly of component equations, the global nodal displacement vector is rearranged in the following manner:

$$\{r\} = \{u_1 \ w_1 \ \theta_1 \ u_2 \ w_2 \ \theta_2 \ \dots \ u_{NN} \ w_{NN} \ \theta_{NN}\}^T. \quad (22)$$

The longitudinal and lateral nodal displacements are related to the global displacement vector through transformation matrices $[T_u^e]$ and $[T_w^e]$ as follows:

$$\{q_u^e\} = [T_u^e]\{r\}, \quad \{q_w^e\} = [T_w^e]\{r\}. \quad (23)$$

Expressions for kinetic, strain, and dissipation and electric energies in nodal displacements. If N_e beam finite elements are used for the piezoelectric structure, the kinetic energy (excluding the rotary inertia), the strain energy, the Rayleigh dissipation energy function, and the electrical energy for the dynamical system may be written in terms of the nodal displacements and the voltage across a single layer of piezoelectric material may be written as

$$\begin{aligned} T &= \frac{1}{2} \{\dot{r}\}^T [M] \{\dot{r}\} + \dot{w}_b \{\dot{r}\}^T \{B\} + \frac{1}{2} \bar{m} l \dot{w}_b^2, & U &= \frac{1}{2} \{\dot{r}\}^T [C] \{\dot{r}\}, \\ V &= \frac{1}{2} \{r\}^T [K] \{r\} - \frac{1}{2} \gamma v \{r\}^T \{\Theta\}, & W_e &= \frac{1}{2} v \{r\}^T \{\Theta\} + 2\left(\frac{1}{2} c_0 v^2\right), \end{aligned} \quad (24)$$

where

$$\begin{aligned}
[C] &= \sum_{e=1}^{NE} \left[[T_u^e]^T [\alpha_u [M_u^e] + \beta_u [K_u^e]] [T_u^e] \right] + \sum_{e=1}^{NE} [T_w^e]^T [\alpha_w [M_w^e] + \beta_w [K_w^e]] [T_w^e], \\
[M] &= \sum_{e=1}^{NE} \left[[T_u^e]^T [M_u^e] [T_u^e] + [T_w^e]^T [M_w^e] [T_w^e] \right] + [M_{\text{mass}}], \quad [K] = \sum_{e=1}^{NE} \left[[T_u^e]^T [K_u^e] [T_u^e] + [T_w^e]^T [K_w^e] [T_w^e] \right], \\
\{B\} &= \sum_{e=1}^{NE} [T_w^e]^T \{B_w^e\} + \{B_{\text{mass}}\}, \quad \{\Theta\} = \sum_{e=1}^{NE} [T_w^e]^T \{\Theta_w^e\}, \\
[M_u^e] &= [D_1^e]^T \left[\int_0^{l_e} \bar{m} [N_1]^T [N_1] d\xi \right] [D_1^e], \quad [M_w^e] = [D_2^e]^T \left[\int_0^{l_e} \bar{m} [N_2]^T [N_2] d\xi \right] [D_2^e], \\
[K_u^e] &= [D_1^e]^T \left[\int_0^{l_e} R_u [N_1']^T [N_1'] d\xi \right] [D_1^e], \quad [K_w^e] = [D_2^e]^T \left[\int_0^{l_e} R_w [N_2'']^T [N_2''] d\xi \right] [D_2^e], \\
\{\Theta\} &= [D_2^e]^T \left\{ \int_0^{l_e} [N_2'']^T d\xi \right\}, \quad \{B_w^e\} = [D_2^e]^T \left[\int_0^{l_e} \bar{m} [N_2]^T d\xi \right], \\
[M_{\text{mass}}] &= \begin{bmatrix} \mathbf{0} & \mathbf{0} \\ \mathbf{0} & [\bar{M}_{\text{mass}}] \end{bmatrix}, \quad [\bar{M}_{\text{mass}}] = \begin{bmatrix} m & 0 & -mc_G \\ 0 & m & ma_G \\ -mc_G & ma_G & \bar{J}_y \end{bmatrix}, \\
\{B_{\text{mass}}\} &= \{0 \ 0 \ \dots \ 0 \ m \ ma_G\}^T, \quad \bar{J}_y = ma_G^2 + mc_G^2 + J_{G,y}.
\end{aligned}$$

Governing equations. The Lagrangian for the electromechanical system may now be written as

$$L = T - V + W_e = \frac{1}{2} \{\dot{r}\}^T [M] \{\dot{r}\} - \frac{1}{2} \{q\}^T [K] \{r\} + \gamma \{r\}^T \{\Theta\} v + 2\left(\frac{1}{2} c_0 v^2\right). \quad (25)$$

Two sets of governing equations for the electromechanical system can be derived from the following Lagrange equations:

$$\frac{d}{dt} \frac{\partial L}{\partial \{\dot{r}\}^T} + \frac{\partial U}{\partial \{\dot{r}\}^T} - \frac{\partial L}{\partial \{r\}^T} = \mathbf{0}, \quad \frac{d}{dt} \frac{\partial L}{\partial \dot{v}} - \frac{\partial L}{\partial v} = Q_R. \quad (26)$$

Substituting (25) into (26), the equations of motion of the piezoelectric structure and the equation of the electrical power generation are written as

$$[M] \{\ddot{r}\} + [C] \{\dot{r}\} + [K] \{r\} - \gamma [\Theta]^T v = -\{B\} \ddot{w}_b, \quad \gamma [\Theta]^T \{r\} + 2c_0 v = Q_R. \quad (27)$$

When the electrical output from the piezoelectric structure is connected to a resistor load and the two piezoelectric layers are connected in parallel, the voltage is related to the rate of charge as $v = R\dot{q}$. Incorporating the above electrical boundary condition and the first relation in (20) into (27), the governing equations for the coupled electromechanical system may be rewritten in terms of the mechanical displacements and the electric charge, for a sinusoidal base motion, $w_b = A \sin(\omega t + \phi)$, as follows:

$$\begin{bmatrix} [M] & \mathbf{0} \\ \mathbf{0} & 0 \end{bmatrix} \begin{Bmatrix} \{\ddot{r}\} \\ \ddot{q} \end{Bmatrix} + \begin{bmatrix} [C] & -\gamma R[\Theta] \\ \mathbf{0} & R \end{bmatrix} \begin{Bmatrix} \{\dot{r}\} \\ \dot{q} \end{Bmatrix} + \begin{bmatrix} K & \mathbf{0} \\ [\Theta]^T \frac{\gamma}{2c_0} & \frac{1}{2c_0} \end{bmatrix} \begin{Bmatrix} \{r\} \\ q \end{Bmatrix} = A\omega^2 \sin(\omega t + \phi) \begin{Bmatrix} \{B\} \\ 0 \end{Bmatrix}. \quad (28)$$

Equation (28) is valid for two piezoelectric layers connected in parallel. The voltages across the two piezoelectric layers are each equal to the voltage across the resistor.

In the case where the two piezoelectric layers are connected in series, the voltage across the resistor is twice the voltage across each piezoelectric layer, that is, $v = R\dot{q}/2$. In the case of a series connection, one obtains the following governing equations for the electromechanical system:

$$\begin{bmatrix} [M] & \mathbf{0} \\ \mathbf{0} & 0 \end{bmatrix} \begin{Bmatrix} \{\dot{r}\} \\ \dot{q} \end{Bmatrix} + \begin{bmatrix} [C] & -[\Theta]\gamma\frac{R}{2} \\ \mathbf{0} & R \end{bmatrix} \begin{Bmatrix} \{\dot{r}\} \\ \dot{q} \end{Bmatrix} + \begin{bmatrix} K & \mathbf{0} \\ [\Theta]^T\frac{\gamma}{c_0} & \frac{2}{c_0} \end{bmatrix} \begin{Bmatrix} \{r\} \\ q \end{Bmatrix} = A\omega^2 \sin(\omega t + \phi) \begin{Bmatrix} \{B\} \\ 0 \end{Bmatrix}. \quad (29)$$

Handling mechanical boundary conditions. If the base is considered rigid, the piezoelectric beam is clamped to the base. The axial displacement, the lateral displacement, and the angle of rotation of the beam with respect to the base are zero. The boundary conditions at the clamping end can be easily handled using the elimination method or the penalty method [Bathe 1995]. In this paper, the elimination method is employed. It is noted that other boundary conditions, such as elastically restrained edges simulating less than rigid constraints between the base and the beam, can also be handled in the framework of the finite element formulation.

Deleting the first three equations and the first three nodal variables in the remaining equations in (28), the governing equations for the electromechanical system, which satisfy all electrical and mechanical boundary conditions for the parallel connection of the two piezoelectric layers, may now be written as

$$\begin{bmatrix} [\tilde{M}] & \mathbf{0} \\ \mathbf{0} & 0 \end{bmatrix} \begin{Bmatrix} \{\ddot{r}\} \\ \ddot{q} \end{Bmatrix} + \begin{bmatrix} [\tilde{C}] & -\gamma R[\tilde{\Theta}] \\ \mathbf{0} & R \end{bmatrix} \begin{Bmatrix} \{\dot{r}\} \\ \dot{q} \end{Bmatrix} + \begin{bmatrix} \tilde{K} & \mathbf{0} \\ [\tilde{\Theta}]^T\frac{\gamma}{2c_0} & \frac{1}{2c_0} \end{bmatrix} \begin{Bmatrix} \{\tilde{r}\} \\ q \end{Bmatrix} = A\omega^2 \sin(\omega t + \phi) \begin{Bmatrix} \{\tilde{B}\} \\ 0 \end{Bmatrix}, \quad (30)$$

where matrices with a tilde on top are the result of their corresponding matrices with the first three rows and columns deleted, and vectors with a tilde are the result of their corresponding vectors with the first three elements deleted.

Similarly, Equation (29) for the series connection of the two piezoelectric layers can also be modified to satisfy the boundary condition at the clamped end. The governing equations for the coupled electromechanical system may be written as

$$\begin{bmatrix} [\tilde{M}] & \mathbf{0} \\ \mathbf{0} & 0 \end{bmatrix} \begin{Bmatrix} \{\ddot{r}\} \\ \ddot{q} \end{Bmatrix} + \begin{bmatrix} [\tilde{C}] & -[\tilde{\Theta}]\gamma\frac{R}{2} \\ \mathbf{0} & R \end{bmatrix} \begin{Bmatrix} \{\dot{r}\} \\ \dot{q} \end{Bmatrix} + \begin{bmatrix} \tilde{K} & \mathbf{0} \\ [\tilde{\Theta}]^T\frac{\gamma}{c_0} & \frac{2}{c_0} \end{bmatrix} \begin{Bmatrix} \{\tilde{r}\} \\ q \end{Bmatrix} = A\omega^2 \sin(\omega t + \phi) \begin{Bmatrix} \{\tilde{B}\} \\ 0 \end{Bmatrix}. \quad (31)$$

Equation (30) for the coupled electromechanical system can be written in a unified manner as

$$[M_{em}]\{\ddot{x}_{em}\} + [C_{em}]\{\dot{x}_{em}\} + [K_{em}]\{x_{em}\} = \{F_{em}\} \sin(\omega t + \phi), \quad (32)$$

where the subscript em in the above equations stands for electromechanical. Other quantities are defined as follows for the two piezoelectric layers in parallel:

$$[M_{em}] = \begin{bmatrix} [\tilde{M}] & \mathbf{0} \\ \mathbf{0} & 0 \end{bmatrix}, [C_{em}] = \begin{bmatrix} [\tilde{C}] & -\gamma R[\tilde{\Theta}] \\ \mathbf{0} & R \end{bmatrix}, [K_{em}] = \begin{bmatrix} \tilde{K} & \mathbf{0} \\ [\tilde{\Theta}]^T\frac{\gamma}{2c_0} & \frac{1}{2c_0} \end{bmatrix}, \{x_{em}\} = \begin{Bmatrix} \{\tilde{r}\} \\ q \end{Bmatrix}, \{F_{em}\} = A\omega^2 \begin{Bmatrix} \{\tilde{B}\} \\ 0 \end{Bmatrix}.$$

For the two piezoelectric layers in series, the electromechanical mass matrix and the load vector are identical to those given above. However, the electromechanical damping matrix and the electromechanical stiffness matrix are different and are given as:

$$[C_{em}] = \begin{bmatrix} [\tilde{C}] & -[\tilde{\Theta}]\frac{\gamma R}{2} \\ \mathbf{0} & R \end{bmatrix}, \quad [K_{em}] = \begin{bmatrix} \tilde{K} & \mathbf{0} \\ [\tilde{\Theta}]^T \frac{\gamma}{c_0} & \frac{2}{c_0} \end{bmatrix}.$$

Steady-state solution. A steady-state solution to (32) may be sought in the following manner:

$$\{x_{em}\} = \{X\}_c \cos(\omega t + \phi) + \{X\}_s \sin(\omega t + \phi), \tag{33}$$

where $\{X\}_c$ and $\{X\}_s$ are constant vectors.

Substituting (33) into the governing differential equations and comparing the coefficients associated with the cosine and sine harmonics, one obtains the following set of inhomogeneous algebraic equations for the two unknown vectors:

$$\begin{bmatrix} [K_{em}] - [M_{em}]\omega^2 & [C_{em}]\omega \\ -[C_{em}]\omega & [K_{em}] - [M_{em}]\omega^2 \end{bmatrix} \begin{Bmatrix} \{X\}_c \\ \{X\}_s \end{Bmatrix} = \begin{Bmatrix} \mathbf{0} \\ \{F_{em}\} \end{Bmatrix}. \tag{34}$$

Once $\{X\}_c$ and $\{X\}_s$ are determined, the amplitudes for the mechanical variables (nodal displacements) and the electrical variable can be computed. A postprocessing scheme can be employed to obtain the amplitudes for the current, voltage and power. It is noted that there are two ways to determine the power output: the peak power and the average power. For the sinusoidally varying current and voltage across an electrical load, the average power is one half of the peak power.

For a piezoelectric system under sinusoidal base motion, (34) can be used to obtain the mechanical and electrical responses provided that the damping ratio accounts for the loss of energy in the form of structural damping. For small scale vibration, the air resistance is negligible.

4. Validation of the proposed model

The model proposed in this paper is validated by comparing the simulation results obtained using the model with the experimental results of two piezoelectric bimorph beam power harvesters. One design, with the two piezoelectric layers connected in series and a proof mass simplified as a point mass, is available in the literature. The other design, with the two piezoelectric layers connected in parallel and a proof mass which cannot be simplified as a point mass, is built and tested in this paper for investigating the effect of the mass moment of inertia and mass center offset.

A cantilever piezoceramic structure carrying a point mass. The first system, sketched in Figure 3, is a piezoceramic harvester developed in [Erturk and Inman 2009]. The dimensions of the proof mass in the

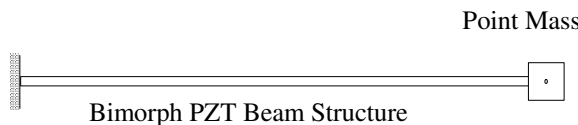


Figure 3. Sketch of the piezoelectric structure carrying a small point mass.

plane of base motion are relatively small and thus it is treated as a point mass. The two piezoelectric layers are connected in a series manner to power a resistive load.

To validate the finite element model described in this paper, simulations were conducted for four different meshing schemes. The bimorph piezoelectric beam consists of a shim core of brass and two layers of piezoceramic materials. Parameters for the piezoelectric power harvester are given in [Table 1](#) for reference. The proof mass is treated as a point mass, that is, the effects of the mass moment of inertia and the mass center offset are ignored in this paper and in [\[Erturk and Inman 2009\]](#). An electrical load of $R = 470 \text{ k}\Omega$ was used. The peak powers, peak voltages, and optimal frequencies, obtained using one, two, four, and seven beam finite elements, are given in [Table 2](#). Here the optimal frequencies are the frequencies at which a maximum power (or voltage) is generated for a given resistive load and base excitation amplitude. It can be seen that the results converge rapidly if four or more elements are

Parameters	Symbol	Values
Piezoelectric structure		
Length (mm)	l	50.8
Width (mm)	b	31.8
Damping ratio	ζ	0.027
Shim material (brass)		
Thickness (mm)	t_s	0.14
Modulus of elasticity (GPa)	E_s	105
Shim density (kg/m^3)	ρ_s	9000
Piezoelectric material (PZT-5A)		
Thickness of each piezoelectric layer (mm)	t_p	0.26
Modulus of elasticity (GPa)	E_p	66
Density (kg/m^3)	ρ_p	7800
Piezoelectric constant (pm/V)	d_{31}	190
Piezolayer permittivity (F/m)	ϵ_{33}	$1500\epsilon_0$
Proof mass		
Mass (g)	m	12.0
Mass moment of inertia (kg m^2)	J_G	0
Mass center x -location (mm)	a_G	0
Mass center z -location (mm)	c_G	0
Base motion (harmonic)		
Acceleration magnitude (m/s^2)	A	1 g or 9.81
Frequency range for testing (Hz)	ω or f	30–70

Table 1. Parameters for a bimorph piezoelectric harvester carrying a small proof mass [\[Erturk and Inman 2009\]](#). The finite element model has $N_e = 7$ elements, except for convergence studies, where different numbers of finite elements were used. The resistance R of the resistor is variable. The two piezoelectric layers are connected in series.

Number of beam elements used	Peak power (mW)	Peak voltage (V)	Optimal frequency (Hz)
1	18.470	93.170	48.040
2	18.479	93.194	48.050
4	18.470	93.170	48.050
7	18.470	93.170	48.050

Table 2. Convergence studies for a bimorph beam of [Roundy et al. 2004] for $R = 470 \text{ k}\Omega$.

used. Based on this, seven beam finite elements are used for all simulations in this paper. Use of an unnecessarily large number of elements is not desired for bimorph beams of small length-to-width ratios (about 1.6 for the bimorph beam used in [Erturk and Inman 2009]).

For $R = 470 \text{ k}\Omega$, the experimental peak powers of [Erturk and Inman 2009] were digitized and plotted against the simulation results obtained using the procedure proposed in this paper. It can be seen from Figure 4 that the simulation results are in good agreement with the data of [Erturk and Inman 2009].

A cantilever piezoelectric power harvester with a nonpoint mass. The second power harvester, designed, fabricated, and tested in this paper, is shown in Figure 5. In this design, the mass moment of inertia and mass center offset of the proof mass contribute significantly to the structural natural frequencies and the electrical power generation. Thus the mass cannot be treated as a point mass. The power harvester is tested on a vibration shaker. The shaker is made to vibrate sinusoidally with a peak acceleration amplitude of 0.5 g and adjustable excitation frequencies (20–120 Hz). The entire experimental setup,

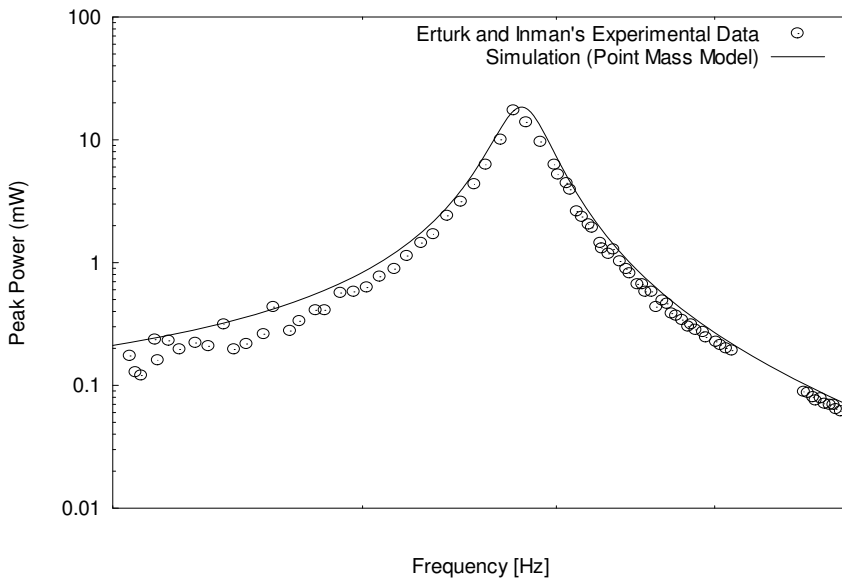


Figure 4. Comparison of simulated peak power outputs with the experimental data in [Erturk and Inman 2009] for $R = 470 \text{ k}\Omega$.

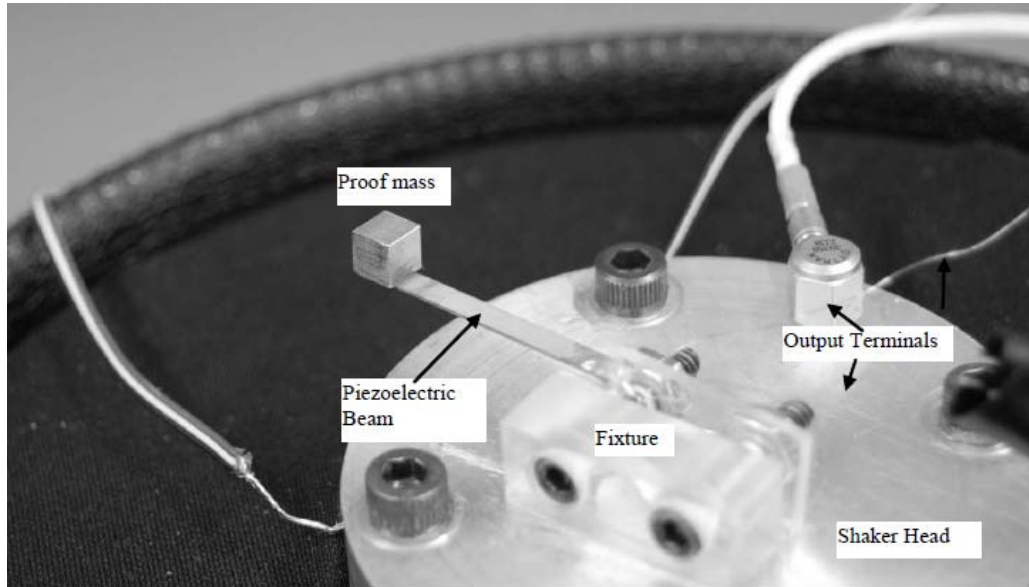


Figure 5. Photograph of the piezoelectric structure carrying a large proof mass.

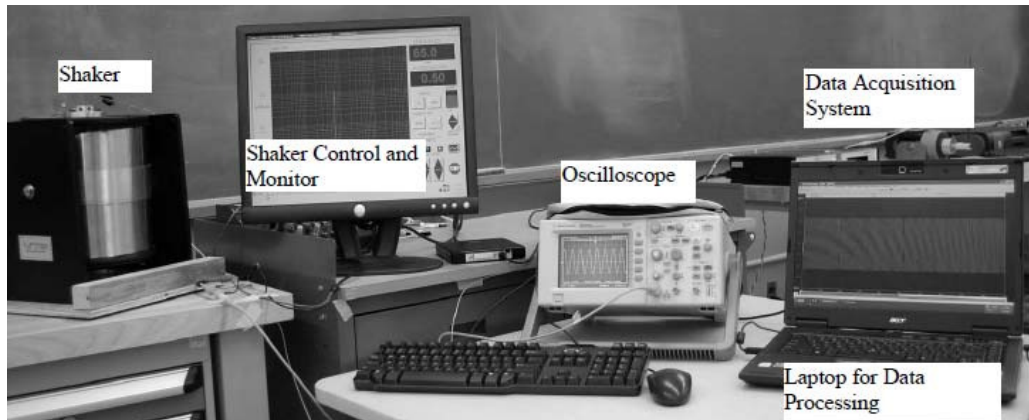


Figure 6. Photograph of the entire experimental setup.

consisting of the shaker, the piezoelectric harvester, a resistor load, a digital oscilloscope, and a data acquisition system, is shown in [Figure 6](#).

The average power outputs for frequencies between 20 Hz and 120 Hz were measured and computed using the procedure described in the previous section for six different electric loads (20, 70, 150, 250, 350, and 500 k Ω). Two proof mass models, the comprehensive mass model and the point mass model, were used in the simulations. The comprehensive model takes into consideration the mass, mass moment of inertia, axial offset, and vertical offset of the mass center with respect to the bimorph beam and mass interface. The point mass model takes into consideration only the mass concentrated at the beam-mass interface. In an impact test, the damping ratio was found to be 0.024 for the experimental setup.

This damping ratio is used for all simulations. According to [Figure 7](#), for all six resistive loads, the comprehensive model yields a good match with the experimental data while the point mass model leads to significant discrepancy between the calculated results and the experimental data in terms of resonant frequencies and the generated power.

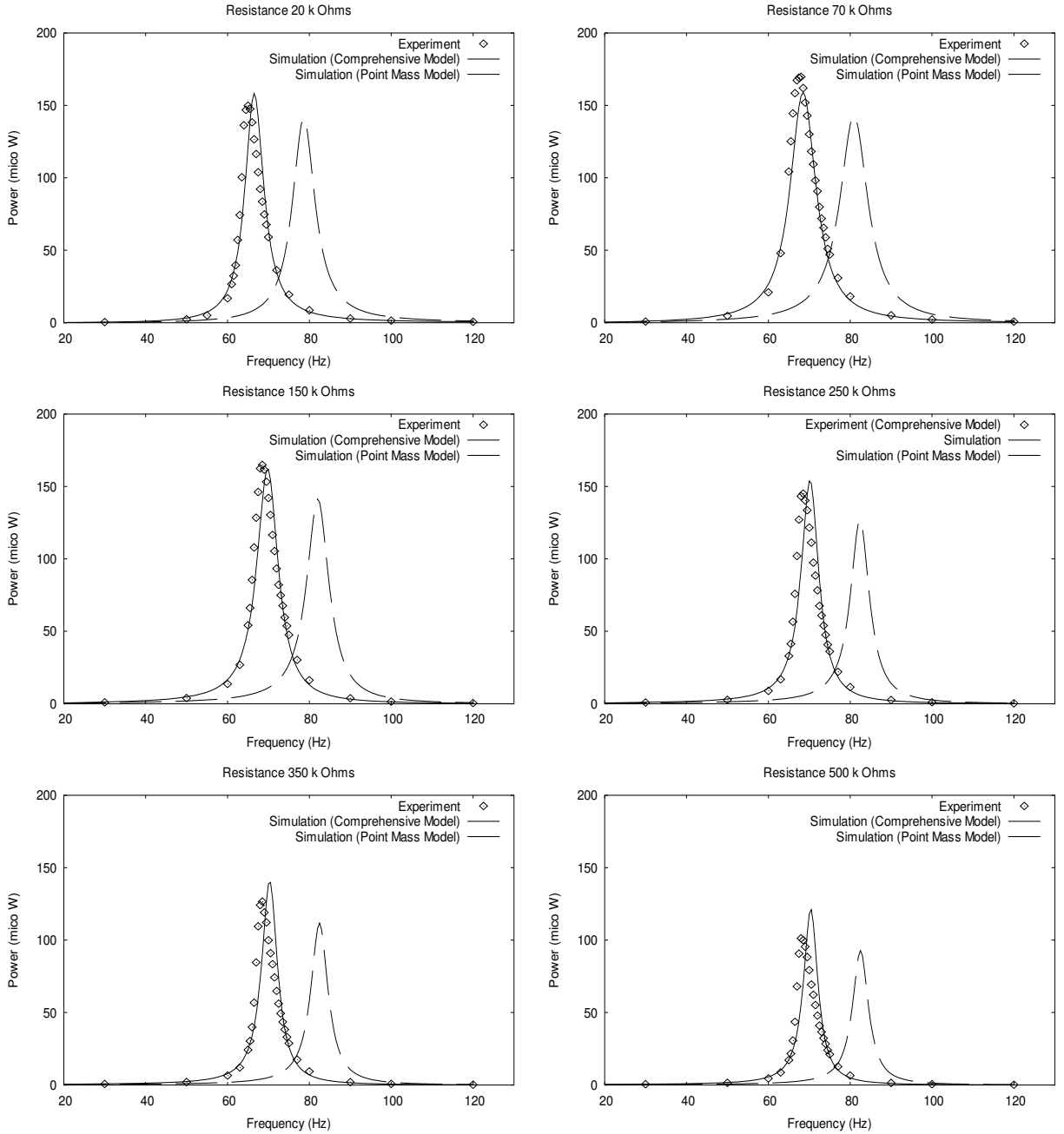


Figure 7. Comparisons of simulated average power outputs with experimental data for ranges of excitation frequencies and electrical loads.

5. Effects of the dimension and geometry of the proof mass on power output

To reduce the overall dimensions, heavy materials such as tungsten are commonly used to make the proof mass for a cantilever-based bimorph piezoelectric structure. However, this reduction does not validate the use of a point model. In this section, the effects on power generation when different proof masses are attached are investigated for the piezoelectric system described in Table 3. The system is excited by sinusoidal base motion with a 0.5 g acceleration magnitude and variable frequencies.

Four different configurations of proof masses of parallelepiped shapes, as shown in Figure 8, are studied. These mass shapes and attachments are used in typical designs in the literature. All masses have a dimension of 5 mm in the y -direction. The first three masses have their mass centers located at the beam neutral axis. There is only a horizontal offset between the proof mass center and the structure-mass

Parameters	Symbol	Values
Piezoelectric structure		
Length (mm)	l	21.85
Width (mm)		3.2
Damping ratio (1st mode)	ζ	0.024
Shim material (brass)		
Thickness (mm)	t_s	0.102
Modulus of elasticity (GPa)	E_s	100
Shim density (kg/m ³)	ρ_s	8.4
Piezoelectric material (PZT-5E)		
Thickness of each piezoelectric layer (mm)	t_p	0.139
Modulus of elasticity (GPa)	E_p	62
Density (kg/m ³)	ρ_p	7800
Piezoelectric constant (m/V)	d_{31}	0.320×10^{-9}
Piezolayer permittivity (F/m)	ϵ_{33}	3.364×10^{-8}
Proof mass		
Mass (kg)	m	0.975×10^{-3}
Mass moment of inertia (kg m ²)	J_G	0.406×10^{-8}
Length (mm)	a	5
Width (mm)	b	5
Height (mm)	c	5
Base motion (harmonic)		
Acceleration magnitude (m/s ²)	A	4.905
Frequency range for testing (Hz)	ω or f	20–120

Table 3. Parameters for an experimental bimorph piezoelectric harvester carrying a large proof mass on top. The resistance R of the resistor is variable. The finite element model has $N_e = 7$ elements. The two piezoelectric layers are connected in parallel.

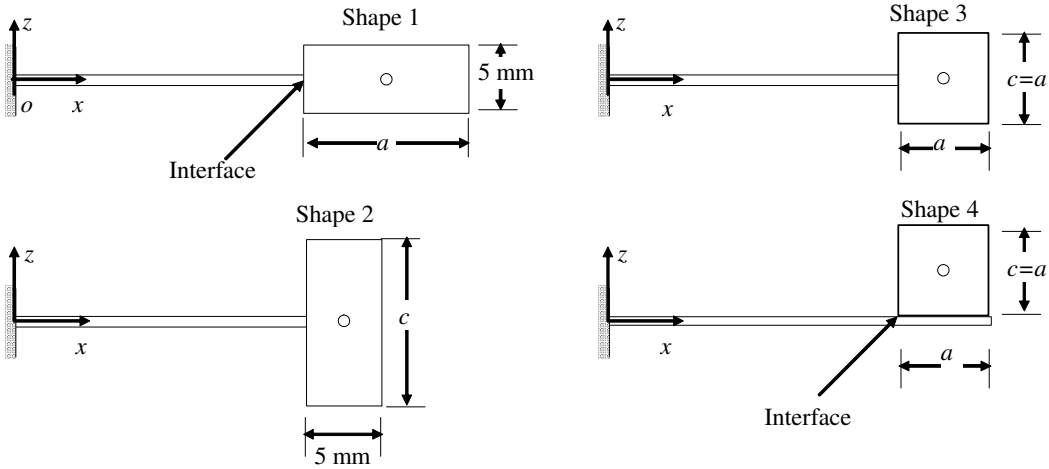


Figure 8. Four different proof masses and configurations. All parallelepiped proof masses have a thickness of 5 mm in the y -direction.

interface. The fourth mass is placed on top of the beam, and therefore has both a horizontal and a vertical offset between the proof mass center and the structure-mass interface. From the mass matrix composition in the governing equations, the vertical offset, c_G , couples the axial deformation and vertical bending. The presence of a nonzero vertical offset requires that the axial deformation be considered. Overall, the point mass model, in which the mass moment of inertia and the mass center offset are ignored, tends to overpredict the structural natural frequencies. As a result, when the piezoelectric structure is connected to a resistive load, the resonant frequency of the electromechanical system is shifted upwards.

The results shown in [Figure 9](#) indicate that the fundamental natural frequencies vary considerably with the characteristic dimension of the four masses. The point mass model yields acceptable results only when the overall dimensions of the proof mass in the x - z plane are small. This is especially true for the third and fourth shapes, which have a square aspect ratio; the proof masses shrink to a point if the characteristic dimensions (lengths and heights) reduce to zero. However, for the first shape, the characteristic dimension of the proof mass is the length with a fixed height of 5 mm; the natural frequencies do not quite converge to those for a point mass. For the second proof mass shape, the point mass model does not yield satisfactory results even if the characteristic dimension (height) approaches zero.

Accurate predictions of power generation from a beam-mass cantilever piezoelectric system depend strongly on the reliable prediction of the structural natural frequencies. Errors in predicting the structural natural frequencies will result in errors in power generation. The simulated power outputs in the frequency range 0–200 Hz are shown in [Figure 10](#) for parallel connection and a resistive load of $R = 70 \text{ k}\Omega$ for the piezoelectric structure defined in [Table 3](#). It can be seen clearly from the simulation results that the proof mass dimension and geometry shift the occurrence of peak powers considerably. It is noted that for the fourth shape, the second spike corresponding to the second resonant frequency appears at 180 Hz from the comprehensive model.

According to the above simulations and analysis, the mass moment of inertia, axial offset, and vertical offset of the mass center due to the nonnegligible dimension and the geometry of the proof mass have

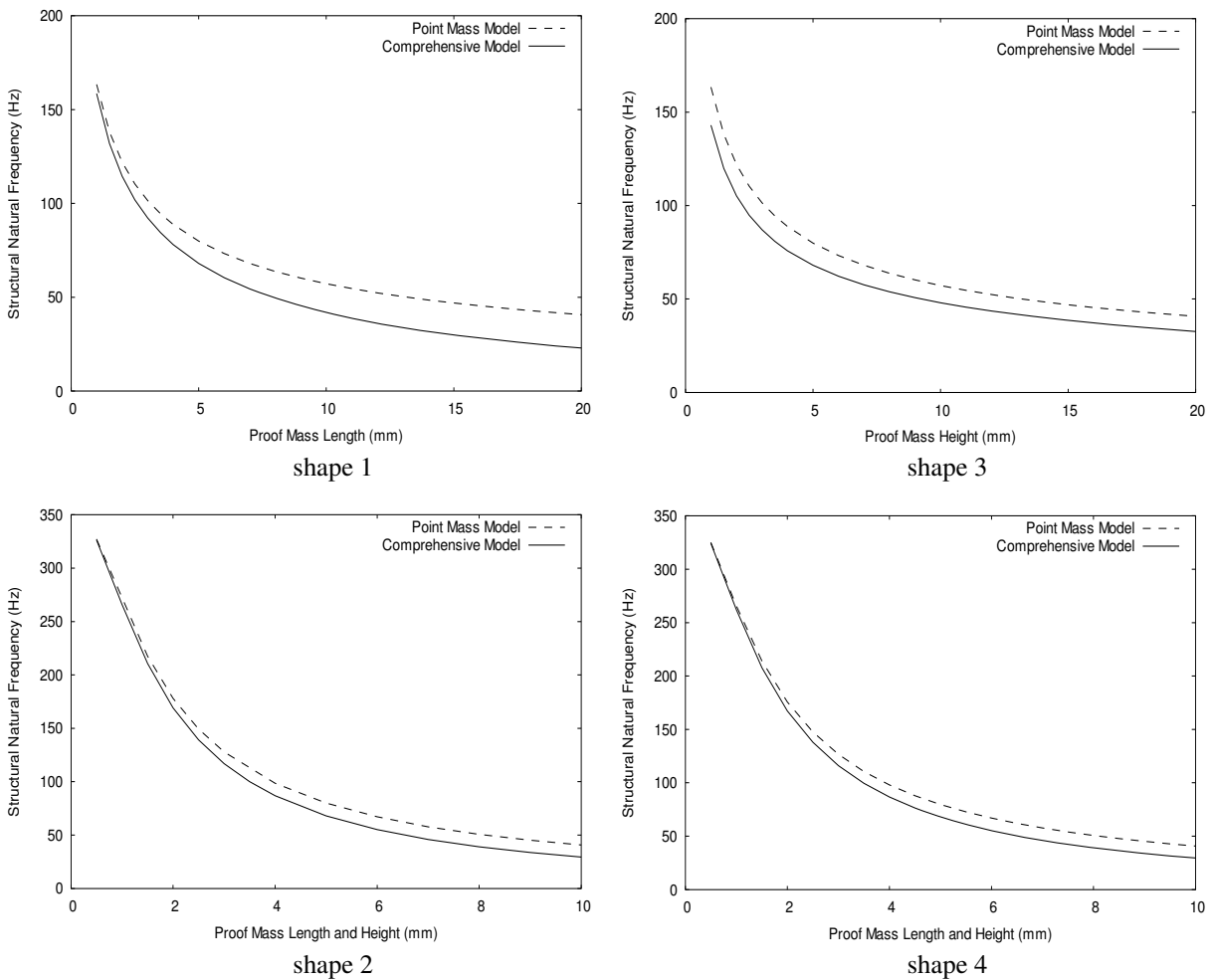


Figure 9. Effects of proof masses and configurations on structural natural frequencies.

significant effects on the resonant frequency of the piezoelectric beam power harvesters and the output power. The comprehensive finite element model presented in this paper can readily take the effects of the proof mass dimension and geometry into consideration and thus is able to accurately predict the performance of piezoelectric power harvesters. However, it can be very difficult to consider those effects in analytical models or equivalent circuit models. As a result, the comprehensive finite element model is more advantageous than the simplified analytical model in simulating piezoelectric power harvesters.

For the block type proof mass photographed in [Figure 5](#), the resonant frequencies predicted by the comprehensive model are in excellent agreement with the experimental resonant frequencies for a wide range of resistive loads. However, the point mass model overpredicts the resonant frequencies by 18%. As for the peak powers and voltages, the errors of predicted values using the point mass model vary with the resistive loads. At 70 k Ω , the point mass model underpredicts the peak power by 9.5%. It should be pointed out here that, for proof masses of complex configurations, the predictions of the point mass model may be completely unacceptable.

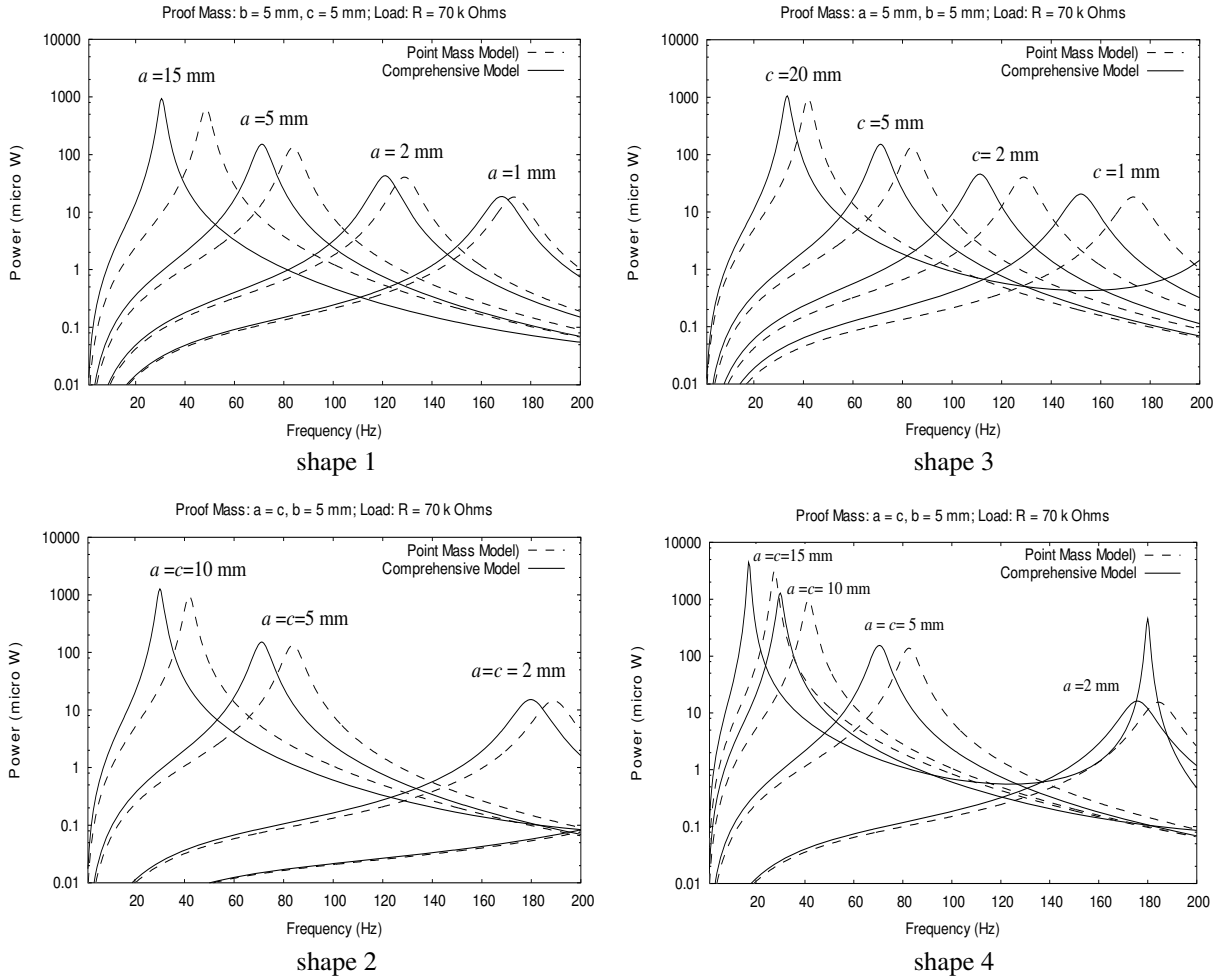


Figure 10. Effects of proof masses on output powers for $R = 70 \text{ k}\Omega$.

Conclusions

A comprehensive model, along with a point mass model, is developed in this paper to simulate the mechanical motion and electrical power of piezoelectric bimorph energy harvesters. The mass moment of inertia and bending-axial stretching coupling effects due to a nonsymmetric proof mass configuration are considered in the comprehensive model. The simulation results from the point mass and comprehensive models are compared with independent data available in the literature for a series connection between the two PZT layers and newly obtained experimental data for a parallel connection. Excellent agreement was achieved between the theoretical predictions from the comprehensive model and the measurements for both sets of experiments. It is found that the point mass model produces significant errors for both the resonant frequencies and electrical powers. Sensitivity studies conducted using the comprehensive model show that the effects of mass, mass moment inertia, and mass center offset of a proof mass on the electrical power harvesting are significant and must all be taken into consideration in simulations.

References

- [Anton and Sodano 2007] S. R. Anton and H. A. Sodano, “A review of power harvesting using piezoelectric materials: 2003–2006”, *Smart Mater. Struct.* **16**:3 (2007), R1.
- [Bathe 1995] K.-J. Bathe, *Finite element procedures*, 2nd ed., Prentice Hall, Englewood Cliffs, NJ, 1995.
- [Dutoit et al. 2005] N. E. Dutoit, B. L. Wardle, and S.-G. Kim, “Design considerations for MEMS-scale piezoelectric mechanical vibration energy harvesters”, *Integr. Ferroelectr.* **71**:1 (2005), 121–160.
- [Erturk and Inman 2008a] A. Erturk and D. J. Inman, “Comment on ‘Modeling and analysis of a bimorph piezoelectric cantilever beam for voltage generation’”, *Smart Mater. Struct.* **17**:5 (2008), 058001.
- [Erturk and Inman 2008b] A. Erturk and D. J. Inman, “Issues in mathematical modeling of piezoelectric energy harvesters”, *Smart Mater. Struct.* **17**:6 (2008), 065016.
- [Erturk and Inman 2009] A. Erturk and D. J. Inman, “An experimentally validated bimorph cantilever model for piezoelectric energy harvesting from base excitations”, *Smart Mater. Struct.* **18**:2 (2009), 025009.
- [Glynne-Jones et al. 2004] P. Glynne-Jones, M. J. Tudor, S. P. Beeby, and N. M. White, “An electromagnetic, vibration-powered generator for intelligent sensor systems”, *Sens. Actuators A Phys.* **110**:1–3 (2004), 344–349.
- [Liao and Sodano 2008] Y. Liao and H. A. Sodano, “Model of a single model energy harvester and properties for optimal power generation”, *Smart Mater. Struct.* **17**:6 (2008), 065026.
- [Mitcheson et al. 2004] P. D. Mitcheson, P. Miao, B. H. Stark, E. M. Yeatman, A. S. Holmes, and T. C. Green, “MEMS electrostatic micropower generator for low frequency operation”, *Sens. Actuators A Phys.* **115**:2–3 (2004), 523–539.
- [Roundy et al. 2004] S. Roundy, P. K. Wright, and J. M. Rabaey, *Energy scavenging for wireless sensor networks: with special focus on vibrations*, Kluwer Academic Publishers, Boston, 2004.
- [Sodano et al. 2004] H. A. Sodano, G. Park, and D. J. Inman, “A review of power harvesting from vibration using piezoelectric materials”, *Shock Vib. Digest* **36**:3 (2004), 197–205.
- [Wang et al. 2007] F. Wang, G. J. Tang, and D. K. Li, “Accurate modeling of a piezoelectric composite beam”, *Smart Mater. Struct.* **16**:5 (2007), 1595–1602.
- [Yang 2006] J. Yang, *Analysis of piezoelectric devices*, World Scientific, Singapore, 2006.
- [Yu and Cleghorn 2002] S. D. Yu and W. L. Cleghorn, “Dynamic instability analysis of high-speed flexible four-bar mechanisms”, *Mech. Mach. Theory* **37**:11 (2002), 1261–1285.

Received 24 Jun 2009. Revised 26 Nov 2009. Accepted 26 Nov 2009.

SHUDONG YU: syu@ryerson.ca

Department of Mechanical and Industrial Engineering, Ryerson University, 350 Victoria Street, Toronto M5B 2K3, Canada

SIYUAN HE: s2he@ryerson.ca

Department of Mechanical and Industrial Engineering, Ryerson University, 350 Victoria Street, Toronto M5B 2K3, Canada

WEN LI: w3li@ryerson.ca

Department of Mechanical and Industrial Engineering, Ryerson University, 350 Victoria Street, Toronto M5B 2K3, Canada

SHAKEDOWN WORKING LIMITS FOR CIRCULAR SHAFTS AND HELICAL SPRINGS SUBJECTED TO FLUCTUATING DYNAMIC LOADS

PHAM DUC CHINH

Under quasiperiodic fluctuating dynamic loads, a structure made of elastic plastic material may fail by incremental collapse (ratcheting) or alternating plasticity (fatigue). For the kinematic hardening materials considered, the only two crucial material parameters needed are the initial and ultimate yield stresses, but not the generally deformation-history-dependent hardening curve between them. With the high-cycle loading we suggest taking the fatigue limit as the initial yield stress, and taking the stress corresponding to a certain allowable amount of plastic deformation from the empirical Ramberg–Osgood curve (or the particular cyclic yield strength corresponding to the amount 0.2% of plastic deformation) as the ultimate yield stress in our shakedown analysis of structures. The approach is practical and well founded within our shakedown theory, while the small deformation assumption framework of the classical plasticity theory is kept. As illustrations, we derive explicit expressions of the working load limits for the circular shaft and helical spring, which are based on the shakedown analysis and can be used for safety design of the structures with given loading conditions.

1. Introduction

The design of machine elements made of elastic plastic materials, including shafts and springs [Lubliner 1990; Beer and Johnston 1992; Parmley 2000; Okopny et al. 2001; Akiniwa et al. 2008], requires the determination of plastic collapse loads for the structures. A plastic load limit is reached when an entire section of a determinate structure yields plastically, or full plastic yielding happens at a number of sections within an indeterminate structure to make it a mechanism. Many practical machine elements are subjected to fluctuating dynamic loads, whether periodic [Gavarini 1969] or quasiperiodic [Pham 1992; 2008]. Under such fluctuating dynamic loads, a structure would not collapse instantaneously according to the classical plastic limit theory, thanks to the inertia effect, but would fail incrementally (ratcheting mode) or by alternating plasticity (fatigue mode). The problem can be solved in the framework of shakedown theory [Koiter 1963; Gokhfeld and Cherniavski 1980; König 1987; Bree 1989; Pham 1992; 2003; 2005; 2007; 2008; Pham and Stumpf 1994; Pham and Weichert 2001; Weichert and Maier 2002].

Machines and structures are often made of elastic plastic materials that can be described by various sophisticated kinematic hardening models [Prager 1949; Armstrong and Frederick 1966; Ohno and Wang 1993; Pham 2007; Chaboche 2008], in which the hardening curve is generally nonlinear and depends on the plastic deformation history. However it was established in [Pham 2007; 2008] that for the shakedown safety assessment of a structure, the only plastic parameters needed are the initial and ultimate yield

Keywords: shakedown, dynamic high-cycle loading, ratcheting, fatigue, circular shaft, helical spring.
Work supported by Vietnam's National Foundation for Science and Technology Development.

stresses, not the particular hardening curve between them. Further development of the theory and its practical implementation will be demonstrated as it applies to shaft and spring structures in this study.

2. Circular shaft

Consider a circular shaft along the central axis z ($0 \leq z \leq L$), attached to a fixed support at one end ($z = 0$), as presented in [Figure 1](#). When the shaft is subjected to torsion, every cross-section remains plane and undistorted. That implies the kinematic assumption for the tangential angular displacement in the shaft's circular cross-section:

$$u_\varphi = C(z)r, \quad (1)$$

where C is a function of z , and r is the radial distance from the neutral axis of the shaft. The respective shear strain is

$$\gamma = \frac{\partial u_\varphi}{\partial z} = \frac{dC}{dz}r = C_1(z)r. \quad (2)$$

As the torque $M(L)$ is applied to the free end ($z = L$) of the shaft, the shaft will twist, with its cross-section at z rotating through an angle $\varphi(z)$, which, in the elastic range, is related to the elastic moment $M^e(z)$ via the differential relation

$$\frac{d\varphi}{dz} = \frac{M^e}{GJ_p}, \quad (3)$$

where G is the elastic shear modulus and J_p is the polar moment of inertia, which for a circular hollow shaft of constant cross-section, with inner and outer radii R_1 and R_2 , has the expression

$$J_p = \frac{\pi}{2}(R_2^4 - R_1^4). \quad (4)$$

The elastic shear stress in the shaft is

$$\tau_\varphi^e = \frac{M^e}{J_p}r, \quad R_1 \leq r \leq R_2. \quad (5)$$

The shaft is made of an elastic plastic kinematic hardening material with initial and ultimate yield stresses τ_Y^i and τ_Y^u [[Pham 2007; 2008](#)].

As the torque increases, the maximal shear stress at the outer radius R_2 from (5) reaches the initial yield value τ_Y^i , and the moment over the whole section achieves the initial yield value

$$M_Y^i = \tau_Y^i \frac{J_p}{R_2}. \quad (6)$$

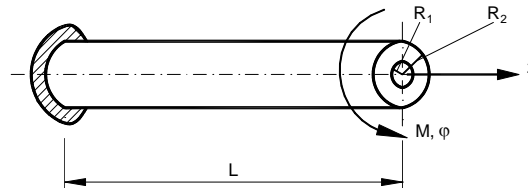


Figure 1. Conventions for a circular shaft.

The whole section of the shaft yields plastically at the ultimate yield moment

$$M_Y^u = \int_{R_1}^{R_2} r \tau_Y^u 2\pi r dr = \tau_Y^u \frac{2\pi}{3} (R_2^3 - R_1^3). \quad (7)$$

M_Y^u is considered the plastic collapse limit for the shaft subjected to static torque.

Assume that the free end of the shaft is subjected to the quasiperiodic dynamic torque

$$M(L) = M_p(t) + M_q(\underline{t}) \sin[\omega(t)t], \quad (8)$$

where $M_p(t)$, $M_q(\underline{t})$ and $\omega(t)$, with an underlined time variable, are slowly-varying functions of time (so their time derivatives can be neglected in comparison with the functions themselves), varying within the limits

$$M_p^- \leq M_p(t) \leq M_p^+, \quad |M_p^-| \leq M_p^+, \quad 0 \leq M_q(\underline{t}) \leq M_q^+, \quad 0 \leq \omega(\underline{t}) \leq \omega^+ < \omega_I = \frac{\pi}{2L} \sqrt{\frac{G}{m}}, \quad (9)$$

Here ω_I is the principal natural frequency of the shaft (in twisting vibration), and m is the shaft's mass density.

We need to determine the collapse load limits for the shaft in the space of external load parameters $M_p^-, M_p^+, M_q^+, \omega^+$.

The equilibrium equation for the problem is

$$\frac{dM}{dz} = m J_p \frac{d^2 \varphi}{dt^2}. \quad (10)$$

The elastic moment solution of the problem (10)+(3) with boundary conditions (8) and $\varphi(0) = 0$ is

$$M^e = M_p + M_q \frac{\cos(\sqrt{m/G}\omega z)}{\cos(\sqrt{m/G}\omega L)} \sin(\omega t). \quad (11)$$

The shakedown kinematic theorem [Pham 2007; 2008], applied to the problem and expressed through the shakedown safety factor k_s (at $k_s < 1$ the structure collapses, at $k_s > 1$ it is safe, and $k_s = 1$ determines the shakedown boundary in the space of external load parameters), has the form

$$k_s^{-1} = \max \{I, A\}, \quad (12)$$

where I and A describe respectively the incremental and alternating plasticity collapse modes:

$$\begin{aligned} I &= \sup_{\tau_\phi^e; \gamma} \frac{\int_0^L \int_{R_1}^{R_2} \max_t (\tau_\phi^e \gamma) 2\pi r dr dz}{\int_0^L \int_{R_1}^{R_2} \tau_Y^u |\gamma| 2\pi r dr dz} = \sup_{M^e; C_1} \frac{J_p^{-1} \int_0^L \int_{R_1}^{R_2} \max_t M^e C_1 r^3 dr dz}{\tau_Y^u \int_0^L \int_{R_1}^{R_2} |C_1| r^2 dr dz} \\ &= \sup_{C_1} \frac{\int_0^L \max_t \left[M_p + M_q \frac{\cos(\sqrt{m/G}\omega z)}{\cos(\sqrt{m/G}\omega L)} \sin(\omega t) \right] C_1(z) \int_{R_1}^{R_2} r^3 dr dz}{J_p \tau_Y^u \int_0^L |C_1(z)| \int_{R_1}^{R_2} r^2 dr dz} \\ &= \sup_{C_1} \frac{\int_0^L \left[M_p^+ + M_q^+ \frac{\cos(\sqrt{m/G}\omega^+ z)}{\cos(\sqrt{m/G}\omega^+ L)} \right] C_1(z) dz}{M_Y^u \int_0^L |C_1(z)| dz} = \frac{1}{M_Y^u} \left[M_p^+ + \frac{M_q^+}{\cos(\sqrt{m/G}\omega^+ L)} \right], \quad (13) \end{aligned}$$

$$\begin{aligned}
 A &= \sup_{z,r,t_1,t_2} \frac{\tau^e(z,r,t_1) - \tau^e(z,r,t_2)}{2\tau_Y^i} \\
 &= \sup_{z,r} \frac{\left[M_p^+ - M_p^- + 2M_q^+ \frac{\cos(\sqrt{m/G}\omega^+z)}{\cos(\sqrt{m/G}\omega^+L)} \right] r}{2\tau_Y^i J_p} = \frac{1}{2M_Y^i} \left[M_p^+ - M_p^- + \frac{2M_q^+}{\cos(\sqrt{m/G}\omega^+L)} \right]. \quad (14)
 \end{aligned}$$

Here γ is the compatible plastic strain increment of the type (2), and τ^e is the elastic stress from (5) and (11). To obtain the last equality in (13), we applied a theorem on the norm of a linear functional. The optimal field $C_1(z)$ in (13) is proportional to $\delta(z)$, the Dirac delta function, which means the incremental collapse mode (13) happens at the section $z = 0$. The alternating plasticity collapse mode (14) takes place at $z = 0$ and $r = R_2$.

Two-surface models for kinematic hardening materials involving the initial and ultimate yield stresses have been used widely in literature; see, among others, [Halphen and Nguyen 1975; Mandel 1976; Weichert and Gross-Weege 1988; Polizzotto et al. 1991; Stein et al. 1992; Corigliano et al. 1995; Pham and Weichert 2001; Nguyen 2003; Pham 2005]. Our model leaves unspecified the hardening curve, which generally depends on the plastic deformation history, but assumes it satisfies the positive hysteresis postulate ($\oint \alpha d\epsilon^p \geq 0$ for any closed cycle, where α is the back stress and ϵ^p the plastic deformation). This postulate seems to be supported by the experimental data in the literature [Pham 2007].

For our particular problem, the plastic deformation does change proportionally at every point within the structure over loading cycles; hence the expressions (12)–(14) are exact, not just an upper bound, for the shakedown safety factor k_s . For more details, consult [Pham and Stumpf 1994].

From the relations (12)–(14), the safety criterion against incremental plastic collapse (ratcheting) of the shaft can be represented as

$$M_p^+ + \frac{M_q^+}{\cos(\sqrt{m/G}\omega^+L)} \leq M_Y^u \quad (\text{i.e., } I \leq 1), \quad (15)$$

while the safety against alternating plasticity collapse (fatigue) requires

$$M_p^+ - M_p^- + \frac{2M_q^+}{\cos(\sqrt{m/G}\omega^+L)} \leq 2M_Y^i \quad (\text{i.e., } A \leq 1). \quad (16)$$

At $M_q^+ = 0$, (15) reduces to the known criterion for safety of the shaft against static plastic collapse stated in (7).

The shear initial yield stress τ_Y^i appearing in the expression (6) for the initial yield moment M_Y^i in (14) and (16), which is responsible for the alternating plasticity mode, is generally not the convenient one corresponding to the amount 0.2% of plastic deformation, but may take its value as small as the fatigue stress limit τ_Y^f , since (16) determines the alternating plasticity collapse at the high-number of loading cycles (about 10^6 – 10^7 cycles). For particular loading processes with smaller numbers of cycles, τ_Y^i (and hence M_Y^i) may be given larger values, up to the ultimate shear yield stress τ_Y^u (corresponding to M_Y^u), and can be taken from the fatigue curve for the particular material making the shaft.

Similarly, the shear ultimate yield stress τ_Y^u appearing in the expression (7) for the ultimate yield moment M_Y^u in (13) and (15), which is responsible for the incremental mode, is generally not that determined from a monotonic loading experiment, but may be smaller and can be taken from ratcheting

experiments on high number of cycles corresponding to those met in particular loading conditions of the material. The ratcheting (ultimate yield) stress may also be taken as that corresponding to a certain amount of allowable plastic deformation. Fatigue and ratcheting are observed widely in experiments on the mechanical properties of materials.

We need the experimental ratcheting curve (yield stress versus number of cycles) for a material, like the known fatigue curve, for application in our shakedown safety assessment procedure, in particular for the incremental mode.

Introduce the dimensionless parameters and variables

$$a = \frac{M_p^-}{M_p^+}, \quad f = \frac{M_Y^i}{M_Y^u} = \frac{3(R_2^4 - R_1^4)\tau_Y^i}{4R_2(R_2^3 - R_1^3)\tau_Y^u}, \quad P = \frac{M_p^+}{M_Y^u}, \quad Q = \frac{M_q^+}{M_Y^u}, \quad W = \sqrt{\frac{m}{G}}\omega^+ L \frac{2}{\pi}. \quad (17)$$

Then (15) and (16) can be represented as

$$P + \frac{Q}{\cos(W\pi/2)} \leq 1 \quad (\text{i.e., } I \leq 1), \quad (18)$$

$$P(1-a) + \frac{2Q}{\cos(W\pi/2)} \leq 2f \quad (\text{i.e., } A \leq 1). \quad (19)$$

The incremental collapse curve $I = 1$, through the W - Q relation, can be written as

$$Q = (1 - P) \cos(W\pi/2), \quad (20)$$

while the alternating plasticity collapse curve $A = 1$ is

$$Q = (f - P(1-a)/2) \cos(W\pi/2). \quad (21)$$

Comparing (20) and (21), one sees that, at

$$P > \frac{2(1-f)}{1+a}, \quad (22)$$

the curve (20) lies under the curve (21); thus, according to (12), the collapse mode is incremental, while at

$$P < \frac{2(1-f)}{1+a} \quad (23)$$

the curve (21) is lower; hence the collapse mode is alternating plasticity.

As numerical illustrations, we present in Figure 2 the shakedown curve (20) and (21) in the W - Q coordinate plane for these particular cases (the domain under the curve is the safety domain):

- $a = 0$, $f = \frac{1}{2}$, $P = \frac{1}{4}$, fatigue mode ($A = 1$): $Q = \frac{3}{8} \cos(W\pi/2)$;
- $a = 1$, $f = \frac{1}{3}$, $P = \frac{7}{10}$, ratcheting mode ($I = 1$): $Q = \frac{3}{10} \cos(W\pi/2)$;
- $a = 1$, $f = \frac{1}{2}$, $P = \frac{3}{4}$, ratcheting mode ($I = 1$): $Q = \frac{1}{4} \cos(W\pi/2)$;
- $a = \frac{1}{2}$, $f = \frac{1}{3}$, $P = \frac{1}{2}$, fatigue mode ($A = 1$): $Q = \frac{5}{24} \cos(W\pi/2)$.

On approaching the principal natural frequency of the structure ($W \rightarrow 1$), the safety limit on Q reduces to 0.

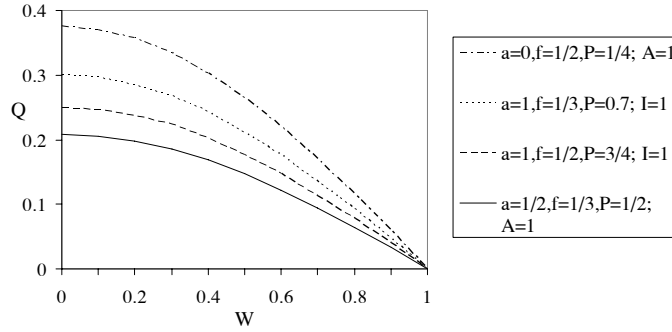


Figure 2. Shakedown curves (and modes) in the plane of external torque’s frequency-amplitude parameters, at various values of a, f, P .

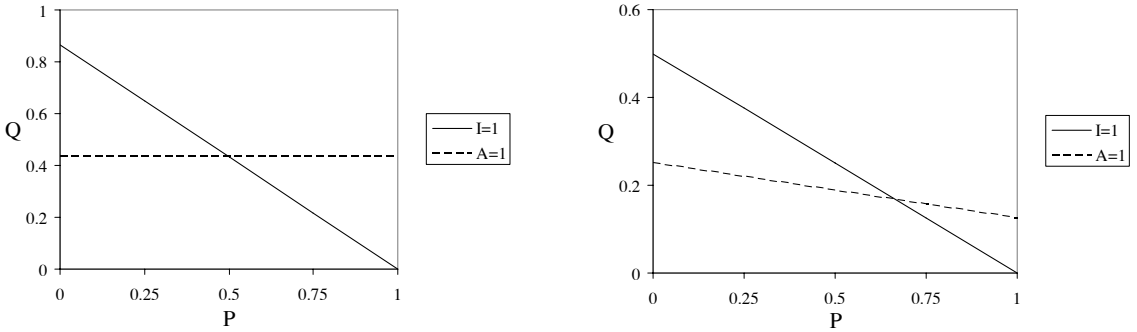


Figure 3. Incremental ($I = 1$) and alternating plasticity ($A = 1$) lines in the plane of external torque’s amplitudes’ parameters, at $a = 1, W = \frac{1}{3}$ (left) and at $a = \frac{1}{2}, W = \frac{2}{3}$ (right).

Alternatively, the incremental collapse line $I = 1$ from (18) and the alternating plasticity collapse line $A = 1$ from (19) are plotted in Figure 3 in the P - Q coordinate plane for these two cases:

- $a = 1, W = \frac{1}{3}$, corresponding to $I = P + \frac{2}{\sqrt{3}}Q = 1, A = \frac{4}{\sqrt{3}}Q = 1$;
- $a = \frac{1}{2}, W = \frac{2}{3}$, corresponding to $I = P + 2Q = 1, A = \frac{1}{2}P + 4Q = 1$.

The shakedown domain is what lies under both the incremental (ratcheting) $I = 1$ and alternating plasticity (fatigue) $A = 1$ lines. At the intersect of the lines, the collapse mode changes from one mode to the other

3. Helical spring

Consider a cylindrical coiled spring Figure 4 with small angle of lifting of coil $\alpha \ll 1$ and the central axis z ($0 \leq z \leq L$, not counting the two irregular short ends) along the wire making the spring; D is the pitch diameter of spring; R_1 and R_2 are inner and outer radii of the circular hollow wire. One end of the spring is fixed, while the other end is subjected to the dynamic quasiperiodic fluctuating load

$$F = F_p(t) + F_q(t) \sin[\omega(t)t], \tag{24}$$

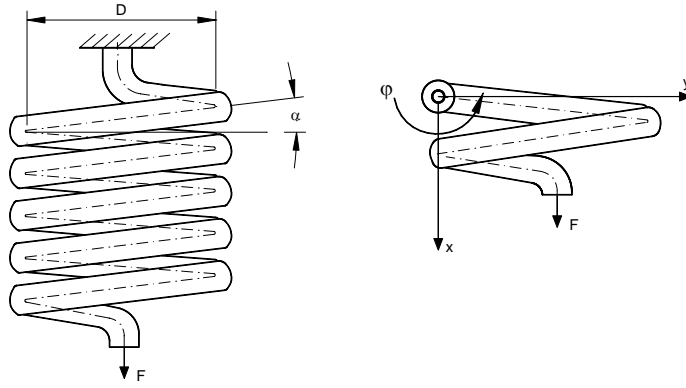


Figure 4. Conventions for a helical spring.

where $F_p(\underline{t})$, $F_q(\underline{t})$, $\omega(\underline{t})$ with underlined time variable are slowly-varying functions of time, which vary within the limits

$$F_p^- \leq F_p(\underline{t}) \leq F_p^+, \quad |F_p^-| \leq F_p^+, \quad 0 \leq F_q(\underline{t}) \leq F_q^+, \quad 0 \leq \omega(\underline{t}) \leq \omega^+ < \omega_I, \quad (25)$$

ω_I is the principal natural frequency of the spring. We have to determine the collapse load limits for the spring in the space of external load parameters $F_p^-, F_p^+, F_q^+, \omega^+$.

The elastic shear stress on a cross-section of the spring's wire is composed of the two parts: the torsional shear stress (M^e and F^e are the torque and cutting load acting on the section, r is the radial distance from the section's center)

$$\tau_\varphi^e = \frac{M^e}{J_p} r = \frac{F^e}{2J_p} Dr, \quad (26)$$

and the cutting shear stress

$$\tau_x^e = \frac{F^e}{\pi(R_2^2 - R_1^2)}. \quad (27)$$

Comparing (26) and (27), one sees that under the condition

$$R \ll D, \quad (28)$$

we have

$$|\tau_x^e| \ll |\tau_\varphi^e|, \quad (29)$$

and the component τ_x^e can be disregarded as a small contribution (compared to τ_φ^e). The effect of the two irregular short ends of the spring is also disregarded (they are considered as rigid).

The elastic moment on the wire's sections in response to load (24) is

$$M^e = F_p \frac{D}{2} + F_q \frac{D}{2} \frac{\cos(\sqrt{m/G}\omega z)}{\cos(\sqrt{m/G}\omega L)} \sin(\omega t). \quad (30)$$

Then, similar to the problem of the previous section, the shakedown kinematic theorem applied to the problem has the particular form

$$k_s^{-1} = \max \{I, A\}, \quad (31)$$

with

$$I = \frac{P}{g} + \frac{Q}{g \cos(W\pi/2)}, \quad A = P \frac{1-a}{2} + \frac{Q}{\cos(W\pi/2)}, \quad (32)$$

where

$$P = \frac{F_p^+}{F_Y^i}, \quad Q = \frac{F_q^+}{F_Y^i}, \quad W = \sqrt{\frac{m}{G}} \omega^+ L \frac{2}{\pi}, \quad a = \frac{F_p^-}{F_p^+}, \quad (33)$$

$$g = \frac{F_Y^u}{F_Y^i} = \frac{4R_2(R_2^3 - R_1^3)\tau_Y^u}{3(R_2^4 - R_1^4)\tau_Y^i}, \quad F_Y^i = \tau_Y^i \frac{\pi}{DR_2} (R_2^4 - R_1^4), \quad F_Y^u = \tau_Y^u \frac{4\pi}{3D} (R_2^3 - R_1^3).$$

The expressions (31)–(32) are similar to those in (12)–(14), with F_p^+ , F_p^- , F_q^+ , F_Y^i , F_Y^u replacing M_p^+ , M_p^- , M_q^+ , M_Y^i , M_Y^u , respectively; hence the shakedown analysis follows the same line.

As already stated in our previous works, the initial yield stress should be taken as small as the fatigue limit for the shakedown safety in the general path-independent spirit of the shakedown theorems. The ultimate yield stress is expected to be the lowest limit from those obtained in multicycle loading experiments rather than that obtained in the standard monotonic loading experiment. However the high-cycle ultimate yield strength as well as the monotonic one are often attained at the large plastic deformations, which fall far outside the small deformation assumption framework of the classical plasticity theory and the shakedown theorems. Also the design requirement of many structures would not allow excessive global configuration changes due to the large plastic deformations. Hence we suggest taking for the ultimate yield stress (of the quasistatic or low-cycle processes) - the yield stress corresponding to some allowable small amount of plastic deformation from the standard monotonic loading experiment, such as that from the broadly used Ramberg–Osgood empirical formula (the unnecessary for our purpose elastic part of the relationship is dropped)

$$\sigma_Y = K(\varepsilon^p)^n, \quad (34)$$

where σ_Y is the yield strength, ε^p the plastic deformation, K the strength coefficient, and n the strain hardening exponent. The best known one is the yield strength $\sigma_Y^{(0.2)}$ corresponding to 0.2% of plastic deformation; this is considered as the first significant amount of irreversible strain:

$$\sigma_Y^{(0.2)} = K(0.002)^n. \quad (35)$$

Note that though a local plastic deformation at the amount 0.2% may be insignificant for the global geometry of a structure because of the global compatible strain constraint, when a global incremental mechanism $I = 1$ is formed with $\sigma_Y^u = \sigma_Y^{(0.2)}$, a significant global compatible plastic strain increment arises leading to a significant configuration change of the structure. Still, Equations (34) and (35), obtained from the monotonic loading experiment, are the only first approximations for our ultimate yield stress σ_Y^u of multicycle loading processes, which should be established from high-cycle loading experiments (such as those in the fatigue tests). Ideally we need the stress-controlled cyclic loading experiments leading to certain allowable amount of plastic deformation. For cyclic softening materials, we may rely on the strain-controlled cyclic loading experiments, as those presented in [Tucker et al. 1979; Roessle and Fatemi 2000; Li et al. 2009]. From the multicycle tests they got the Ramberg–Osgood type relationship

$$\sigma_{Yc} = K'(\varepsilon^p)^{n'}, \quad (36)$$

Alloy steel	K'	n'	σ_{Yf}	$\sigma_{Yc}^{(0.2)}$	$\sigma_Y^{(0.2)}$	σ_{Yb}	ε_{Yb}
SAE 1141*	1127	0.124	433	591	814	925	0.88
SAE 1038	1009	0.208	248	364	410	649	1.10
SAE 1541	1622	0.194	228	424	475	783	0.80
SAE 1090	1310	0.174	350	545	735	1090	0.15
08 Si ₂ Mn	524	0.110	195	248	400	414	1.02
20 Si ₂ Mn	772	0.180	152	241	262	441	0.96
40 Si ₂ Mn	1434	0.140	403	600	883	931	1.02
60 Si ₂ Mn	1358	0.120	381	648	789	1000	0.41

* Aluminum fine grain

Table 1. Strength properties of some alloy steels. K' is the cyclic strength coefficient, n' the cyclic strain hardening exponent, σ_{Yf} the fatigue limit, $\sigma_{Yc}^{(0.2)}$ the cyclic yield strength (0.2%); $\sigma_Y^{(0.2)}$ the yield strength (0.2%), σ_{Yb} the ultimate yield strength, and ε_{Yb} the corresponding ultimate plastic strain. All strength parameters are given in MPa, except the dimensionless parameters n' and ε_{Yb} .

where σ_{Yc} is the cyclic yield stress amplitude, ε^p is the cyclic plastic deformation amplitude, K' is the cyclic strength coefficient, and n' is the cyclic strain hardening exponent. The most significant strength parameter might be the cyclic yield strength $\sigma_{Yc}^{(0.2)}$ corresponding to the amount 0.2% of plastic deformation, which we could adopt as the ultimate yield stress σ_Y^u for the incremental collapse mode

$$\sigma_{Yc}^{(0.2)} = K'(0.002)^{n'}. \quad (37)$$

It designates the critical point, beyond which the excessive global compatible plastic deformation increments of the structure are expected. Because the small plastic deformation assumption is kept, application of the classical plasticity theory and our path-independent shakedown theorems is legitimate.

The cyclic yield strength $\sigma_{Yc}^{(0.2)}$, cyclic strength coefficient K' , cyclic strain hardening exponent n' , as well as the fatigue limit σ_{Yf} , yield strength $\sigma_Y^{(0.2)}$, ultimate yield strength σ_{Yb} and corresponding ultimate plastic strain ε_{Yb} for a number of alloy steels are given in [Tucker et al. 1979; Roessle and Fatemi 2000; Li et al. 2009], some of which are presented in Table 1. All the strength parameters are given in MPa, except the dimensionless parameters n' and ε_{Yb} . Note that the ultimate yield strength σ_{Yb} generally is reached at the large amount of plastic deformation ε_{Yb} , and the cyclic yield strength $\sigma_{Yc}^{(0.2)}$ may be much different from the yield strength $\sigma_Y^{(0.2)}$.

As numerical illustrations of Equations (31)–(33) we choose SAE-1090 steel, $a = \frac{3}{4}$, $W = \frac{2}{3}$, and the following situations:

- The alternating plasticity collapse mode $A = 1$ with $\tau_Y^i = \frac{1}{2}\sigma_Y^i = \frac{1}{2}\sigma_{Yf} = 175$ MPa,
- The incremental collapse mode $I = 1$ with $\tau_Y^u = \frac{1}{2}\sigma_Y^u = \frac{1}{2}\sigma_{Yc}^{(0.2)} = 272.5$ MPa,
- The incremental collapse mode ($I =$) $I' = 1$ with $\tau_Y^u = \frac{1}{2}\sigma_Y^u = \frac{1}{2}\sigma_Y^{(0.2)} = 367.5$ MPa,
- The incremental collapse mode ($I =$) $I'' = 1$ with $\tau_Y^u = \frac{1}{2}\sigma_Y^u = \frac{1}{2}\sigma_{Yb} = 545$ MPa.

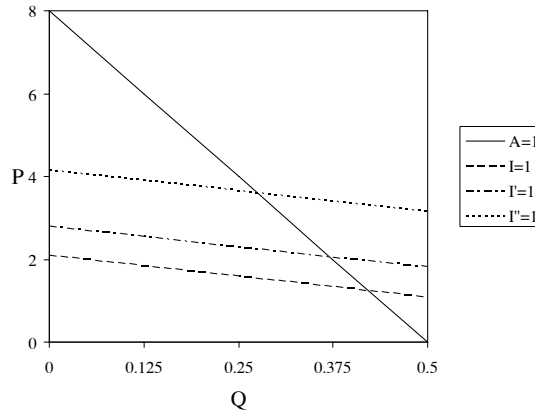


Figure 5. Alternating plasticity line $A = 1$; Incremental lines $I = 1$ ($\sigma_Y^u = \sigma_{Yc}^{(0.2)}$), $I' = 1$ ($\sigma_Y^u = \sigma_Y^{(0.2)}$), and $I'' = 1$ ($\sigma_Y^u = \sigma_{Yb}$) in the plane of external load's amplitude parameters.

The results of calculations are presented in the plane of dimensionless load amplitude parameters Q - P in Figure 5. The shakedown working domain is bounded above by the lower envelope of the ratcheting (incremental) and fatigue (alternating plasticity) lines. On the boundary of the domain, the collapse mode changes from the ratcheting one at small values of Q to the fatigue one at sufficiently high values of Q .

One should keep in mind that, in the light of shakedown analysis, the alternating plasticity (fatigue) mode is local, while the incremental (ratcheting) mode is global [Pham 2000].

4. Conclusion

Our shakedown theory has been applied to determine the working load limits for some typical elements of machines subjected to quasiperiodic dynamic loads. In the static limit, the results reduce to those plastic limit ones often used in design of the structures. It is clear that for dynamic loading, the load amplitude limits may decrease significantly, especially when the frequency of the acting load approaches the natural frequencies of a structure. The two distinct nonshakedown collapse modes: the incremental and alternating plasticity ones are separated.

In shakedown safety analysis for elastic plastic kinematic hardening materials, the only plastic parameters required are the initial and ultimate yield stresses. However for high-cycle loadings, which are usual for structures under working dynamic fluctuating loads, the initial and ultimate yield stresses should not be taken as the convenient and usual ones from monotonic loading experiments, but may be much lower and are to be taken from the fatigue and ratcheting curves experimentally constructed for the materials under high-cycle loadings (up to 10^6 – 10^7 cycles). Application of shakedown theorems should be kept within the framework of the small plastic deformation assumption. Here, in particular, we take the fatigue limit as the initial yield stress, and the cyclic yield strength (corresponding to 0.2% of plastic deformation) as the ultimate yield stress for the shakedown safety assessment of the structures subjected to dynamic high-cycle loading.

Though used here to analyze only simple shaft and spring structures as illustrations, our approach involving two nonshakedown modes (and the corresponding recommendations) applies to general elastic

plastic kinematic hardening structures. The approach is supported by the shakedown theorems in [Pham 2007; 2008].

References

- [Akiniwa et al. 2008] Y. Akiniwa, S. Stanzl-Tschegg, H. Mayer, M. Wakita, and K. Tanaka, “Fatigue strength of spring steel under axial and torsional loading in the very high cycle regime”, *Int. J. Fatigue* **30**:12 (2008), 2057–2063.
- [Armstrong and Frederick 1966] P. J. Armstrong and C. O. Frederick, “A mathematical representation of the multiaxial Bauschinger effect”, CEBG Report RD/B/N731, Berkeley Nuclear Laboratories, Berkeley, Gloucestershire, 1966.
- [Beer and Johnston 1992] F. P. Beer and E. R. Johnston, Jr., *Mechanics of materials*, 2nd ed., McGraw-Hill, New York, 1992.
- [Bree 1989] J. Bree, “Plastic deformation of a closed tube due to interaction of pressure stresses and cyclic thermal stresses”, *Int. J. Mech. Sci.* **31**:11-12 (1989), 865–892.
- [Chaboche 2008] J. L. Chaboche, “A review of some plasticity and viscoplasticity constitutive theories”, *Int. J. Plast.* **24**:10 (2008), 1642–1693.
- [Corigliano et al. 1995] A. Corigliano, G. Maier, and S. Pycko, “Dynamic shakedown analysis and bounds for elastic-plastic structures with nonassociative, internal variable constitutive laws”, *Int. J. Solids Struct.* **32**:21 (1995), 3145–3166.
- [Gavarini 1969] C. Gavarini, “Sul rientro in fase elastica delle vibrazioni forzate elasto-plastiche”, *G. Genio Civ.* **107**:4–5 (1969), 251–261.
- [Gokhfeld and Cherniavski 1980] D. A. Gokhfeld and O. F. Cherniavski, *Limit analysis of structures at thermal cycling*, Sijthoff and Noordhoff, Alphen aan den Rijn, 1980.
- [Halphen and Nguyen 1975] B. Halphen and Q. S. Nguyen, “Sur les matériaux standards généralisés”, *J. Méc.* **14**:1 (1975), 39–63.
- [Koiter 1963] W. T. Koiter, “General theorems for elastic-plastic solids”, pp. 165–221 in *Progress in solids mechanics*, edited by I. N. Sneddon and R. Hill, North Holland, Amsterdam, 1963.
- [König 1987] A. König, *Shakedown of elastic-plastic structures*, Elsevier, Amsterdam, 1987.
- [Li et al. 2009] J. Li, Q. Sun, Z. Zhang, C. Li, and Y. Qiao, “Theoretical estimation to the cyclic yield strength and fatigue limit for alloy steels”, *Mech. Res. Commun.* **36**:3 (2009), 316–321.
- [Lubliner 1990] J. Lubliner, *Plasticity theory*, McMillan, New York, 1990.
- [Mandel 1976] J. Mandel, “Adaptation d’une structure plastique écrouissable et approximations”, *Mech. Res. Commun.* **3**:6 (1976), 483–488.
- [Nguyen 2003] Q.-S. Nguyen, “On shakedown analysis in hardening plasticity”, *J. Mech. Phys. Solids* **51**:1 (2003), 101–125.
- [Ohno and Wang 1993] N. Ohno and J.-D. Wang, “Kinematic hardening rules with critical state of dynamic recovery, I: Formulation and basic features for ratchetting behavior”, *Int. J. Plast.* **9**:3 (1993), 375–390.
- [Okopny et al. 2001] Y. A. Okopny, V. P. Radin, and V. P. Chirkov, *Механика материалов и конструкций*, Mashinostroenie, Moscow, 2001.
- [Parmley 2000] R. O. Parmley (editor), *Illustrated sourcebook of mechanical components*, McGraw-Hill, New York, 2000.
- [Pham 1992] Pham D. C., “Extended shakedown theorems for elastic plastic bodies under quasi-periodic dynamic loading”, *Proc. R. Soc. Lond. A* **439**:1907 (1992), 649–658.
- [Pham 2000] Pham D. C., “From local failure toward global collapse of elastic plastic structures in fluctuating fields”, *Int. J. Mech. Sci.* **42** (2000), 819–829.
- [Pham 2003] Pham D. C., “Shakedown theory for elastic-perfectly plastic bodies revisited”, *Int. J. Mech. Sci.* **45**:6–7 (2003), 1011–1027.
- [Pham 2005] Pham D. C., “Shakedown static and kinematic theorems for elastic-plastic limited linear kinematic-hardening solids”, *Eur. J. Mech. A Solids* **24**:1 (2005), 35–45.
- [Pham 2007] Pham D. C., “Shakedown theory for elastic plastic kinematic hardening bodies”, *Int. J. Plast.* **23**:7 (2007), 1240–1259.

- [Pham 2008] Pham D. C., “On shakedown theory for elastic-plastic materials and extensions”, *J. Mech. Phys. Solids* **56**:5 (2008), 1905–1915.
- [Pham and Stumpf 1994] D. C. Pham and H. Stumpf, “Kinematical approach to shakedown analysis of some structures”, *Quart. Appl. Math.* **52**:4 (1994), 707–719.
- [Pham and Weichert 2001] D. C. Pham and D. Weichert, “Shakedown analysis for elastic-plastic bodies with limited kinematic hardening”, *Proc. R. Soc. Lond. A* **457**:2009 (2001), 1097–1110.
- [Polizzotto et al. 1991] C. Polizzotto, G. Borino, S. Caddemi, and P. Fuschi, “Shakedown problems for mechanical models with internal variables”, *Eur. J. Mech. A Solids* **10**:6 (1991), 621–639.
- [Prager 1949] W. Prager, “Recent developments in the mathematical theory of plasticity”, *J. Appl. Phys.* **20**:3 (1949), 235–241.
- [Roessle and Fatemi 2000] M. L. Roessle and A. Fatemi, “Strain-controlled fatigue properties of steels and some simple approximations”, *Int. J. Fatigue* **22**:6 (2000), 495–511.
- [Stein et al. 1992] E. Stein, G. Zhang, and J. A. König, “Shakedown with nonlinear strain-hardening including structural computation using finite element method”, *Int. J. Plast.* **8**:1 (1992), 1–31.
- [Tucker et al. 1979] L. E. Tucker, R. W. Landgraf, and W. R. Brose, “Technical report on fatigue properties”, Technical report SAE J1099, Society of Automotive Engineers, 1979.
- [Weichert and Gross-Weege 1988] D. Weichert and J. Gross-Weege, “The numerical assessment of elastic-plastic sheets under variable mechanical and thermal loads using a simplified two-surface yield condition”, *Int. J. Mech. Sci.* **30**:10 (1988), 757–767.
- [Weichert and Maier 2002] D. Weichert and G. Maier (editors), *Inelastic behaviour of structures under variable repeated loads: direct analysis methods*, CISM Courses and Lectures **432**, Springer, Vienna, 2002.

Received 12 Jul 2009. Revised 17 Oct 2009. Accepted 30 Oct 2009.

PHAM DUC CHINH: pdchinh@imech.ac.vn

Vietnamese Academy of Science and Technology, Institute of Mechanics, Vien Co Hoc, 264 Doi Can, Ba Dinh, Hanoi, Vietnam

WAVE PROPAGATION IN CARBON NANOTUBES: NONLOCAL ELASTICITY-INDUCED STIFFNESS AND VELOCITY ENHANCEMENT EFFECTS

C. W. LIM AND Y. YANG

We establish the physics and understanding of nonlocal nanoscale wave propagation in carbon nanotubes (CNTs) based on nonlocal elastic stress field theory. This is done by developing an analytical nonlocal nanotube model based on the variational principle for wave propagation in CNTs. Specifically, we successfully derive benchmark governing equations of motion for analyzing wave propagation based on an analytical nonlocal shear deformable model. The physical insights of the analytical nonlocal stress model are presented through examples. Analytical solutions with significant observation of wave propagation have been predicted and the prediction compares favorably with molecular dynamic simulations. Qualitative comparisons with other non-nonlocal approaches, including the strain gradients model, the couple stress model and experiments, justify the stiffness enhancement conclusion as predicted by the new nonlocal stress model. New dispersion and spectrum relations derived using this analytical nonlocal model bring an important focus onto the critical wavenumber: stiffness of CNTs and wave propagation are enhanced below the critical wavenumber, while beyond that a sharp decrease in wave propagation is observed. The physics of nanoscale wave propagation in nanotubes are further illustrated by relating the nanoscale and the phase velocity ratio.

1. Introduction

The discovery of carbon nanotubes (CNTs) in the early 1990s [Iijima 1991] created enormous interest among physicists, chemists and engineers, thanks to their unusual mechanical, electrical, electronic, chemical and thermal conductivity properties [Iijima 1991; Treacy et al. 1996; Ajayan and Zhou 2001; Ball 2001; Baughman et al. 2002].

There are many cross disciplinary research works in analytical and computational approaches for CNTs which consider their physical, electrical, chemical and engineering characteristics. There have been comparatively fewer experimental studies on CNTs because at such length scale it is extremely difficult to control, operate precisely and test the specimen. Furthermore, many experimental reports disagree considerably in the measurement of various properties under slightly different test environment. To complement such shortages, a number of continuum and discrete models for CNTs have been proposed.

Molecular dynamic (MD) simulation is the most common computational approach for analyzing CNTs. Using this method, every molecule is single-walled or double-walled CNTs is modeled as a discrete point mass the web of thousands or millions of point masses are constituted in a structured configuration

Keywords: critical wavenumber, nanotube, nonlocal elasticity, wave propagation.

Work supported by a grant from Research Grants Council of the Hong Kong Special Administrative Region, Project Ref. CityU 117406.

through intermolecular bonds and forces [Brenner et al. 2002; Liew et al. 2004a; Liew et al. 2004b; Liew et al. 2005; Kitipornchai et al. 2005]. Although MD has been successful to a certain extent and in a number of cases of study, it is bounded by computational, memory and other hardware constraints. This approach has been restrictive in many cases when very many molecules are required in a nanostructural model. Any premature breakdown of computation due to either algorithmic flaw itself or external power interruption may require the jobs to be restarted or repeated. Hence, the MD analysis has been common for moderate configurations of CNTs and restrictive for complicated CNTs.

To complement MD simulations, continuum elastic models of CNTs have been developed and applied in a number of studies since the middle of 1990s. The early models involve the classical beam, tube or shell models coupled with appropriate molecular potentials to study the mechanical characteristics such as static bending and buckling [Yakobson et al. 1996; Ru 2000a; Ru 2000b; Parnes and Chiskis 2002; Han et al. 2005] and dynamic vibration and wave propagation [Zhang et al. 2005; Yoon et al. 2005; Natsuki et al. 2005; Wang et al. 2006a; Wang and Varadan 2006] of CNTs. The study of wave propagation in CNTs has attracted intensive attention in research because many crucial physical properties such as electrical conductance, optical transition and some dynamic behavior of CNTs are very sensitive to the presence of wave [Zhang et al. 2005]. Among the early studies, the continuum shell model was developed by Natsuki [Natsuki et al. 2005] to predict wave propagation in single-walled CNT embedded in an elastic medium. [Wang and Varadan 2006] applied the elastic beam theory to study the wave characteristics of single-walled and double-walled CNTs base on both thin and thick beam models.

Another continuum model applicable to the analysis of CNTs is the nonlocal elasticity stress field theory which was first proposed in [Eringen and Edelen 1972; Eringen 1972a; 1972b; 1983; 2002]. According to this theory, the stress at a point within a continuous domain with nanoscale effects is dependent not only on the strain at that point but it is also significantly influenced by the stress of all points in the domain through a nonlocal modulus in an integral sense. With such consideration, the nonlocal forces at long-range between molecules and lattice lead to the nonlocal stress-strain equation with higher-order strain gradients. Because of its simplicity and superiority, the analysis of wave propagation in CNTs using the nonlocal stress approach was recently reported [Wang and Hu 2005; Wang 2005; Wang et al. 2006c; Lu et al. 2007; Heireche et al. 2008; Liew et al. 2008]. In particular, [Lu et al. 2007] derived the equation of motion for a nonlocal Timoshenko beam to investigate the wave propagation characteristics in single-walled and double-walled CNTs. Other nonlocal shell models were also employed for further research in a number of studies [Wang 2006; Wang et al. 2006b; Wang and Varadan 2007; Xie et al. 2007a; Xie et al. 2007b; Wang et al. 2008; Hu et al. 2008].

Virtually all published works [Wang and Hu 2005; Wang 2005; Wang et al. 2006c; Lu et al. 2007; Heireche et al. 2008; Liew et al. 2008; Wang 2006; Wang et al. 2006b; Wang and Varadan 2007; Xie et al. 2007a; Xie et al. 2007b; Wang et al. 2008; Hu et al. 2008] in wave propagation using the nonlocal stress approach regarded the nanoscale to only affect the constitutive relation for nonlocal stress and strain. Without rigorous validation, the classical equilibrium equations or equations of motion for beam and shell models were adopted completely for all nonlocal static and dynamic problems. Such directly extended nonlocal models, termed the partial nonlocal stress models, results in two fundamental suspicions that: (a) in many cases of study the nanoscale effect is surprisingly missing in the ultimate analytical solution, for instance the bending of a cantilever nanotube with point force at its end; and (b) the no-existence of any higher-order boundary conditions associated with the higher-order differential equation of motion

[Lim 2008; 2009; 2010]. The second statement above simply implies that the partial nonlocal stress models derives a higher-order equation of motion but, unfortunately, without the corresponding higher-order boundary conditions which is obviously inconsistent. In [Lim 2008; 2009; 2010] we successfully established a new analytical nonlocal stress model and proved that stiffness of a nanobeam is strengthened with the presence of a nonlocal nanoscale. By deriving the exact nonlocal strain energy density, higher-order governing differential equation with the corresponding higher-order boundary conditions was derived via the variational principle. New predictions for bending of nanobeams were presented and discussed.

Applying the identical nonlocal stress model but without making any assumptions on the static and dynamic conditions a priori, a new higher-order dynamics differential equation of motion are derived via exact variational principle here. Consistent higher-order boundary conditions and insightful predictions using this new model are presented. Implications of the defective formulation and intriguing conclusions in wave propagation in CNTs using the partial nonlocal stress models are also discussed in detail. The CNTs considered here are shear deformable using the thick-walled tube model in order to better reflect the nature of CNTs. Benchmarked analytical dispersion relations are derived and the contribution of nonlocal nanoscale in the governing equation of motion is highlighted. Qualitative comparisons [Nix and Gao 1998; Lam et al. 2003; Park and Hao 2006; 2008; Ma et al. 2008; Li and Chou 2004; Was and Foecke 1996; McFarland and Colton 2005] with other non-nonlocal approaches towards the end of the paper including molecular dynamics simulation, strain gradients model, couple stress model and experiments justify that the stiffness enhancement conclusion as predicted by the new nonlocal stress model.

2. Nonlocal elasticity stress field theory and nonlocal stress models

Basic nonlocal constitutive equations and nonlocal stress. The nonlocal elastic stress field theory first proposed by Eringen concerns the state of stress at a reference point \mathbf{r}' within a domain. The nonlocal stress depends not only on the strain at that location but also on the strains at all other points within the domain in a diminishing influence away from the central location. This phenomenon was first observed in atomic theory of lattice dynamics and also from experiment observation on phonon dispersion. In the absence of the nonlocal effects of strains at points $\mathbf{r} \neq \mathbf{r}'$, the nonlocal field theory reverts to the local or classical elasticity theory [Eringen 1983; 2002]. For homogeneous and isotropic solids with nonlocal effects, the nonlocal elastic field theory is governed by

$$\sigma_{ij,i} + \rho(f_j - \ddot{u}_j) = 0, \quad \sigma_{ij}(\mathbf{r}) = \int_V \alpha(|\mathbf{r}' - \mathbf{r}|, \tau) \sigma'_{ij}(\mathbf{r}') dV(\mathbf{r}'), \quad (1)$$

$$\sigma'_{ij}(\mathbf{r}') = \lambda e_{kk}(\mathbf{r}') \delta_{ij} + 2\mu e_{ij}(\mathbf{r}'), \quad e_{ij}(\mathbf{r}') = \frac{1}{2} \left(\frac{\partial u_j(\mathbf{r}')}{\partial r'_i} + \frac{\partial u_i(\mathbf{r}')}{\partial r'_j} \right), \quad (2)$$

where $\sigma_{ij}(\mathbf{r})$ is the nonlocal stress tensor, ρ the mass density, f_j the body force density, and u_j the displacement vector at a reference point \mathbf{r} in the body, at time t , while \ddot{u}_j , the second derivative of u_j with respect to time t , is the acceleration vector at \mathbf{r} . The indices i, j run over the sets $\{1\}$, $\{1, 2\}$ or $\{1, 2, 3\}$ depending on the dimension.

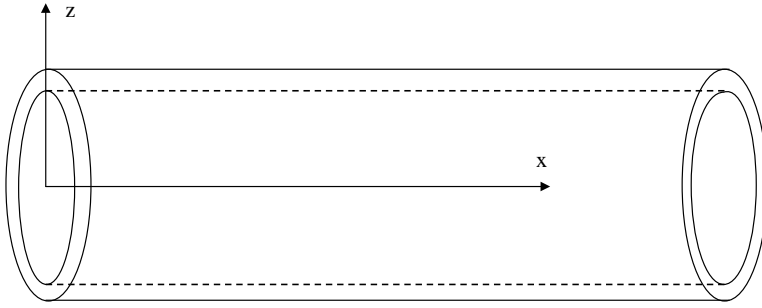


Figure 1. Cylindrical nanotube and coordinate system.

Equation (2)₁ shows the classical constitutive relation of Hooke's law where the classical or local stress tensor at \mathbf{r}' , denoted as $\sigma'_{ij}(\mathbf{r}')$, is related to the linear strain tensor $e_{ij}(\mathbf{r}')$ at any point \mathbf{r}' in the body at time t , with λ and μ being Lamé constants, and δ_{ij} being Kronecker delta. It is clear that the classical or local constitutive relation (2)₁ has to be replaced by the nonlocal constitutive relation (1)₂, according to which $\sigma_{ij}(\mathbf{r})$ at \mathbf{r} depends not only on the classical local stress $\sigma'_{ij}(\mathbf{r}')$ at that particular point but also on a nonlocal modulus $\alpha(|\mathbf{r}' - \mathbf{r}|, \tau)$, where $|\mathbf{r}' - \mathbf{r}|$ is the Euclidean distance between \mathbf{r}' and \mathbf{r} and τ is a dimensionless length scale defined by

$$\tau = \frac{e_0 a}{L}, \quad (3)$$

a being the internal characteristic length such that the lattice parameter, C-C bond length, or granular distance, L an external characteristic length such as the crack length or wavelength, and e_0 is a material constant obtainable experimentally or through other molecular or continuum models.

Due to the difficulty in deriving an analytical solution, it is possible in an approximate sense to convert the integrodifferential equation (1)₂ to a general partial differential equation [Eringen 1983; 2002]. Furthermore, when only the uniaxial stress and strain are considered for a nanotube, the classical Hooke's law for uniaxial stress in one dimension is replaced by a nonlocal stress relation (loc. cit.) as

$$\sigma(x) - (e_0 a)^2 \frac{d^2 \sigma(x)}{dx^2} = E \varepsilon(x), \quad (4)$$

where E is the Young's modulus and $\sigma(x)$ and $\varepsilon(x)$ are the normal stress and strain in the axial direction of the nonlocal nanotube. For limiting nanoscale $e_0 a \rightarrow 0$, the nonlocal effect can be neglected and the nonlocal stress σ approaches that of the corresponding classical stress $\sigma' = E \varepsilon(x)$. It is noted that (4) is a one-dimensional ordinary differential equation.

Figure 1 shows the shear deformable nanotube in Cartesian coordinate while x and z are the axial and transverse coordinates respectively. According to the classical elastic theory for a long tube, the bending moment M_{xx} in the transverse direction and strain are denoted by

$$M_{xx} = \int z \sigma \, dA, \quad \varepsilon = -z \frac{d\varphi}{dx}, \quad (5)$$

where z is the normal coordinate measured from the midplane, $\varphi(x, t)$ is the rotation angle of cross section at point x and time t , and A is the cross sectional area. Multiplying (4) by z , integrating over the

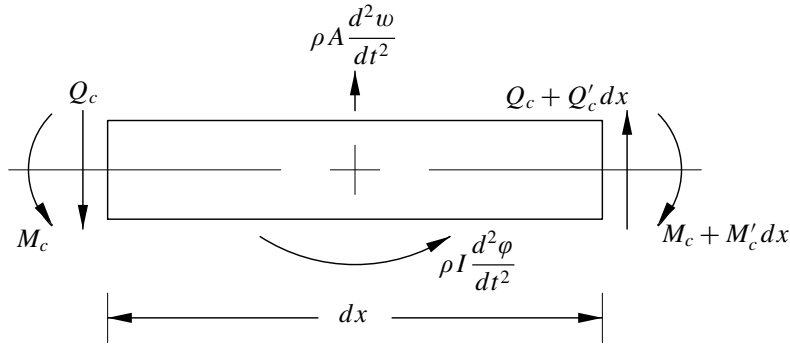


Figure 2. Geometry of a nanobeam, coordinate system and sign convention.

cross section and substituting Equations (5) yield the nonlocal bending moment relation as

$$M_{xx} - (e_0 a)^2 \frac{\partial^2 M_{xx}}{\partial x^2} = -EI \frac{\partial \phi}{\partial x} \quad (6)$$

while $I = \int z^2 dA$ is the second moment of area over the cross section.

For simplicity and standardization, the following dimensionless terms

$$\bar{x} = \frac{x}{L}, \quad \bar{z} = \frac{z}{L} \quad (7)$$

are introduced, where L can be taken as the length of the nanotube. The dimensionless solutions of (4) and (6) can be expressed as [Lim 2009; 2010]

$$\bar{\sigma}_{xx} = \sum_{n=1}^{\infty} \tau^{2(n-1)} \varepsilon_{xx}^{(2(n-1))} = -\bar{z} \sum_{n=1}^{\infty} \tau^{2(n-1)} \phi^{(2n-1)}, \quad \bar{M}_{xx} = -\sum_{n=1}^{\infty} \tau^{2(n-1)} \phi^{(2n-1)}, \quad (8)$$

where $\bar{\sigma}_{xx} = \sigma_{xx}/E$, $\bar{M}_{xx} = M_{xx}L/EI$ and $\langle \rangle$ denotes partial differentiation with respect to \bar{x} . Therefore, the exact solution for the nonlocal constitutive equation of nanotube described above are expressed in infinite series in terms of strain gradients for nonlocal stress and displacement gradients for nonlocal moment in (8).

Dynamic equations of motion. For a thick nanotube represented by the classical shear deformable model, the effect of shear and rotation on the nanotube cross section is significant and they should be considered. The classical dynamic governing equations of motion for transverse motion and rotational motion are respectively [Hagedorn and Dasgupta 2007]

$$\frac{dQ_c}{dx} = \rho A \frac{d^2 w}{dt^2}, \quad \frac{dM_c}{dx} - Q_c = -\rho I \frac{d^2 \phi}{dt^2}, \quad (9)$$

where subscript 'c' represents classical terms, ρ , Q_c , M_c , $w(x, t)$ are the mass density, shear force on the nanotube cross section, bending moment and deflection of the nanotube in the z -direction as shown in Figure 2.

The classical dimensionless expressions of (9) are

$$\frac{EI}{L^3} \frac{d\bar{Q}_c}{d\bar{x}} = \frac{\rho AL}{T^2} \frac{d^2\bar{w}}{d\bar{t}^2}, \quad \bar{Q}_c - \frac{d\bar{M}_c}{d\bar{x}} = \frac{\rho L^2}{ET^2} \frac{d^2\varphi}{d\bar{t}^2}, \quad (10)$$

where T is the period of vibration, $\bar{t} = t/T$ is dimensionless time, $\bar{M}_c = M_c L/EI$ is the dimensionless classical bending moment and $\bar{Q}_c = Q_c L^2/EI$ is the dimensionless classical shear force on the cross section. In the presence of a nonlocal elastic stress field, it has been a common practice to directly replace the classical \bar{M}_c in the equation of motion above and in Figure 1 with the nonlocal moment \bar{M}_{xx} defined in (8) [Wang and Hu 2005; Wang 2005; Wang et al. 2006c; Lu et al. 2007; Heireche et al. 2008; Liew et al. 2008; Wang 2006; Wang et al. 2006b; Wang and Varadan 2007; Xie et al. 2007a; Xie et al. 2007b; Wang et al. 2008; Hu et al. 2008; Lim and Wang 2007]. Such models are termed the partial nonlocal models. For bending of a nanotube, it has been shown through a rigorous derivation via the variational principle that such direct replacement in the partial nonlocal derivation is not only unjustified but also results in intriguing solutions with respect to physical intuition, modeling and numerical simulation using other non-nonlocal approaches such as strain gradient, coupled stress, molecular dynamic simulation, etc., as well as experiments considering nanoscale effects. It will be verified herein that this statement can also be extended to wave propagation in shear deformable carbon nanotubes.

Unlike virtually all previous analyses using nonlocal stress modeling, a true nonlocal nanotube requires that the equilibrium conditions and dynamic equations of motion should be consistently derived through consideration of a nonlocal stress field. For a thick nanotube, the correct governing equations can be derived from the virtual work variational principle by considering strain energy and kinetic energy. The strain energy density of a nanotube consists of two parts: the normal deformation strain energy density [Lim 2009; 2010]

$$u_n = u_1 + u_2 + u_3, \quad (11)$$

where

$$u_1 = \frac{1}{2} E \varepsilon_{xx}^2, \quad u_2 = \frac{1}{2} E \sum_{n=1}^{\infty} (-1)^{n+1} \tau^{2n} (\varepsilon_{xx}^{(n)})^2, \quad u_3 = E \sum_{n=1}^{\infty} \left(\tau^{2(n+1)} \sum_{m=1}^n (-1)^{m+1} \varepsilon_{xx}^{(m)} \varepsilon_{xx}^{(2(n+1)-m)} \right), \quad (12)$$

and the shear deformation strain energy on the nanotube cross section

$$u_s = \frac{1}{2} G \gamma_{xz}^2, \quad (13)$$

where G is the shear modulus and γ_{xz} is the shear strain when $\gamma_{xz} = \partial\bar{w}/\partial\bar{x} - \varphi$. Details of the derivation of u_n are given in the Appendix. The total strain energy of the deformed nanotube with volume V is

$$U = \int_v (u_n + u_s) dV. \quad (14)$$

The kinetic energy K of a nanotube is

$$K = \frac{\rho}{2} \int_0^L \left(A \left(\frac{dw}{dt} \right)^2 + I \left(\frac{d\varphi}{dt} \right)^2 \right) dx = \frac{\rho AL^3}{2T^2} \int_0^1 \left(\left(\frac{d\bar{w}}{d\bar{t}} \right)^2 + \frac{I}{AL^2} \left(\frac{d\varphi}{d\bar{t}} \right)^2 \right) d\bar{x}. \quad (15)$$

The first term in the integral contributes to the translational kinetic energy while the second term contributes to the rotational kinetic energy. Define the total energy functional F as

$$F = U - K. \quad (16)$$

Substituting Equations (11)–(15) into (16) yields the variation of the energy functional F as

$$\begin{aligned} \delta F &= \delta(U - K) \\ &= \delta \int_0^1 \int_V \left(\frac{1}{2} E \varepsilon_x^2 + \frac{1}{2} E \sum_{n=1}^{\infty} (-1)^{n+1} \tau^{2n} (\varepsilon_x^{(n)})^2 \right. \\ &\quad \left. + E \sum_{n=1}^{\infty} \left(\tau^{2(n+1)} \sum_{m=1}^n (-1)^{m+1} \varepsilon_x^{(m)} \varepsilon_x^{(2(n+1)-m)} \right) + \frac{1}{2} G \gamma_{xz}^2 \right) dV d\bar{t} \\ &\quad - \delta \frac{\rho AL^3}{2T^2} \int_0^1 \int_0^1 \left(\left(\frac{\partial \bar{w}}{\partial \bar{t}} \right)^2 + \frac{I}{AL^2} \left(\frac{\partial \varphi}{\partial \bar{t}} \right)^2 \right) d\bar{x} d\bar{t} \\ &= \delta \int_0^1 \int_V \left(-\frac{1}{2} E z \left(\frac{\partial \varphi}{\partial \bar{x}} \right)^2 - \frac{1}{2} E z \sum_{n=1}^{\infty} (-1)^{n+1} \tau^{2n} (\varphi^{(n+1)})^2 \right. \\ &\quad \left. + E z^2 \sum_{n=1}^{\infty} \left(\tau^{2(n+1)} \sum_{m=1}^n (-1)^{m+1} \varphi^{(m+1)} \varphi^{(2n-m+1)} \right) + \frac{1}{2} G \left(\frac{\partial \bar{w}}{\partial \bar{x}} - \varphi \right)^2 \right) dV d\bar{t} \\ &\quad - \delta \frac{\rho AL^3}{2T^2} \int_0^1 \int_0^1 \left(\left(\frac{\partial \bar{w}}{\partial \bar{t}} \right)^2 + \frac{I}{AL^2} \left(\frac{\partial \varphi}{\partial \bar{t}} \right)^2 \right) d\bar{x} d\bar{t} \\ &= \int_0^1 \int_V \left(-E z \varphi^{(1)} \delta \varphi^{(1)} - E z \sum_{n=1}^{\infty} (-1)^{n+1} \tau^{2n} \varphi^{(n+1)} \delta \varphi^{(n+1)} \right. \\ &\quad \left. + E z^2 \sum_{n=1}^{\infty} \left(\tau^{2(n+1)} \sum_{m=1}^n (-1)^{m+1} (\delta \varphi^{(m+1)} \varphi^{(2n-m+1)} + \varphi^{(m+1)} \delta \varphi^{(2n-m+1)}) \right) \right. \\ &\quad \left. + \frac{1}{2} G (2\bar{w}^{(1)} \delta \bar{w}^{(1)} - 2\bar{w}^{(1)} \delta \varphi - 2\varphi \delta \bar{w}^{(1)} + 2\varphi \delta \varphi) \right) dV d\bar{t} \\ &\quad - \frac{\rho AL^3}{2T^2} \int_0^1 \int_0^1 \left(2\ddot{\bar{w}} \delta \ddot{\bar{w}} + \frac{2I}{AL^2} \ddot{\varphi} \delta \ddot{\varphi} \right) d\bar{x} d\bar{t}. \quad (17) \end{aligned}$$

Integrating (17) by parts for each term in the integrand, we obtain

$$\begin{aligned} \delta F &= \frac{EI}{L} \int_0^1 \int_0^1 \left(\frac{AG\kappa L^2}{EI} \left(\frac{\partial \bar{w}}{\partial \bar{x}} - \varphi \right) - \sum_{n=1}^{\infty} (2n-3) \tau^{2(n-1)} \varphi^{(2n)} - \frac{\rho L^2}{ET^2} \frac{\partial^2 \varphi}{\partial \bar{t}^2} \right) \delta \varphi d\bar{x} d\bar{t} \\ &\quad + \int_0^1 \int_0^1 \left(AG\kappa L \left(\frac{\partial^2 \bar{w}}{\partial \bar{x}^2} - \frac{\partial \varphi}{\partial \bar{x}} \right) - \frac{\rho AL^3}{T^2} \frac{\partial^2 \bar{w}}{\partial \bar{t}^2} \right) \delta \bar{w} d\bar{x} d\bar{t} \\ &\quad + \frac{EI}{L} [\varphi \delta \varphi]_0^1 + \frac{EI}{L} \sum_{n=1}^{\infty} \left((-1)^{n+1} \tau^{2n} \sum_{m=0}^{n+1} \varphi^{(n+1+m)} \delta \varphi^{(n-m)} \Big|_0^1 \right) \\ &\quad + \frac{EI}{L} \sum_{n=1}^{\infty} \tau^{2(n+1)} \sum_{m=1}^n \left(\sum_{i=0}^{2n+1-m} (-1)^{m+i+1} \varphi^{(2+m+i)} \delta \varphi^{(2n+1-m-i)} \Big|_0^1 \right. \\ &\quad \left. + \sum_{i=0}^{m-1} (-1)^{m+i+1} \varphi^{(2n+2-m+i)} \delta \varphi^{(1+m-i)} \Big|_0^1 \right), \quad (18) \end{aligned}$$

Using the definition of nonlocal bending moment in (8)₂, the variation of the energy functional in (18) can be rewritten as

$$\begin{aligned} \delta F = & \int_0^1 \int_0^1 \left(\frac{EI}{L} \left(\bar{Q} - \bar{M}_{xx}^{(1)} + 2 \sum_{n=1}^{\infty} \tau^{2n} \bar{M}_{xx}^{(2n+1)} - \frac{\rho L^2}{ET^2} \frac{\partial^2 \varphi}{\partial \bar{t}^2} \right) \delta \varphi + \left(\frac{EI}{L} \frac{\partial \bar{Q}}{\partial \bar{x}} - \frac{\rho AL^3}{T^2} \frac{\partial^2 \bar{w}}{\partial \bar{t}^2} \right) \delta \bar{w} \right) d\bar{x} d\bar{t} \\ & + \frac{EI}{L} \left[\left(\bar{Q} - \bar{M}_{xx}^{(1)} - 2 \sum_{n=1}^{\infty} \tau^{2n} \bar{M}_{xx}^{(2n+1)} \right) \delta \varphi + \left(-\bar{M}_{xx} + 2 \sum_{n=1}^{\infty} \tau^{2n} \bar{M}_{xx}^{(2n)} \right) \delta \varphi^{(1)} \right. \\ & - \left(\tau^2 \bar{M}_{xx}^{(1)} + 2 \sum_{n=1}^{\infty} \tau^{2(n+1)} \bar{M}_{xx}^{(2n+1)} \right) \delta \varphi^{(2)} + \left(2\tau^4 \sum_{n=1}^{\infty} \tau^{2(n-1)} \bar{M}_{xx}^{(2n)} \right) \delta \varphi^{(3)} \\ & \left. - \left(\tau^4 \bar{M}_{xx}^{(1)} + 2 \sum_{n=1}^{\infty} \tau^{2(n+2)} \bar{M}_{xx}^{(2n+1)} \right) \delta \varphi^{(4)} + \left(\tau^6 \bar{M}_{xx}^{(2)} + 2 \sum_{n=1}^{\infty} \tau^{2(n+3)} \bar{M}_{xx}^{(2(n+1))} \right) \delta \varphi^{(5)} \dots \right]_0^1, \quad (19) \end{aligned}$$

where

$$\bar{Q} = \frac{AG\kappa L^2}{EI} \left(\frac{\partial \bar{w}}{\partial \bar{x}} - \varphi \right) \quad (20)$$

is the dimensionless form of the shear force $Q = \int_A G\gamma_{xz} dA = AG\kappa(\partial w/\partial x - \varphi)$ on the cross section of the nanotube [Hagedorn and Dasgupta 2007], and κ is the shear correction factor due to shear deformation in nanotube.

The variational principle requires the variation of energy function to be zero at an extremum:

$$\delta F = \delta(U - K) = 0. \quad (21)$$

Because \bar{w} , φ , $\varphi^{(1)}$, $\varphi^{(2)}$, $\varphi^{(3)}$, ... are arbitrary functions whose variations do not vanish, the variational principle requires that their multipliers be zero. From the first two terms in the integrand in (19), the governing equations of motion for a shear deformable nanotube are

$$\frac{EI}{L} \frac{\partial \bar{Q}}{\partial \bar{x}} = \frac{\rho AL^3}{T^2} \frac{\partial^2 \bar{w}}{\partial \bar{t}^2}, \quad \bar{Q} - \frac{\partial \bar{M}_{xx}}{\partial \bar{x}} + 2 \sum_{n=1}^{\infty} (\tau)^{2n} \frac{\partial^{(2n+1)} \bar{M}_{xx}}{\partial \bar{x}^{(2n+1)}} = \frac{\rho L^2}{ET^2} \frac{\partial^2 \varphi}{\partial \bar{t}^2} \quad (22)$$

the second of which can be rewritten as

$$\bar{Q} - \frac{\partial \bar{M}_{ef}}{\partial \bar{x}} = \frac{\rho L^2}{ET^2} \frac{\partial^2 \varphi}{\partial \bar{t}^2}, \quad (23)$$

where

$$\bar{M}_{ef} = \bar{M}_{xx} - 2 \sum_{n=1}^{\infty} \tau^{2n} \bar{M}_{xx}^{(2n)} = \sum_{n=1}^{\infty} (2n - 3) \tau^{2(n-1)} \varphi^{(2n-1)} \quad (24)$$

is defined as the effective dimensionless nonlocal moment \bar{M}_{ef} . The remaining terms in (19) constitute the higher-order boundary conditions which have been unavailable in all other research papers of nonlocal wave propagation [Wang and Hu 2005; Wang 2005; 2006; Wang et al. 2006b; 2006c; 2008; Lu et al. 2007; Heireche et al. 2008; Liew et al. 2008; Wang and Varadan 2007; Xie et al. 2007a; 2007b; Hu et al. 2008]. These equations of motion and the corresponding higher-order boundary conditions are new and their physical interpretation and consequence will be discussed at length in due course.

Equations (22) and (23) represent the transverse equation of motion and rotational equation of motion, respectively, and they are expressed in terms of nonlocal stress resultants. These two equations can also be expressed in terms of dimensionless deflection \bar{w} and angle of rotation φ as

$$G\kappa L \left(\frac{\partial^2 \bar{w}}{\partial \bar{x}^2} - \frac{\partial \varphi}{\partial \bar{x}} \right) - \frac{\rho L^3}{T^2} \frac{\partial^2 \bar{w}}{\partial \bar{t}^2} = 0, \quad (25)$$

$$\frac{AG\kappa L^2}{EI} \left(\frac{\partial \bar{w}}{\partial \bar{x}} - \varphi \right) - \sum_{n=1}^{\infty} (2n-3) \tau^{2(n-1)} \varphi^{(2n)} - \frac{\rho L^2}{ET^2} \frac{\partial^2 \varphi}{\partial \bar{t}^2} = 0. \quad (26)$$

Equations (25) and (26) are obtained from the first two terms in the integration in (18). Alternatively, (25) and (26) can be obtained by substituting (8)₂ and (20) into (23) and (24).

Wave propagation in a shear deformable carbon nanotube. For analyzing the effect of τ on wave propagation in a carbon nanotube, terms of order $O(\tau^6)$ in the equations of motion are omitted. The corresponding expressions for (25) and (26) are

$$G\kappa L \left(\frac{\partial^2 \bar{w}}{\partial \bar{x}^2} - \frac{\partial \varphi}{\partial \bar{x}} \right) = \frac{\rho L^3}{T^2} \frac{\partial^2 \bar{w}}{\partial \bar{t}^2}, \quad (27)$$

$$\frac{AG\kappa L^2}{EI} \left(\frac{\partial \bar{w}}{\partial \bar{x}} - \varphi \right) + \frac{\partial^2 \varphi}{\partial \bar{x}^2} - \tau^2 \frac{\partial^4 \varphi}{\partial \bar{x}^4} - 3\tau^4 \frac{\partial^6 \varphi}{\partial \bar{x}^6} = \frac{\rho L^2}{ET^2} \frac{\partial^2 \varphi}{\partial \bar{t}^2}. \quad (28)$$

For wave propagation, the functions of deflection $\bar{w}(\bar{x}, \bar{t})$ and rotation $\varphi(\bar{x}, \bar{t})$ are expressed as

$$\bar{w}(x, t) = \bar{W} e^{i(\bar{k}\bar{x} - \bar{\omega}\bar{t})}, \quad (29)$$

$$\varphi(x, t) = \Phi e^{i(\bar{k}\bar{x} - \bar{\omega}\bar{t})}, \quad (30)$$

where k is wavenumber, ω is angle frequency and the dimensionless forms of these two variables are $\bar{k} = kL$ and $\bar{\omega} = \omega T$. Hence (27) and (28) can be reduced to linear system

$$\left(\frac{\rho L^3}{T^2} \bar{\omega}^2 - \frac{G\kappa}{L} \bar{k}^2 \right) \bar{W} - i \frac{G\kappa}{L} \bar{k} \Phi = 0, \quad (31)$$

$$i \frac{AG\kappa L^2}{EI} \bar{k}^3 \bar{W} + \left(\frac{\rho L^2}{ET^2} \bar{\omega}^2 - \frac{AG\kappa L^2}{EI} - k^2 - \tau^2 \bar{k}^4 + 3\tau^4 \bar{k}^6 \right) \Phi = 0, \quad (32)$$

or, in matrix form, as

$$A\mathbf{x} = 0, \quad (33)$$

where the elements of the matrix A are

$$\begin{aligned} a_{11} &= \frac{\rho L^3}{T^2} \bar{\omega}^2 - \frac{G\kappa}{L} \bar{k}^2, & a_{12} &= -i \frac{G\kappa}{L} \bar{k}, & a_{21} &= i \frac{AG\kappa L^2}{EI} \bar{k}^3, \\ a_{22} &= \frac{\rho L^2}{ET^2} \bar{\omega}^2 - \frac{AG\kappa L^2}{EI} - k^2 - \tau^2 \bar{k}^4 + 3\tau^4 \bar{k}^6, \end{aligned} \quad (34)$$

and the vector of generalized displacements is

$$\mathbf{x} = \{ \bar{W} \quad \Phi \}^T. \quad (35)$$

For nontrivial solutions of \bar{W} and Φ in (33), we must have $|A| = 0$ in (34), which yields the characteristic equation

$$\frac{\rho^2 L^5}{ET^4} \bar{\omega}^4 - \frac{GL\kappa\rho}{ET^2} \left(\bar{k}^2 + \frac{AL^4}{I} \right) \bar{\omega}^2 + \left(\frac{G\kappa}{L} - \frac{\rho L^3}{T^2} \right) (1 + \tau^2 \bar{k}^2 - 3\tau^4 \bar{k}^4) \bar{k}^2 = 0. \quad (36)$$

This is a quartic equation whose roots are

$$\bar{\omega}_{1,2,3,4} = \pm \sqrt{\frac{-b_1 \pm \sqrt{b_1^2 - 4a_1 c_1}}{2a_1}}, \quad (37)$$

where a_1 , b_1 and c_1 are defined in terms of \bar{k} as

$$a_1 = \frac{\rho^2 L^5}{ET^4}, \quad b_1 = -\frac{GL\kappa\rho}{ET^2} \left(\bar{k}^2 + \frac{AL^4}{I} \right), \quad c_1 = \left(\frac{G\kappa}{L} - \frac{\rho L^3}{T^2} \right) (1 + \tau^2 \bar{k}^2 - 3\tau^4 \bar{k}^4) \bar{k}^2. \quad (38)$$

Equations (37) and (38) give the spectrum relation between ω and k based on this new analytical nonlocal shear deformable nanotube model. Using the partial nonlocal nanotube model, the corresponding relation is identical to (37) except that a_1 , b_1 , c_1 be replaced by a_2 , b_2 , c_2 , given by [Liew et al. 2008]

$$a_2 = \frac{\rho^2 L^5}{ET^4}, \quad b_2 = -\frac{GL\kappa\rho}{ET^2} \left(\bar{k}^2 + \frac{AL^4}{I} \right), \quad c_2 = \left(\frac{G\kappa}{L} - \frac{\rho L^3}{T^2} \right) (1 - \tau^2 \bar{k}^2 + \tau^4 \bar{k}^4) \bar{k}^2. \quad (39)$$

Obviously the only difference between the solutions of this new analytical nonlocal stress model and the existing partial nonlocal stress model [Liew et al. 2008] is contributed by c_1 and c_2 . The difference leads to different characteristics of the two dispersion relations and spectrum relations for wave propagation in CNTs as discussed in great details in the following section.

3. Results and discussion

Effects of nanoscale on dispersion relation. We now present some numerical examples to illustrate the contrast between the analytical nonlocal shear deformable nanotube model (ANT) and the partial nonlocal shear deformable nanotube model (PNT) for wave propagation in a nonlocal nanotube with respect to the classical shear deformable tube model (CT). In these examples, the nanotubes are considered as homogeneous and isotropic with geometric and materials properties as in [Liew et al. 2008]: diameter $d = 5$ nm, thickness $t = 0.34$ nm, length $L = 10$ nm, Young's modulus $E = 0.72$ TPa, Poisson's ratio $\nu = 0.254$, density $\rho = 2.3$ g/cm³, vibration period $T = 4 \times 10^{-13}$ s and shear correction factor $\kappa = \frac{10}{9}$.

The dispersion relation between the dimensionless phase velocity \bar{c} and the dimensionless wave number \bar{k} (where $\bar{c} = \bar{\omega}/\bar{k}$) with various τ is illustrated in Figure 3 for shear deformable nanotube models based on the PNT solution in (37) and (39) and the ANT solution in (37) and (38). The classical wave propagation solution for the classical shear deformable nanotube without nonlocal effects can be deduced by substituting $\tau = 0$ in (38) or (39).

The different dispersion relations based on ANT, PNT and CT are indicated in Figure 3. For the dispersion relation based on the CT model, the phase velocity increases linearly for $\bar{k} < 15$ approximately, while a constant \bar{c} is observed at higher wavenumbers. For PNT models, there exists a critical wavenumber \bar{k}_{cri} below which the dispersion relation is close to linear and similar to the classical CT solution. Past \bar{k}_{cri} , linearity fails, and eventually the velocity starts dropping as the wavenumber becomes sufficiently

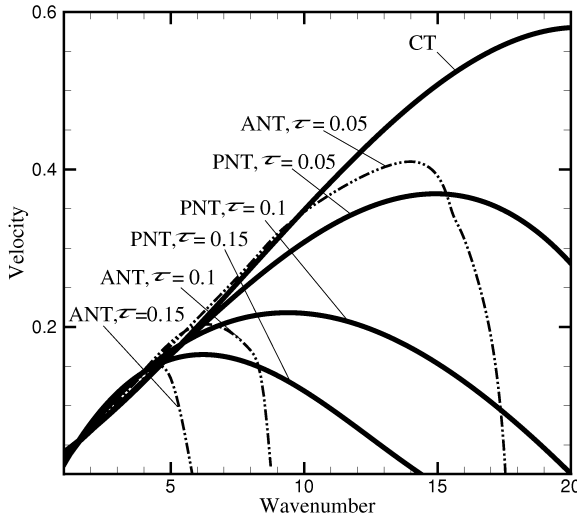


Figure 3. Dispersion relation obtained from shear deformable nanotube model.

high. For ANT models, there is also a critical wavenumber below which the phase velocity exceeds the PNT and CT values. For instance, for $\bar{k} = 5$ and $\tau = 0.1$, the phase velocity is $\bar{c} = 0.18$ according to ANT, $\bar{c} = 0.17$ for CT and $\bar{c} = 0.16$ for PNT. In other words, nonlocality in nanotubes has a stiffening effect (increase in phase velocity) according to ANT, relative to the classical solutions, but the opposite effect according to PNT. Past the critical wavenumber, the ANT-predicted phase velocity drops sharply, differing significantly from the of CT and PNT solutions. Thus, according to ANT, wave propagation in shear deformable nanotubes decay rapidly after the wavenumber exceeds critical value.

Figure 4 plots the dimensionless angle frequency $\bar{\omega}$ versus the wavenumber \bar{k} for various τ based on the different nanotube models. For the classical model, the predicted frequency keeps increasing with

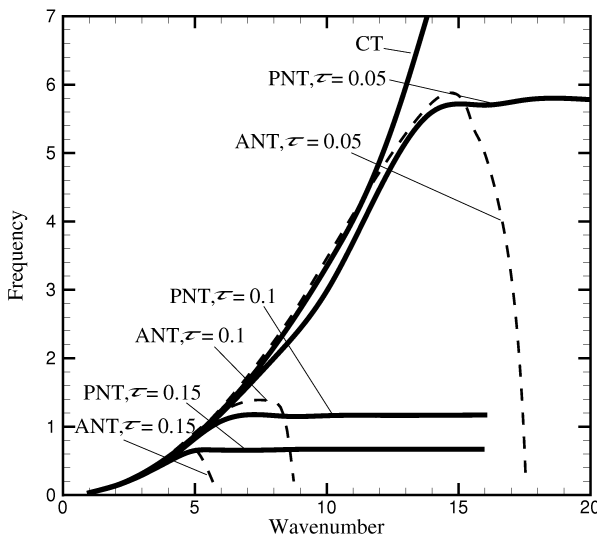


Figure 4. Spectrum relation obtained from shear deformable nanotube model.

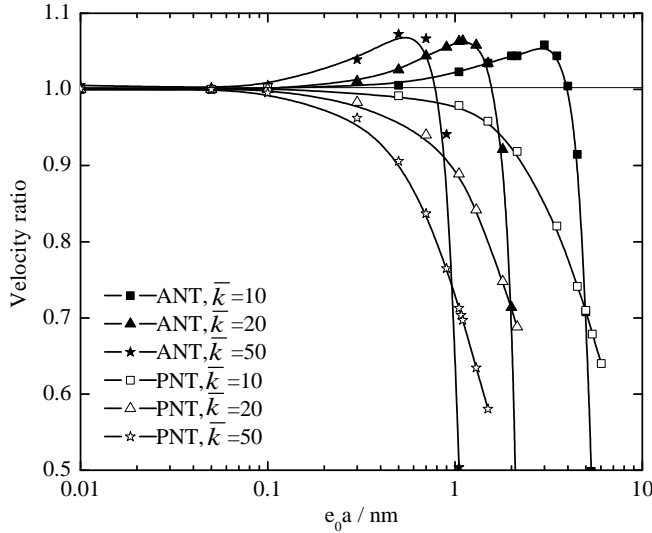


Figure 5. Effect of scale parameter (τ) on the ratio of the phase velocity predicted by our models (ANT and PNT) to the classical (CT) solution, for the shear deformable nanotube model.

the wavenumber. For PNT, it flattens out for wavenumbers beyond the critical value \bar{k}_{cri} . For ANT, the frequency at first increases as in the first two models but then drops sharply.

As we saw in connection with Figure 3, ANT predicts stiffening below the critical wavenumber, while the opposite is predicted by PNT. This can also be observed in the frequency/wavenumber relation: for $\bar{k} = 4$ and $\tau = 0.1$, the predicted frequency is $\bar{\omega} = 0.8$ according to ANT, $\bar{\omega} = 0.7$ according to PNT, and $\bar{\omega} = 0.75$ according to CT.

The presence of a frequency maximum under ANT and the subsequent decay are mainly due to the strong nanoscale effect contributed by the nonlocal (long-range) stress between molecules and lattice at high wavenumbers. The critical wavenumber decreases from 14 to 5 as the nanoscale parameter τ increases from 0.05 to 0.15. It implies for stronger nanoscale effect, the decay wave propagation in nanotube is more ready to be induced at lower a wavenumber.

The influence of a small scale effect on the dispersion relations is further illustrated in Figure 5, which plots the velocity ratio relative to the classical solution as a function of τ , for different values of \bar{k} . We see in this figure that the phase velocity according to the ANT and PNT nonlocal models are very close to the classical solutions for $\tau < 0.03$; thus wave propagation in the nanotube is hardly influenced by nanoscale effects in this range. A sharp reduction in wave propagation velocity then occurs for larger τ . A critical point τ_{cri} is seen on each ANT and PNT, which decreases as the wave number increases. Thus, ANT predicts the values 0.6, 1.2, and 2 for τ_{cri} when $\bar{k} = 50, 20$, and 10, respectively. This is consistent with the expectation that propagation at a higher wavenumber requires more kinetic energy. The contribution due to the presence nanoscale τ is decreasingly sufficient to sustain such status of wave propagation and hence a smaller τ_{cri} corresponds to a higher wavenumber.

As stated in (3), τ is dimensionless quantity representing the small scale parameter $e_0 a$. According to Eringen's theory of nonlocal elasticity [Eringen and Edelen 1972; Eringen 1972a; 1972b; 1983; 2002], the internal characteristic length a of material is a simple lattice parameter such as the granular distance

or bond length. For CNTs, this value could be considered as the C-C bond length, or $a = 0.142$ nm on average [Wang 2005; 2006; Wang et al. 2006b; 2006c; 2008; Lu et al. 2007; Heireche et al. 2008; Liew et al. 2008; Wang and Varadan 2007; Xie et al. 2007a; 2007b; Hu et al. 2008]. The material constant e_0 is a parameter that indicates the small scale effect on the material properties [Eringen 2002] and it was stated as $e_0 = 0.39$ in [Eringen 1983; 2002]. This result should be further confirmed by experiment or other approaches such as MD or matching the dispersion relation of atomic lattice dynamics. Furthermore, the value of e_0 is not a constant for different materials and small scale nanostructures. For research of wave propagation in CNTs, the value of e_0 could possibly be in the range $0 < e_0 a < 210$ nm [Wang 2005]. In this paper, $0 \leq \tau \leq 5$ is assumed for comparison between ANT and PNT. For a specific CNT with $L = 10$ nm, this implies $0 < e_0 a < 50$ nm. As shown in Figure 5, wave propagation decays very fast when $\tau > \tau_{\text{cri}}$, which means $e_0 a$ could not be too high and its specific range depends on L .

It is also clear from Figure 5 that the phase velocity ratios of PNT are never beyond unity while the corresponding ANT solutions are different for small τ below the critical value. Thus stiffness enhancement of nanotube by the presence of nanoscale effect via ANT is further confirmed in this example.

Comparison with molecular dynamic simulation. The MD approach is considered as an authoritative means to analyze CNTs and extensive research based on MD simulation on the mechanics properties of CNTs has been published [Liew et al. 2004a; 2004b; 2005; 2008; Kitipornchai et al. 2005; Wang and Hu 2005; Wang et al. 2006b; 2008; Hu et al. 2008]. Other approaches or models are often compared with MD to verify the solutions. For this reason and to further confirm the validity of the ANT solutions, we present in Figure 6 a comparison of the various dispersion relations with MD results [Liew et al. 2008] for a (5, 5) CNT. In this example, the parameters and properties of nanotube are the same as in the previous subsection, except that we take the Young's modulus to be $E = 0.897$ TPa, the diameter $d = 0.96$ nm and $\tau = 0.00355$.

As shown in Figure 6, all solutions seem to agree well for $\bar{k} < 1$ with respect to the classical solutions. Consistent with the previous example, the MD simulation also predicts the presence of a critical wave

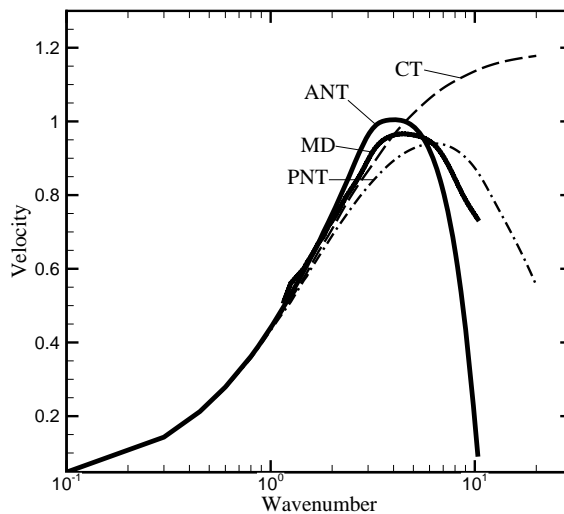


Figure 6. Dispersion relation obtained from different models.

velocity for sufficiently high wavenumber. In this case, wave velocity decreases for $\bar{k} > \bar{k}_{\text{cri}}$. In addition, the ANT and MD solutions both predict $\bar{k}_{\text{cri}} \approx 4$ and they agree more as compared to PNT which predicts $\bar{k}_{\text{cri}} \approx 6$. The classical model fails to predict the existence of any critical wavenumber at all.

The comparison should be interpreted in the following manner. The classical solutions without nanoscale effects should be viewed as the demarcation between the various models. As the wavenumber increases (smaller wavelength) which indicates more prominent nanoscale influence, on one side of the demarcation shows increasing wave velocity or equivalently higher stiffness (wave propagates faster in a more stiff medium) while on the other side of the demarcation shows decreasing wave velocity and hence decreasing stiffness. It is clear that the analytical nonlocal stress and MD approaches both predict comparable solutions while the partial nonlocal stress model predicts otherwise. This comparison with MD solutions concludes that the analytical nonlocal stress model is consistent with MD solutions. It should be noted that for very high wavenumber, the curves do not agree well. At such length scales which attain sub-nano ranges, one full wavelength only covers a limited number of molecules and the medium may not be continuous. In such sub-nano ranges, the validity of all continuum CNT models has to be further investigated.

In conclusion, it is confirmed that the ANT model predicts more agreeable solutions with respect to MD simulations in terms of critical values as well stiffness and wave velocity enhancement as compared to PNT.

4. Further discussion on the analytical nonlocal and partial nonlocal modeling

Equations (22) and (23) express the governing equations of motion for a shear deformable nanotube which is derived from the variational principle. Comparing with the classical tube dynamic conditions in (9), consequently, it is concluded that the transverse equation of motion is identical for both the classical model and the nonlocal stress model, or

$$Q_c = Q \quad (40)$$

while for the bending moment equation of motion, the classical bending moment \bar{M}_c should be replaced by the effective nonlocal bending moment \bar{M}_{ef} defined in (24) for a nanotube with nonlocal effects.

In virtually all published works in wave propagation based on the partial nonlocal stress model [Wang and Hu 2005; Wang 2005; Wang et al. 2006c; Lu et al. 2007; Heireche et al. 2008; Liew et al. 2008; Wang 2006; Wang et al. 2006b; Wang and Varadan 2007; Xie et al. 2007a; Xie et al. 2007b; Wang et al. 2008; Hu et al. 2008], the dynamic equations of motion were derived by directly replacing the classical bending moment condition in (9)₂ with the nonlocal bending moment defined in (6). The direct replacement yields

$$\bar{Q} - \frac{\partial \bar{M}_{xx}}{\partial \bar{x}} = \frac{\rho L^2}{ET^2} \frac{\partial^2 \varphi}{\partial \bar{t}^2} \quad (41)$$

which was not consistent with the variational principle. By retaining terms of $O(\tau^4)$ in (23) in order to analyze the effect of nanoscale τ , a truncated dynamic equation is obtained as expressed in (28). Similarly, by substituting the expression (8)₂ for the nonlocal moment \bar{M}_{xx} in into (40) and retaining terms of $O(\tau^4)$, we obtain

$$\frac{AG\kappa L^2}{EI} \left(\frac{\partial \bar{w}}{\partial \bar{x}} - \varphi \right) + \frac{\partial^2 \varphi}{\partial \bar{x}^2} + \tau^2 \frac{\partial^4 \varphi}{\partial \bar{x}^4} + \tau^4 \frac{\partial^6 \varphi}{\partial \bar{x}^6} = \frac{\rho L^2}{ET^2} \frac{\partial^2 \varphi}{\partial \bar{t}^2}. \quad (42)$$

Comparing (23) and (40), or equivalently comparing (28) and (42) for terms $O(\tau^4)$, it is concluded that the partial nonlocal stress model predicts different nonlocal responses for bending and wave propagation as what have been illustrated in the previous examples.

Equations (22) and (23) in terms of nonlocal stress resultants, or (25) and (26) in terms of displacement and rotation, are novel governing dynamic equations of motion for a nanotube with nonlocal effect derived using an exact variational principle. These two equations govern the exact dynamic motion for a nonlocal shear deformable nanotube. These are new equations of motion first derived here and they are fundamentally distinct with respect to virtually all previous works. Verification and application of this new analytical model for analyzing the wave propagation in nanotubes have been demonstrated in the previous sections.

The conclusion of stiffness strengthening effect of nanotubes with increasing nanoscale effect is consistent qualitatively with other published research works via other non-nonlocal elasticity approaches. Some noted instances including the strain gradient theory [Nix and Gao 1998; Lam et al. 2003]; a modified couple stress theory at microscale [Park and Hao 2006; 2008, Ma et al. 2008]; computational atomistic modeling for free vibration of a carbon nanotube [Li and Chou 2004] which concluded that the fundamental frequencies of the classical solution could be significantly lower than the atomistic simulation solutions by 40% to 60%; as well as experimental studies on monolithic films [Was and Foecke 1996], on harness of nanoindentation of crystalline materials [Nix and Gao 1998], on significant increased bending stiffness of a nano-cantilever [Lam et al. 2003; McFarland and Colton 2005]. It is noted that some of the analyses above [Park and Hao 2006; 2008, Ma et al. 2008] considered only effects at microscale instead of nanoscale. It is not a concern here as to whether it is still valid at nanoscale. In this paper, the formulations are all non-dimensionalized and hence the presence of a small-scale τ indicates the deviation expected from the classical theory when size effect is present, irrespective of the actual size of τ . The paper concludes that the presence of τ induces a minute structure with higher stiffness and the conclusion is consistent with the prediction of the modified couple stress theory [Park and Hao 2006; 2008, Ma et al. 2008].

5. Conclusions

An analytical nonlocal stress model for wave propagation in CNTs has been established through consistent variational principle. The CNTs are simulated as shear deformable nanotubes with size dependent nonlocal effects. New dynamic equations of motion for wave propagation in CNTs have been derived and new wave propagation behaviors that nonlocal stress enhances stiffness and wave velocity in CNTs have been predicted.

Analytical expressions for the dispersion relation which relates wavenumber and phase velocity and the spectrum relation (frequency versus wavenumber) are presented through the analytical nonlocal stress approach. It has been shown that there exist critical points for the dispersion relation and spectrum relation by the analytical nonlocal models and these points depend on the nanoscale parameter. For wavenumber beyond these critical values, wave propagation is decreased sharply. Furthermore, the analytical nonlocal model confirms that the nanoscale effect promotes wave propagation in nanotube for wavenumber below the critical points. The phenomenon is verified by comparison with molecular dynamic simulation.

Appendix

The strain energy density of a nanotube due to normal deformation u_n as presented in (10) and (11) [Lim 2009; 2010] can be derived as follows. From (8)₁, u_n can be expressed as

$$u_n = \int_0^{\varepsilon_{xx}} \sigma_{xx} d\varepsilon_{xx} = E \sum_{n=1}^{\infty} \tau^{2(n-1)} \int_0^{\varepsilon_{xx}} \varepsilon_{xx}^{(2(n-1))} d\varepsilon_{xx}.$$

Since we have

$$\begin{aligned} \int_0^{\varepsilon_{xx}} \varepsilon_{xx} d\varepsilon_{xx} &= \frac{1}{2} \varepsilon_{xx}^2, \\ \int_0^{\varepsilon_{xx}} \varepsilon_{xx}^{(2)} d\varepsilon_{xx} &= \int_0^{\varepsilon_{xx}} \varepsilon_{xx}^{(1)} d\varepsilon_{xx}^{(1)} = \frac{1}{2} (\varepsilon_{xx}^{(1)})^2, \\ \int_0^{\varepsilon_{xx}} \varepsilon_{xx}^{(4)} d\varepsilon_{xx} &= \int_0^{\varepsilon_{xx}} \varepsilon_{xx}^{(1)} d\varepsilon_{xx}^{(3)} = \varepsilon_{xx}^{(1)} \varepsilon_{xx}^{(3)} \Big|_0^{\varepsilon_{xx}} - \int_0^{\varepsilon_{xx}} \varepsilon_{xx}^{(3)} d\varepsilon_{xx}^{(1)} = \varepsilon_{xx}^{(1)} \varepsilon_{xx}^{(3)} - \int_0^{\varepsilon_{xx}} \varepsilon_{xx}^{(2)} d\varepsilon_{xx}^{(2)} \\ &= \varepsilon_{xx}^{(1)} \varepsilon_{xx}^{(3)} - \frac{1}{2} (\varepsilon_{xx}^{(2)})^2, \\ \int_0^{\varepsilon_{xx}} \varepsilon_{xx}^{(6)} d\varepsilon_{xx} &= \int_0^{\varepsilon_{xx}} \varepsilon_{xx}^{(1)} d\varepsilon_{xx}^{(5)} = \varepsilon_{xx}^{(1)} \varepsilon_{xx}^{(5)} \Big|_0^{\varepsilon_{xx}} - \int_0^{\varepsilon_{xx}} \varepsilon_{xx}^{(5)} d\varepsilon_{xx}^{(1)} = \varepsilon_{xx}^{(1)} \varepsilon_{xx}^{(5)} - \int_0^{\varepsilon_{xx}} \varepsilon_{xx}^{(4)} d\varepsilon_{xx}^{(2)} \\ &= \varepsilon_{xx}^{(1)} \varepsilon_{xx}^{(5)} - \varepsilon_{xx}^{(2)} \varepsilon_{xx}^{(4)} \Big|_0^{\varepsilon_{xx}} + \int_0^{\varepsilon_{xx}} \varepsilon_{xx}^{(4)} d\varepsilon_{xx}^{(2)} = \varepsilon_{xx}^{(1)} \varepsilon_{xx}^{(5)} - \varepsilon_{xx}^{(2)} \varepsilon_{xx}^{(4)} + \int_0^{\varepsilon_{xx}} \varepsilon_{xx}^{(3)} d\varepsilon_{xx}^{(3)} \\ &= \varepsilon_{xx}^{(1)} \varepsilon_{xx}^{(5)} - \varepsilon_{xx}^{(2)} \varepsilon_{xx}^{(4)} + \frac{1}{2} (\varepsilon_{xx}^{(3)})^2, \end{aligned}$$

or, concisely,

$$\begin{aligned} \int_0^{\varepsilon_{xx}} \varepsilon_{xx}^{(2(n-1))} d\varepsilon_{xx} &= \varepsilon_{xx}^{(1)} \varepsilon_{xx}^{(2(n-1)-1)} - \varepsilon_{xx}^{(2)} \varepsilon_{xx}^{(2(n-1)-2)} + \dots + (-1)^{n-1} \varepsilon_{xx}^{(n-2)} \varepsilon_{xx}^{(n)} + (-1)^n \frac{1}{2} (\varepsilon_{xx}^{(n-1)})^2 \\ &= \sum_{m=1}^{n-2} ((-1)^{m+1} \varepsilon_{xx}^{(m)} \varepsilon_{xx}^{(2(n-1)-m)}) + (-1)^n \frac{1}{2} (\varepsilon_{xx}^{(n-1)})^2, \end{aligned}$$

which is valid for $n \geq 3$, we conclude that the strain energy u_n at a point is $u_n = u_1 + u_2 + u_3$, where the u_i are given by (13).

References

- [Ajayan and Zhou 2001] M. Ajayan and O. Z. Zhou, “Applications of carbon nanotubes”, pp. 391–425 in *Carbon nanotubes: synthesis, structure, properties, and applications*, edited by M. S. Dresselhaus et al., Topics in Applied Physics **80**, 2001.
- [Ball 2001] Ball, “Roll up for the revolution”, *Nature* **414** (2001), 142–144.
- [Baughman et al. 2002] R. H. Baughman, A. A. Zakhidov, and W. A. de Heer, “Carbon nanotubes—the route toward applications”, *Science* **297** (2002), 787–792.
- [Brenner et al. 2002] D. W. Brenner, O. A. Shenderova, J. A. Harrison, S. J. Stuart, B. Ni, and S. B. Sinnott, “A second-generation reactive empirical bond order (REBO) potential energy expression for hydrocarbons”, *J. Phys. Condens. Mater.* **14** (2002), 783–802.
- [Eringen 1972a] A. C. Eringen, “Nonlocal polar elastic continua”, *Int. J. Eng. Sci.* **10** (1972), 1–16.

- [Eringen 1972b] A. C. Eringen, “Linear theory of nonlocal elasticity and dispersion of plane waves”, *Int. J. Eng. Sci.* **10** (1972), 425–435.
- [Eringen 1983] A. C. Eringen, “On differential equations of nonlocal elasticity and solutions of screw dislocation and surface waves”, *J. Appl. Phys.* **54** (1983), 4703–4710.
- [Eringen 2002] A. C. Eringen, *Nonlocal continuum field theories*, Springer, New York, 2002.
- [Eringen and Edelen 1972] A. C. Eringen and D. G. B. Edelen, “On nonlocal elasticity”, *Int. J. Eng. Sci.* **10** (1972), 233–248.
- [Hagedorn and Dasgupta 2007] P. Hagedorn and A. Dasgupta, *Vibration and waves in continuous mechanical system*, Wiley, UK, 2007.
- [Han et al. 2005] Q. Han, G. X. Lu, and L. M. Dai, “Bending instability of an embedded double-walled carbon nanotube based on Winkler and van der Waals models”, *Compos. Sci. Technol.* **65** (2005), 1337–1346.
- [Heireche et al. 2008] H. Heireche, A. Tounsi, and A. Benzair, “Scale effect on wave propagation of double-walled carbon nanotubes with initial axial loading”, *Nanotechnology* **19** (2008), 185703.
- [Hu et al. 2008] Y. G. Hu, K. M. Liew, Q. Wang, X. Q. He, and B. I. Yakobson, “Nonlocal shell model for elastic wave propagation in single- and double-walled carbon nanotubes”, *J. Mech. Phys. Solids* **56** (2008), 3475–3485.
- [Iijima 1991] S. Iijima, “Helical microtubules of graphitic carbon”, *Nature* **354** (1991), 56–58.
- [Kitipornchai et al. 2005] S. Kitipornchai, X. Q. He, and K. M. Liew, “Buckling analysis of triple-walled carbon nanotubes embedded in an elastic matrix”, *J. Appl. Phys.* **97** (2005), 114318.
- [Lam et al. 2003] D. C. C. Lam, F. Yang, A. C. M. Chong, J. Wang, and P. Tong, “Experiments and theory in strain gradient elasticity”, *J. Mech. Phys. Solids* **51** (2003), 1477–1508.
- [Li and Chou 2004] C. Y. Li and T. W. Chou, “Vibrational behaviors of multi-walled carbon nanotube-based nanomechanical resonators”, *Appl. Phys. Lett.* **84** (2004), 121–123.
- [Liew et al. 2004a] K. M. Liew, X. Q. He, and C. H. Wong, “On the study of elastic and plastic properties of multi-walled carbon nanotubes under axial tension using molecular dynamics simulation”, *Acta Materialia* **52**:9 (2004), 2521–2527.
- [Liew et al. 2004b] K. M. Liew, C. H. Wong, X. Q. He, M. J. Tan, and S. A. Meguid, “Nanomechanics of single and multi-walled carbon nanotubes”, *Phys. Rev. B* **69** (2004), 115429.
- [Liew et al. 2005] K. M. Liew, C. H. Wong, and M. J. Tan, “Buckling properties of carbon nanotube bundles”, *Appl. Phys. Lett.* **87**:4 (2005), 041901.
- [Liew et al. 2008] K. M. Liew, Y. Hu, and X. Q. He, “Flexural wave propagation in single-walled carbon nanotubes”, *J. Comput. Theoretical Nanoscience* **5** (2008), 581–586.
- [Lim 2008] C. W. Lim, “A discussion on the nonlocal elastic stress field theory for nanobeams”, in *The Eleventh East Asia–Pacific Conference on Structural Engineering and Construction* (EASEC-11) (Taipei, Taiwan, 2008), 2008.
- [Lim 2009] C. W. Lim, “Equilibrium and static deflection for bending of a nonlocal nanobeam”, *Adv. Vibr. Eng.* **8**:4 (2009), 277–300.
- [Lim 2010] C. W. Lim, “On the truth of nanoscale for nanobeams based on nonlocal elastic stress field theory: Equilibrium, governing equation and static deflection”, *Appl. Math. Mech.* **31**:1 (2010), 37–54.
- [Lim and Wang 2007] C. W. Lim and C. M. Wang, “Exact variational nonlocal stress modeling with asymptotic higher-order strain gradients for nanobeams”, *J. Appl. Phys.* **101** (2007), 054312.
- [Lu et al. 2007] P. Lu, H. P. Lee, C. Lu, and P. Q. Zhang, “Application of nonlocal beam models for carbon nanotubes”, *Int. J. Solids Struct.* **44** (2007), 5289–5300.
- [Ma et al. 2008] H. M. Ma, X. L. Gao, and J. N. Reddy, “A microstructure-dependent Timoshenko beam model based on a modified couple stress theory”, *J. Mech. Phys. Solids* **56**:12 (2008), 3379–3391.
- [McFarland and Colton 2005] A. W. McFarland and J. S. Colton, “Role of material microstructure in plate stiffness with relevance to microcantilever sensors”, *J. Micromech. Microeng.* **15** (2005), 1060–1067.
- [Natsuki et al. 2005] T. Natsuki, T. Hayashi, and M. Endo, “Wave propagation of carbon nanotubes embedded in an elastic medium”, *J. Appl. Phys.* **97** (2005), 044307.
- [Nix and Gao 1998] W. Nix and H. Gao, “Indentation size effects in crystalline materials: A law for strain gradient plasticity”, *J. Mech. Phys. Solids* **46**:3 (1998), 411–425.

- [Park and Hao 2006] S. K. Park and X. L. Hao, “Bernoulli–Euler beam model based on a modified couple stress theory”, *J. Micromech. Microeng.* **16** (2006), 2355–2359.
- [Park and Hao 2008] S. K. Park and X. L. Hao, “Variational formulation of a modified couple stress theory and its application to a simple shear problem”, *Z. Angew. Math. Phys.* **59** (2008), 904–917.
- [Parnes and Chiskis 2002] R. Parnes and A. Chiskis, “Buckling of nano-fibre reinforced composites: a re-examination of elastic buckling”, *J. Mech. Phys. Solids* **50** (2002), 855–879.
- [Ru 2000a] C. Q. Ru, “Effective bending stiffness of carbon nanotubes”, *Phys. Rev. B* **62** (2000), 9973–9976.
- [Ru 2000b] C. Q. Ru, “Elastic buckling of singlewalled carbon nanotube ropes under high pressure”, *Phys. Rev. B* **62** (2000), 10405–10408.
- [Treacy et al. 1996] M. M. J. Treacy, T. W. Ebbesen, and J. M. Gibson, “Exceptionally high Young’s modulus observed for individual carbon nanotubes”, *Nature* **381** (1996), 680–687.
- [Wang 2005] Q. Wang, “Wave propagation in carbon nanotubes via nonlocal continuum mechanics”, *J. Appl. Phys.* **98** (2005), 124301.
- [Wang 2006] Q. Wang, “Axi-symmetric wave propagation of carbon nanotubes with non-local elastic shell model”, *Int. J. Struct. Stab. Dyn.* **6** (2006), 285–296.
- [Wang and Hu 2005] L. F. Wang and H. Y. Hu, “Flexural wave propagation in single-walled carbon nanotubes”, *Phys. Rev. B* **71** (2005), 195412.
- [Wang and Varadan 2006] Q. Wang and V. K. Varadan, “Wave characteristics of carbon nanotubes”, *Int. J. Solids Struct.* **43** (2006), 254–265.
- [Wang and Varadan 2007] Q. Wang and V. K. Varadan, “Application of nonlocal elastic shell theory in wave propagation analysis of carbon nanotubes”, *Smart Mater. Struct.* **16** (2007), 178–190.
- [Wang et al. 2006a] C. Y. Wang, C. Q. Ru, and A. Mioduchowski, “Vibration of microtubules as orthotropic elastic shells”, *Physica E* **35** (2006), 48–56.
- [Wang et al. 2006b] L. F. Wang, H. Y. Hu, and W. L. Guo, “Validation of the non-local elastic shell model for studying longitudinal waves in single-walled carbon nanotubes”, *Nanotechnology* **17** (2006), 1408–1415.
- [Wang et al. 2006c] Q. Wang, G. Y. Zhou, and K. C. Lin, “Scale effect on wave propagation of double-walled carbon nanotubes”, *Int. J. Solids Struct.* **43** (2006), 6071–6084.
- [Wang et al. 2008] L. F. Wang, W. L. Guo, and H. Y. Hu, “Group velocity of wave propagation in carbon nanotubes”, *Proc. R. Soc. A-Math Phys. Eng. Sci.* **464** (2008), 1423–1438.
- [Was and Foecke 1996] G. S. Was and T. Foecke, “Deformation and fracture in microlaminates”, *Thin Solid Films* **286** (1996), 1–31.
- [Xie et al. 2007a] G. Q. Xie, X. Han, and S. Y. Long, “Characteristic of waves in a multi-walled carbon nanotubes”, *Computers, Materials and Continua* **6** (2007), 1–11.
- [Xie et al. 2007b] G. Q. Xie, X. Han, and S. Y. Long, “Effect of small size on dispersion characteristics of wave in carbon nanotubes”, *Int. J. Solids Struct.* **44**:3-4 (2007), 1242–1255.
- [Yakobson et al. 1996] B. I. Yakobson, C. J. Brabec, and J. Bernholc, “Nanomechanics of carbon tubes: instabilities beyond linear range”, *Phys. Rev. Lett.* **76** (1996), 2511–2514.
- [Yoon et al. 2005] J. Yoon, C. Q. Ru, and A. Mioduchowski, “Terahertz vibration of short carbon nanotubes modeled as Timoshenko-beams”, *J. Appl. Mech.-Trans. ASME.* **72** (2005), 10–17.
- [Zhang et al. 2005] Y. Q. Zhang, G. R. Liu, and H. Xu, “Transverse vibrations of double-walled carbon nanotubes under compressive axial load”, *Phys. Lett. A* **340** (2005), 258–266.

Received 17 Jul 2009. Revised 24 Nov 2009. Accepted 24 Nov 2009.

C. W. LIM: bccwlim@cityu.edu.hk

Department of Building and Construction, City University of Hong Kong, Tat Chee Avenue, Kowloon, Hong Kong

Y. YANG: yanyang6@student.cityu.edu.hk

Department of Building and Construction, City University of Hong Kong, Tat Chee Avenue, Kowloon, Hong Kong

DYNAMIC COMPRESSIVE RESPONSE OF COMPOSITE CORRUGATED CORES

BENJAMIN P. RUSSELL, ADAM MALCOM, HAYDN N. G. WADLEY AND VIKRAM S. DESHPANDE

The dynamic out-of-plane compressive response of E-glass composite corrugated sandwich cores have been measured for impact velocities ranging from quasistatic to 175 ms^{-1} . Laboratory scale sandwich cores of relative density $\bar{\rho} \approx 33\%$ were manufactured from 3D woven E-glass and stitched to S2-glass face-sheets via a double line of Kevlar yarn. Two variants of the sandwich cores were investigated: sandwich cores with the empty spaces between the corrugations filled with a PVC foam, and unfilled corrugations. The stresses on the rear faces of the dynamically compressed sandwich cores were measured using a direct impact Kolsky bar. The compression tests on both the corrugated cores and the parent strut wall material confirmed that these relatively high relative density corrugated cores failed by microbuckling of the strut wall material under quasistatic loading. Moreover, the foam filling did not have any significant effect on the measured responses. The peak stresses of both the strut wall material and corrugated cores increased approximately linearly with strain rate for applied strain rates less than about 4000 s^{-1} . This increase was attributed to the strain rate sensitivity of the composite matrix material that stabilised the microbuckling failure mode of the E-glass composite. At higher applied strain rates the response was reasonably rate insensitive with compressive crushing of the glass fibres being the dominant failure mode. A simple model utilising the measured dynamic properties of the strut wall material accurately predicts the measured peak strengths of the filled and unfilled corrugated cores.

1. Introduction

Lightweight materials and structures utilised in transportation systems are sometimes subjected to dynamic loads due to impact events or the impingement of shock waves created by nearby explosions. The development of multifunctional materials and structures that provide dynamic load mitigation capabilities in addition to their normal structural requirements are therefore important to a number of fields such as crash protection, petro-chemical safety, infrastructure protection and many military applications. There has been much interest in sandwich structures for use in dynamic loading scenarios and several theoretical and experimental studies on metallic materials have shown there to be significant advantages of sandwich structures over monolithic structures of equivalent mass, see for example [Xue and Hutchinson 2003; Fleck and Deshpande 2004; Wei et al. 2008; Dharmasena et al. 2008].

There are two effects that combine to endow sandwich panels with their superior resistance to shock front loading: (i) an increased flexural strength and (ii) fluid-structure interaction (FSI) effects, which mean that a smaller fraction of the shock impulse is transmitted into sandwich panels compared with monolithic plates of equal mass per unit area (areal density). This FSI effect for explosively created shocks in water was assessed experimentally in [Dharmasena et al. 2009; 2010]. Water shock tube

Keywords: composite lattice cores, impact testing, dynamic loads, material rate-dependence.

Work supported by the Office of Naval Research under ONR grant number N00014-07-1-0764 (Dr. David Shifler, Program manager).

methods developed in [Deshpande et al. 2006] were used in [Mori et al. 2008] to enable the dynamic deflections of sandwich panels to be observed using Moire interferometry. The increased flexural strength of sandwich panel systems is achieved by the use of stiff, strong, fracture resistant face sheets separated by a lightweight core. Significant research is therefore underway to explore the design of lightweight sandwich panel cores that are sufficiently strong that they do not completely crush under an impulsive load.

Much of this effort in sandwich panel core design for dynamic applications has concentrated on highly ductile metallic lattice core and face sheet structures. For example, Radford et al. [2007], Ferri et al. [2006] and Tilbrook et al. [2007] have investigated the dynamic response of stainless steel square-honeycomb cores, I-cores and prismatic Y-frames and corrugated cores respectively. These studies have demonstrated that inertial stabilisation significantly delays the onset of buckling in these lattice cores; consequently, the dynamic strength exceeds the quasistatic strength by nearly a factor of four at impact velocities around 50 ms^{-1} . Moreover, the experiments of [Radford et al. 2007] and [Tilbrook et al. 2007] have demonstrated that the peak stress on the impacted (front) face increases approximately linearly with impact velocity while the distal (rear) face stress remains approximately constant; i.e., plastic shock wave effects play a significant role at these impact velocities. These features of the dynamic compression of cellular cores results in pressure transmitted to the back face of fully back supported sandwich panels exposed to underwater shocks [Wadley et al. 2008].

There is a natural progression to adopt material systems which intrinsically have high specific strength and stiffness. Composite polymer systems reinforced with strong fibres such as carbon, glass and aramids, offer such properties. Indeed, they find extensive use within sandwich configurations in specialist automotive and aerospace markets. Some recent studies have reported the static performance of composite sandwich cores. These include an investigation of the compressive response of Z-pinned reinforced foam cores in [Marasco et al. 2006], the compressive and shear response of carbon fibre square honeycomb cores in [Russell et al. 2008], the compressive response of carbon fibre pyramidal truss cores in [Finnegan et al. 2007] and titanium coated SiC monofilaments such as those investigated in [Moongkhamklang et al. 2008]. Experimental and theoretical work on the static properties of composite corrugated cores has also been recently reported in [Kazemahvazi and Zenkert 2009] and [Kazemahvazi et al. 2009]. However, to date there is a scarcity of data in the literature on the dynamic properties of composite sandwich cores.

In this study we report the dynamic performance of composite corrugated cores. The related investigation of metallic corrugated cores in [Tilbrook et al. 2007] demonstrated that three effects give an enhanced strength to such cores under dynamic loading. These effects are: (i) material strain rate effects; (ii) inertial stabilisation of the core struts against elastic buckling and (iii) plastic shock wave effects that localise deformation near the impacted face and result in the stresses on the impacted face exceeding those on the on the face distal from the impact. However, the role that these effects play in the dynamic compression of composite corrugated cores is as yet unclear. Moreover, based on theoretical work on the dynamic compression of unidirectional composites in [Slaughter et al. 1996] and experiments in [Lankford 1995] we also anticipate that dynamic stabilisation of the microbuckling failure mode in composites will play a role in setting the dynamic performance of composite corrugated cores. We thus focus here on investigating the dynamic properties of the core material — this entails constraining the back face of the core. This boundary condition is very different from that in a sandwich plate or beam test but enables us to investigate the inherent properties of the core, absent the particular structural context.

The outline of the paper is as follows. First, the manufacturing techniques employed for making laboratory scale E-glass corrugated cores are detailed. Next, the quasistatic and dynamic out-of-plane compressive response of foam-filled and unfilled corrugated cores and the strut wall material are reported. The dynamic measurements are conducted using a direct impact Kolsky bar, and high speed photography is employed to observe the dynamic deformation modes. Based on these measurements and visual observations we finally report a simple model to relate the dynamic responses of the corrugated cores to the measured properties of the strut wall material.

2. Materials and manufacturing

Foam-filled composite corrugated sandwich cores, as sketched in Figure 1, were manufactured from 3D woven fabric (3WEAVE fabric, 3tex Inc.) and Divinycell H130 PVC foam (DIAB Inc., Desoto, TX 75115, USA). The 2.8 mm thick face sheets comprised a single layer of S2-glass (areal mass of dry fabric 3.29 kg m^{-2}) while the corrugated core was made from two layers of E-glass (areal mass of each layer 1.83 kg m^{-2}), refer to Table 1 for details of these fabrics. Each of the 3D fabric layers comprised three

	E-glass			S2-glass		
	weft (x_f)	warp (y_f)	z yarn (z_f)	weft (x_f)	warp (y_f)	z yarn (z_f)
weight	48.8%	50.3%	0.9%	48.0%	48.5%	3.6%
tows	3	2	—	3	2	—

Table 1. Details of the 3D woven glass fabrics manufactured by 3Tex: E-glass of areal mass 1.83 kg m^{-2} and S2-glass of areal mass 3.29 kg m^{-2} . The coordinate system for the fabrics is illustrated in Figure 1, right.

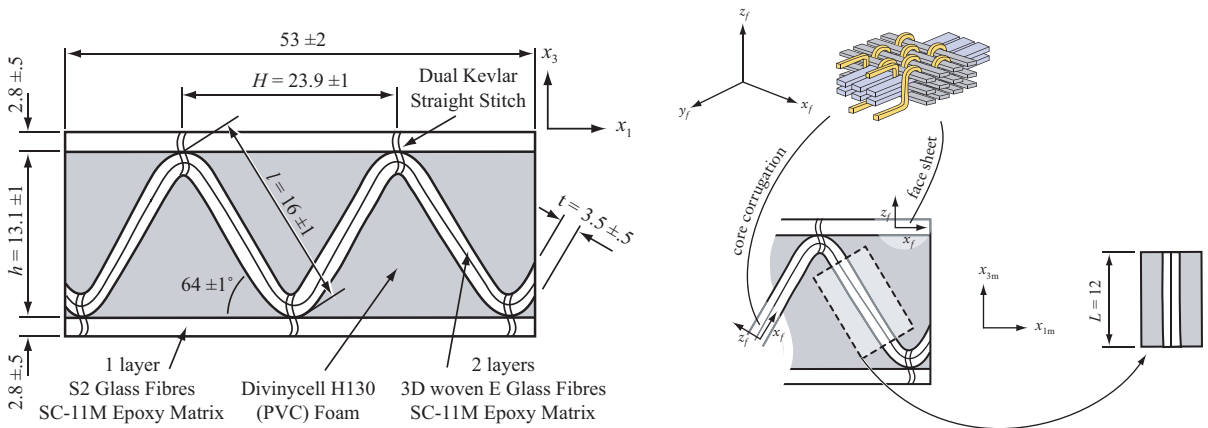


Figure 1. Left: Sketch of the corrugated core test specimens with all leading dimensions and materials used for the various components labelled. Right: Sketch illustrating the 3D fibre lay-ups in the specimens and the geometry of the test coupon used to investigate material properties of the corrugated core strut material. The coordinate systems referred to in the text are included in the figure and all dimensions are in mm.

tows in the weft direction, two tows in the warp direction and a z -yarn, all of the same fibre material. The fibre orientations in the core and face sheets are illustrated in Figure 1, right.

The corrugated core comprised struts of length $l = 16 \pm 1$ mm, thickness $t = 3.5 \pm 0.5$ mm, spaced at $H = 23.9 \pm 1$ mm. The resulting sandwich core thickness is $h = 13.1 \pm 1$ mm and has a relative density (defined here as the volume fraction of space occupied by corrugated core) $\bar{\rho} \approx 33\%$; see Figure 1, left. The variations in the dimensions are due to manufacturing variability and denote the as-measured maximum and minimum dimensions for all specimens tested in this study.

Fabrication process. The fabrication process is illustrated in Figure 2. The E-glass fabric was conformed around equilateral triangular prisms of Divinycell H130 PVC foam to form corrugations. The apexes of these corrugations were stitched to the S2-glass face sheets with Kevlar 29, size 69 thread, using a approximately 6 stitches per cm of a dual straight stitch. This whole assembly was then vacuum bagged and resin infiltrated with SC-11M epoxy (Applied Poleramic Inc., Benicia, CA 94510, USA). The SC-11M epoxy was supplied by Applied Poleramic Inc. (Benicia, California). It is a two component, two-phase (rubber toughened) system developed for shock loading applications and vacuum assisted resin transfer moulding manufacturing techniques. After mixing, the epoxy system had a viscosity of 900 cps, sufficient to permit vacuum assisted infiltration of a $500 \text{ mm} \times 500 \text{ mm}$ corrugated glass core panel in 30 minutes. The panels were then cured at 72°C for 6 hours. Test specimens approximately $53 \text{ mm} \times 53 \text{ mm}$ with the corrugated core arranged as shown in Figure 1, left, were then cut from these panels using a diamond cutting wheel.

In order to investigate the effect of the Divinycell foam core, specimens were also manufactured without the foam filling. Subsequently, the specimen with and without the foam filling will be referred to as the *filled* and *unfilled* specimens, respectively. In order to ensure that the unfilled specimens had the same corrugation geometry and had undergone an identical process cycle to the filled specimens, the foam filling was removed from the fully cured specimens by melting with a hot bar. This method resulted in minimal damage occurring to the corrugations and faces. The areal densities of the sandwich cores (not inclusive of faces) were 5.79 and 4.66 kg m^{-2} for the *filled* and *unfilled* geometries respectively. Additionally, sandwich specimens of the same dimensions as the corrugated cored specimens ($53 \text{ mm} \times 53 \text{ mm}$) were fabricated using just the Divinycell H130 PVC foam core.

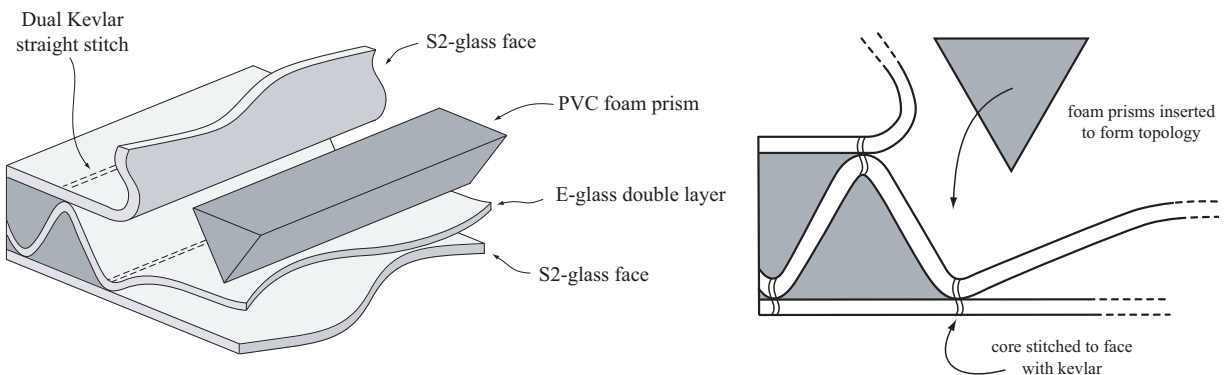


Figure 2. Sketch of the process used to assemble the dry (uninfused) corrugated cores.

3. Experimental protocol

The quasistatic and dynamic compressive responses of the *filled* and *unfilled* corrugated cores were measured along with the corresponding compressive responses of the parent infused E-glass material comprising the struts of the corrugated core.

Specimen configurations. To measure the quasistatic and dynamic compressive responses of the infused E-glass material comprising the struts of the corrugated core, rectangular specimens of height $L = 12$ mm were cut out from the filled sandwich core as shown in Figure 1, right. These 12 mm high specimens were sufficiently stocky that under compression, Euler buckling was not the operative collapse mode and the measured responses were representative of the material rather than structural behaviours. These specimens were then compressed along the x3m direction in order to determine the axial compressive response of the strut material. As seen in the figure, some foam remained attached to the sides of the cut out rectangular specimens: since this foam had a negligible contribution to the axial compressive response of the specimen, we did not attempt to scrape it off so as to avoid any damage to the underlying composite.

The compressive tests on the sandwich specimens were conducted on the 53 mm \times 53 mm sandwich specimens sketched in Figure 1, left. Initial compression experiments on these specimens exposed a failure mode that involved the breaking of the Kevlar stitches and lateral spreading of the corrugated core as shown in Figure 3a. This failure mode, while active towards the edges of a large corrugated core sandwich panel, will not be the dominant mode over the central section. We thus sought to avoid this failure mode and investigate the compressive response of the corrugated core, absent lateral spreading. This was accomplished by using the lateral steel confinement set-up as shown in Figure 3b. It is worth noting here that this confinement set-up restricted the compression of the sandwich core to a nominal compressive strain of less than 70%.

Quasistatic compression. The quasistatic compression tests were conducted in a screw-driven test machine at a nominal applied strain rate of 10^{-3} s^{-1} . The applied load was measured using the load cell of the test machine and used to obtain the applied stress while the through-thickness compressive strains

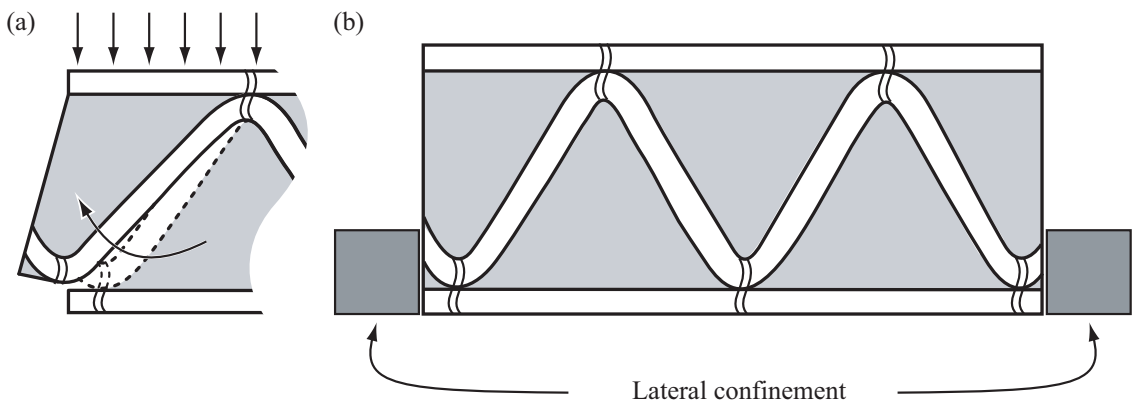


Figure 3. (a) Sketch illustrating the failure of the Kevlar stitches resulting in the lateral spreading of the corrugated core in a compression test. (b) Sketch of the lateral confinement used to prevent the failure mode illustrated in (a).

were obtained from laser extensometer measurements. Unloading-reloading cycles were also conducted in order to extract the compressive modulus of the specimens.

Dynamic compression. The dynamic out-of-plane compressive responses of the corrugated sandwich core, the strut material specimens and the H130 foam were measured from a series of direct impact tests in which the forces on the face distal from the impact were measured via a strain-gauged Kolsky bar [1949]. The specimens were placed centrally on the stationary Kolsky bar and the striker bar fired at the specimen from a gas gun as sketched in Figure 4 for the corrugated core specimens and strut material specimens respectively. The force transmitted by the specimen was measured as function of time for a range of impact velocities of the striker bar.

The kinetic energy of the projected striker governs the level of compression attained and the imposed transient velocity at the impacted end of the specimen. We wished to compress the specimens at an approximately constant velocity and chose the striker masses accordingly. It was therefore necessary to impact the samples with an initial momentum that was large compared to the change in momentum due to the dynamic resistive forces offered by the samples. The impact experiments were performed at velocities ranging from 25 ms^{-1} to 150 ms^{-1} . In the experiments on sandwiches conducted at low velocity ($v_0 \leq 50 \text{ ms}^{-1}$) a striker of mass $M = 2.5 \text{ kg}$ was employed, while a striker of mass $M = 0.75 \text{ kg}$ sufficed for the high velocity $v_0 > 50 \text{ ms}^{-1}$ experiments. For the materials test, a striker of mass $M = 0.1 \text{ kg}$ was sufficient for all velocities: high-speed photographs taken during these experiments confirm that these striker masses are sufficient to provide almost constant velocity compression for nominal compressive strains of up to 40%.

The striker was given the required velocity by firing it from a gas gun of barrel length of 4.5 m. No sabot was employed as the cylindrical strikers had a diameter equal to the inner diameter of the gun

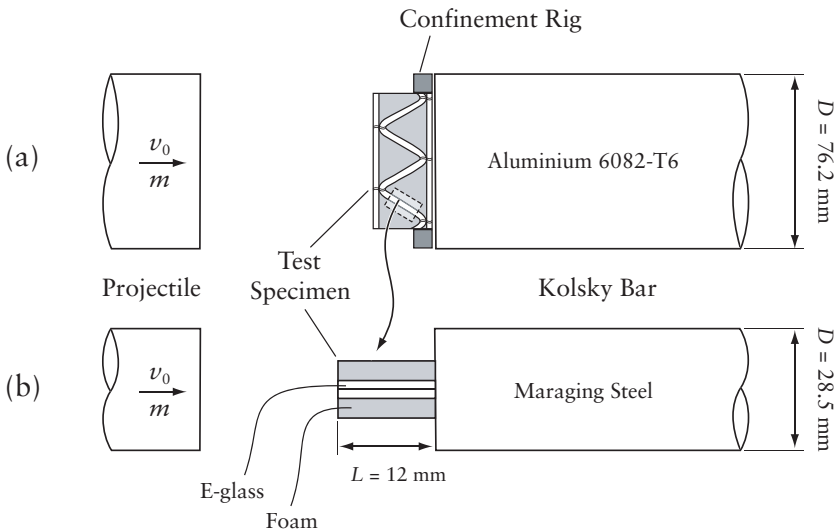


Figure 4. Sketches of the Kolsky bar setup arrangements for dynamic testing of the (a) corrugated core specimens and (b) the E-glass test coupons cut from the struts of the corrugated cores.

barrel and also equal to the diameter of the Kolsky bar. The bursting of copper shim diaphragms formed the breech mechanism of the gun. The impact experiments were performed at velocities ranging from approximately 10 ms^{-1} to 150 ms^{-1} . The velocity of the projectile was measured at the exit of the barrel using laser-velocity gates and the impacted end of the Kolsky bar was placed 100 mm from the open end of the gun barrel.

The set-up of the Kolsky pressure bar is standard. A circular cylindrical bar of length 2.0 m was used. The pressure history on the impacted end of the bar was measured by diametrically opposed axial strain gauges placed approximately 10 diameters from the impact end of the bar. The elastic strain histories in the bars were monitored using the two 120Ω TML foil gauges of gauge length 1 mm in a half-Wheatstone bridge configuration. A strain bridge amplifier of cut-off frequency 500 kHz was used to provide the bridge input voltage and a digital storage oscilloscope was used to record the output signal. The bridge system was calibrated dynamically over the range of strains measured during the experiments and was accurate to within 3%. Two separate Kolsky bars were used for testing the corrugated core specimens and the material test coupons (Figure 1, right), as follows:

- (i) a 76.2 mm diameter bar from aluminium alloy (AL-P6082T6, yield strength 310 MPa) was used in the corrugated core tests, while
- (ii) a 28.5 mm, diameter bar from maraging steel (yield strength exceeding 1000 MPa) was used in the material coupon tests.

These two different diameter bars were used so as to ensure that the difference between the cross-sectional areas of the specimens and the Kolsky bars were kept to a practical minimum. The longitudinal elastic wave speed was measured at 5092 ms^{-1} in the aluminium alloy bar, and 4906 ms^{-1} in the maraging steel bar. Taking into account that the strain gauges are placed approximately 10 bar diameters from the impacted end, this gives a time-window of $487 \mu\text{s}$ and $781 \mu\text{s}$ in the aluminium and steel Kolsky bars, respectively before elastic reflections from the distal end of the bar complicated the measurement of stress.

The response time and accuracy of the measurement system were gauged from a series of calibration tests. We report the result of one such representative test on the maraging steel Kolsky bar. A maraging steel striker of diameter 28.4 mm and length 460 mm was fired at the Kolsky bar at a velocity $v_0 = 6.6 \text{ ms}^{-1}$. The measured stress versus time response measured by the strain gauges on the Kolsky bar is plotted in Fig.5. With time $t = 0$ corresponding to the instant of impact, the stress pulse arrives at the gauge location at $t = 58 \mu\text{s}$. Elastic wave theory predicts that the axial stress in the bar is $\rho cv_0/2 = 131 \text{ MPa}$, where ρ and c are the density and longitudinal elastic wave speed of steel respectively. The measured peak value of the stress is within 1% of this prediction. However, the measurement system has a finite response time, with the stress rising to this peak value in approximately $13 \mu\text{s}$ (see the insert in Figure 5). This rise time places an operational limit on measuring the dynamic response of the specimens. It becomes significant at the higher velocities because significant compression of the specimen is achieved within the first $5 \mu\text{s}$. The measured stress in the calibration test drops back to zero at $t = 273 \mu\text{s}$; due to the reflection of the elastic wave from the distal end of the striker bar.

In a number of the experiments, high-speed photographic sequences were taken using a Phantom V12 camera, thereby allowing observation of the deformation process.

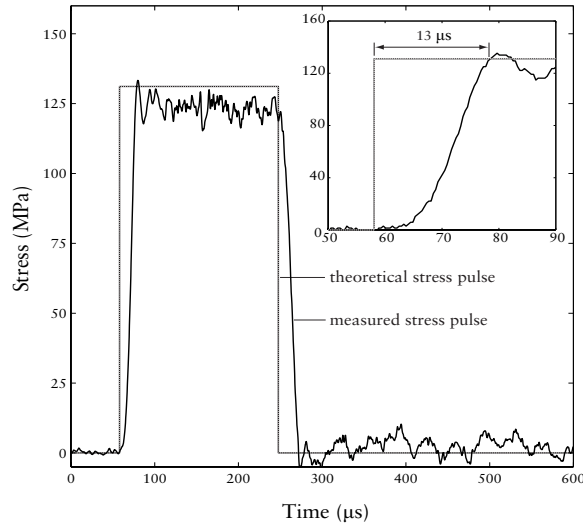


Figure 5. Stress versus time history measured in the $D = 28.5$ mm maraging steel Kolsky bar during a calibration test in which a 460 mm long steel striker ($D = 28.5$ mm) was fired at the Kolsky bar at $v_0 = 6.6 \text{ ms}^{-1}$. The theoretical prediction based on 1D elastic wave theory is included, along with a magnified graph of the stress pulse's onset.

4. Quasistatic response

The measured compressive responses of the corrugated core strut wall material are plotted in [Figure 6](#), left. The material test coupons were compressed along the x_{3m} direction (refer to [Figure 1](#), right), which corresponds to the x_f fibre direction of the fabric. Results from three repeat tests are shown to indicate

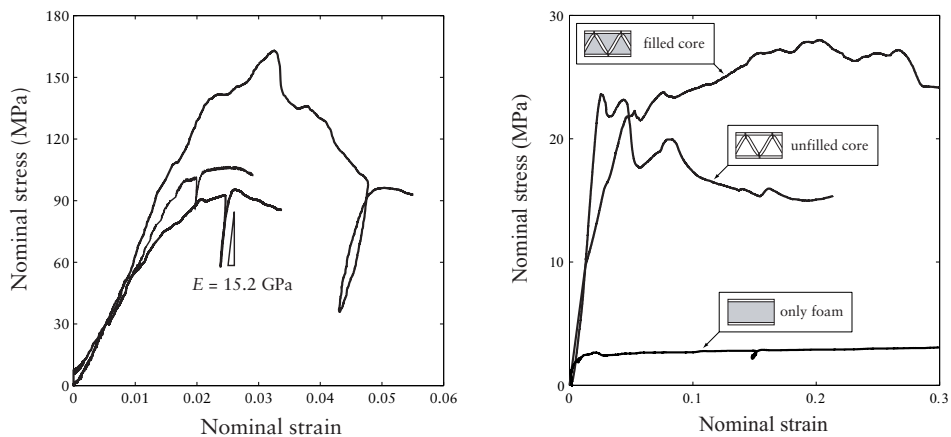


Figure 6. The measured quasistatic stress versus strain responses of the E-glass composites comprising the struts of the corrugated cores (left) and the filled, unfilled corrugated cores and the H130 Divinycell foam cores (right). The compressive response of the E-glass composite was measured along the x_f direction (see [Figure 1](#), right).

the variability in the measured responses: this scatter is mainly a result of manufacturing variability that resulted in variations in the amount of infused matrix from specimen to specimen. The average measured peak strength was approximately $\sigma_s = 100$ MPa while the compressive modulus of the specimens was determined to be about $E_s = 15$ GPa. Photographs of two representative deformed specimens at a nominal compressive strain of approximately 3% are shown in Figure 7a: a clear microbuckle is visible, confirming that the peak strength measured in these quasistatic experiments is set by the microbuckling strength of the E-glass composites.

Measurements of the quasistatic compressive responses of the *filled* and *unfilled* corrugated cores are plotted in Figure 6, right, along with the compressive response of the H130 Divinycell foam. Following an initial linear elastic response, a nonlinear response sets in at about 22 MPa and 23 MPa for the *filled* and *unfilled* cores respectively. However, while the *unfilled* core then displays a softening response the *filled* core exhibits a moderate hardening. The H130 foam is much weaker than the corrugated cores with a plateau strength around 2.5 MPa.

A montage of photographs showing the deformation of the *filled* and *unfilled* corrugated cores is included in Figure 7b. The first microbuckle develops in both cores at a compressive strain of about 3% and is reminiscent of the microbuckle observed in the compressive test performed on the strut wall material (Figure 7a). This suggests that the onset of nonlinearity in the compressive responses of the cores

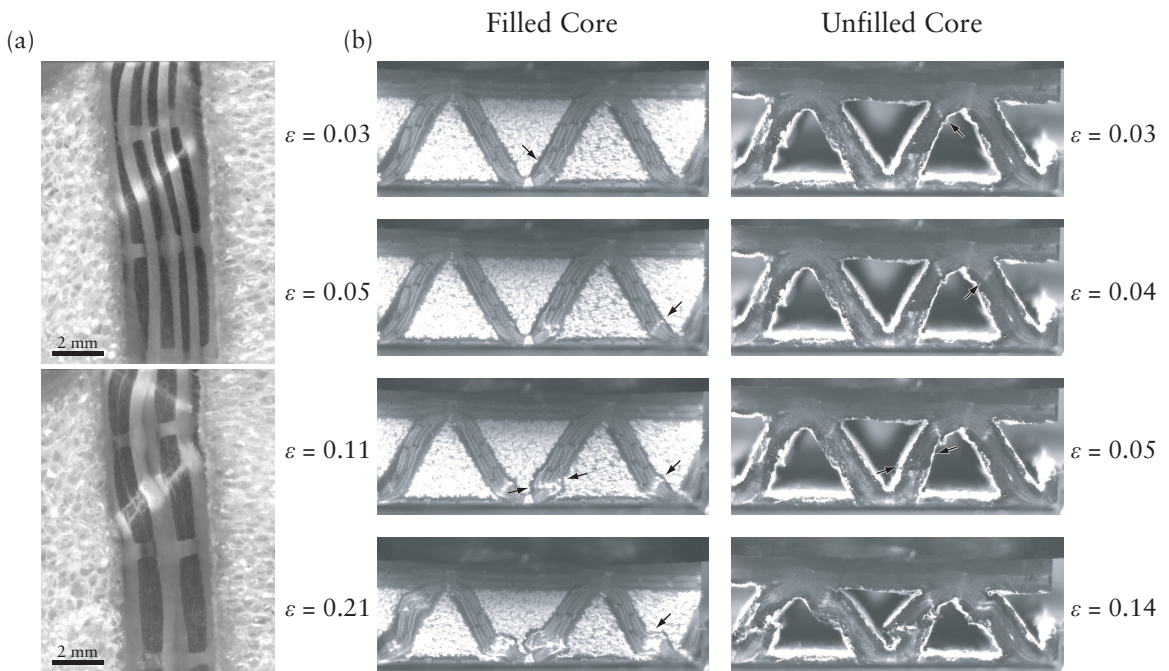


Figure 7. (a) Two representative photographs (at a compressive strain of about 3%) showing the microbuckle failure of the E-glass composite during the quasistatic compression of the test coupons. (b) A montage of photographs showing the sequences of deformation during the quasistatic compression of the filled and unfilled corrugated core test specimens.

is a result of the microbuckling of the E-glass composite material. Additional microbuckles subsequently appear in adjacent struts and the struts then begin to shear over. This shearing process is impeded by the H130 foam in the *filled* core which results in the mild hardening observed in [Figure 6](#), right. By contrast, the shearing of the *unfilled* core is unimpeded, resulting in a softening response after the onset of microbuckling in the struts.

The peak strength σ_p of the *unfilled* corrugated core is expected to be set by either the Euler buckling or microbuckling of the struts and given in terms of the core geometry and strut wall material properties by [\[Côté et al. 2006\]](#)

$$\sigma_p = \begin{cases} \frac{\pi^2}{6} \left(\frac{t}{l}\right)^3 \frac{h}{H} E_s & \text{if } \frac{\sigma_s}{E_s} > \frac{\pi^2}{12} \left(\frac{t}{l}\right)^2, \\ 2 \frac{t}{l} \frac{h}{H} \sigma_s, & \text{otherwise.} \end{cases} \quad (1)$$

This expression clearly shows that the peak strength of the corrugated core investigated here is set by the microbuckling of the struts. Note that this does not involve any modelling of the microbuckle stress σ_s itself but rather takes as an input, the experimentally measured value. Inserting the strut geometry and material parameters in (1) predicts that $\sigma_p = 24$ MPa and is in good agreement with the measurements.

Foam support is expected to enhance the Euler buckling strength of the struts of the corrugated core [\[Cartié and Fleck 2003\]](#). Given that the strength of the unfilled corrugated core is set by the microbuckling strength of the E-glass composite struts, it is not surprising that the initial “yield” strength is unaffected by the foam filling we anticipate that the peak strength of an E-glass corrugated core with significantly more slender struts (i.e., lower relative density) will be enhanced with a foam filling.

5. Dynamic response

Strut wall material. The measured dynamic compressive responses of the $L = 12$ mm high E-glass specimens cut from the strut walls is plotted in [Figure 8](#), left, for impact velocities in the range $25 \text{ ms}^{-1} \leq v_0 \leq 150 \text{ ms}^{-1}$. In the figures the compressive responses are plotted in terms of the nominal stress as measured at the distal end of the specimen (i.e., the nonimpacted end of the specimen) versus the applied nominal strain $v_0 t/L$, where t is the time measured after the initiation of deformation. The measured peak stress σ_f is seen to increase from about 200 MPa for $v_0 = 25 \text{ ms}^{-1}$ to 400 MPa at $v_0 = 150 \text{ ms}^{-1}$. It is worth noting here that the peak stress is achieved at $t \approx 12 \mu\text{s}$ for $v_0 \geq 50 \text{ ms}^{-1}$: this time is approximately equal to the response time of the Kolsky bar apparatus (see [Figure 5](#)) and thus while the peak stress measurements reported here are accurate, the data cannot be used to extract the dynamic modulus of the E-glass composite.

Given the measured Young’s modulus E_s and the density (2550 kg m^{-3}) of the E-glass composite, we anticipate that the longitudinal elastic wave speed for the E-glass composite is approximately 4000 ms^{-1} . Thus, within the $12 \mu\text{s}$ required to achieve peak stress, about 4 elastic reflections take place in the $L = 12$ mm specimen. It is therefore reasonable to assume that the specimen is in axial equilibrium at the instant that the peak stress is measured, and that the measured peak strength is a material property independent of the specimen dimensions. Given this, we summarise the measured peak strengths σ_f as a function of the applied nominal strain rate $\dot{\epsilon} \equiv v_0/L$ in [Figure 8](#), right. The measurements are well-fitted by a bilinear curve with the peak strength increasing linearly with strain rate for $\dot{\epsilon} \leq 4000 \text{ s}^{-1}$ and reasonably rate-independent at higher values of $\dot{\epsilon}$.

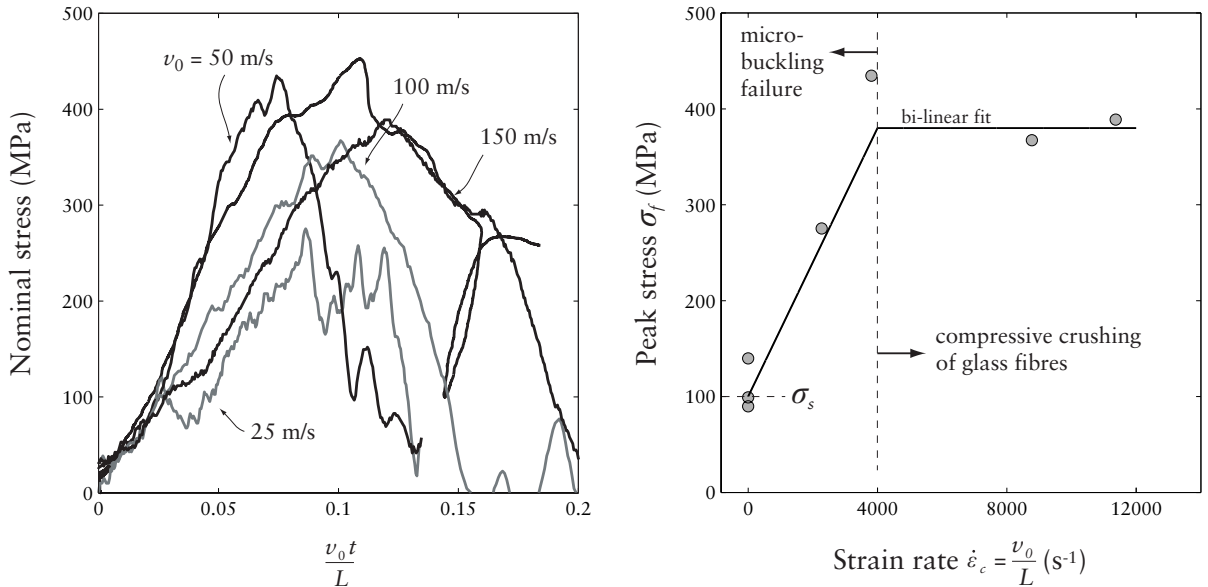


Figure 8. Left: The measured dynamic stress versus nominal strain responses of the E-glass material coupons for a range of impact velocities. Right: Summary of the measured peak stresses E-glass specimens as a function of applied strain rate. The compressive response of the E-glass composite was measured along the x_f direction (see Figure 1, right).

Recall that the peak strength under quasistatic loading is set by the microbuckling failure stress. Increasing the applied strain rate results in stabilisation of the microbuckle failure mode resulting in the peak strength increasing with $\dot{\epsilon}$. This stabilisation can be due to either (i) inertial stabilisation of the buckling or (ii) matrix strain rate effects. Theoretical work by [Fan and Slaughter \[1997\]](#) suggests that inertial effects become significant for strain rates greater than about 4000 s^{-1} . We therefore expect that this measured rate sensitivity is due to matrix strain rate effects. The increase in the microbuckling strength due to matrix strain rate effects can be understood as follows. An approximate expression for the microbuckling strength in terms of the matrix shear strength τ_y is, according to [\[Argon 1972\]](#),

$$\sigma_c = \frac{\tau_y}{\bar{\phi}}, \quad (2)$$

where $\bar{\phi}$ is the fibre misalignment angle. Thus, the enhanced matrix shear strength at higher strain rates is expected to also increase the microbuckling strength σ_c . The measurements indicate that the measured peak strength rises to a maximum of about 400 MPa. This maximum peak strength is not set by microbuckling of the fibres but rather by the compressive crush strength of glass fibres. This is rationalised as follows. The volume fraction of fibres in the direction of the loading is about 20%, which implies that the corresponding fibre stress is about 2 GPa [\[CES 2009\]](#). This is equal to the compressive crush strength of glass, confirming that the maximum compressive strength of the E-glass composites at high strain rates is governed by the compressive crush strength of the constituent glass fibres.

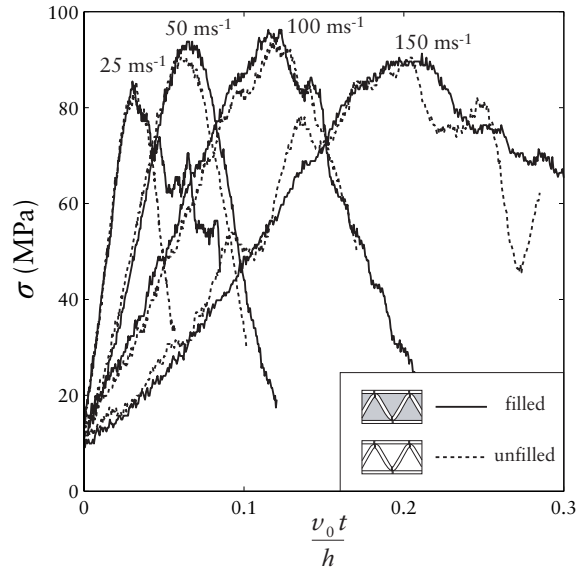


Figure 9. The measured dynamic stress versus nominal strain responses of the filled and unfilled corrugated core specimens. The stresses are measured on the rear faces of the specimen distal from the impacted face.

Corrugated cores. The measured dynamic compressive responses of the *filled* and *unfilled* corrugated cores are plotted in Figure 9 using axes of the compressive stress σ versus nominal strain $v_0 t/h$, where time $t = 0$ corresponds to the instant that the striker bar impacts the specimen. Recall that the stress σ is measured on the rear face of the specimen distal from the impacted face. The responses of the *filled* and *unfilled* specimens are almost identical with the measured peak stress of approximately 90 MPa over the velocity range $25 \text{ ms}^{-1} \leq v_0 \leq 175 \text{ ms}^{-1}$. Again we note that the peak stress is observed to occur at time t in the range $15 \mu\text{s} - 18 \mu\text{s}$. This is similar to the response time of the Kolsky bar apparatus (Figure 5) and so these measurements again cannot be used to infer the dynamic compressive moduli of the specimens.

Montages showing the sequence of deformation of the *filled* and *unfilled* corrugated cores impacted at $v_0 = 50 \text{ ms}^{-1}$ and 150 ms^{-1} are included in Figures 10 and 11, respectively. While the deformation modes of the corrugated cores impacted at 50 ms^{-1} look similar to those observed under quasistatic deformation (Figure 7b), a marked difference is seen when $v_0 = 150 \text{ ms}^{-1}$. At this high velocity, deformation is more localised near the impacted face with the corrugated core “stubbing” against the impacted face. This deformation mode was also observed in metallic corrugated cores by [Tilbrook et al. 2007]. Given this highly localised deformation near the impacted face we anticipate that the stresses on the impacted face are higher than the stresses measured at the distal end, i.e., the specimen is not in axial equilibrium in line with the finite element calculations of [Tilbrook et al. 2007]. These differences between the stresses on the impacted and distal surfaces cannot be measured in this direct Kolsky bar set-up as the inertia of the impacted face-sheet dominates the measurements; see [Tilbrook et al. 2007] for further discussion. We emphasise that this localised deformation mode was observed only for $v_0 \geq 150 \text{ ms}^{-1}$; at the lower impact

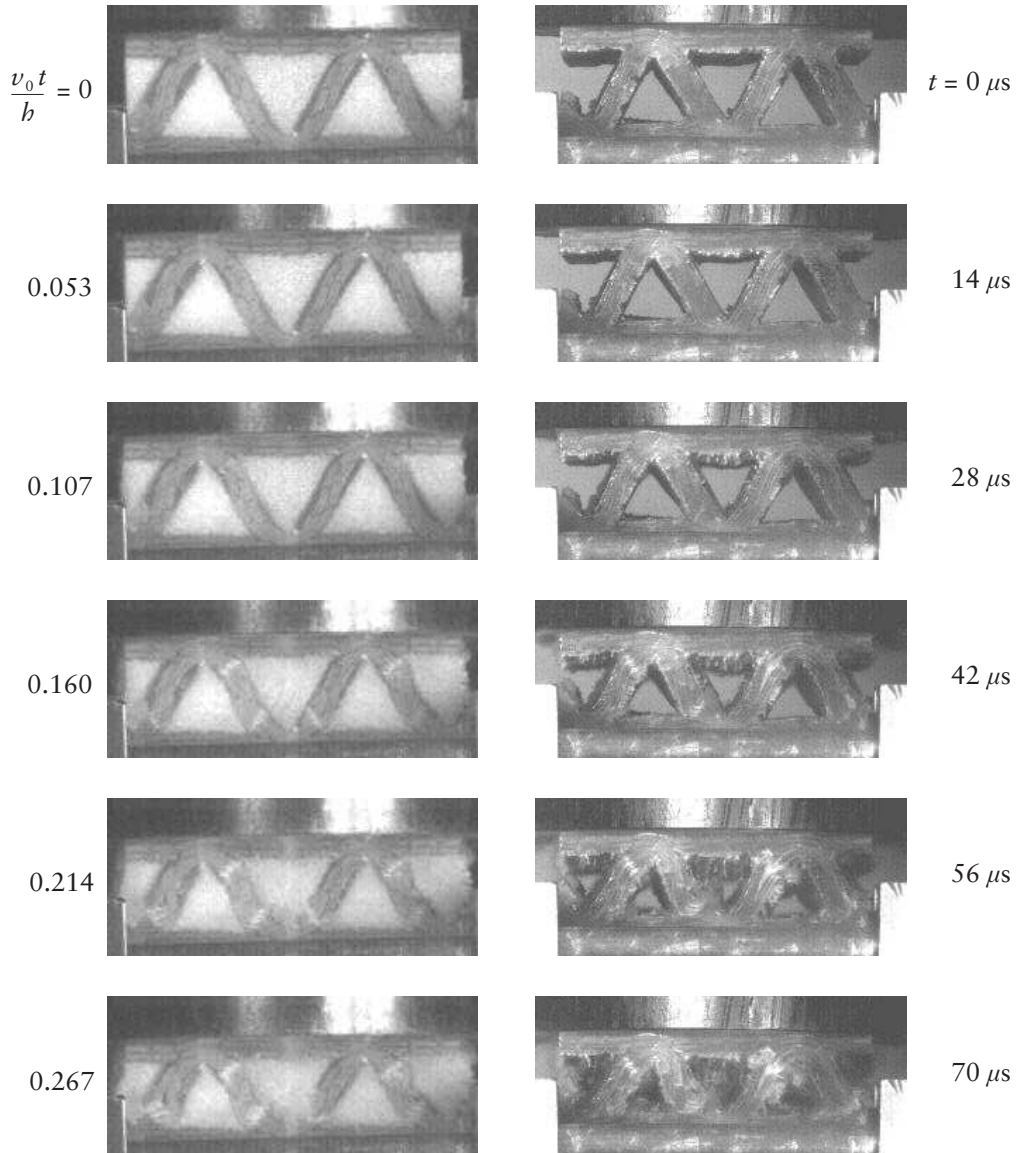


Figure 10. Deformation sequences in the filled (left) and unfilled (right) corrugated core specimens impacted at a velocity $v_0 = 50 \text{ ms}^{-1}$. Impact occurs on the top face of the specimens in the photographs.

velocities the deformation was reasonably uniform through the core, suggesting that the specimens were in axial equilibrium at lower impact velocities.

The measured peak stresses on the rear face of the filled and unfilled corrugated cores specimens (i.e., distal from the impacted face) are plotted in [Figure 12](#) as a function of the impact velocity v_0 and applied strain rate $\dot{\epsilon}_c \equiv v_0/h$ (upper scale). The dependence of the peak strengths of the corrugated cores on strain rate is similar to the parent strut wall material ([Figure 8](#), right), with the peak stress increasing with strain

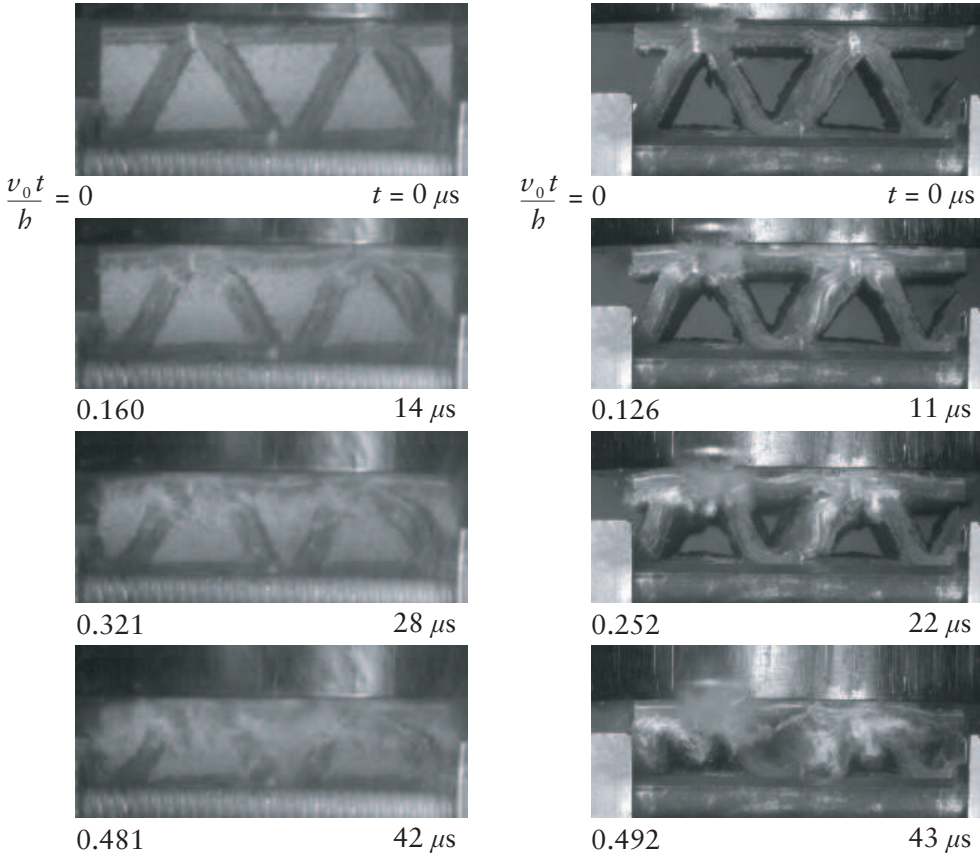


Figure 11. Deformation sequences in the filled (left) and unfilled (right) corrugated core specimens impacted at a velocity $v_0 = 150 \text{ ms}^{-1}$. Impact occurs on the top face of the specimens in the photographs.

rate for $\dot{\epsilon}_c < 4000 \text{ s}^{-1}$ and being reasonably rate insensitive at higher values of $\dot{\epsilon}_c$. This clearly indicates that there exist two regimes of deformation: (i) microbuckling of the strut wall for $\dot{\epsilon}_c < 4000 \text{ s}^{-1}$ and (ii) compressive crushing of the glass fibres at higher strain rates. We proceed to report a simplified analysis for relating the peak strengths of the corrugated cores to the measured E-glass properties (Figure 8, right). This is made possible by the fact that (i) Euler buckling is not the operative failure mode over the entire range of impact velocities investigated here and (ii) except at the highest impact velocity ($v_0 \geq 150 \text{ ms}^{-1}$) the specimens are in axial equilibrium. The peak strength of the corrugated core as a function of the applied strain rate $\dot{\epsilon}_c$ is then specified from (1) as

$$\sigma_P(\dot{\epsilon}_c) = 2 \left(\frac{t}{l} \right) \left(\frac{h}{H} \right) \sigma_f(\dot{\epsilon}), \quad \text{where } \dot{\epsilon} = \dot{\epsilon}_c \left(\frac{h}{l} \right)^2. \quad (3)$$

The strut material strength as a function of strain rate, $\sigma_f(\dot{\epsilon})$, is given in Figure 8, right. The predictions of Equation (3) are plotted in Figure 12. Two bounds on the predictions are shown based on the measured variations of the specimen dimensions (Figure 1, left). These predictions adequately bound the measured

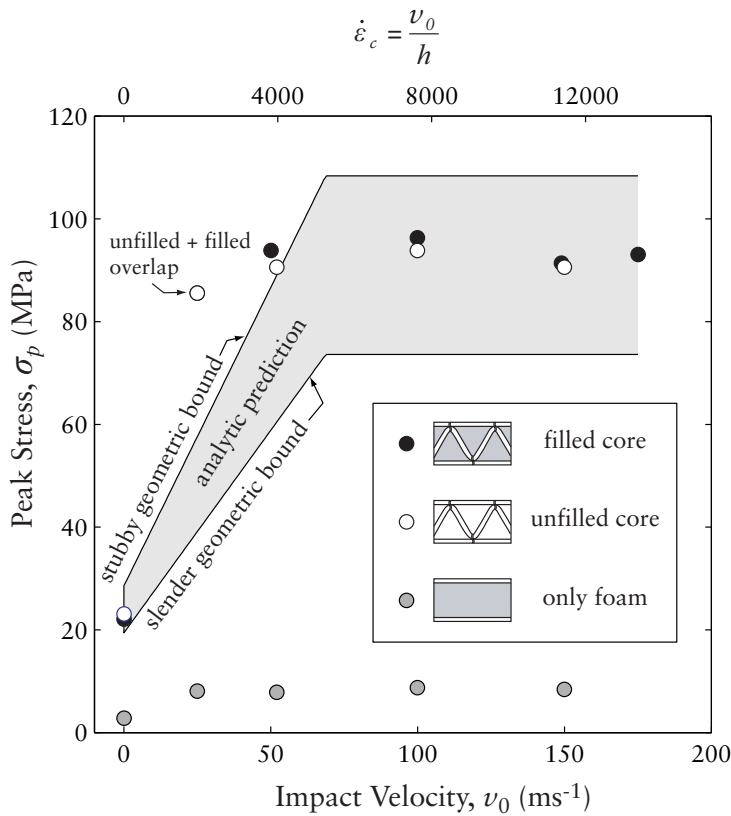


Figure 12. Summary of the measured peak stresses in the filled and unfilled corrugated core specimens as function of the impact velocity (lower x-axis) and applied nominal strain rate (upper x-axis). The measured peak stresses in the H130 Divinycell foam are also included.

dynamic peak strengths of the *filled* and *unfilled* corrugated cores, indicating that over the range of impact velocities investigated here, the strain rate sensitivity of the high relative density corrugated cores is governed by the rate sensitivity of the parent strut wall material and is not significantly affected by inertial stabilisation against elastic buckling as observed in the low relative density metallic corrugated cores investigated by [Tilbrook et al. 2007]. The exceptions are data points at 25 ms^{-1} , that fall outside of the bounds of the analytical prediction. The discrepancy here is attributed to the simplicity of the model which assumes an empirically based bilinear relationship of strength with strain rate which is not expected to be accurate near the transition in the strain rate response.

Recall that in the present study, the struts of the corrugated core are sufficiently stubby as to not fail by Euler buckling, even under quasistatic loading. This meant that the dynamic tests were unable to reveal strength enhancements due to microinertial effects but rather only displayed strength enhancements due to material strain rate effects. Tests on corrugated cores with significantly more slender struts would enable us to investigate the microinertial effects in composite cores: current manufacturing methods preclude this at present but this is suggested as a topic for future investigation.

6. Concluding remarks

E-glass corrugated sandwich cores of relative density $\bar{\rho} \approx 33\%$ were manufactured by wrapping 3D woven E-glass fabric over triangular prismatic PVC foam inserts and then stitching the assembly to S2-glass face sheets. The entire assembly was then infused with an epoxy resin. The foam inserts were scraped out of some of the specimens and the dynamic out-of-plane compressive stresses on the rear faces of the *filled* and *unfilled* corrugated core specimens measured at impact velocities ranging from quasistatic to 175 ms^{-1} using a direct impact Kolsky bar.

The corrugated cores had stubby struts and failed by microbuckling of these struts under quasistatic compression. The foam filling had only a minor effect, stabilising the postpeak strut failure response of the corrugated core. Under dynamic loading, the deformation of the specimens was reasonably uniform through the core thickness for impact velocities less than about 150 ms^{-1} ; at higher impact velocities deformation was localised near the impacted face, suggesting that the specimens were not in axial equilibrium and shock effects came into play. Foam filling had nearly no effect on the measured dynamic properties of the corrugated cores with the peak stresses of both the strut wall material and corrugated cores increasing approximately linearly with strain rate for applied strain rates less than about 4000 s^{-1} . This increase was attributed to the strain rate sensitivity of the composite matrix that stabilised the microbuckling failure mode of the E-glass composite. At higher applied strain rates the response was reasonably rate insensitive with compressive crushing of the glass fibres being the dominant failure mode. A simple model utilising the measured dynamic properties of the strut wall material accurately predicts the measured peak strengths of the *filled* and *unfilled* corrugated cores.

References

- [Argon 1972] A. S. Argon, “Fracture of composites”, *Treatise Mater. Sci. Technol.* **1** (1972), 79–114.
- [Cartié and Fleck 2003] D. D. Cartié and N. A. Fleck, “The effect of pin reinforcement upon the through-thickness compressive strength of foam-cored sandwich panels”, *Compos. Sci. Technol.* **63**:16 (2003), 2401–2409.
- [CES 2009] “CES Materials Selector Database”, *Granta Design Limited, UK* (2009).
- [Côté et al. 2006] F. Côté, V. S. Deshpande, N. A. Fleck, and A. G. Evans, “The compressive and shear responses of corrugated and diamond lattice materials”, *Int. J. Solids Struct.* **43**:20 (2006), 6220–6242.
- [Deshpande et al. 2006] V. S. Deshpande, A. Heaver, and N. A. Fleck, “An underwater shock simulator”, *Proc. R. Soc. Lond. A* **462**:2067 (2006), 1021–1041.
- [Dharmasena et al. 2008] K. P. Dharmasena, H. N. G. Wadley, Z. Y. Xue, and J. W. Hutchinson, “Mechanical response of metallic honeycomb sandwich panel structures to high-intensity dynamic loading”, *Int. J. Impact Eng.* **35**:9 (2008), 1063–1074.
- [Dharmasena et al. 2009] K. Dharmasena, D. Queheillalt, H. Wadley, Y. Chen, P. Dudt, D. Knight, Z. Wei, and A. Evans, “Dynamic response of a multilayer prismatic structure to impulsive loads incident from water”, *Int. J. Impact Eng.* **36**:4 (2009), 632–643.
- [Dharmasena et al. 2010] K. P. Dharmasena, D. T. Queheillalt, H. N. G. Wadley, P. Dudt, Y. Chen, D. Knight, A. G. Evans, and V. S. Deshpande, “Dynamic compression of metallic sandwich structures during planar impulsive loading in water”, *Eur. J. Mech. A Solids* **29**:1 (2010), 56–67.
- [Fan and Slaughter 1997] J. Q. Fan and W. S. Slaughter, “High strain rate compression of fiber composites”, *J. Mech. Phys. Solids* **45**:5 (1997), 731–751.
- [Ferri et al. 2006] E. Ferri, E. Antinucci, M. Y. He, J. W. Hutchinson, F. W. Zok, and A. G. Evans, “Dynamic buckling of impulsively loaded prismatic cores”, *J. Mech. Mater. Struct.* **1**:8 (2006), 1345–1365.

- [Finnegan et al. 2007] K. Finnegan, G. Kooistra, H. N. G. Wadley, and V. S. Deshpande, “The compressive response of carbon fiber composite pyramidal truss sandwich cores”, *Int. J. Mater. Res. Z. Metallkd.* **12** (2007), 1264–1272.
- [Fleck and Deshpande 2004] N. A. Fleck and V. S. Deshpande, “The resistance of clamped sandwich beams to shock loading”, *J. Appl. Mech. (ASME)* **71**:3 (2004), 386–401.
- [Kazemahvazi and Zenkert 2009] S. Kazemahvazi and D. Zenkert, “Corrugated all-composite sandwich structures, I: modeling”, *Compos. Sci. Technol.* **69**:7–8 (2009), 913–919.
- [Kazemahvazi et al. 2009] S. Kazemahvazi, D. Tanner, and D. Zenkert, “Corrugated all-composite sandwich structures, II: failure mechanisms and experimental programme”, *Compos. Sci. Technol.* **69**:7–8 (2009), 920–925.
- [Kolsky 1949] H. Kolsky, “An investigation of the mechanical properties of materials at very high rates of loading”, *Proc. Phys. Soc. B* **62**:11 (1949), 676–700.
- [Lankford 1995] J. Lankford, “The failure of fiber-reinforced ceramic-matrix composites under dynamic loading”, *JOM* **47**:5 (1995), 64–68.
- [Marasco et al. 2006] A. I. Marasco, D. D. R. Cartié, I. K. Partridge, and A. Rezai, “Mechanical properties balance in novel Z-pinned sandwich panels: out-of-plane properties”, *Compos. A Appl. Sci. Manuf.* **37**:2 (2006), 295–302.
- [Moongkhamklang et al. 2008] P. Moongkhamklang, D. M. Elzey, and H. N. G. Wadley, “Titanium matrix composite lattice structures”, *Compos. A Appl. Sci. Manuf.* **39**:2 (2008), 176–187.
- [Mori et al. 2008] L. F. Mori, D. T. Queheillalt, H. N. G. Wadley, and H. D. Espinosa, “Deformation and failure modes of i-core sandwich structures subjected to underwater impulsive loads”, *Exp. Mech.* **49**:2 (2008), 257–275.
- [Radford et al. 2007] D. D. Radford, G. J. McShane, V. S. Deshpande, and N. A. Fleck, “Dynamic compressive response of stainless-steel square honeycombs”, *J. Appl. Mech. (ASME)* **74**:4 (2007), 658–67.
- [Russell et al. 2008] B. P. Russell, V. S. Deshpande, and H. N. G. Wadley, “Quasistatic deformation and failure modes of composite square honeycombs”, *J. Mech. Mater. Struct.* **3**:7 (2008), 1315–1340.
- [Slaughter et al. 1996] W. S. Slaughter, J. Q. Fan, and N. A. Fleck, “Dynamic compressive failure of fiber composites”, *J. Mech. Phys. Solids* **44**:11 (1996), 1867–1890.
- [Tilbrook et al. 2007] M. T. Tilbrook, D. D. Radford, V. S. Deshpande, and N. A. Fleck, “Dynamic crushing of sandwich panels with prismatic lattice cores”, *Int. J. Solids Struct.* **44**:18–19 (2007), 6101–6123.
- [Wadley et al. 2008] H. Wadley, K. Dharmasena, Y. C. Chen, P. Dudt, D. Knight, R. Charette, and K. Kiddy, “Compressive response of multilayered pyramidal lattices during underwater shock loading”, *Int. J. Impact Eng.* **35**:9 (2008), 1102–1114.
- [Wei et al. 2008] Z. Wei, V. S. Deshpande, A. G. Evans, K. P. Dharmasena, D. T. Queheillalt, H. N. G. Wadley, Y. V. Murty, R. K. Elzey, P. Dudt, Y. Chen, D. Knight, and K. Kiddy, “The resistance of metallic plates to localized impulse”, *J. Mech. Phys. Solids* **56**:5 (2008), 2074–2091.
- [Xue and Hutchinson 2003] Z. Y. Xue and J. W. Hutchinson, “Preliminary assessment of sandwich plates subject to blast loads”, *Int. J. Mech. Sci.* **45**:4 (2003), 687–705.

Received 21 Oct 2009. Revised 8 Mar 2010. Accepted 14 Mar 2010.

BENJAMIN P. RUSSELL: bpr23@cam.ac.uk

University of Cambridge, Engineering Department, Trumpington Street, Cambridge, CB2 1PZ, United Kingdom

ADAM MALCOM: am4uz@virginia.edu

University of Virginia, Department of Materials Science and Engineering, Charlottesville, VA 22904, United States

HAYDN N. G. WADLEY: haydn@virginia.edu

University of Virginia, Department of Materials Science and Engineering, Charlottesville, VA 22904, United States

VIKRAM S. DESHPANDE: vsd@eng.cam.ac.uk

University of Cambridge, Engineering Department, Trumpington Street, Cambridge, CB2 1PZ, United Kingdom

EFFECTS OF SURFACE DEFORMATION ON THE COLLECTIVE BUCKLING OF AN ARRAY OF RIGID BEAMS ON AN ELASTIC SUBSTRATE

HAOJING LIN, ZIGUANG CHEN, JIASHI YANG AND LI TAN

We analyze the collective buckling of a row of rigid beams with their lower ends built into an elastic substrate. The beams interact among themselves through the deformation of the substrate. The present analysis is more sophisticated than previous ones in that the lower ends of the beams are allowed to move vertically and horizontally, in addition to rotation. From the linear theory of elasticity and rigid body statics, an eigenvalue problem is formulated and solved. Calculations showed that periodic deformations resulted atop the compliant substrate after restrictions on the beam base displacements were released. Consequently, the refined model found good match with the height measurements from Atomic Force Microscope (AFM). Our work suggests that both the compliant substrate and the interaction of neighboring beams through the deformation of the substrate dominate the collective buckling. Furthermore, these results contribute toward the understanding, design and application of soft nanostructures produced by soft lithography in a variety of fields.

1. Introduction

Periodic arrays of 100 nm thick and wide beams and walls composed of elastic polymers can be manufactured on a surface of the same material by soft lithography [Xia and Whitesides 1998], nanoimprint lithography [Chou et al. 1995; 1996] and other techniques. Thermal, electrical or magnetic features can also be added to the structures [Liu et al. 2010] such that they are useful in a variety of fields like optical gratings, sensor arrays, actuators, and nanofabrication. Due to the deformability of the soft structures and the substrates, structural instability is a common issue in soft lithography. This results in buckling or collapsing of the structures [Xia and Whitesides 1998; Chou et al. 1995; 1996; Delamarche et al. 1997; Schmid and Michel 2000; Evans et al. 2007], which seriously affects their functionality and limits their applications.

The buckling of soft nanostructures has aspects that are different from conventional structural engineering and it has recently caught wider attention. What is unique is that the substrate of the structures is very compliant so that neighboring structures interact through the deformation of the substrate. The results from the buckling analysis in conventional structural engineering are usually for a single beam [Greenhill 1881; Timoshenko 1936]. Some of the structural engineering results are relevant for the buckling of soft nanostructures, e.g., the buckling of a beam under its own weight [Greenhill 1881]; the buckling of a beam resting on an elastic foundation [Timoshenko 1936]; and the lateral torsional buckling of a high aspect ratio beam [Alfutov 2000]. The results from structural engineering on the buckling of elastic beams were used in [Hui et al. 2002] for the buckling of a single beam and the contact of two beams on a buckled surface in soft lithography, but the substrate deformation and the beam interaction

Keywords: buckling, nanostructures, beams, soft lithography.

through the substrate were not considered. Therefore the results in [Hui et al. 2002] can only provide limited understanding of the situation.

A major progress in the buckling analysis of periodic soft nanostructures was made in our recent work [Lin et al. 2007]. Due to the inclusion of the most basic and important mechanism into our theoretical model, i.e., neighboring beams interact through the deformation of the substrate, we were able to describe the most basic collective buckling behavior of the soft structures and obtain results qualitatively matching experimental findings. The model in [Lin et al. 2007] was later generalized and applied to the case of a two-dimensional array of rigid beams on an elastic foundation [Chen et al. 2008], a nonuniform one-dimensional array of rigid beams [Li et al. 2010], and a one-dimensional array of elastic beams [Feng and Li 2009; Lin et al. 2010].

In [Lin et al. 2007; Chen et al. 2008; Li et al. 2010; Feng and Li 2009; Lin et al. 2010], the beam bottoms in the substrate were allowed to rotate which is the major deformation, but their vertical and horizontal displacements were neglected. While this could describe the collective buckling of beam arrays, the restriction on beam bottom displacements renders the system too stiff. Therefore there remains an issue on the effect of horizontal and vertical displacements of the beam bottoms.

In this paper we generalize the analysis in [Lin et al. 2007] by removing the restrictions on the beam bottom displacements. The bottoms of the beams can move in both horizontal and vertical directions. The results show periodic deformations atop the compliant substrate and such behaviors closely match with the experimental evidence.

2. Mechanics model

Consider the structure shown in Figure 1, which consists of an array of rigid beams on an elastic substrate. Each beam represents the cross section of a wall that extends uniformly in the direction perpendicular to the plane of the paper. There is no displacement and no variation in this direction. A unit thickness of the structure in the direction perpendicular to the paper is taken. We have a so-called plane-strain problem in elasticity. Weight has often been considered as the cause of buckling [Hui et al. 2002; Sharp et al. 2004]. Other effects including van der Waals, Coulomb, or capillary forces could also contribute to the situation [Evans et al. 2007; Chuang et al. 2005; Hsia et al. 2005]. We will consider weight below as the

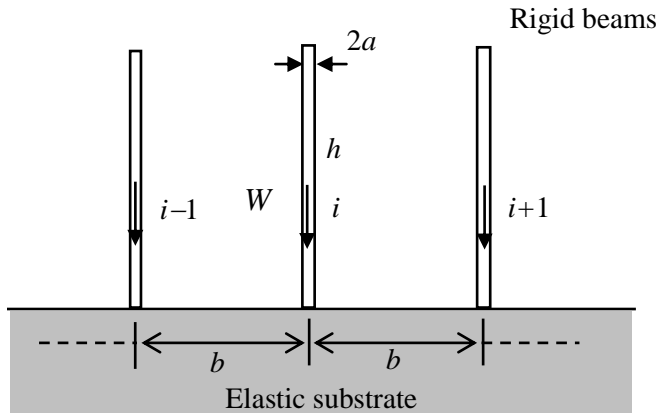


Figure 1. A system of rigid beams on an elastic substrate.

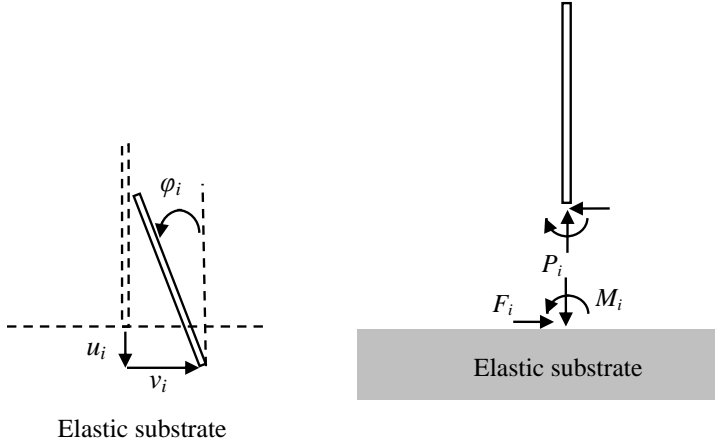


Figure 2. End displacements and end forces of a typical beam.

only load and the substrate deformability as the only interaction. Effectively other possible forces either modify the load or the interaction coefficients in our model. The weight of the beams is considered as the resultant of a uniformly distributed load. The intensity of the load is given by q per unit length of the beams. Let the height and width of the beams be h and $2a$, and the spacing between the center lines of two neighboring beams be b (see Figure 1). We have $q = \rho g 2a$. The weight $W = \rho g 2ah$ acts at the center of the beam. The beams are assumed to be rigid, as in [Lin et al. 2007; Chen et al. 2008; Li et al. 2010]. In contrast with these works (and also with [Feng and Li 2009] and [Lin et al. 2010]), here we allow the bottoms of the beams to move in both the horizontal and vertical directions, in addition to rotation. The substrate is modeled as an elastic half-space.

For the bottom of a typical beam, with index i , let the vertical and horizontal displacements be u_i and v_i , the vertical and horizontal forces P_i and F_i , the rotation ϕ_i , and the moment M_i (see Figure 2).

For simplicity we construct the two vectors

$$\mathbf{u}_i = \begin{Bmatrix} u_i \\ v_i \\ \phi_i \end{Bmatrix}, \quad \mathbf{f}_i = \begin{Bmatrix} P_i \\ F_i \\ M_i \end{Bmatrix}, \tag{1}$$

whose components are shown in Figure 2. Within the linear theory of elasticity, by superposition, we can write

$$\mathbf{u}_i = \sum_{j=1}^{\infty} \mathbf{A}_{ij} \mathbf{f}_j \approx \mathbf{A}_{i(i-1)} \mathbf{f}_{i-1} + \mathbf{A}_{ii} \mathbf{f}_i + \mathbf{A}_{i(i+1)} \mathbf{f}_{i+1}, \tag{2}$$

where the \mathbf{A}_{ij} are 3×3 matrices whose columns representing the substrate deformation at the i -th location due to a unit load at the j -th location only, the loads at all other locations being zero. The \mathbf{A}_{ij} can be derived from the theory of elasticity; see the Appendix. Equation (2) can be inverted to yield

$$\mathbf{f}_i = \sum_{j=1}^{\infty} \mathbf{B}_{ij} \mathbf{u}_j \approx \mathbf{B}_{i(i-1)} \mathbf{u}_{i-1} + \mathbf{B}_{ii} \mathbf{u}_i + \mathbf{B}_{i(i+1)} \mathbf{u}_{i+1} \tag{3}$$

where the columns of \mathbf{B}_{ij} represent the load at the i -th location due to a unit deformation at the j -th

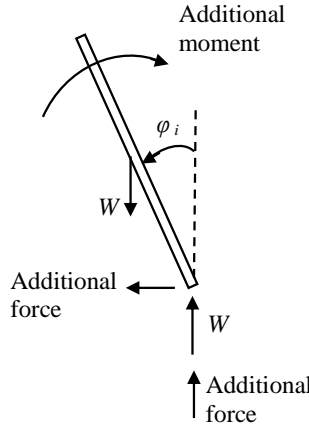


Figure 3. Free body diagram of a buckled beam.

location only, the deformations at all other locations being zero. In (3) and (4) we have made an approximation by considering interactions between a beam and its two immediate neighbors, which is known to be accurate enough for what we are interested [Li et al. 2010]. Long distance interactions among nonneighboring beams are neglected.

When the i -th beam buckles, its free body diagram is shown in Figure 3, where the vertical load W and the corresponding vertical reaction with the same magnitude exist in both the unbuckled and buckled states. The rest are possible additional loads due to buckling. The equilibrium of the beam requires that

$$\begin{aligned}
 \sum_{j=1}^{\infty} ([B_{ij}]_{11}u_j + [B_{ij}]_{12}v_j + [B_{ij}]_{13}\phi_j) &= 0, \\
 \sum_{j=1}^{\infty} ([B_{ij}]_{21}u_j + [B_{ij}]_{22}v_j + [B_{ij}]_{23}\phi_j) &= 0, \\
 -W\frac{h}{2}\phi_i + \sum_{j=1}^{\infty} ([B_{ij}]_{31}u_j + [B_{ij}]_{32}v_j + [B_{ij}]_{33}\phi_j) &= 0.
 \end{aligned}
 \tag{4}$$

Equations (4)₁ and (4)₂ say that the additional horizontal and vertical forces due to buckling are zero, while (4)₃ is the moment equation about the bottom of the beam. In (4), $[B_{ij}]_{11}$ represents the (1,1) element of the 3×3 matrix B_{ij} , and the rest are similar. In (4) we have a system of linear homogeneous equations. The trivial solution with all $u_i = 0$ is the unbuckled state. We are interested in nontrivial solutions of (4) representing buckled states. Then (4) is an eigenvalue problem. We look for values of $Wh/2$ corresponding to which nontrivial solutions of u_i exist.

3. Numerical results and discussion

As an example, we still consider the same twenty beams as in [Lin et al. 2007] with the same geometric and material parameters. The system (4) is solved numerically on a computer. Within three significant digits, the numerical results for the eigenvalues $Wh/2$ are those in Table 1. They are the same as those in [Lin et al. 2007], where the beam bottom horizontal and vertical displacements were not allowed.

8.96	9.00	9.05	9.13	9.23	9.34	9.48	9.63	9.80	9.98
10.16	10.36	10.55	10.74	10.92	11.08	11.23	11.35	11.43	11.49

Table 1. Numerically calculated eigenvalues $Wh/2$ for the 20-beam system, in nN.

The buckled states determined from the eigenvectors are different from the previous analysis and are shown in Figure 4, left, where they are also ranked according to the magnitude of the eigenvalues. Even though the buckled states near the bottom and top of the figure have a one-to-one correspondence with the results of [Lin et al. 2007], the ones near the middle of the figure differ from the corresponding ones in that reference by having both rotation rearrangements and surface deformations. The latter change is the new finding by relaxing restrictions on displacement of beam bases. We enlarged the calculated surface topographies in Figure 4, right, to view the details of such change. Among the twenty instability modes, all the substrates have a periodic, wave-like feature where topography fluctuates between landmarks like hilltops and valleys. The periodicity of the fluctuation gradually increases from 400 nm in mode #1 to more than 4000 nm in mode #20. In contrast, amplitude variance is more complex. Figure 5, left, indicates the contrast between two fluctuating surfaces with minimum and maximum amplitudes, where a 6-fold difference in the magnitude of the amplitude is observed between mode #13 and #1. Qualitatively, this proves that more energy is needed to cause instability such as in mode #13.

In Figure 5, right, we superposed beam locations atop the fluctuating surface topographies. It is clear that the multibeam-like buckling feature is mostly concentrated in valleys. In other words, the beams having a larger tendency to rotate will result in more significant displacements on bases, giving rise to noticeable up- or downhill portions in topography. More interestingly, since the buckled features

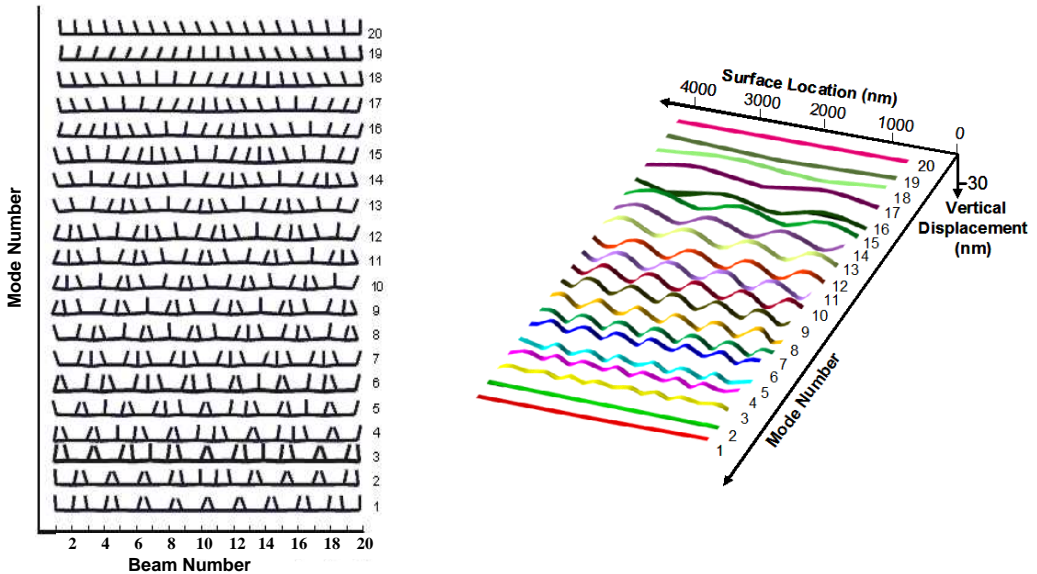


Figure 4. Theoretical results of collective buckling. Left: Buckled beams and substrate deformation. Right: surface fluctuations in each individual buckling mode. Both graphs show modes ranked by the magnitude of their eigenvalues.

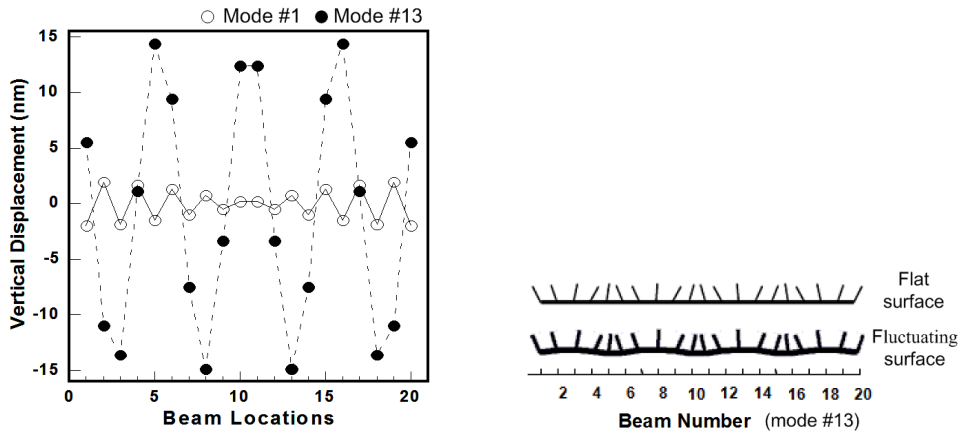


Figure 5. Theoretical results of collective buckling. Left: surface topographies of buckling modes with the maximum (#13) and minimum (#1) fluctuations. Right: comparison of beam displacements and rotations atop a flat surface (model in [Lin et al. 2007]) and a fluctuating surface (current model).

are all localized in the valleys of the fluctuated surfaces, open surfaces will reside on hilltops of those fluctuations. This latter statement could help us to understand the following experimental results more accurately than before.

To give us a visual picture of the buckling in soft nanostructures, we used the easy-to-perform process of embossing/imprinting lithography [Chou et al. 1996; Xia and Whitesides 1998] and created periodic nanostructures atop an elastic poly(dimethylsiloxane) (PDMS) substrate. The soft nanostructure was formed by spin-coating the PDMS precursor mixture on a rigid mold and baking at an elevated temperature for an extended period of time. To obtain a uniform pattern on PDMS, it is necessary to treat the rigid mold (Si or SiO₂ with grating lines with a pitch size of 200 nm, a linewidth of 100 nm and a depth of 150 nm) with O₂ plasma, followed by a perfluorosilane treatment in toluene (0.2 M, 5 min). The soft nature of the PDMS material, plus the high aspect ratio of the copied nanostructures from the mold, suggest an appearance of collective buckling, as we mentioned before.

We used atomic force microscopy (AFM) to evaluate the topography of the buckled lines. The advantages of AFM are that it is a high-resolution imaging tool, which allows us to survey the overall buckling of soft structures at the nanometer scale; and that the noncontact nature of the AFM tapping mode eliminates any contact forces between the tip and the underlying nanostructure.

Figure 6, left, shows the topography of the rigid stamp with one-dimensional grating features. The resulting PDMS copies show extensive surface buckling features, displayed in by Figure 6, middle, where both multibeam and multimode buckling phenomena are in evidence, and which we discuss in more detail shortly.

The first case of instability in Figure 4 (mode #1, two-beam pairing) has been observed by several researchers [Delamarche et al. 1997; Xia and Whitesides 1998; Hui et al. 2002; Chuang et al. 2005] during nanofabrication, and is often used as a classic picture for nanostructure buckling. In those findings, a rigid substrate backing or a thick PDMS sample are often selected to limit large deformation to the

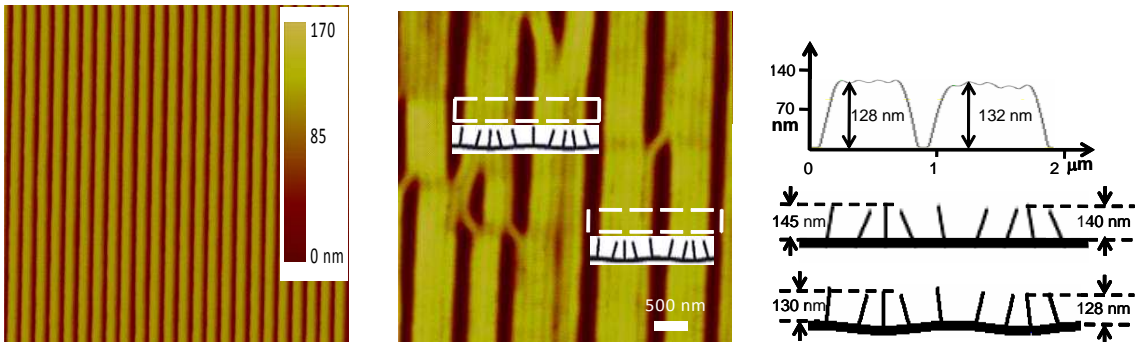


Figure 6. AFM topographical images and cursor plots of a rigid mold and fabricated PDMS structures from embossing/imprinting. Left: original mold with a pitch of 200 nm and a depth of 150 nm. Middle: multibeam and multimode buckling features, with superimposed sketches showing rotations of individual beams in selected areas: collective buckling follows mode #12 in the upper area and mode #13 in the lower area, as predicted by Figure 4. A branching angle of 45° is evident in boundaries between two different buckled patches. Right: cursor plot of buckled features in the middle figure, and comparison with theoretical calculations.

stamp material [Schmid and Michel 2000], so minimum energy impact is ensured for the occurrence of pairing. In contrast, when no precautions are taken with the stamp material or when substantial deformation occurs in the nanostructuring process, multibeam buckling modes at higher energy levels should be expected; the fluctuation of those energy impacts could even generate multiple buckling modes.

We saw a good match of these predictions in our experimental data, as exemplified in Figure 6. For example, selected areas of Figure 6, middle, match with predicted buckling modes #12 and #13; these modes are sketched underneath the corresponding areas in the figure. A branching angle of 45° between the two neighboring buckling modes suggests a shear or rotation nature of these impacts, validating our approximation of buckling in elastic beams with rotation of rigid ones.

In Figure 6, top right, we see the cursor plot of AFM measurements for one of the buckling features, indicating a depth value of 128–132 nm for those landmarks. We saw a mismatch between this number with our previous analysis in [Lin et al. 2007]. When the restriction on beam displacements is not released, as in that earlier reference, the feature depth in buckled beams is expected to depend mainly on the rotation of beams. When minimal rotation is assumed, the depth should be close to the depth of the rigid mold ($h = 150$ nm).

The middle portion of Figure 6, right, illustrates the buckled beams in such a condition, where beams are resting on a flat ground and the height difference, i.e., 140–145 nm, between the top center of the multibeam and the open area is calculated. Clearly, our experimental data suggest otherwise; and the number obtained is more than 13% smaller than what we have estimated. While difficult to explain from our previous modeling results in [Lin et al. 2007], this could be justified by taking beam displacements into consideration. Figure 6, bottom right, shows the buckled beams without the restriction on beam displacements. Surface fluctuation from the base lowered the height of the multibeam and simultaneously increased the level of hilltops in open areas. Accordingly, the new calculation leads to a value for the

beam depth of 128–130 nm, much closer to the observed one. Overall, this analysis supplies the refined model with good experimental evidence.

4. Conclusion

A mechanical model is developed for analyzing the collective buckling of an array of beams on an elastic substrate; it includes the refinement of allowing the bottom of the beams to move both horizontally and vertically, as well as rotating. Numerical results from the model show that periodic surface deformations resulted atop the compliant substrate, which found a better match with the height measurements from AFM. Our work suggests that both the compliant substrate and the interaction of neighboring structures through the deformation of the substrate dominate the collective buckling. This makes the buckling of periodic soft nanostructures unique and different from conventional structural engineering.

Acknowledgments

The project described was made possible by NSF MRSEC and the Layman Fund from the University of Nebraska. H. Lin appreciates many helpful discussions with Mr. Ocelio Lima and Dr. Lanping Yue.

Appendix: Calculation of A_{ij}

First consider the case of a vertical load on a half-space in plane-strain elasticity (see Figure 7). The stress and displacement fields are given in [Timoshenko and Goodier 1970]:

$$\sigma_r = -\frac{2P \cos \theta}{\pi r}, \quad \sigma_\theta = 0, \quad \tau_{r\theta} = 0,$$

$$u = -\frac{2P}{\pi E} \cos \theta \ln \frac{r}{d} - \frac{(1-\nu)P}{\pi E} \theta \sin \theta, \tag{5}$$

$$v = \frac{(1+\nu)P}{\pi E} \sin \theta - \frac{(1-\nu)P}{\pi E} \theta \cos \theta + \frac{2P}{\pi E} \sin \theta \ln \frac{r}{d}, \tag{6}$$

$$\frac{1}{2} \left(\frac{\partial v}{\partial r} - \frac{1}{r} \frac{\partial u}{\partial \theta} + \frac{v}{r} \right) = \frac{2P}{\pi E} \frac{\sin \theta}{r} \tag{7}$$

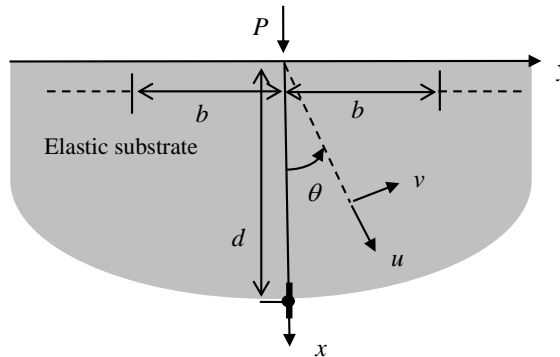


Figure 7. A half-space under a vertical load.

In obtaining (5)–(7), the following conditions are imposed at $\theta = 0$ and $r = d$ for determining the displacement field uniquely:

$$u = 0, \quad v = 0, \quad \frac{\partial v}{\partial r} = 0. \quad (8)$$

The value of d serves as a common reference point. From (5)–(7) we calculate

$$[A_{i(i-1)}]_{11} = -v(b, \pi/2) = -\frac{(1+\nu)P}{\pi E} - \frac{2P}{\pi E} \ln \frac{b}{d},$$

$$[A_{i(i-1)}]_{21} = u(b, \pi/2) = -\frac{(1-\nu)P}{2E},$$

$$[A_{i(i-1)}]_{31} = \frac{1}{2} \left(\frac{\partial v}{\partial r} - \frac{1}{r} \frac{\partial u}{\partial \theta} + \frac{v}{r} \right)_{r=b, \theta=\pi/2} = \frac{2P}{\pi E b},$$

$$[A_{ii}]_{11} = u|_{r=a, \theta=0} = -\frac{2P}{\pi E} \ln \frac{a}{d}, \quad [A_{ii}]_{21} = 0, \quad [A_{ii}]_{31} = 0,$$

$$[A_{i(i+1)}]_{11} = v(b, -\pi/2) = -\frac{(1+\nu)P}{\pi E} - \frac{2P}{\pi E} \ln \frac{b}{d},$$

$$[A_{i(i+1)}]_{21} = -u(b, -\pi/2) = \frac{(1-\nu)P}{2E},$$

$$[A_{i(i+1)}]_{31} = \frac{1}{2} \left(\frac{\partial v}{\partial r} - \frac{1}{r} \frac{\partial u}{\partial \theta} + \frac{v}{r} \right)_{r=b, \theta=-\pi/2} = -\frac{2P}{\pi E b}.$$

Next consider the case of a tangential load (see Figure 8). The stress field is given in [Timoshenko and Goodier 1970], and can be integrated to obtain the displacement field:

$$\sigma_r = -\frac{2F \sin \theta}{\pi} \frac{1}{r}, \quad \sigma_\theta = 0, \quad \tau_{r\theta} = 0,$$

$$u = -\frac{2F}{\pi E} \sin \theta \ln \frac{r}{d} + \frac{(1-\nu)F}{\pi E} (\theta \cos \theta - \sin \theta), \quad (9)$$

$$v = -\frac{2F}{\pi E} \cos \theta \ln \frac{r}{d} - \frac{2F}{\pi E} \cos \theta - \frac{(1-\nu)F}{\pi E} \theta \sin \theta + \frac{2F}{\pi E} \frac{r}{d}, \quad (10)$$

$$\frac{1}{2} \left(\frac{\partial v}{\partial r} - \frac{1}{r} \frac{\partial u}{\partial \theta} + \frac{v}{r} \right) = -\frac{2F \cos \theta}{\pi E} \frac{1}{r} + \frac{2F}{\pi E} \frac{1}{d}. \quad (11)$$

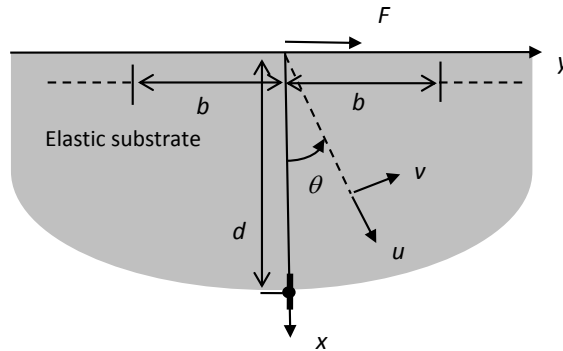


Figure 8. A half-space under a tangential load.

From (9)–(11) we calculate

$$\begin{aligned}
 [\mathbf{A}_{i(i-1)}]_{12} &= -v(b, \pi/2) = -\frac{(1-\nu)F}{2E} - \frac{2F}{\pi E} \frac{b}{d}, \\
 [\mathbf{A}_{i(i-1)}]_{22} &= u(b, \pi/2) = -\frac{2F}{\pi E} \ln \frac{b}{d} - \frac{(1-\nu)F}{\pi E}, \\
 [\mathbf{A}_{i(i-1)}]_{32} &= \frac{1}{2} \left(\frac{\partial v}{\partial r} - \frac{1}{r} \frac{\partial u}{\partial \theta} + \frac{v}{r} \right)_{r=b, \theta=\pi/2} = \frac{2F}{\pi E} \frac{1}{d}, \\
 [\mathbf{A}_{ii}]_{12} &= 0, \quad [\mathbf{A}_{ii}]_{22} = v|_{r=a, \theta=0} = -\frac{2F}{\pi E} \ln \frac{a}{d} - \frac{2F}{\pi E} + \frac{2F}{\pi E} \frac{a}{d}, \\
 [\mathbf{A}_{ii}]_{32} &= \frac{1}{2} \left(\frac{\partial v}{\partial r} - \frac{1}{r} \frac{\partial u}{\partial \theta} + \frac{v}{r} \right)_{r=a, \theta=0} = -\frac{2F}{\pi E} \frac{1}{a} + \frac{2F}{\pi E} \frac{1}{d}, \\
 [\mathbf{A}_{i(i+1)}]_{12} &= v(b, -\pi/2) = -\frac{(1-\nu)F}{2E} + \frac{2F}{\pi E} \frac{b}{d}, \\
 [\mathbf{A}_{i(i+1)}]_{22} &= -u(b, -\pi/2) = -\frac{2F}{\pi E} \ln \frac{b}{d} - \frac{(1-\nu)F}{\pi E}, \\
 [\mathbf{A}_{i(i+1)}]_{32} &= \frac{1}{2} \left(\frac{\partial v}{\partial r} - \frac{1}{r} \frac{\partial u}{\partial \theta} + \frac{v}{r} \right)_{r=b, \theta=-\pi/2} = \frac{2F}{\pi E} \frac{1}{d}
 \end{aligned}$$

The last case is shown in Figure 9. The stress field is given in [Timoshenko and Goodier 1970], and can be integrated to obtain the displacement field:

$$\begin{aligned}
 \sigma_r &= \frac{2M \sin 2\theta}{\pi r^2}, \quad \sigma_\theta = 0, \quad \tau_{r\theta} = -\frac{M}{\pi} \frac{1 + \cos 2\theta}{r^2}, \\
 u &= -\frac{2M \sin 2\theta}{\pi E r} - \frac{4\nu M}{\pi E d} \sin \theta,
 \end{aligned} \tag{12}$$

$$v = -\frac{(1-\nu)M \cos 2\theta}{\pi E r} - \frac{4\nu M}{\pi E d} \cos \theta + \frac{2\nu M}{\pi E d^2} r + \frac{(1+\nu)M}{\pi E} \frac{1}{r}, \tag{13}$$

$$\frac{1}{2} \left(\frac{\partial v}{\partial r} - \frac{1}{r} \frac{\partial u}{\partial \theta} + \frac{v}{r} \right) = \frac{2M \cos 2\theta}{\pi E r^2} + \frac{2\nu M}{\pi E d^2}. \tag{14}$$

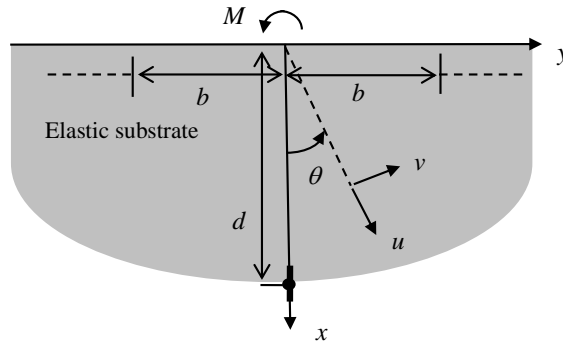


Figure 9. A half-space under a load couple.

From (12)–(14) we calculate

$$\begin{aligned}
 [\mathbf{A}_{i(i-1)}]_{13} &= -v(b, \pi/2) = -\frac{(1-v)M}{\pi E} \frac{1}{b} - \frac{2vM}{\pi E d^2} b - \frac{(1+v)M}{\pi E} \frac{1}{b}, \\
 [\mathbf{A}_{i(i-1)}]_{23} &= u(b, \pi/2) = -\frac{4vM}{\pi E d}, \\
 [\mathbf{A}_{i(i-1)}]_{33} &= \frac{1}{2} \left(\frac{\partial v}{\partial r} - \frac{1}{r} \frac{\partial u}{\partial \theta} + \frac{v}{r} \right)_{r=b, \theta=\pi/2} = -\frac{2M}{\pi E} \frac{1}{b^2} + \frac{2vM}{\pi E d^2}, \\
 [\mathbf{A}_{ii}]_{13} &= 0, \quad [\mathbf{A}_{ii}]_{23} = v|_{r=a, \theta=0} = -\frac{(1-v)M}{\pi E} \frac{1}{a} - \frac{4vM}{\pi E d} + \frac{2vM}{\pi E d^2} a + \frac{(1+v)M}{\pi E} \frac{1}{a}, \\
 [\mathbf{A}_{ii}]_{33} &= \frac{1}{2} \left(\frac{\partial v}{\partial r} - \frac{1}{r} \frac{\partial u}{\partial \theta} + \frac{v}{r} \right)_{r=a, \theta=0} = \frac{2M}{\pi E} \frac{1}{a^2} + \frac{2vM}{\pi E d^2}, \\
 [\mathbf{A}_{i(i+1)}]_{13} &= v(b, -\pi/2) = \frac{(1-v)M}{\pi E} \frac{1}{b} + \frac{2vM}{\pi E d^2} b + \frac{(1+v)M}{\pi E} \frac{1}{b}, \\
 [\mathbf{A}_{i(i+1)}]_{23} &= -u(b, -\pi/2) = -\frac{4vM}{\pi E d}, \\
 [\mathbf{A}_{i(i+1)}]_{33} &= \frac{1}{2} \left(\frac{\partial v}{\partial r} - \frac{1}{r} \frac{\partial u}{\partial \theta} + \frac{v}{r} \right)_{r=b, \theta=-\pi/2} = -\frac{2M}{\pi E} \frac{1}{b^2} + \frac{2vM}{\pi E d^2}
 \end{aligned}$$

For plane-strain problems the following change in material constants is needed:

$$E \rightarrow \frac{E}{1-\nu^2}, \quad \nu \rightarrow \frac{\nu}{1-\nu}.$$

These fields and interaction coefficients are for beams on a semi-infinite half space. In reality the soft beams are built on a plate with a finite thickness. To compensate for the effect of the finite plate thickness, when comparing with experimental results, we varied d in the above equations and finally chose $d = 1000a$ in our calculations for best agreement with experimental results.

References

- [Alfutov 2000] N. A. Alfutov, *Stability of elastic structures*, Springer, Germany, 2000.
- [Chen et al. 2008] Z. G. Chen, J. S. Yang, and L. Tan, “Collective buckling of a two-dimensional array of nanoscale columns”, *J. Phys. Chem. B.* **112** (2008), 14766–14771.
- [Chou et al. 1995] S. Y. Chou, P. R. Krauss, and P. J. Renstrom, “Imprint of sub-25 nm vias and trenches in polymers”, *Appl. Phys. Lett.* **67** (1995), 3114–3116.
- [Chou et al. 1996] S. Y. Chou, P. R. Krauss, and P. J. Renstrom, “Nanoimprint lithography”, *J. Vac. Sci. Technol. B.* **14** (1996), 4129–4133.
- [Chuang et al. 2005] W. C. Chuang, C. T. Ho, and W. C. Wang, “Fabrication of a high-resolution periodical structure using a replication process”, *Opt. Express.* **13** (2005), 6685–6692.
- [Delamarche et al. 1997] E. Delamarche, H. Schmid, B. Michel, and H. Biebuyck, “Stability of molded polydimethylsiloxane microstructures”, *Adv. Mater.* **9** (1997), 741–746.
- [Evans et al. 2007] B. A. Evans, A. R. Shields, R. L. Carroll, S. Washburn, M. R. Falvo, and R. Superfine, “Magnetically actuated nanorod arrays as biomimetic cilia”, *Nano Lett.* **7** (2007), 1428–1434.
- [Feng and Li 2009] K. Feng and Z. Li, “Buckling analysis of soft nanostructures in nanoimprinting”, *Chin. Phys. Lett.* **26** (2009), 126202.

- [Greenhill 1881] A. G. Greenhill, “Determination of the greatest height consistent with stability that a vertical pole or mast can be made, and the greatest height to which a tree of given proportions can grow”, *Proc. Cambridge Phil. Soc.* **4** (1881), 65–73.
- [Hsia et al. 2005] K. J. Hsia, Y. Huang, E. Menard, J. U. Park, W. Zhou, J. Rogers, and J. M. Fulton, “Collapse of stamps for soft lithography due to interfacial adhesion”, *Appl. Phys. Lett.* **86** (2005), 154106.
- [Hui et al. 2002] C. Y. Hui, A. Jagota, Y. Y. Lin, and E. J. Kramer, “Constraints on microcontact printing imposed by stamp deformation”, *Langmuir*. **18** (2002), 1394–1407.
- [Li et al. 2010] Z. Li, K. Feng, J. S. Yang, L. Tan, and H. Lin, “Collective buckling of nonuniform nanobeams interacting through an elastic substrate”, *Acta Mech.* **209** (2010), 285–293.
- [Lin et al. 2007] H. J. Lin, J. Yang, L. Tan, J. Xu, and Z. Li, “Collective buckling of periodic soft nanostructures on surfaces and promotion for nanolithography”, *J. Phys. Chem. C*. **111** (2007), 13348–13356.
- [Lin et al. 2010] H. J. Lin, H. L. Du, J. S. Yang, and L. Tan, “Collective buckling of an elastic beam array on an elastic substrate for applications in soft lithography”, *Acta Mech.* (2010).
- [Liu et al. 2010] Y. M. Liu, D. N. Weiss, and J. Y. Li, “Rapid nanoimprinting and excellent piezoresponse of polymeric ferroelectric nanostructures”, *ACS Nano* **4** (2010), 83–90.
- [Schmid and Michel 2000] H. Schmid and B. Michel, “Siloxane polymers for high-resolution and high accuracy soft lithography”, *Macromolecules*. **33** (2000), 3042–3049.
- [Sharp et al. 2004] K. G. Sharp, G. S. Blackman, N. J. Glassmaker, A. Jagota, and C. Y. Hui, “Effect of stamp deformation on the quality of microcontact printing: Theory and experiment”, *Langmuir*. **20** (2004), 6430–6438.
- [Timoshenko 1936] S. P. Timoshenko, *Theory of elastic stability*, McGraw-Hill, New York, 1936.
- [Timoshenko and Goodier 1970] S. P. Timoshenko and J. N. Goodier, *Theory of elasticity*, McGraw-Hill, New Jersey, 1970.
- [Xia and Whitesides 1998] Y. N. Xia and G. M. Whitesides, “Soft lithography”, *Annu. Rev. Mater. Sci.* **28** (1998), 153–184.

Received 4 Dec 2009. Revised 30 Mar 2010. Accepted 7 Apr 2010.

HAOJING LIN: linhaojing1983@gmail.com

Department of Engineering Mechanics, University of Nebraska-Lincoln, P.O. Box 880526, Lincoln, NE 68588-0526, United States

ZIGUANG CHEN: chenziguang@huskers.unl.edu

Department of Engineering Mechanics, University of Nebraska-Lincoln, P.O. Box 880526, Lincoln, NE 68588-0526, United States

JIASHI YANG: jyang1@unl.edu

Department of Engineering Mechanics, University of Nebraska-Lincoln, P.O. Box 880526, Lincoln, NE 68588-0526, United States

LI TAN: ltan4@unl.edu

Department of Engineering Mechanics, University of Nebraska-Lincoln, P.O. Box 880526, Lincoln, NE 68588-0526, United States

IMPROVED HYBRID ELEMENTS FOR STRUCTURAL ANALYSIS

C. S. JOG

Hybrid elements, which are based on a two-field variational formulation with the displacements and stresses interpolated separately, are known to deliver very high accuracy, and to alleviate to a large extent problems of locking that plague standard displacement-based formulations. The choice of the stress interpolation functions is of course critical in ensuring the high accuracy and robustness of the method. Generally, an attempt is made to keep the stress interpolation to the minimum number of terms that will ensure that the stiffness matrix has no spurious zero-energy modes, since it is known that the stiffness increases with the increase in the number of terms. Although using such a strategy of keeping the number of interpolation terms to a minimum works very well in static problems, it results either in instabilities or fails to converge in transient problems. This is because choosing the stress interpolation functions *merely* on the basis of removing spurious energy modes can violate some basic principles that interpolation functions should obey. In this work, we address the issue of choosing the interpolation functions based on such basic principles of interpolation theory and mechanics. Although this procedure results in the use of more number of terms than the minimum (and hence in slightly increased stiffness) in many elements, we show that the performance continues to be far superior to displacement-based formulations, and, more importantly, that it also results in considerably increased robustness.

1. Introduction

Ever since the pioneering work of Pian et al. [1984; 1986], it is known that hybrid stress-based formulations, which are based on a two-field variational formulation involving displacement and stresses, are much less susceptible to locking than standard displacement-based formulations. In fact, Simo et al. [Simo et al. 1989, p. 70], while discussing their interpolation procedure for membrane stresses state, "... the interpolation procedure is closely related to the mixed formulation for plane stress proposed by Pian and Sumihara (which appears to be optimal)." As discussed in [Jog and Kelkar 2006], conventional shell elements suffer from a number of shortcomings such as the need to develop reduced constitutive models, the need for transition elements while interfacing with brick elements, significant reformulation for thick shells etc. Thus, recently, there has been a significant effort towards the development of three-dimensional solid-shell elements with only displacement degrees of freedom. However, since a kinematic assumption is being made in their development, even these elements would need a significant reformulation for thick shells.

Since no kinematic assumption is being made in the development of hybrid elements, since the treatment is full three-dimensional with no plane-stress or any other such assumption being made (which allows for easy implementation of material nonlinearities), since there are no stabilization parameters that need to be adjusted as in some "strain-based" formulations, and since they are relatively much

Keywords: hybrid finite elements, linear/nonlinear, static/transient, structural analysis.

more immune to locking, and converge more rapidly than standard displacement-based elements, hybrid elements can be used very effectively (with no modification of the formulation) to model problems as diverse as beams/plates/shells on one hand, and problems involving “chunky” geometries on the other. Even from a user viewpoint, since the stress degrees of freedom are condensed out at an element level, the formulation ultimately involves only displacement degrees of freedom, so that the same input data (nodal coordinates, connectivity, boundary conditions etc.) that is used for conventional displacement-based elements can be used for the hybrid formulation also. The drawback of hybrid elements that is often mentioned is the need to invert a small matrix to construct the element stiffness matrix. However, since the element stiffness matrices can be constructed independent of each other, this process can be easily parallelized. Even without parallelization, this cost is negligible compared to the cost of solving the global set of equations, and, as already mentioned, this is considerably less in the case of hybrid elements due to the coarser meshes that are required to achieve a given level of accuracy.

Needless to say, the choice of the stress interpolation functions is critical in ensuring the accuracy of hybrid elements. Almost all works, such as [Punch and Atluri 1984; Lee and Rhiu 1986; Rhiu and Lee 1987], choose the stress interpolation function based on removal of spurious zero-energy modes so that the element stiffness matrix is full-rank (apart from rigid-body modes). It is well-known that the minimum number of stress-interpolation terms to ensure a full-rank element stiffness matrix is equal to the number of displacement degrees of freedom minus the number of rigid-body modes. It is also well known that adding more terms to the stress interpolation adds more stiffness. In the light of these two facts, efforts have naturally focused on keeping the number of stress interpolation terms to a minimum; henceforth, we will call such an interpolation with the minimum number of terms as a minimal stress interpolation. While such a strategy works extremely well for *static* problems, it was found recently in [Jog and Motamarri 2009] that it can result in instabilities on *transient* problems.

The cause of these problems is that the minimal stress interpolation in most (but not all) elements violates some basic tenets that interpolation functions should obey. To give a simple example, [Lee and Rhiu 1986; Rhiu and Lee 1987] discuss the interpolations for a 9-node quadrilateral element; the authors recommend dropping the term η^2 from the stress interpolation for the normal stress $\tau^{\xi\xi}$, where (ξ, η) denote the natural coordinates, since the kinematic mode which this term suppresses is non-communicable. Thus, the interpolation for $\tau^{\xi\xi}$ uses the set $\{1, \xi, \eta, \xi\eta, \xi\eta^2\}$, and in a similar manner, the interpolation for $\tau^{\eta\eta}$ uses the set $\{1, \xi, \eta, \xi\eta, \xi^2\eta\}$. Although the use of this interpolation yields excellent results on static problems, it results in instabilities on transient problems [Jog and Motamarri 2009]. The instabilities do not arise immediately (in fact, the results at small times match quite well with the expected results), but gradually creep in as the simulation progresses, and finally pollute the entire solution. The exclusion of η^2 and ξ^2 in the interpolations for $\tau^{\xi\xi}$ and $\tau^{\eta\eta}$ violates one of the basic principles that an interpolation function should obey, namely, that all terms *starting from the lowest and upto the highest order* should be included, and is the cause of the aforementioned instability. Another problem that commonly occurs in a minimal interpolation is that a β term is shared, or in other words, some stress components are coupled. As we will show, this can cause spurious stresses to arise even in static problems.

The focus of this work is to formulate a set of rules for the selection of the stress interpolation functions, so that problems of the type mentioned above do not occur, thus increasing the robustness of the resulting hybrid elements. Of course, adherence to these rules can result in an increase in the number of terms in the stress interpolation, and hence to a (slight) stiffening of the elements. But as we show by means

of several challenging examples (including nonlinear static and transient problems), the performance of the resulting hybrid elements continues to be far better than the displacement-based elements. To give an analogy, in a displacement-based formulation, reduced integration yields better results in many cases as compared to full integration, but can lead to spectacular failures as well. Thus, just as full integration results in elements that are stiffer but more robust, the rules enumerated here (which, besides the requirement that the element be free of spurious zero-energy modes, are based on some basic principles that interpolation functions should satisfy) result in stress interpolations with more terms than the minimal one for several elements, but are more robust in the sense that they do not result either in instabilities or in spurious stresses. We also mention that since we are usually using more terms than the minimal one, the satisfaction of the inf-sup conditions [Xue et al. 1985] is not affected.

2. Choice of stress interpolation functions

In this section, we discuss the choice of stress interpolation functions for some three-dimensional hybrid elements in the light of our experience with static and transient simulations. If d is the number of displacement degrees of freedom, and r is the number of rigid body modes, then it is known that to obtain a formulation free of spurious energy modes, the number of chosen stress interpolation modes s must be at least $d - r$ [Punch and Atluri 1984]. As mentioned in the Introduction, since each additional mode adds more stiffness, an attempt is usually made to keep the number of stress modes to a minimum, i.e., $s = d - r$. However, it was shown in [Jog and Motamarri 2009] that some higher-order hybrid elements that satisfy this requirement, and are free of zero-energy modes, can still give rise to instabilities in transient problems. It was shown that if the normal stresses are obtained by differentiating the displacement field, then these instabilities do not arise. It is possible to interpolate the normal stresses in this manner, and such that the requirement $s = d - r$, and the requirement that the element matrix be free of spurious modes are still satisfied (see [Jog and Motamarri 2009] for examples). However, this involves dropping some of the lower-order terms in the shear interpolation, and this results in bad performance even on static problems. Thus, in order to obtain a robust element, one necessarily needs $s > d - r$ at least for some elements. Since static solutions can be considered as steady-state solutions to transient problems, one should use the same stress interpolations in static and transient simulations. To conclude, although using more stress modes than the minimal one does result in a slight stiffening, it is essential from the viewpoint of increased robustness of the element.

Based on this discussion, we propose the following set of rules (besides the obvious one that there be no spurious zero-energy modes) for choosing the stress interpolation functions in a hybrid formulation:

- (1) The normal stress components should be obtained simply by differentiating the displacement interpolation functions. For example, in a three-dimensional hexahedral element, the interpolations for $\tau^{\xi\xi}$, $\tau^{\eta\eta}$ and $\tau^{\zeta\zeta}$ are obtained by differentiating the displacement interpolation functions with respect to ξ , η and ζ respectively.
- (2) All the lower-order terms should be incorporated in the shear interpolation functions, e.g., a constant term in the case of a 8-node hexahedral element, or trilinear terms in the case of a 27-node hexahedral element. The higher-order terms in the shear interpolation are chosen so as to eliminate any spurious zero-energy modes, so that the element stiffness matrix is full-rank (apart from rigid-body modes). In addition, all the terms of the corresponding order of interpolation should also be

included (although they may not suppress any zero-energy mode). For example, in the case of the 27-node hexahedral element, only the higher-order terms ($\zeta^2\xi$, $\zeta^2\eta$) are required in the interpolation for the shear component $S^{\xi\eta}$ to suppress the zero-energy modes. However, all the terms of the corresponding order (bilinear) of interpolation, namely (ζ^2 , $\zeta^2\xi$, $\zeta^2\eta$, $\zeta^2\xi\eta$), should be included. Using an interpolation that violates this rule results in the transient algorithm diverging after a few time steps in the example discussed in [Section 3H](#).

- (3) The stress components should be allowed to vary independently of each other, i.e., there should be no shared β terms between stress components. This is especially important in problems involving either orthotropic materials where the three shear moduli G_{xy} , G_{yz} and G_{xz} could be different, or in materials with nonlinear constitutive relations where the shear stresses are not simply proportional to the corresponding shear strains. Not enforcing this requirement can result in spurious stresses even in linear problems, as we show below in the case of the 6-node wedge element.
- (4) Finally, the stress interpolations should be such that the same results are obtained irrespective of the order of node-numbering in the connectivity specification. As we shall see, this requirement is difficult to satisfy in wedge elements.

We now discuss the choice of stress interpolation functions for several hybrid elements in the literature in the light of the rules above. Once the stress interpolation functions are chosen, the stiffness matrices are constructed as in [\[Jog and Kelkar 2006\]](#) and [\[Jog and Motamarri 2009\]](#) for the (nonlinear) static and transient cases, respectively. In what follows \mathbf{S} denotes the second Piola-Kirchhoff stress tensor, while (u, v, w) denote the displacement components.

2A. Eight-node hexahedral element. We use the same interpolation for \mathbf{S} as suggested by Pian and Tong [\[Pian and Tong 1986\]](#) in the context of linear problems, i.e.,

$$\begin{aligned} S^{\xi\xi} &= \beta_1 + \beta_2\eta + \beta_3\zeta + \beta_4\eta\zeta, & S^{\eta\eta} &= \beta_5 + \beta_6\xi + \beta_7\zeta + \beta_8\xi\zeta, & S^{\zeta\zeta} &= \beta_9 + \beta_{10}\xi + \beta_{11}\eta + \beta_{12}\xi\eta, \\ S^{\xi\eta} &= \beta_{13} + \beta_{14}\zeta, & S^{\eta\zeta} &= \beta_{15} + \beta_{16}\xi, & S^{\xi\zeta} &= \beta_{17} + \beta_{18}\eta. \end{aligned}$$

This stress interpolation satisfies all the rules specified above. If the Jacobian matrix is given by

$$\mathbf{J} = \begin{bmatrix} \partial x/\partial\xi & \partial y/\partial\xi & \partial z/\partial\xi \\ \partial x/\partial\eta & \partial y/\partial\eta & \partial z/\partial\eta \\ \partial x/\partial\zeta & \partial y/\partial\zeta & \partial z/\partial\zeta \end{bmatrix} \equiv \begin{bmatrix} a_1 & b_1 & c_1 \\ a_2 & b_2 & c_2 \\ a_3 & b_3 & c_3 \end{bmatrix}, \quad (2-1)$$

then the transformation relation between the stress components expressed with respect to the natural and Cartesian coordinate systems is given by

$$\begin{bmatrix} S_{xx} \\ S_{yy} \\ S_{zz} \\ S_{xy} \\ S_{yz} \\ S_{xz} \end{bmatrix} = \mathbf{T} \begin{bmatrix} S^{\xi\xi} \\ S^{\eta\eta} \\ S^{\zeta\zeta} \\ S^{\xi\eta} \\ S^{\eta\zeta} \\ S^{\xi\zeta} \end{bmatrix}, \quad (2-2)$$

where

$$\mathbf{T} = \begin{bmatrix} a_1^2 & a_2^2 & a_3^2 & 2a_1a_2 & 2a_2a_3 & 2a_1a_3 \\ b_1^2 & b_2^2 & b_3^2 & 2b_1b_2 & 2b_2b_3 & 2b_1b_3 \\ c_1^2 & c_2^2 & c_3^2 & 2c_1c_2 & 2c_2c_3 & 2c_1c_3 \\ a_1b_1 & a_2b_2 & a_3b_3 & (a_2b_1+a_1b_2) & (a_2b_3+a_3b_2) & (a_1b_3+a_3b_1) \\ b_1c_1 & b_2c_2 & b_3c_3 & (b_2c_1+b_1c_2) & (b_2c_3+b_3c_2) & (b_1c_3+b_3c_1) \\ a_1c_1 & a_2c_2 & a_3c_3 & (a_1c_2+a_2c_1) & (a_3c_2+a_2c_3) & (a_3c_1+a_1c_3) \end{bmatrix}.$$

2B. Twenty-seven-node hexahedral element. We use the following “90 β ” interpolation:

$$\begin{aligned} S^{\xi\xi} &= \beta_1 + \beta_2\xi + \beta_3\eta + \beta_4\zeta + \beta_5\xi\eta + \beta_6\eta\zeta + \beta_7\xi\zeta + \beta_8\xi\eta\zeta \\ &\quad + \beta_9\xi\eta^2 + \beta_{10}\xi\zeta^2 + \beta_{11}\xi\eta\zeta^2 + \beta_{12}\xi\eta^2\zeta + \beta_{13}\xi\eta^2\zeta^2 \\ &\quad + \beta_{14}\eta^2 + \beta_{15}\zeta^2 + \beta_{16}\eta^2\zeta + \beta_{17}\eta\zeta^2 + \beta_{18}\eta^2\zeta^2, \\ S^{\eta\eta} &= \beta_{19} + \beta_{20}\xi + \beta_{21}\eta + \beta_{22}\zeta + \beta_{23}\xi\eta + \beta_{24}\eta\zeta + \beta_{25}\xi\zeta + \beta_{26}\xi\eta\zeta \\ &\quad + \beta_{27}\xi^2\eta + \beta_{28}\eta\zeta^2 + \beta_{29}\xi^2\eta\zeta + \beta_{30}\xi\eta\zeta^2 + \beta_{31}\xi^2\eta\zeta^2 \\ &\quad + \beta_{32}\xi^2 + \beta_{33}\zeta^2 + \beta_{34}\xi^2\zeta + \beta_{35}\xi\zeta^2 + \beta_{36}\xi^2\zeta^2, \\ S^{\zeta\zeta} &= \beta_{37} + \beta_{38}\xi + \beta_{39}\eta + \beta_{40}\zeta + \beta_{41}\xi\eta + \beta_{42}\eta\zeta + \beta_{43}\xi\zeta + \beta_{44}\xi\eta\zeta \\ &\quad + \beta_{45}\xi^2\zeta + \beta_{46}\eta^2\zeta + \beta_{47}\xi^2\eta\zeta + \beta_{48}\xi\eta^2\zeta + \beta_{49}\xi^2\eta^2\zeta \\ &\quad + \beta_{50}\xi^2 + \beta_{51}\eta^2 + \beta_{52}\xi^2\eta + \beta_{53}\xi\eta^2 + \beta_{54}\xi^2\eta^2, \\ S^{\xi\eta} &= \beta_{55} + \beta_{56}\xi + \beta_{57}\eta + \beta_{58}\zeta + \beta_{59}\xi\eta + \beta_{60}\eta\zeta + \beta_{61}\xi\zeta + \beta_{62}\xi\eta\zeta \\ &\quad + \beta_{63}\xi\zeta^2 + \beta_{64}\eta\zeta^2 + \beta_{85}\zeta^2 + \beta_{88}\zeta^2\xi\eta, \\ S^{\eta\zeta} &= \beta_{65} + \beta_{66}\xi + \beta_{67}\eta + \beta_{68}\zeta + \beta_{69}\xi\eta + \beta_{70}\eta\zeta + \beta_{71}\xi\zeta + \beta_{72}\xi\eta\zeta \\ &\quad + \beta_{73}\xi^2\eta + \beta_{74}\xi^2\zeta + \beta_{86}\xi^2 + \beta_{89}\xi^2\eta\zeta, \\ S^{\xi\zeta} &= \beta_{75} + \beta_{76}\xi + \beta_{77}\eta + \beta_{78}\zeta + \beta_{79}\xi\eta + \beta_{80}\eta\zeta + \beta_{81}\xi\zeta + \beta_{82}\xi\eta\zeta \\ &\quad + \beta_{83}\xi\eta^2 + \beta_{84}\eta^2\zeta + \beta_{87}\eta^2 + \beta_{90}\xi\eta^2\zeta. \end{aligned} \tag{2-3}$$

The transformation to Cartesian components is carried out using (2-2).

The minimum number of interpolation terms required for this element is 75, and indeed such an interpolation was developed in [Jog 2005] within a linear context. However, such an interpolation violates Rules (1) and (3), and results in instabilities in some transient problems [Jog and Motamarri 2009]. Thus, increased robustness necessitates using the 90 β element above, although it is stiffer compared to the 75 β element (but note that it is still more flexible compared to the 8-node hexahedral element for a given number of degrees of freedom). As per Rule (1), one constructs the interpolation for the normal stresses simply by differentiating the displacement interpolation functions. To construct the shear-interpolation, one first includes all the lower-order (i.e., trilinear) terms. Among the higher-order terms, the (β_{63} , β_{64}), (β_{73} , β_{74}) and (β_{83} , β_{84}) terms are included to suppress the zero-energy modes

$$\begin{aligned} u &= \alpha_1(1 - 3\eta^2)(1 - 3\zeta^2), \quad v = 0, \quad w = 0; \\ u &= 0, \quad v = \alpha_2(1 - 3\xi^2)(1 - 3\zeta^2), \quad w = 0; \\ u &= 0, \quad v = 0, \quad w = \alpha_3(1 - 3\xi^2)(1 - 3\eta^2). \end{aligned}$$

These modes can be suppressed by using only three β terms. However, this would violate Rule (3) that the stress components be allowed to vary independently. The β_{85} – β_{90} terms are included to comply with Rule (2). According to this rule, along with the terms $\zeta^2\xi$ and $\zeta^2\eta$ which are required to suppress the zero-energy modes in $S^{\xi\eta}$, one should also include the terms ζ^2 and $\zeta^2\xi\eta$; thus, the terms in the interpolation for $S^{\xi\eta}$ that one finally obtains are given by products of the set $\{1, \xi, \eta, \xi\eta\}$ with the set $\{1, \zeta, \zeta^2\}$. Note that in both the 8-node and 27-node hexahedral elements, the terms in the final interpolations for the shear stresses S^{ij} are the terms that are common in the interpolations for the normal stresses S^{ii} and S^{jj} .

2C. Six-node wedge element. The requirement imposed by Rule (4) is difficult to satisfy in the case of wedge elements. In particular, if one formulates the stress modes in terms of natural coordinates as in the case of hexahedral elements, *and* if one uses the minimum number of stress modes, then this requirement is violated. To overcome this problem, Sze et al. [Sze et al. 2004a] proposed a novel idea of using a local Cartesian system to express the stress interpolation functions. Their proposed interpolation with respect to this local Cartesian system x' - y' - z' is

$$\begin{aligned} S_{x'x'} &= \beta_1 + \beta_2\zeta, & S_{y'y'} &= \beta_3 + \beta_4\zeta, & S_{z'z'} &= \beta_5 + \beta_6\xi + \beta_7\eta, \\ S_{x'y'} &= \beta_8 + \beta_9\zeta, & S_{y'z'} &= \beta_{10} + \beta_{12}x', & S_{x'z'} &= \beta_{11} - \beta_{12}y'. \end{aligned}$$

Quite unfortunately, it violates the requirement that the stresses be allowed to vary independently of each other since β_{12} is shared between $S_{y'z'}$ and $S_{x'z'}$. If one considers a single element, with the local and global coordinate systems coinciding, then the displacement field $u = 0$, $v = xz$, $w = 0$, within a linear context, yields $S_{yz} = Gx$, $S_{xz} = 0$, while the numerical strategy yields a nonzero S_{xz} due to its coupling with S_{yz} ; thus, using a shared β results in a spurious S_{xz} component. One would surmise that the situation can be corrected by using

$$\begin{aligned} S_{x'x'} &= \beta_1 + \beta_2\zeta, & S_{y'y'} &= \beta_3 + \beta_4\zeta, & S_{z'z'} &= \beta_5 + \beta_6\xi + \beta_7\eta, \\ S_{x'y'} &= \beta_8 + \beta_9\zeta, & S_{y'z'} &= \beta_{10} + \beta_{12}x', & S_{x'z'} &= \beta_{11} + \beta_{13}y'. \end{aligned}$$

However, numerical experiments show that such an interpolation fails to converge on the (nonlinear) pinched hemisphere problem even with the use of a large number of load steps.

Hence, we finally use the following interpolation which, similar to hexahedral elements, uses the natural coordinate system:

$$\begin{aligned} S^{\xi\xi} &= \beta_1 + \beta_2\zeta, & S^{\eta\eta} &= \beta_3 + \beta_4\zeta, & S^{\zeta\zeta} &= \beta_5 + \beta_6\xi + \beta_7\eta, \\ S^{\xi\eta} &= \beta_8 + \beta_9\zeta, & S^{\eta\zeta} &= \beta_{10} + \beta_{11}\xi + \beta_{12}\eta, & S^{\xi\zeta} &= \beta_{13} + \beta_{14}\xi + \beta_{15}\eta. \end{aligned}$$

The transformation to Cartesian components is carried out using (2-2). Since the $S^{\eta\zeta}$ and $S^{\xi\eta}$ components use interpolations that are symmetric in ξ and η , Rule (4) is satisfied.

Once again, we see that compliance with the 4 requirements results in an element with higher number of β 's than the minimum, which is 12. Numerical experiments show that this element is only marginally better than the displacement-based 6-node wedge element.

2D. Eighteen-node wedge element. The displacement shape functions are obtained as the product of the standard 6-node (quadratic) triangle shape functions with the quadratic one-dimensional shape functions.

The stress interpolation functions are

$$\begin{aligned}
S^{\xi\xi} &= \beta_1 + \beta_2\xi + \beta_3\eta + \beta_4\zeta + \beta_5\xi\zeta + \beta_6\eta\zeta + \beta_7\zeta^2 + \beta_8\xi\zeta^2 + \beta_9\eta\zeta^2, \\
S^{\eta\eta} &= \beta_{10} + \beta_{11}\xi + \beta_{12}\eta + \beta_{13}\zeta + \beta_{14}\xi\zeta + \beta_{15}\eta\zeta + \beta_{16}\zeta^2 + \beta_{17}\xi\zeta^2 + \beta_{18}\eta\zeta^2, \\
S^{\zeta\zeta} &= \beta_{19} + \beta_{20}\xi + \beta_{21}\eta + \beta_{22}\xi^2 + \beta_{23}\xi\eta + \beta_{24}\eta^2 + \beta_{25}\zeta \\
&\quad + \beta_{26}\xi\zeta + \beta_{27}\eta\zeta + \beta_{28}\xi^2\zeta + \beta_{29}\eta^2\zeta + \beta_{30}\xi\eta\zeta, \\
S^{\xi\eta} &= \beta_{31} + \beta_{32}\xi + \beta_{33}\eta + \beta_{34}\zeta + \beta_{35}\xi\zeta + \beta_{36}\eta\zeta + \beta_{37}\zeta^2 + \beta_{38}\xi\zeta^2 + \beta_{39}\eta\zeta^2, \\
S^{\eta\zeta} &= \beta_{40} + \beta_{41}\xi + \beta_{42}\eta + \beta_{43}\zeta + \beta_{44}\xi\zeta + \beta_{45}\eta\zeta, \\
S^{\xi\zeta} &= \beta_{46} + \beta_{47}\xi + \beta_{48}\eta + \beta_{49}\zeta + \beta_{50}\xi\zeta + \beta_{51}\eta\zeta.
\end{aligned} \tag{2-4}$$

The transformation to Cartesian components is carried out using (2-2). An 18-point (6×3) Gauss quadrature rule is used to carry out the integrations.

Notes. • Removing the β_{37} term does not affect the rank of the element stiffness matrix (or, in other words, this term does not suppress any zero energy modes). But excluding this term violates Rules (2) and (4); i.e., the results become sensitive to the order of numbering in the connectivity list. Thus, again, a slightly higher number of stress functions than the minimum are required to ensure robustness.

• Numerical experiments show that although the 21-node wedge element of [Jog 2005] performs slightly better than the above 18-node wedge element on coarser meshes, the convergence of the latter element with mesh refinement is more rapid. The reason is that derivatives of the bubble function introduced in the 21-node element formulation are part of the shear interpolation shape functions, which tends to make the 21-node stiffness matrix over stiff, especially in plate or shell structures. The development of the 18-node wedge element is also simpler because there is no bubble function — no local Cartesian system needs to be introduced as in the 21-node element to ensure insensitivity to node numbering.

• Even from a mesh-generation viewpoint, using the 18-node wedge element is advantageous since it is a standard element that is offered by many meshing softwares.

2E. Tetrahedral elements. Since meshing is far easier with tetrahedral elements than with hexahedral elements, the question naturally arises if tetrahedral elements can be improved using the hybrid element methodology. Since the shape functions of the 4-node linear and 10-node quadratic tetrahedral elements involve complete polynomials, the displacement-based and hybrid methodologies yield identical results for these elements. Lo and Ling [2000] suggested an improvement for the 10-node tetrahedral element based on an incompatible displacement field. Here, we shall investigate if an improvement in this element is possible by introducing a bubble mode associated with a node in the interior (say, at the centroid) of this element. Thus, let ξ, η, ζ be the standard volume coordinates, let $\alpha = 1 - \xi - \eta - \zeta$, and let $N_b = \xi\eta\zeta\alpha$ be the bubble mode associated with the eleventh node. The displacement shape functions are now

$$\begin{aligned}
N_1 &= \xi(2\xi - 1) + 32N_b, & N_5 &= 4\xi\eta - 64N_b, & N_9 &= 4\eta\alpha - 64N_b, \\
N_2 &= \eta(2\eta - 1) + 32N_b, & N_6 &= 4\eta\zeta - 64N_b, & N_{10} &= 4\zeta\alpha - 64N_b, \\
N_3 &= \zeta(2\zeta - 1) + 32N_b, & N_7 &= 4\xi\zeta - 64N_b, & N_{11} &= 256N_b. \\
N_4 &= \alpha(2\alpha - 1) + 32N_b, & N_8 &= 4\xi\alpha - 64N_b, & &
\end{aligned}$$

The stress shape functions can be formulated directly with respect to the global Cartesian system as

$$\begin{aligned} S_{xx} &= \beta_1 + \beta_7\xi + \beta_{13}\eta + \beta_{19}\zeta + \beta_{25} \partial N_b/\partial x, \\ S_{yy} &= \beta_2 + \beta_8\xi + \beta_{14}\eta + \beta_{20}\zeta + \beta_{26} \partial N_b/\partial y, \\ S_{zz} &= \beta_3 + \beta_9\xi + \beta_{15}\eta + \beta_{21}\zeta + \beta_{27} \partial N_b/\partial z, \\ S_{xy} &= \beta_4 + \beta_{10}\xi + \beta_{16}\eta + \beta_{22}\zeta, \\ S_{yz} &= \beta_5 + \beta_{11}\xi + \beta_{17}\eta + \beta_{23}\zeta, \\ S_{xz} &= \beta_6 + \beta_{12}\xi + \beta_{18}\eta + \beta_{24}\zeta, \end{aligned}$$

where, with \mathbf{J} given by (2-1), we have

$$\begin{bmatrix} \partial N_b/\partial x \\ \partial N_b/\partial y \\ \partial N_b/\partial z \end{bmatrix} = \mathbf{J}^{-1} \begin{bmatrix} \partial N_b/\partial \xi \\ \partial N_b/\partial \eta \\ \partial N_b/\partial \zeta \end{bmatrix}.$$

Unfortunately, the improvement of the 11-node hybrid element over the displacement-based 10-node tetrahedral element is marginal, so it is preferable simply to use the 10-node displacement-based element.

2F. Four-node axisymmetric element. With the Jacobian matrix given by

$$\mathbf{J} = \begin{bmatrix} \partial r/\partial \xi & \partial z/\partial \xi \\ \partial r/\partial \eta & \partial z/\partial \eta \end{bmatrix},$$

we use the same shape functions for \mathbf{S} as developed in [Jog and Annabatula 2006] for linear problems, namely,

$$\begin{bmatrix} S_{rr} \\ S_{zz} \\ S_{rz} \end{bmatrix} = \begin{bmatrix} J_{11}^2 & J_{21}^2 & 2J_{11}J_{21} \\ J_{12}^2 & J_{22}^2 & 2J_{12}J_{22} \\ J_{11}J_{12} & J_{21}J_{22} & J_{11}J_{22} + J_{12}J_{21} \end{bmatrix} \begin{bmatrix} S^{\xi\xi} \\ S^{\eta\eta} \\ S^{\xi\eta} \end{bmatrix} \quad \text{and} \quad S_{\theta\theta} = \beta_6 + \beta_7(J_{12}\xi + J_{22}\eta),$$

where

$$S^{\xi\xi} = \beta_1 + \beta_4\eta, \quad S^{\eta\eta} = \beta_2 + \beta_5\xi, \quad S^{\xi\eta} = \beta_3.$$

2G. Nine-node axisymmetric element. With the Jacobian matrix as in the case of the 4-node axisymmetric element, the shape functions are given by

$$\begin{bmatrix} S_{rr} \\ S_{zz} \\ S_{rz} \end{bmatrix} = \begin{bmatrix} J_{11}^2 & J_{21}^2 & 2J_{11}J_{21} \\ J_{12}^2 & J_{22}^2 & 2J_{12}J_{22} \\ J_{11}J_{12} & J_{21}J_{22} & J_{11}J_{22} + J_{12}J_{21} \end{bmatrix} \begin{bmatrix} S^{\xi\xi} \\ S^{\eta\eta} \\ S^{\xi\eta} \end{bmatrix}$$

and

$$S_{\theta\theta} = \beta_{17} + \beta_{18}\xi + \beta_{19}\eta + \beta_{20}\xi\eta + \beta_{21}\xi^2 + \beta_{22}\eta^2 + \beta_{23}(J_{12}\xi^2\eta + J_{22}\xi\eta^2),$$

where

$$\begin{aligned} S^{\xi\xi} &= \beta_1 + \beta_2\xi + \beta_3\eta + \beta_4\xi\eta + \beta_5\eta^2 + \beta_6\xi\eta^2, \\ S^{\eta\eta} &= \beta_7 + \beta_8\xi + \beta_9\eta + \beta_{10}\xi\eta + \beta_{11}\xi^2 + \beta_{12}\xi^2\eta, \\ S^{\xi\eta} &= \beta_{13} + \beta_{14}\xi + \beta_{15}\eta + \beta_{16}\xi\eta. \end{aligned}$$

The higher-order terms in $S_{\theta\theta}$ are chosen to be of the same order as S_{rr} . Although excluding them would still ensure a full-rank stiffness matrix (modulo the rigid-body mode), including them ensures that one gets an almost symmetrical solution in the thick sphere problem of [Section 3F](#).

3. Numerical examples

In this section, we present several linear and nonlinear example problems, both static and transient, to demonstrate the good performance of the hybrid elements. The displacement-based and hybrid n -noded (where n is either 8 or 27) brick elements are denoted by Bn and Sn respectively, the displacement-based and hybrid n -noded wedge elements (where n is either 6 or 18) are denoted by Bn and Wn respectively, while the displacement-based and hybrid n -noded (where n is either 4 or 9) axisymmetric elements are denoted by Bn and An respectively. The WSMP sparse matrix solver [[Gupta 2000; 2002](#)] is used. Full integration is used to construct the element stiffness matrices in all cases. We use the expressions given by Equation (30) of [[Jog and Kelkar 2006](#)] to compute the stiffness and load vectors in the case of pressure loading for both the displacement-based and hybrid elements. For axisymmetric problems, with 1, 2 and 3 denoting the r , z and θ directions, the matrix \mathbf{R} and vector $(\mathbf{cof} \mathbf{F})\tilde{\mathbf{n}}^0$ in these expressions are

$$\mathbf{R}^k = \begin{bmatrix} 0 & 0 & -F_{33}^k \tilde{n}_2^0 & F_{33}^k \tilde{n}_1^0 & F_{22}^k \tilde{n}_1^0 - F_{21}^k \tilde{n}_2^0 \\ F_{33}^k \tilde{n}_2^0 & -F_{33}^k \tilde{n}_1^0 & 0 & 0 & F_{11}^k \tilde{n}_2^0 - F_{12}^k \tilde{n}_1^0 \end{bmatrix}, \quad (\mathbf{cof} \mathbf{F}^k)\tilde{\mathbf{n}}^0 = \begin{bmatrix} F_{22}^k F_{33}^k \tilde{n}_1^0 - F_{21}^k F_{33}^k \tilde{n}_2^0 \\ -F_{12}^k F_{33}^k \tilde{n}_1^0 + F_{11}^k F_{33}^k \tilde{n}_2^0 \end{bmatrix},$$

where $(\tilde{n}_1^0, \tilde{n}_2^0) = (\partial z / \partial \xi, -\partial r / \partial \xi)$ denotes the normal in the reference configuration, and k denotes the iteration number.

As in [[Jog and Kelkar 2006](#)], to ensure a fair comparison of the results, meshes with the *same number of global degrees of freedom* are used; e.g., on any given problem involving hexahedral elements, results obtained using $8N$ eight-node brick elements are compared with those obtained using N twenty-seven-node brick elements, with identical nodal coordinate data and boundary conditions used in both meshes. In all problems, uniform meshes are used. In the case of the hybrid elements, the nodal stresses are obtained by finding the nodal values in each element using the stress interpolation and then averaging, while in the case of the displacement-based elements, the stresses are found by extrapolating the values from the Gauss points, followed by averaging. A Saint Venant–Kirchhoff material model (default) or a neo-Hookean material model with strain energy density and constitutive relation either given by

$$\begin{aligned} W(\mathbf{C}) &= \frac{1}{8} \lambda (\log \det \mathbf{C})^2 + \frac{1}{2} \mu (\text{tr} \mathbf{C} - 3 - \log \det \mathbf{C}), \\ \mathbf{S}(\mathbf{C}) &= 2 \frac{\partial W}{\partial \mathbf{C}} = \frac{\lambda}{2} (\log \det \mathbf{C}) \mathbf{C}^{-1} + \mu (\mathbf{I} - \mathbf{C}^{-1}), \end{aligned} \quad (3-1)$$

or by

$$\begin{aligned} W(\mathbf{C}) &= c_1 (\bar{I}_1 - 3) + \frac{1}{2} \kappa (J - 1)^2, \\ \mathbf{S}(\mathbf{C}) &= \left(-\frac{2}{3} c_1 I_1 I_3^{-1/3} + \kappa (I_3 - I_3^{1/2}) \right) \mathbf{C}^{-1} + 2c_1 I_3^{-1/3} \mathbf{I}, \end{aligned} \quad (3-2)$$

where $\mathbf{C} = \mathbf{F}^T \mathbf{F}$, $I_1 = \text{tr} \mathbf{C}$, $I_3 = \det \mathbf{C}$, $\bar{I}_1 = (I_3)^{-1/3} I_1$, and $\kappa = \lambda + 2\mu/3$ is the bulk modulus, is used in all the examples (the strains are recovered from the stresses as outlined in [[Jog and Kelkar 2006](#)]). Typically, on all the static nonlinear shell-type problems presented, convergence is achieved in

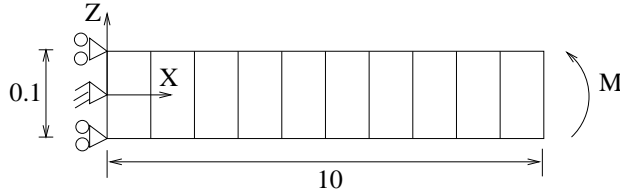


Figure 1. Rollup of a beam. The beam is shown discretized using ten 27-node elements.

about a tenth of the number of iterations reported in [Sze et al. 2004b]. As expected, the results obtained using the proposed hybrid elements are slightly stiffer compared to results obtained using elements with minimal stress interpolations. This is the cost for the increased robustness; however, as we show, the performance is still much better compared to displacement-based elements.

3A. Roll-up of a beam (elastica problem). An initially flat shell of length $L = 10$, width $w = 1$ and thickness $t = 0.1$ is subjected to a bending moment as shown in Figure 1. The moment is applied through a linearly varying distributed traction on the right face. The material properties are $E = 12 \times 10^6$ and $\nu = 0$. The *shell* solution for the tip displacements of the midsurface is

$$u = R \sin \frac{X}{R}, \quad v = 0, \quad w = R \left(1 - \cos \frac{X}{R} \right), \quad (3-3)$$

where $R = EI/M$ is the radius of curvature. For $M = 2\pi EI/L$, the beam rolls up into a complete circle. We apply the linearly varying traction corresponding to this value of the moment; note that, since this traction remains normal to the surface as the beam deforms, we have to consider the loading as deformation dependent. The deformed shapes obtained using the S27 and B27 elements, obtained using approximately a total of 60 and 90 iterations, respectively, are shown in Figure 2, and should be compared with the solution in Figure 4 of [Jog and Kelkar 2006], which was obtained using the minimum number of stress interpolation terms, namely 75. It is evident from this figure that the 90β interpolation used in this work does not result in any additional stiffening compared to the 75β interpolation, and continues to perform much better compared to the displacement-based element which not only locks, but also takes more number of iterations to converge. The small deviation from the exact solution seen in the S27 element results could be because the load is not being applied in a manner consistent with the three-dimensional exact solution (since this exact solution is not known), but rather in an approximate



Figure 2. Deformed geometries for the elastica problem obtained using the S27 (left) and the B27 (right) elements.

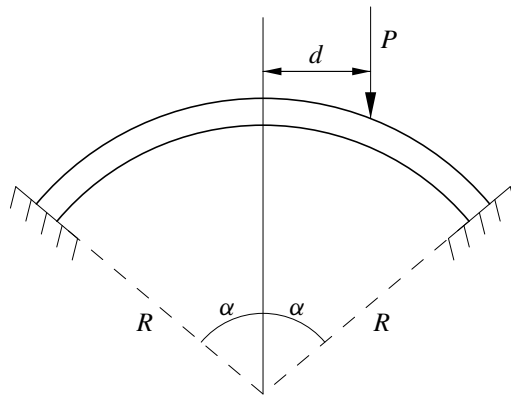


Figure 3. Shallow spherical cap subjected to an asymmetric point load P .

way. Sze et al. [2004b] report having to use more than 700 iterations to solve this problem using shell elements from a commercial software.

3B. Shallow spherical cap subjected to an asymmetric point load. This example was solved in [Danielson and Tielking 1993] using Fourier elements. The setup is shown in Figure 3. The geometric parameters shown are $R = 4.76$ in, $d = 0.328$ in and $\alpha = 10.9^\circ$, and the thickness is 0.01576 in. The material parameters are $E = 10^7$ psi and $\nu = 0.3$. Meshes $n_R \times n_\alpha \times n_\phi$ of $1 \times 7 \times 8$ and $2 \times 14 \times 16$ of higher and lower-order wedge/hexahedral elements are used to discretize the structure. Wedge elements are used in the layer closest to the apex, and hexahedral elements are used elsewhere. The load-deflection curves for the displacement at the apex and under the point load are shown in Figure 4, and should be compared with Danielson and Tielking's Figures 8 and 9. The number of iterations required to converge at each load step is about 4 or 5. As mentioned in their article, this problem is challenging because the shell almost buckles as it folds through: the final deflection at $P = 60$ lb is more than an order of magnitude greater than the linear solution.

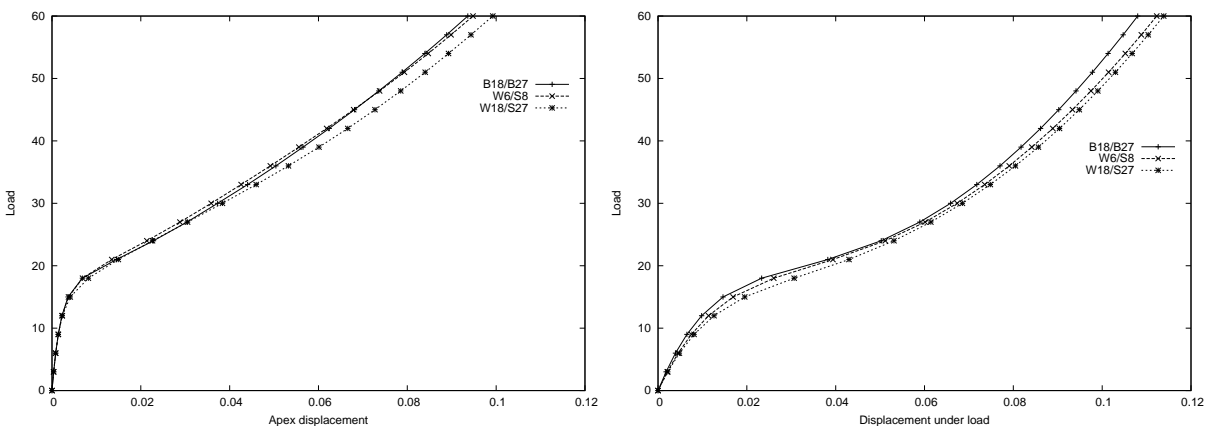


Figure 4. Load deflection curves for apex and loading point for the shallow spherical cap problem.

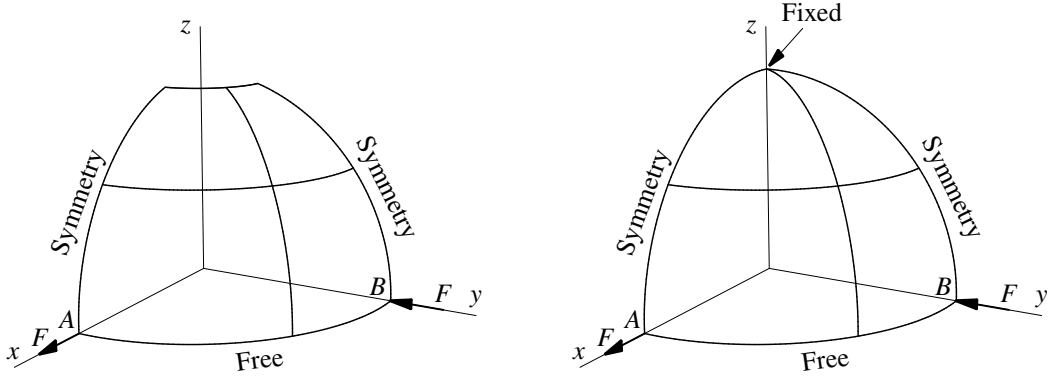


Figure 5. Pinched hemispherical shell with and without an 18° hole; only a quadrant is modelled in both problems due to symmetry.

3C. Hemispherical shell subjected to alternating radial loads. A hemisphere with and without an 18° hole at the top is subjected to pinching loads; only a quadrant is modelled due to symmetry as shown in Figure 5 with $F = 1$ and $F = 200$ for the linear and nonlinear cases respectively. The properties are $E = 6.825 \times 10^7$, $\nu = 0.3$, mean radius $R = 10$, and thickness $h = 0.04$. Meshes of $4 \times 4 \times 2$, $8 \times 8 \times 2$ and $16 \times 16 \times 2$ eight-node brick elements, and $2 \times 2 \times 1$, $4 \times 4 \times 1$ and $8 \times 8 \times 1$ twenty-seven-node brick elements are used in the case where the hemisphere has a hole; meshes with the same number of nodes per side are used for the full hemisphere case, with the layer around to the pole being modelled by wedge elements. For the linear case, the results for the displacement at the point of application of the forces, normalized against the solutions of 0.09355 and 0.0924, are presented in Table 1.

For the nonlinear case, the reference solutions for the displacements at points A and B are 4.067 and 8.178 in the case of the hemisphere with a hole, and 4.0754 and 8.1449 in the case of the hemisphere without a hole [Sze et al. 2004b]. The normalized results are presented in Table 2. The solutions in all

Nodes/side	Hemisphere with hole			Hemisphere without hole		
	B27	S8	S27	B18/B27	W6/S8	W18/S27
5	0.00146	0.0896	0.5879	0.00109	0.0186	0.0437
9	0.02174	0.8645	0.9514	0.01157	0.4120	0.7846
17	0.25715	0.9942	0.9892	0.19478	0.9561	0.9849

Table 1. Normalized displacements for the pinched hemisphere problem: linear case.

Nodes per side	Hemisphere with hole						Hemisphere without hole					
	Point A			Point B			Point A			Point B		
	B27	S8	S27	B27	S8	S27	B18/B27	W6/S8	W18/S27	B18/B27	W6/S8	W18/S27
5	.00669	.30582	.59848	.00334	.20494	.58447	.00494	.08113	.14896	.00267	.04395	.16284
9	.09463	.76729	.82610	.05130	.70661	.76408	.06869	.67206	.79258	.03619	.57386	.72805
17	.50568	.94674	.96256	.37750	.93283	.94663	.45291	.93293	.95312	.30843	.91480	.93710

Table 2. Normalized displacements for the pinched hemisphere problem: nonlinear case.

cases are obtained using a single load step, and the number of iterations is approximately 9 for the hybrid elements, while with the use of the finest mesh, the number of iterations required for the two problems with the displacement-based approach is 21 and 18 respectively.

3D. Thick and thin shell subjected to line loading. This example has been solved in [Reese et al. 2000] using an enhanced strain method. A hollow cylindrical shell of mean radius 9 mm is simply supported at its bottom, and subjected to a uniform line load q at the top as shown in Figure 6. Two cases are considered: (i) a moderately thick shell with $t = 2$ mm and $q = 500$ N/mm, and (ii) a thin shell with $t = 0.2$ mm and $q = 8.5/15$ N/mm. As in that reference, only a quarter of the domain is modelled by using meshes $n_r \times n_\theta \times n_z$ of $1 \times 8 \times 4$, $1 \times 16 \times 8$ and $1 \times 32 \times 16$ 27-node hexahedral elements, and $2 \times 16 \times 8$, $2 \times 32 \times 16$ and $2 \times 64 \times 32$ 8-node hexahedral elements. The material model used is the compressible neo-Hookean model given by (3-1) with $\lambda = 24000$ N/mm² and $\mu = 6000$ N/mm² (the value of λ is stated as 240000 N/mm² in [Reese et al. 2000] due to a typographical error). The variation of the vertical displacement at A with mesh refinement for the thick and thin shells is shown in Figure 7, and should be compared with Reese’s Figure 2.

As can be seen, the displacement-based elements lock severely in the thin shell case, despite our use of a higher-order element. The number of iterations is also substantially more for the displacement-based

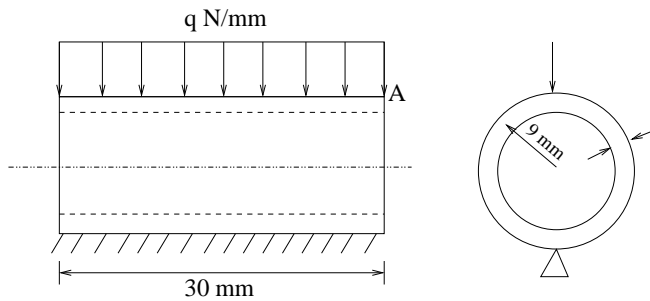


Figure 6. Hollow cylinder subjected to line loading. Only a quarter of the domain is modelled due to symmetry.

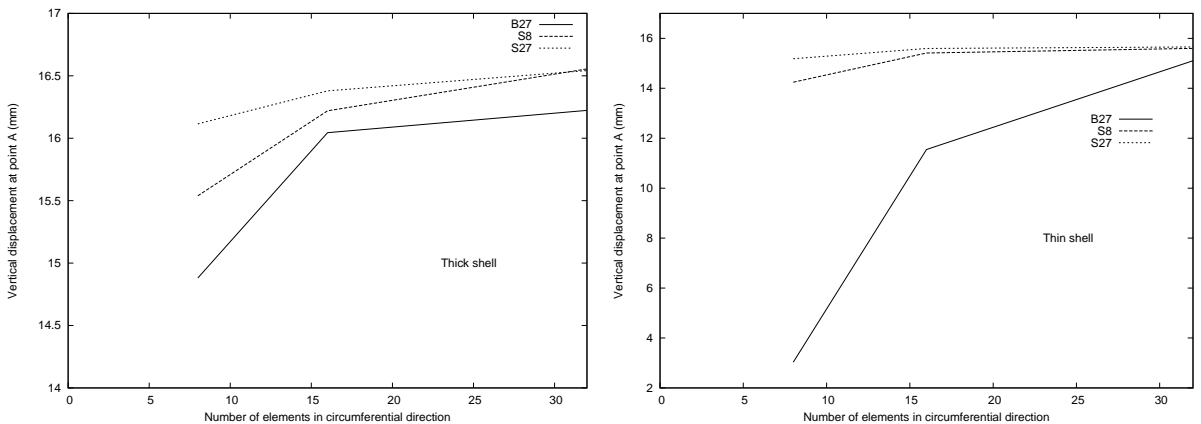


Figure 7. Convergence study for the thick and thin shell examples.

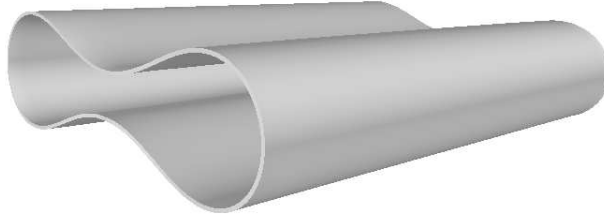


Figure 8. Deformed shape of the thin shell subjected to line load.

elements. Although the performance of the lower-order hybrid elements is slightly poorer compared to their corresponding higher-order hybrid counterparts on coarse meshes, they converge very rapidly with mesh refinement as seen from [Figure 7](#); this is a trend observed in all the examples where a lower-order hybrid element yields slightly poorer results compared to its higher-order counterpart on a coarse mesh. For both the thick and thin shell cases, convergence for both the 8-node and 27-node hexahedral elements is achieved in a single load step and approximately 8 iterations. In contrast, with the finest mesh of B27 elements, convergence is achieved in 5 load steps and a total of 34 iterations for the thick shell case, and 20 load steps and a total of 120 iterations for the thin shell case! To give an idea of the extreme deformation involved in this problem, the deformed shape of the thin shell is shown in [Figure 8](#).

3E. Elastic wave propagation in a circular disk. A part of one face of a circular disk is subjected to an axisymmetric pressure loading while the remainder of the boundary is free of tractions as shown in [Figure 9](#); compare [[Cherukuri and Shawki 1996](#)]. The parameters used are $H = 1$, $R = 1.5$, $r_p = 0.25$, $t_1 = 2 \mu\text{s}$, $t_2 = 5 \mu\text{s}$, $t_3 = 7 \mu\text{s}$, $P = 10^5$, while the material properties are $E = 9.1 \times 10^6$, $\nu = 0.2$ and $\rho = 2.0835 \times 10^{-4}$. A uniform mesh $n_r \times n_z$ of 30×20 A9 elements is used to discretize the domain, and the time step used is $t_\Delta = 0.1 \mu\text{s}$. The energy-momentum conserving algorithm of [[Jog and Motamarri 2009](#)] is used to advance the solution in time. As opposed to the conditionally stable algorithm in [[Cherukuri and Shawki 1996](#)], our time-stepping strategy is unconditionally stable, allowing one to take larger time steps. As noted in this reference, the time required for a longitudinal wave to traverse the thickness once is approximately $4.54 \mu\text{s}$. During the time of interest ($60 \mu\text{s}$), multiple reflections take place, and consequently the numerical strategy should be sufficiently robust to accurately predict the displacements during and after these reflections.

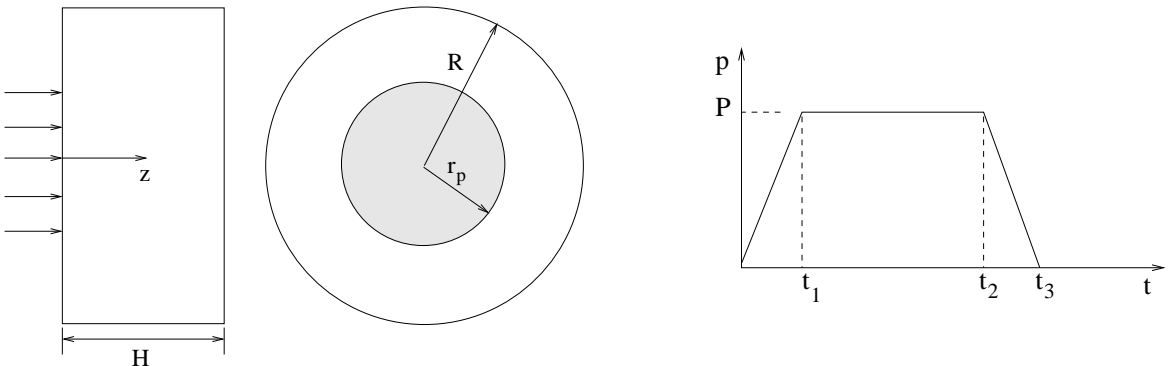


Figure 9. Elastic wave propagation in a circular disk.

The radial and axial displacements obtained using the A9 element are shown in the top two graphs of Figure 10; these should be compared with Figures 10 and 11 of [Cherukuri and Shawki 1996]. Similarly, the radial, longitudinal, shear and hoop stresses are shown in the remaining graphs of Figure 10, which should be compared with Figures 12–15 of the same reference.

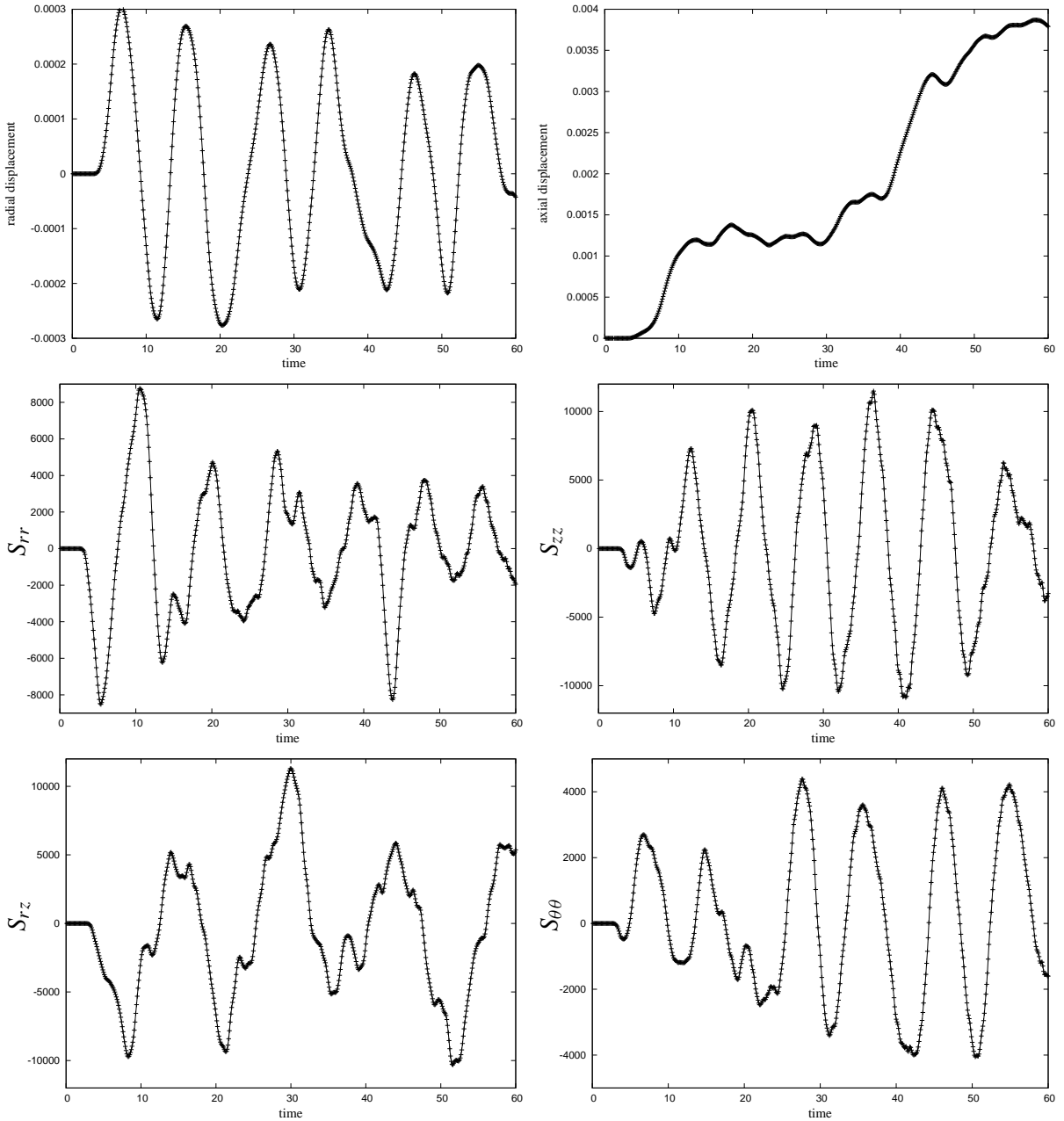


Figure 10. Top row: radial and axial displacement at $(r, z) = (0.7, 0.5)$ as a function of time in the elastic wave propagation problem. Remaining rows: radial, longitudinal, shear and hoop stresses at the same location. Time is measured in μs .

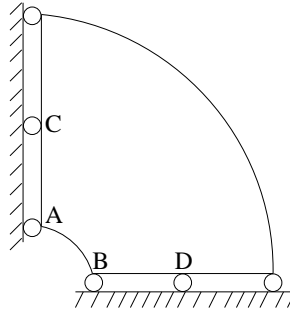


Figure 11. An almost incompressible sphere subjected to internal pressure. Only the part of the domain shown is modelled using axisymmetric elements.

3F. Thick almost incompressible sphere subjected to internal pressure. This example shows the relative immunity of hybrid elements to volumetric locking under finite deformations when the material is an almost incompressible neo-Hookean material [Heisserer et al. 2008]. The inner radius of the sphere is 10 mm and outer radius is 30 mm. Using symmetry, only a part of the domain is modelled using axisymmetric elements as shown in Figure 11. Meshes of 2×2 , 4×4 and 8×8 A9 or B9 elements and 4×4 , 8×8 and 16×16 A4 elements are used to discretize the domain. The neo-Hookean material model given by (3-2) with $c_1 = 0.5$ MPa, $\kappa = 10^5$ MPa (which corresponds to a Poisson ratio of 0.499995) is used. The internal pressure is 1 MPa and the outer surface is traction free. The normalized results for the radial displacement at the inner surface, obtained by using the reference solution of 5.50198336 [Heisserer et al. 2008] are presented in Table 3.

While the displacement-based element locks severely, the performance of the hybrid elements, and especially the A9 element even with a very coarse mesh, is quite remarkable. As already mentioned, adding the higher-order terms to $S_{\theta\theta}$ is critical in ensuring the symmetry of the solution at points A and B, although these terms are not required to remove any zero-energy mode. This is yet another example of an improvement of performance by using more (judiciously chosen) terms in the stress interpolation than the minimum number based purely on elimination of zero-energy modes.

Now consider the linear counterpart of this problem. The inner radius and outer radii of the sphere are now 1 and 5, respectively, and the internal pressure is of unit magnitude. The material properties are $E = 1000$ and $\nu = 0.499$. Uniform meshes of 4×4 , 8×8 and 16×16 A4, and 2×2 , 4×4 and 8×8 A9 meshes are used. The analytical solution for the radial displacement is 7.5556×10^{-4} . The

Nodes/side	Point A			Point B		
	B9	A4	A9	B9	A4	A9
5	0.00040	0.96029	1.01086	0.00040	0.91544	0.99578
9	0.00362	0.99719	1.00278	0.00362	0.97808	1.00094
17	0.05858	1.00076	1.00039	0.05858	0.99447	1.00016

Table 3. Normalized radial displacements at the inner surface in the thick-sphere problem: nonlinear case.

Nodes/side	Point A			Point B		
	B9	A4	A9	B9	A4	A9
5	0.03035	0.80279	0.83023	0.03030	0.80482	0.80708
9	0.14847	0.92708	0.95947	0.14846	0.92369	0.95704
17	0.60879	0.97865	0.99528	0.60881	0.97677	0.99504

Table 4. Normalized radial displacement at the inner surface in the thick-sphere problem: linear case.

Nodes per side	Radial stress						Hoop stress					
	Point C			Point D			Point C			Point D		
	B9	A4	A9	B9	A4	A9	B9	A4	A9	B9	A4	A9
5	-17.857	0.816	-0.601	-17.857	0.881	-0.465	19.579	0.162	3.122	19.579	1.118	3.061
9	-7.068	0.942	0.750	-7.068	0.930	0.772	8.028	0.800	1.201	8.028	0.990	1.179
17	-5.217	0.980	0.948	-5.217	0.977	0.952	6.965	0.952	1.048	6.965	0.993	1.043

Table 5. Normalized radial and hoop stresses in the thick-sphere problem: linear case.

normalized results obtained are presented in Table 4. Note again the severe locking in the displacement-based elements, and the relative immunity of the hybrid elements.

The results for the radial and hoop stresses (in the spherical coordinate system) at points C and D located at the mean radius as shown in Figure 11, normalized against the analytical values of -0.0292712 and 0.0267324 , are presented in Table 5. Note that the even the sign of the radial stress (besides, of course, the magnitude) for the finest B9 mesh is in error.

3G. Circular plate subjected to pressure. A thin circular plate clamped at its outer edge is subjected to pressure loading as shown in Figure 12. This example has been solved using the p-FEM method in [Yosibash et al. 2007]. The neo-Hookean material model given by (3-2) with $c_1 = 0.5$ MPa and $\kappa = 2000$ MPa (which corresponds to a Poisson ratio of 0.49975) is used. We solve this example using both axisymmetric and wedge/hexahedral elements. This example provides an especially good test for the wedge/hexahedral elements since the mesh is distorted (because of the circular domain that is being modelled), the plate is thin, the material is almost incompressible, and the loading is of follower type so that the stiffness matrix depends on the load. Meshes of 8×1 , 16×1 and 32×1 A9 (or B9) elements, 16×2 , 32×2 and 64×2 A4 elements, $8 \times 8 \times 1$ ($n_r \times n_\theta \times n_z$), $16 \times 16 \times 1$ and $32 \times 32 \times 1$ W18/S27 (or

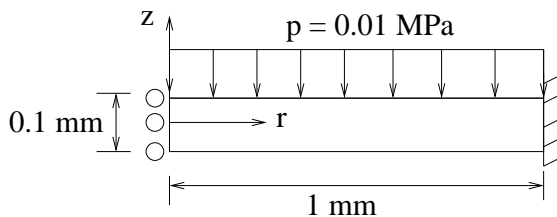


Figure 12. A thin circular plate clamped at its outer edge and subjected to pressure loading.

Nodes/side	Axisymmetric elements			Wedge/hexahedral elements		
	B9	A4	A9	B18/B27	W6/S8	W18/S27
17	0.85562	0.99302	0.98709	0.85559	0.99018	0.98555
33	0.88409	0.99755	0.99524	0.88409	0.99649	0.99456
65	0.89663	0.99996	0.99847	0.89661	0.99956	0.99822

Table 6. Normalized vertical displacement at the center of the top surface of the thin circular plate: nonlinear analysis.

B18/B27) elements, and $16 \times 16 \times 2$, $32 \times 32 \times 2$ and $64 \times 64 \times 2$ W6/S8 elements are used. In the case of wedge/hexahedral elements, only a quarter of the plate is modelled with wedge elements used in the layer closest to the center, and hexahedral elements elsewhere. The displacements at the center of the top surface normalized against the reference solution of 0.182647 [Yosibash et al. 2007] are presented in Table 6.

Note that the results obtained using wedge/hexahedral elements, inspite of the mesh distortion, are almost as good as those obtained using axisymmetric elements. The results for all the hybrid elements are obtained within a total of only 12 iterations. In contrast, the displacement-based elements not only converge very slowly, but also require approximately 280 iterations (spread over 50 load steps) to obtain the solution.

Now consider the linear counterpart of the problem. A simply-supported circular plate of radius 10, and with $\nu = 0.3$, is subjected to a unit pressure load on the top surface. Two cases are considered (i) $E = 10^4$, $h = 1$ (“thick plate”), and (ii) $E = 10^{10}$, $h = 0.01$ (“thin plate”). The analytical solutions for the center-point deflection are 0.70388 and 0.69563, respectively. The normalized results for the center-point deflection are presented in Table 7.

Note the exceptionally high accuracy of the hybrid axisymmetric elements, even when the thickness/radius ratio is as small as 1/1000. One of the interesting features of the stress solution in the thin plate case is that while the A4, A9 and W18/S27 elements yield transverse shear stress values at the

Nodes/side	Thick plate ($h = 1$)					
	B18/B27	W6/S8	W18/S27	B9	A4	A9
5	0.94419	0.88661	0.98465	0.97980	1.02418	1.00277
9	0.99256	0.98659	0.99551	0.99616	1.00749	0.99853
17	0.99551	0.99640	0.99580	0.99607	0.99753	0.99608

Nodes/side	Thin plate ($h=0.01$)					
	B18/B27	W6/S8	W18/S27	B9	A4	A9
5	0.12700	0.63708	0.44493	0.95746	1.02555	1.00453
9	0.66715	0.87905	0.80732	0.98996	1.00898	0.99954
17	0.93986	0.96304	0.97489	0.99984	1.00020	0.99989

Table 7. Normalized center-point displacements in the simply-supported circular plate problem: linear analysis.

center of the plate that are close to zero, the B9 element yields values ranging from 175 to 2600, while the other elements in the table, and the W21 of [Jog 2005] yield values of the order of 10^5 !

3H. Large strain vibration of a long half cylinder. The base of a half-cylinder travelling with a uniform initial velocity v is suddenly brought to rest as shown in Figure 13, left, due to which it vibrates from left to right. This example was solved in [Bonet et al. 2001] using an averaged nodal deformation gradient formulation. The neo-Hookean material model given by (3-2) is used, with $c_1 = 1.7855 \times 10^5$ Pa and $\kappa = 1.667 \times 10^6$ Pa, and the density is 1000 kg/m^3 . Uniform meshes $n_r \times n_\theta \times n_z$ of $4 \times 8 \times 40$ W18/S27 (or B18/B27) and $8 \times 16 \times 80$ W6/S8 elements, and a time step $t_\Delta = 0.0025$ s is used. The deformed centerline at various times is shown in Figure 14, left, and should be compared with Figure 4 of [Bonet et al. 2001].

Although the solutions are shown for the W18/S27 mesh, almost identical solutions are obtained with the W6/S8 and B18/B27 meshes. Moreover, almost identical solutions are also obtained with coarser meshes of $2 \times 4 \times 20$ W18/S27 (or B18/B27) and $4 \times 8 \times 40$ W6/S8 elements, and a time step $t_\Delta = 0.005$ s, showing convergence with respect to mesh refinement. Since the velocity is zero at the base, and since the remaining surface is traction free, the total energy (kinetic+strain energy) should be conserved by the numerical algorithm. As is seen from Figure 14, right, this is achieved by our numerical algorithm. We would like to state that the use of an interpolation obtained by *excluding* Rule (2) fails to converge (after a few time steps) on this problem showing the importance of this rule.

3I. Inflation of a square airbag. This example, in which a flat square isotropic membrane is gradually inflated by a constant pressure until its magnitude reaches 5 kPa, has been solved using a wrinkling model in [Jarasjarungkiat et al. 2009]. The geometry and material properties are shown in Figure 13, right.

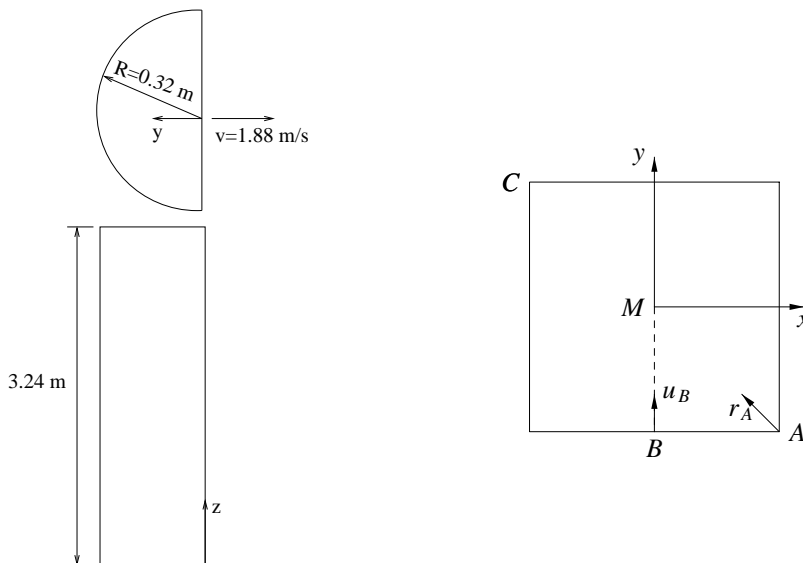


Figure 13. Left: geometry and initial conditions for the long half cylinder problem. Right: geometry and material properties for the airbag problem. The thickness is 0.06 cm , the length AC is 120 cm , and $E = 58.8 \text{ kN/cm}^2$, $\nu = 0.4$.

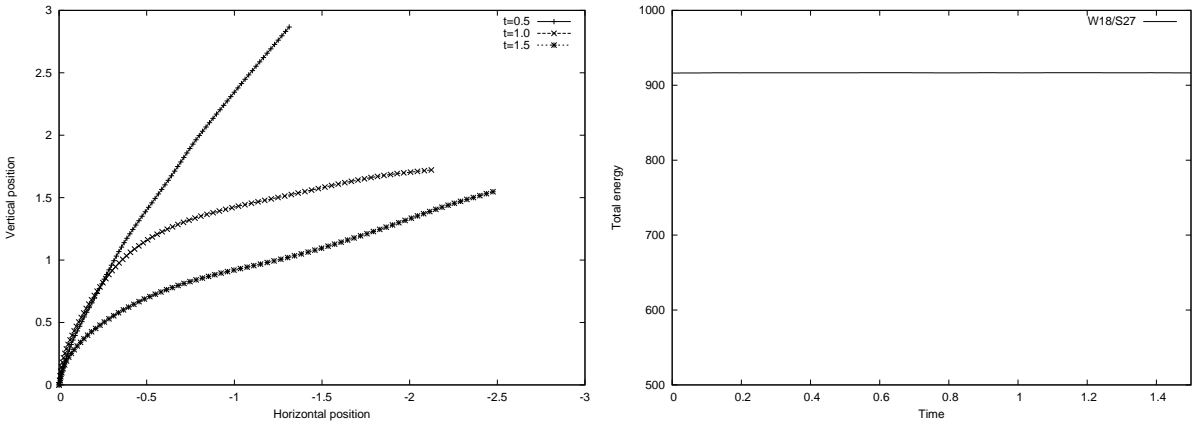


Figure 14. Long half cylinder problem, W18/S27 mesh: deformed centerline of the semicircle at various times (left) and total energy as a function of time (right).

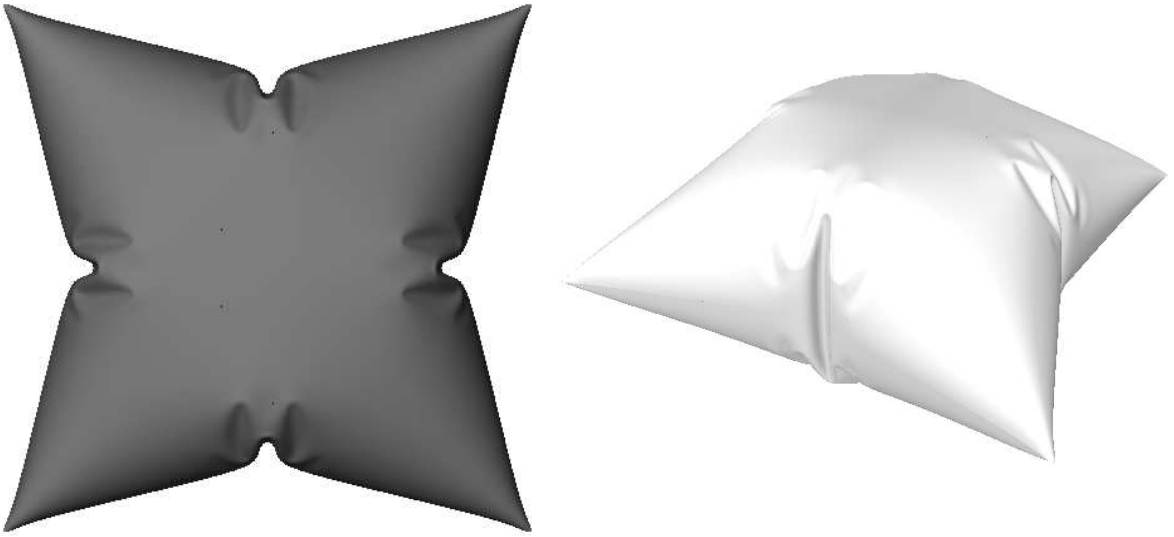


Figure 15. Top and isometric views of the inflated airbag.

Due to the presence of wrinkles, the stiffness matrix can become singular, and hence we solve this problem using the transient algorithm described in [Jog and Motamarri 2009] with an appropriate amount of damping to damp out the transients, and reach to a steady-state solution. A $50 \times 50 \times 1$ mesh of 27-node hybrid hexahedral elements is used to discretize a quarter of the domain due to symmetry. The total pressure of 5 kPa is applied gradually in a linearly varying fashion over the time interval $[0, 5]$, and then maintained constant after that. The time step used in the transient analysis is $t_{\Delta} = 0.002$. The values of density ρ and damping parameter α used are 2700 kg/m^3 and 10^6 , respectively. The steady-state solution is reached after 6 seconds, and is shown in Figure 15.

In contrast to solutions obtained using wrinkle models, the strategy above yields the details of the wrinkles (including the wavelength and amplitude), and accurate values of stresses within the entire

membrane. The values of the displacement w_M , r_A and u_B (in cm) obtained using our method are (21.45, 4.63, 16.63), while the values presented in [Jarasjarungkiat et al. 2009] are (21.669, 6.92, 12.37). The reason for the significant difference in the displacement at point B is that, in reality, there is a sharp ridge around that point (see Figure 15), which is smoothed out when one uses a wrinkle model, as in Figure 6 of that reference.

4. Conclusions

The use of a minimal stress interpolation that does not satisfy the rules enumerated in this work, often results in instabilities, non-convergence or spurious stresses. As shown by means of several examples, stress interpolations obeying these rules result in increased robustness. Although the number of interpolation terms in some of the higher-order elements, such as the 27-node hexahedral and the 9-node axisymmetric elements, is much more than the minimum required, their performance continues to be far superior to the displacement-based elements, and in many problems superior to the 8-node hexahedral and 4-node axisymmetric hybrid elements, respectively. More importantly, they result in far greater robustness, especially in transient simulations, where, as our numerical experiments show, stable solutions are obtained even over very long time simulations. Another advantage is that the rules enumerated, since they require the polynomials to be complete in some sense, result in a unique interpolation function for the stresses. One of the interesting conclusions in the case of the 8-node and 27-node hexahedral elements, the 18-node wedge element, and the 4-node and 9-node axisymmetric elements is that for a robust formulation, the normal stress interpolations (except, of course, the hoop stress interpolation in the case of axisymmetric elements) are obtained simply by differentiating the displacement field, while the interpolations for the shear stress components S^{ij} are composed of terms that are common to the interpolations for the normal stresses S^{ii} and S^{jj} .

References

- [Bonet et al. 2001] J. Bonet, H. Marriott, and O. Hassan, “An averaged nodal deformation gradient linear tetrahedral element for large strain explicit dynamic applications”, *Comput. Methods Appl. Mech. Engrg.* **17** (2001), 551–561.
- [Cherukuri and Shawki 1996] H. P. Cherukuri and T. G. Shawki, “A finite-difference scheme for elastic wave propagation in a circular disk”, *J. Acoust. Soc. Amer.* **100**:4 (1996), 2139–2155.
- [Danielson and Tielking 1993] K. T. Danielson and J. T. Tielking, “Fourier continuum finite elements for large deformation problems”, *Comput. and Structures* **49** (1993), 133–147.
- [Gupta 2000] A. Gupta, “WSMP: Watson Sparse Matrix Package, II: direct solution of general sparse systems”, Research Report RC 21888 (98472), IBM, 2000.
- [Gupta 2002] A. Gupta, “Recent advances in direct methods for solving unsymmetric sparse systems of linear equations”, *ACM Trans. Math. Software* **28**:3 (2002), 301–324.
- [Heisserer et al. 2008] U. Heisserer, S. Hartmann, A. Düster, and Z. Yosibash, “On volumetric locking-free behaviour of p -version finite elements under finite deformations”, *Comm. Numer. Methods Engrg.* **24**:11 (2008), 1019–1032.
- [Jarasjarungkiat et al. 2009] A. Jarasjarungkiat, R. Wuchner, and K. U. Bletzinger, “Efficient sub-grid scale modeling of membrane wrinkling by a projection method”, *Comput. Methods Appl. Mech. Engrg.* **198** (2009), 1097–1116.
- [Jog 2005] C. S. Jog, “A 27-node hybrid brick and a 21-node hybrid wedge element for structural analysis”, *Finite Elem. Anal. Des.* **41** (2005), 1209–1232.
- [Jog and Annabattula 2006] C. S. Jog and R. Annabattula, “The development of hybrid axisymmetric elements based on the Hellinger–Reissner variational principle”, *Internat. J. Numer. Methods Engrg.* **65** (2006), 2279–2291.

- [Jog and Kelkar 2006] C. S. Jog and P. P. Kelkar, “Non-linear analysis of structures using high performance hybrid elements”, *Internat. J. Numer. Methods Engrg.* **68**:4 (2006), 473–501.
- [Jog and Motamarri 2009] C. S. Jog and P. Motamarri, “An energy-momentum conserving algorithm for nonlinear transient analysis within the framework of hybrid elements”, *J. Mech. Mater. Structures* **4**:1 (2009), 157–186.
- [Lee and Rhiu 1986] S. W. Lee and J. J. Rhiu, “A new efficient approach to the formulation of mixed finite element models for structural analysis”, *Internat. J. Numer. Methods Engrg.* **23** (1986), 1629–1641.
- [Lo and Ling 2000] S. H. Lo and C. Ling, “Improvement on the 10-node tetrahedral element for three-dimensional problems”, *Comput. Methods Appl. Mech. Engrg.* **189** (2000), 961–974.
- [Pian and Sumihara 1984] T. H. H. Pian and K. Sumihara, “Rational approach for assumed stress finite elements”, *Internat. J. Numer. Methods Engrg.* **20** (1984), 1685–1695.
- [Pian and Tong 1986] T. H. H. Pian and P. Tong, “Relations between incompatible displacement model and hybrid stress model”, *Internat. J. Numer. Methods Engrg.* **22**:1 (1986), 173–181.
- [Punch and Atluri 1984] E. F. Punch and S. N. Atluri, “Development and testing of stable, invariant, isoparametric curvilinear 2- and 3-d hybrid-stress elements”, *Comput. Methods Appl. Mech. Engrg.* **47** (1984), 331–356.
- [Reese et al. 2000] S. Reese, P. Wriggers, and B. D. Reddy, “A new locking-free brick element technique for large deformation problems in elasticity”, *Comput. and Structures* **75**:3 (2000), 291–304.
- [Rhiu and Lee 1987] J. J. Rhiu and S. W. Lee, “A new efficient mixed formulation for thin shell finite element models”, *Internat. J. Numer. Methods Engrg.* **24** (1987), 581–604.
- [Simo et al. 1989] J. C. Simo, D. D. Fox, and M. S. Rifai, “On a stress resultant geometrically exact shell model, II: the linear theory; computational aspects”, *Comput. Methods Appl. Mech. Engrg.* **73**:1 (1989), 53–92.
- [Sze et al. 2004a] K. Y. Sze, X. H. Liu, and S. H. Lo, “Hybrid-stress six-node prismatic elements”, *Internat. J. Numer. Methods Engrg.* **61** (2004), 1451–1470.
- [Sze et al. 2004b] K. Y. Sze, X. H. Liu, and S. H. Lo, “Popular benchmark problems for geometric nonlinear analysis of shells”, *Finite Elem. Anal. Des.* **40** (2004), 1551–1569.
- [Xue et al. 1985] W.-M. Xue, L. A. Karlovitz, and S. N. Atluri, “On the existence and stability conditions for mixed-hybrid finite element solutions based on Reissner’s variational principle”, *Internat. J. Solids Structures* **21**:1 (1985), 97–116.
- [Yosibash et al. 2007] Z. Yosibash, S. Hartmann, U. Heisserer, and A. Duster, “Axisymmetric pressure boundary loading for finite deformation analysis using p-FEM”, *Comput. Methods Appl. Mech. Engrg.* **196** (2007), 1261–1277.

Received 17 Feb 2010. Revised 28 Jun 2010. Accepted 1 Jul 2010.

C. S. JOG: jogc@mecheng.iisc.ernet.in

Department of Mechanical Engineering, Indian Institute of Science, Bangalore 560012, India

SUBMISSION GUIDELINES

ORIGINALITY

Authors may submit manuscripts in PDF format online at the Submissions page. Submission of a manuscript acknowledges that the manuscript is original and has neither previously, nor simultaneously, in whole or in part, been submitted elsewhere. Information regarding the preparation of manuscripts is provided below. Correspondence by email is requested for convenience and speed. For further information, write to one of the Chief Editors:

Davide Bigoni	bigoni@ing.unitn.it
Iwona Jasiuk	ijasiuk@me.concordia.ca
Yasuhide Shindo	shindo@material.tohoku.ac.jp

LANGUAGE

Manuscripts must be in English. A brief abstract of about 150 words or less must be included. The abstract should be self-contained and not make any reference to the bibliography. Also required are keywords and subject classification for the article, and, for each author, postal address, affiliation (if appropriate), and email address if available. A home-page URL is optional.

FORMAT

Authors can use their preferred manuscript-preparation software, including for example Microsoft Word or any variant of \LaTeX . The journal itself is produced in \LaTeX , so accepted articles prepared using other software will be converted to \LaTeX at production time. Authors wishing to prepare their document in \LaTeX can follow the example file at www.jomms.org (but the use of other class files is acceptable). At submission time only a PDF file is required. After acceptance, authors must submit all source material (see especially Figures below).

REFERENCES

Bibliographical references should be complete, including article titles and page ranges. All references in the bibliography should be cited in the text. The use of Bib \TeX is preferred but not required. Tags will be converted to the house format (see a current issue for examples); however, for submission you may use the format of your choice. Links will be provided to all literature with known web locations; authors can supply their own links in addition to those provided by the editorial process.

FIGURES

Figures must be of publication quality. After acceptance, you will need to submit the original source files in vector format for all diagrams and graphs in your manuscript: vector EPS or vector PDF files are the most useful. (EPS stands for Encapsulated PostScript.)

Most drawing and graphing packages—Mathematica, Adobe Illustrator, Corel Draw, MATLAB, etc.—allow the user to save files in one of these formats. Make sure that what you're saving is vector graphics and not a bitmap. If you need help, please write to graphics@mathscipub.org with as many details as you can about how your graphics were generated.

Please also include the original data for any plots. This is particularly important if you are unable to save Excel-generated plots in vector format. Saving them as bitmaps is not useful; please send the Excel (.xls) spreadsheets instead. Bundle your figure files into a single archive (using zip, tar, rar or other format of your choice) and upload on the link you been given at acceptance time.

Each figure should be captioned and numbered so that it can float. Small figures occupying no more than three lines of vertical space can be kept in the text (“the curve looks like this:”). It is acceptable to submit a manuscript with all figures at the end, if their placement is specified in the text by means of comments such as “Place Figure 1 here”. The same considerations apply to tables.

WHITE SPACE

Forced line breaks or page breaks should not be inserted in the document. There is no point in your trying to optimize line and page breaks in the original manuscript. The manuscript will be reformatted to use the journal's preferred fonts and layout.

PROOFS

Page proofs will be made available to authors (or to the designated corresponding author) at a Web site in PDF format. Failure to acknowledge the receipt of proofs or to return corrections within the requested deadline may cause publication to be postponed.

Chaotic vibrations in a damage oscillator with crack closure effect NOËL CHALLAMEL and GILLES PIJAUDIER-CABOT	369
Elastic buckling capacity of bonded and unbonded sandwich pipes under external hydrostatic pressure KAVEH ARJOMANDI and FARID TAHERI	391
Elastic analysis of closed-form solutions for adhesive stresses in bonded single-strap butt joints GANG LI	409
Theoretical and experimental studies of beam bimorph piezoelectric power harvesters SHUDONG YU, SIYUAN HE and WEN LI	427
Shakedown working limits for circular shafts and helical springs subjected to fluctuating dynamic loads PHAM DUC CHINH	447
Wave propagation in carbon nanotubes: nonlocal elasticity-induced stiffness and velocity enhancement effects C. W. LIM and Y. YANG	459
Dynamic compressive response of composite corrugated cores BENJAMIN P. RUSSELL, ADAM MALCOM, HAYDN N. G. WADLEY and VIKRAM S. DESHPANDE	477
Effects of surface deformation on the collective buckling of an array of rigid beams on an elastic substrate HAOJING LIN, ZIGUANG CHEN, JIASHI YANG and LI TAN	495
Improved hybrid elements for structural analysis C. S. JOG	507